Petit périple aux confins du modèle standard avec HERA

E. Sauvan

CPPM-H-2009-3

Université de la Méditerranée
Aix-Marseille II
Faculté des sciences de Luminy
163, avenue de Luminy – 13288 Marseille cedex 09 – FRANCE

HABILITATION A DIRIGER DES RECHERCHES
Spécialité : Physique des Particules

présentée par

Emmanuel SAUVAN

Petit périple aux confins du modèle standard avec HERA

Soutenue le 30 octobre 2009
devant le jury composé de :

Dr	**P. BLOCH**	Rapporteur
Pr	**W. BUCHMÜLLER**	Rapporteur
Pr	**M.-C. COUSINOU**	
Dr	**E. GALLO**	Rapporteur
Dr	**J.-F. GRIVAZ**	
Dr	**E. KAJFASZ**	Président
Dr	**C. VALLÉE**	

Remerciements

Voici donc la page la plus importante de ce mémoire d'habilitation à diriger des recherches. En lui-même, ce mémoire constitue surtout un exercice de style visant à résumer quelques uns des travaux de recherche que j'ai pu mener au cours de ces huit dernières années. Mais, toute recherche est un travail collectif par nature, basé avant tout sur des échanges d'idées et de compétences. Ainsi, nombre des résultats présentés dans ce mémoire n'auraient pu voir le jour sans l'aide de nombreuses personnes, que je tiens à remercier ici.

Je commencerai par remercier l'ensemble de la collaboration H1, pour l'ambiance chaleureuse qui y règne, pour de longues discussions de physique et de stimulantes passe d'armes. H1 fut un agréable terrain de jeu durant ces huit années passées. Pourquoi en effet faire de la physique, si ce n'est pour garder une âme d'enfant, toujours émerveillé devant un train électrique géant ou tout excité face à quelques petites fluctuations d'événements ?

Malgré le temps important passé à Hambourg, ce travail a principalement été réalisé grâce au support du CPPM. Je tiens donc ici à remercier l'ensemble de son personnel, pour sa bonne humeur, sa disponibilité et surtout pour nous faciliter le quotidien par la prise en charge de toutes ces petites tracasseries administratives ... Un remerciement particulier à Magali Damoiseaux avec qui j'ai pris un grand plaisir à travailler sur quelques expositions grand public ou actions de communication. Merci pour ton enthousiasme constant. Il reste important de faire découvrir, voir peut être aimer, notre métier de chercheur aux générations futures.

Je remercie Madame Elisabetta Gallo et Messieurs Philippe Bloch et Wilfried Buchmüller pour m'avoir fait l'honneur et le plaisir d'être les rapporteurs de ce travail, ainsi que Madame Marie-Claude Cousinou et Monsieur Jean-François Grivaz pour avoir accepté de faire partie du jury. Merci à Eric Kajfasz, actuel directeur du CPPM, pour m'avoir incité à rédiger cette habilitation et pour son soutien à mes travaux dans H1, ainsi qu'à mes autres projets futurs. Merci à Claude Vallée pour m'avoir accueilli dans le groupe H1 du CPPM et avoir su me faire confiance et me laisser une totale liberté dans mes choix et orientations de travail.

Enfin, je tiens à remercier tout particulièrement tous les amies et amis que j'ai pu croiser au cours de ces années passées sur l'expérience H1, et avec qui j'ai pris beaucoup de plaisir à collaborer sur les différents sujets évoqués dans ce mémoire. Sans eux, beaucoup de ces résultats n'auraient probablement pas vu le jour, pas sous cette forme en tous cas. Un très grand merci et toute mon amitié donc à Gerhard Brandt, Cristi Diaconu, Matti Peez, Emmanuelle Perez, Benjamin Portheault, Florian Rothmaier, Laurent Schoeffel et Thi Nguyet Trinh.

Je laisserai le mot de la fin à Boris Vian, sorte de clin d'oeil à ma famille et au monde de la recherche : *« Voilà des mois et des années que j'essaye d'augmenter la portée de ma bombe et je n'me suis pas rendu compte que la seule chose qui compte, c'est l'endroit où c'qu'elle tombe »* ...

(...)
L'interview est alors arrêtée momentanément et reprend
dans le bureau du professeur Feynman.
Mais le magnétophone s'obstine à ne pas vouloir marcher;
après avoir vérifié que le fil et les diverses touches sont bien en place,
Feynman suggère simplement d'enlever puis de remettre la cassette.

Feynman : *Voilà, ça y est. Vous voyez. Y a qu'à connaître le monde !*
C'est ça la physique !
Omni : *Démonter et remonter ?*
Feynman : *Oui. Il y a toujours quelque part une petite cochonnerie ...*
ou une divergence infinie ...
quelque chose, en tout cas.

R. P. Feynman, 1979, interview pour la revue Omni.

Table des matières

Introduction

L'objectif principal de la recherche en physique des particules est de comprendre et de pouvoir décrire la structure de la matière et ses interactions. Selon l'état actuel de nos connaissances, les constituants fondamentaux de la matière sont des fermions, les leptons et les quarks, caractérisés par le nombre leptonique et la saveur des quarks et que l'on peut classer en trois familles. Les leptons sont des particules libres pouvant être détectées. Les quarks, quant à eux, n'existent que sous forme d'états liés, les hadrons. Leur existence peut être déduite des mesures expérimentales des interactions entre particules et de la production de hadrons. La liaison de ces particules entre elles et la cohésion de notre univers semble être assurée par seulement quatre forces : les interactions électromagnétique, faible, forte et gravitationnelle. Seules les trois premières jouent un rôle dans l'étude microscopique de notre univers. Leur description dans un même cadre théorique basé sur des théories de jauge constitue ce que nous appelons communément le modèle standard (MS).

Dans le modèle standard, la description des interactions électromagnétique et faible est basée sur les groupes $SU(2)_L$ d'isospin faible et $U(1)_Y$ d'hypercharge faible. La symétrie est brisée spontanément à ~ 100 GeV en introduisant dans la théorie des mésons scalaires, appelées particules de Higgs. Nous trouvons alors des bosons vecteurs massifs, neutre (Z^0) et chargés ($W^{\pm}$) qui véhiculent l'interaction faible et un boson vecteur neutre sans masse, le photon. Les progrès tant expérimentaux que théoriques accomplis dans la description du secteur électrofaible sont énormes. Les bosons $W^{\pm}$ et Z^0 ont été découverts auprès du collisionneur proton-antiproton du CERN en 1983, et, grâce aux deux collisionneurs électron-positron de haute énergie qu'étaient le SLC et surtout le LEP, les paramètres électrofaibles du MS ont pu être mesurés avec une extrême précision. Les prédictions théoriques et les mesures expérimentales sont en accord à mieux que 10^{-3}. Le boson de Higgs reste cependant la seule inconnue de ce modèle. Les ajustements globaux des paramètres du secteur électrofaible permettent cependant de contraindre sa masse. Actuellement, la valeur centrale de l'ajustement prédit une masse du Higgs de 83^{+30}_{-23} GeV, sans considérer les limites de recherches directes posées par le LEP et, récemment, par le Tevatron. Si ces limites sont prises en compte, la valeur alors prédite pour la masse du boson de Higgs est de $116^{+16}_{-1.3}$ GeV.

Les interactions de quarks et de gluons sont décrites par la chromodynamique quantique (QCD), une théorie de jauge non abélienne basée sur le groupe des symétries de couleurs $SU(3)_C$. La couleur est l'équivalent de la charge électrique des interactions électromagnétiques. Les quarks, chacun de trois couleurs, interagissent par échange de bosons vecteurs électriquement neutres, les gluons, qui forment un octet de couleur. Les gluons ne sont pas neutres de couleur et donc interagissent fortement entre eux. La constante de couplage fort α_s dépend de l'échelle à laquelle le processus QCD a lieu. La solution des équations du

groupe de renormalisation à l'ordre dominant donne :

$$\alpha_s(Q^2) = \frac{4\pi}{\beta_0 \ln(Q^2/\Lambda^2_{QCD})}\,, \tag{1}$$

où Q^2 représente l'échelle à laquelle α_s est sondée et Λ_{QCD} est un paramètre de *cutoff* QCD. Le paramètre β_0 dépend du nombre de saveurs de quarks de la théorie, N_f : $\beta_0 = 11 - 2/3N_f$. Le nombre de saveurs de quarks connues étant de 6, $\beta_0 > 0$ et la constante de couplage diminue à mesure que l'échelle Q^2 augmente. Cette propriété, dite de liberté asymptotique, a été prouvée de manière rigoureuse et est utilisée pour faire des prédictions sur les propriétés des interactions fortes dans le régime perturbatif de QCD, où α_s est faible. Une autre propriété importante de QCD est le confinement qui conserve les quarks liés en hadrons neutre de couleurs et empêche donc toute observation de quarks libres.

En QCD, le degré de liberté de couleur et le confinement expliquent pourquoi les hadrons observés sont constitués soit d'une paire $q\bar{q}$, les mésons, soit de trois quarks qqq (ou antiquarks $\bar{q}\bar{q}\bar{q}$), les baryons. Ces combinaisons assurent que les hadrons soient sans couleur et de charge électrique entière. Le modèle naïf dans lequel les hadrons sont vus comme composés uniquement de quarks ou d'antiquarks libres est appelé le modèle des quarks-partons. Cette image naïve des hadrons doit être modifiée en QCD de façon à prendre en compte les radiations et absorptions de gluons par les quarks, ainsi que les créations de paires $q\bar{q}$ par les gluons. Ainsi, les hadrons sont en fait constitués de quarks et de gluons et nous savons maintenant qu'environ 50% de l'impulsion du proton est en fait portée par les gluons.

La QCD a deux propriétés qui la rendent bien plus difficile à manipuler sur le plan théorique que la théorie électrofaible. Premièrement la constante de couplage α_s est grande, ce qui rend l'emploi des calculs perturbatifs difficile. Deuxièmement, de par la nature non-abélienne de l'interaction, les gluons peuvent interagir entre eux, conduisant au confinement de la couleur. Les distributions de partons des hadrons ne peuvent actuellement être calculées à partir des principes premiers de la QCD. En effet, les calculs doivent alors être faits dans un régime de la QCD où l'approche perturbative n'est pas applicable. Cependant, grâce au théorème de factorisation [Col85], les sections efficaces de réactions dures entre hadrons peuvent être décomposées en un flux universel de partons et une section efficace dure du sous-processus entre partons. La mesure des distributions de partons devient alors un élément essentiel pour tester la validité de la QCD, et calculer les sections efficaces de processus durs impliquant des hadrons.

La QCD a été testée en détail dans le régime perturbatif et permet de bien décrire les mesures. Cependant, les observables expérimentales étant basées sur des états finals de hadrons, plutôt que de partons sur lesquels les calculs perturbatifs s'appliquent, le degré de précision des tests de la QCD reste inférieur à celui des interactions électrofaibles. De plus, jusqu'à maintenant il est très difficile de décrire les processus QCD dans le régime non perturbatif, processus dits mous (*softs*).

Dans ce régime non perturbatif, l'approche phénoménologique de la théorie de Regge [Reg59, Reg60] fournit encore la meilleure description des sections efficaces que nous ayons. A cause de la propriété de confinement de l'interaction forte, à bas transfert d'impulsion, la sous-structure des hadrons n'est pas résolue et l'interaction forte résiduelle a lieu entre des hadrons composites, plutôt qu'entre les quarks et gluons eux-mêmes. La propriété de confinement de la QCD peut être incorporée dans une image où l'interaction forte périphérique qui a lieu entre hadrons n'est pas vue en termes d'échange de bosons de jauge

mais due à l'échange de groupes de partons colorés, incluant des hadrons virtuels singulet de couleur.

Ainsi, la QCD est encore pour une grande part une théorie non résolue. La justification de l'usage de la QCD perturbative (pQCD) reste très largement basée sur l'expérience. Chaque processus d'interaction forte implique une large gamme d'échelles différentes, où la valeur de α_s peut radicalement changer. Ceci, ajouté à un peu d'arbitraire dans la troncature du développement perturbatif, conduit à des incertitudes théoriques non négligeables. Une meilleure compréhension de la transition entre régimes perturbatif et non-perturbatif pourrait donc permettre de les réduire.

Le MS des interactions électrofaible et forte a été confirmé de façon remarquable par l'expérience au cours de ces 30 dernières années. Il reste cependant incomplet et peu satisfaisant par certains aspects et nous pensons qu'il n'est qu'une manifestation à basse énergie d'une théorie plus générale. De nombreuses questions fondamentales restent encore sans réponse dans le cadre du MS.

Ainsi l'observation de trois familles similaires de fermions n'est pas expliquée et pourrait indiquer l'existence d'une nouvelle échelle de sous-structures plus fondamentales.

Le spectre de masse des particules n'est pas expliqué. Dans le MS, les particules acquièrent leur masse via le mécanisme de Higgs, brisure spontanée de la symétrie conduisant à la présence d'une particule scalaire, le boson de Higgs qui reste encore à ce jour non observé. A supposer que le boson de Higgs puisse être observé, le MS lui-même ne peut expliquer la hiérarchie observée des masses des différentes particules, ainsi que l'immense différence entre la masse des bosons faibles, définissant l'échelle de l'interaction faible et la masse de Planck, définissant l'échelle de l'interaction gravitationnelle.

La gravitation n'est elle-même pas incluse dans le cadre théorique du MS, ce qui empêche alors la description de processus à très haute énergie, lorsque les effets de la gravitation ne peuvent être négligés.

Enfin, le MS ne propose aucune particule qui pourrait expliquer la présence de matière noire dans l'univers. Selon les observations cosmologiques actuelles, seulement 4% de la densité totale d'énergie de l'univers proviendrait de la matière *visible*, décrite par le MS, le reste étant composé de matière noire ($\sim 22\%$) et d'énergie noire ($\sim 74\%$), la nature de ces deux dernières composantes restant totalement inconnue.

Le modèle standard de la physique des particules, malgré son pouvoir prédictif incontestable, reste donc avant tout un modèle avec un champ d'application limité. Nous pouvons ainsi distinguer trois grandes frontières au pouvoir prédictif du MS, à l'heure actuelle.

La première concerne la précision des prédictions du MS. En effet, celle-ci dépend, entre autres, des paramètres du modèle, dont les valeurs doivent être déterminées expérimentalement. Dans ce domaine, un des déficits important du MS concerne la description de la structure interne du proton. Actuellement, cette dernière ne peut en effet être déterminée qu'expérimentalement, par la mesure des densités de partons qui constituent le proton. Il s'agit pourtant d'un des ingrédients majeurs dans le calcul des sections efficaces des processus en collisions hadroniques.

Une seconde limitation actuelle du MS est la complexité, qui concerne principalement le secteur de la QCD et des processus de basse énergie. En effet, les calculs de processus régis par l'interaction forte deviennent très complexes hors du domaine d'application du traitement perturbatif ainsi que dans le cas de systèmes denses.

Enfin, différents déficits conceptuels du MS laissent actuellement à penser qu'il ne sera plus applicable pour décrire des processus de très haute énergie. En effet, de nombreuses caractéristiques du MS restent inexpliquées à ce jour. Le nombre important de paramètres du modèle (~ 19, sans compter les masses des neutrinos ni les densités de partons) reflète ainsi notre degré d'ignorance actuel de la structure de la matière. Ainsi, nous espérons pouvoir trouver une théorie plus globale, dont le MS ne serait qu'une modélisation à basse énergie. Des manifestations d'une telle théorie, comme l'observation de nouvelles particules ou des déviations aux prédictions de MS, sont donc recherchées aux plus hautes énergies actuellement atteignables expérimentalement.

Ce mémoire d'habilitation présente donc une exploration expérimentale de ces trois limites actuelles du MS que sont la précision, la complexité, liée au secteur de QCD, et sa frontière à haute énergie. Ces sujets seront abordés à travers les travaux que j'ai pu réaliser dans l'expérience H1 à HERA au cours de ces huit dernières années.

Chapitre 1

Méthodes et outils expérimentaux

L'avantage des réactions lepton-hadron pour l'étude de la structure de la matière réside dans le fait que les leptons sont des objets ponctuels et que leurs interactions sont bien comprises. Historiquement, ce sont des expériences de diffusion de particules quasi-ponctuelles sur la matière qui ont permis d'en révéler les différentes sous-structures. Ainsi, l'expérience de Geiger-Marsden-Rutherford a permis en 1909 d'établir la structure des atomes. L'expérience de diffusion élastique *ep* réalisée en 1955 par Hofstadter *et al.* a permis de montrer que le proton n'était pas une particule ponctuelle [Hof55]. Enfin, c'est la première expérience de diffusion profondément inélastique (DIS) d'électrons sur des protons effectuée à SLAC en 1968 qui a permis de confirmer la structure partonique de ces derniers [Blo69, Bre69].

1.1 La diffusion lepton-proton

Dans le cas le plus général, l'interaction lepton-proton se fait par l'échange d'un boson vecteur virtuel, comme schématisé dans la figure 1.1. Comme le nombre leptonique doit être conservé, un lepton diffusé est alors attendu dans l'état final. Le boson échangé peut être un γ ou un Z^0, l'interaction est alors de type courant neutre (NC), ou bien un boson W, interaction de type courant chargé (CC). Dans ce dernier cas, pour un lepton chargé incident, un neutrino est attendu dans l'état final.

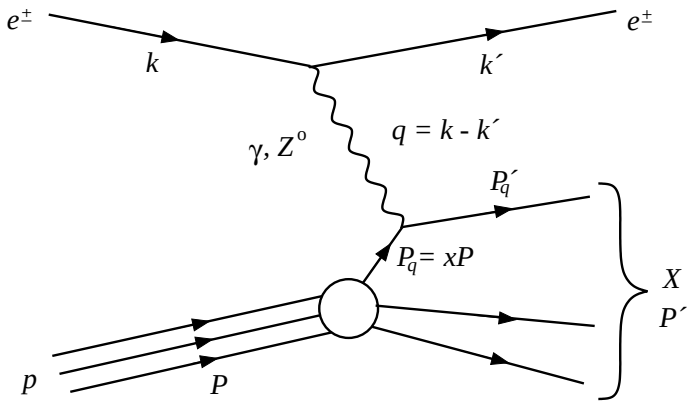

Figure 1.1 : *Diffusion entre un lepton chargé et un hadron.*

Le lepton incident, de quadri-vecteur k, diffuse sur le proton (P) en un lepton dans l'état final de quadri-vecteur k', par l'échange dans la voie t d'un photon virtuel γ^*, ou d'un boson électrofaible, de virtualité Q^2. En cas de diffusion inélastique, seule une partie du proton, un parton, est supposé prendre part à la réaction. La variable de Bjorken x est

alors définie et associée à la fraction d'impulsion du proton portée par le parton diffusé. Les variables usuellement utilisées pour décrire la diffusion électron-proton sont alors :

$$\begin{aligned} Q^2 &= -q^2 = -(k'-k)^2 \,, \\ y &= \frac{P\cdot q}{P\cdot k} \,, \\ x &= \frac{Q^2}{2P\cdot q} \,, \\ \nu &= \frac{P\cdot q}{M_p} \,, \\ W^2 &= (P')^2 = (P+q)^2 \,, \\ s &= (P+k)^2 \,. \end{aligned}$$

La variable $\sqrt{s}$ est l'énergie totale dans le centre de masse de la réaction et l'énergie du système $\gamma^* p$ est donnée par la variable W.

Le carré du moment transféré, q^2, détermine la dureté de la réaction, ou, en d'autres termes, son pouvoir de résolution. Le boson échangé permet alors de sonder des distances dans le proton de l'ordre de sa longueur d'onde, soit :

$$\Delta b \sim \frac{\hbar c}{\sqrt{Q^2}} = \frac{0.197}{\sqrt{Q^2}} \text{ GeV fm} \,. \tag{1.1}$$

La variable ν a une signification simple dans le référentiel du proton au repos. C'est l'énergie perdue par l'électron lors de sa diffusion, $\nu = E_e - E'_e$. La variable y représente quant à elle la fraction d'énergie perdue, $y = \frac{E_e - E'_e}{E_e}$.

Compte tenu du nombre de degrés de liberté de cette cinématique à deux corps, seules deux variables sont indépendantes. Pour une énergie donnée dans le centre de masse électron-proton, la cinématique de la réaction est complètement définie par l'énergie et l'angle de l'électron diffusé. Comme nous le verrons par la suite, la nature partonique du proton fait que les variables (x, Q^2) sont plus communément utilisées pour caractériser de manière unique la cinématique d'un événement de DIS. La variable Q^2 peut alors être exprimée en fonction de l'énergie et de l'angle de diffusion du lepton, $Q^2 = 4E_e E'_e \cos^2\theta/2$. La relation $Q^2 = sxy$ permet de relier les trois variables, et de définir ainsi x à partir de la mesure de y.

A partir de ces relations, nous voyons que la cinématique de la diffusion inélastique peut être reconstruite à partir de la seule mesure de l'électron diffusé. La mesure des hadrons dans l'état final peut être exploitée comme contrainte supplémentaire des diffusions NC. C'est aussi le seul moyen de reconstruire la cinématique des événements CC [Blo79], le neutrino sortant n'étant pas mesuré.

1.2 L'accélérateur HERA

Le projet de construction du collisionneur HERA a commencé en 1985 et les premières collisions électron–proton ont eu lieu en 1992. Le *Hoch Energie Ring Anlage*, HERA, fut le premier, et jusqu'à présent unique, accélérateur mettant en collision des électrons et des protons. La figure 1.2(a) présente un schéma du complexe d'accélération. Celui-ci est composé de deux accélérateurs circulaires, de sens opposé, permettant d'accélérer, de stocker et de mettre en collision les deux faisceaux d'électrons (e^-), ou positrons (e^+), et de protons. Les électrons sont accélérés à une énergie de 27.6 GeV et les protons à une énergie

de 920 GeV. L'énergie totale dans le centre de masse est alors de 320 GeV. Les paquets d'électrons et de protons se croisent toutes les 96 ns. Deux expériences généralistes pour l'étude des collisions ep, H1 et ZEUS, sont installées à HERA.

Durant les premières années de fonctionnement, de 1992 à 1997, l'énergie du faisceau de protons était seulement de 820 GeV. A l'été 2000, HERA a été arrêté et les régions d'interaction ont été modifiées afin de permettre une augmentation de la luminosité. Après plus d'un an passé pour comprendre la nouvelle machine, la prise de données a repris fin 2003. Les deux grandes périodes distinctes de prise de données de 1992 à 2000 puis de 2003 à 2007 sont dénommées respectivement HERA I et HERA II. Durant les derniers mois d'opération de 2007, l'énergie du faisceau de protons a été abaissée successivement à 460 et 575 GeV. Ceci a permis de mesurer ainsi la fonction de structure longitudinale du proton, F_L, pour la première fois de manière directe à bas x [Aar08]. HERA a été définitivement arrêté le 1^{er} juillet 2007, après 15 ans de fonctionnement.

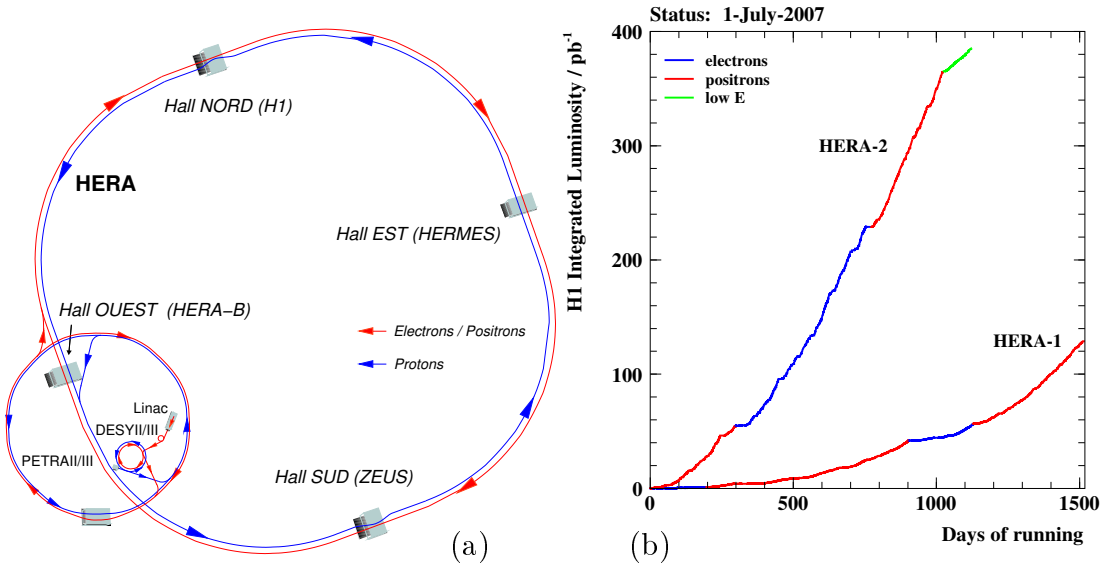

Figure 1.2 : *(a) Schéma de HERA et de ses injecteurs. L'ensemble fait 6.3 km de circonférence et se trouve à une profondeur d'environ trente mètres sous la ville de Hambourg. (b) Luminosité intégrée accumulée par l'expérience H1. La luminosité accumulée en collisions e^+p est indiquée en rouge, celle en collisions e^-p en bleu. La luminosité enregistrée avec une énergie de faisceau de protons plus faible est représentée en vert.*

La luminosité utile accumulée par l'expérience H1 durant les différentes périodes de fonctionnement de HERA est présentée dans la figure 1.2(b). Seules les données enregistrées depuis 1994 sont utilisées dans les analyses actuelles. La période HERA I n'a permis d'enregistrer que peu de données en collisions électron-proton (~ 15 pb^{-1}). Une des avancées de la période HERA II a donc été de permettre l'accumulation d'un lot substantiel de données électron-proton. L'autre nouveauté de la période HERA II a été de pouvoir polariser longitudinalement les faisceaux de lepton au niveau des points d'interaction. La polarisation typique atteinte pour les faisceaux en collision a été de 30 à 40%. En revanche, entre autres à cause de la complexité de la machine, la luminosité totale enregistrée par les expériences s'est révélée être inférieure aux objectifs initiaux du programme HERA II. La phase HERA II a permis d'accumuler, par expérience, un total d'environ 400 pb^{-1}, au lieu

de 1 fb^{-1} initialement prévus. Au total, environ 500 pb^{-1} de données ont été accumulés par chaque expérience, H1 et ZEUS, sur toute la durée de fonctionnement de HERA.

Le plan cinématique en (x, Q^2) qui est accessible avec HERA est présenté dans la figure 1.3. HERA permet d'atteindre des Q^2 de l'ordre de 50000 GeV^2 et des valeurs de x aussi basses que 10^{-5}. Par rapport aux expériences précédentes sur cible fixe, nous voyons donc que HERA a permis d'étendre considérablement le domaine en (x, Q^2) sondé. HERA s'avère aussi être complémentaire des autres collisionneurs de haute énergie que sont le Tevatron à Fermilab (Chicago, $p\bar{p}$, $\sqrt{s} = 1960$ GeV) et le LEP au CERN (Genève, e^+e^-, jusqu'en 2000, $\sqrt{s} \leq 209$ GeV). Le domaine qui sera couvert par le Large Hadron Collider (LHC), devant entrer en opération fin 2009, est aussi représenté. Le LHC devrait mettre en collisions deux faisceaux de protons, avec une énergie dans le centre de masse de 8 à 14 TeV.

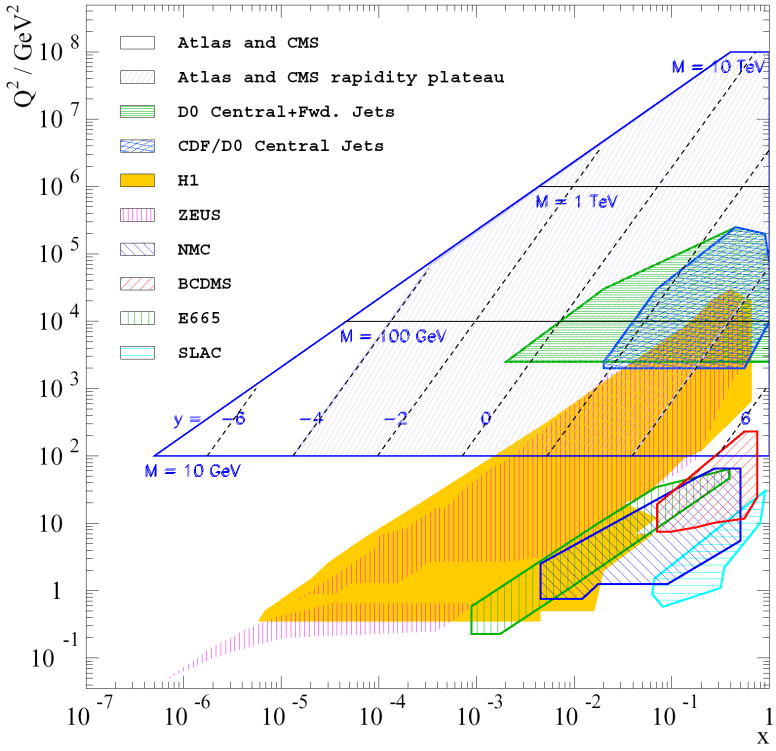

Figure 1.3 : *Le plan cinématique (x, Q^2), avec les régions couvertes par les expériences sur cible fixe, les collisionneurs HERA et Tevatron, ainsi que le futur collisionneur LHC.*

1.3 Le détecteur H1

Deux détecteurs généralistes, H1 et ZEUS, ont servi à enregistrer les produits des collisions *ep* à HERA. Ils ont été construits autour des points d'interaction avec une structure concentrique quasi-hermétique, d'une acceptance d'environ 4π d'angle solide. En partant du point d'interaction vers l'extérieur des détecteurs, nous trouvons successivement les détecteurs internes de traces, mesurant la trajectoire et l'impulsion des particules chargées, puis les calorimètres servant à compléter la mesure du flot total d'énergie. Le tout est plongé dans un champ magnétique d'un peu plus de 1 T. Enfin, la partie la plus externe est équipée de détecteurs de muons.

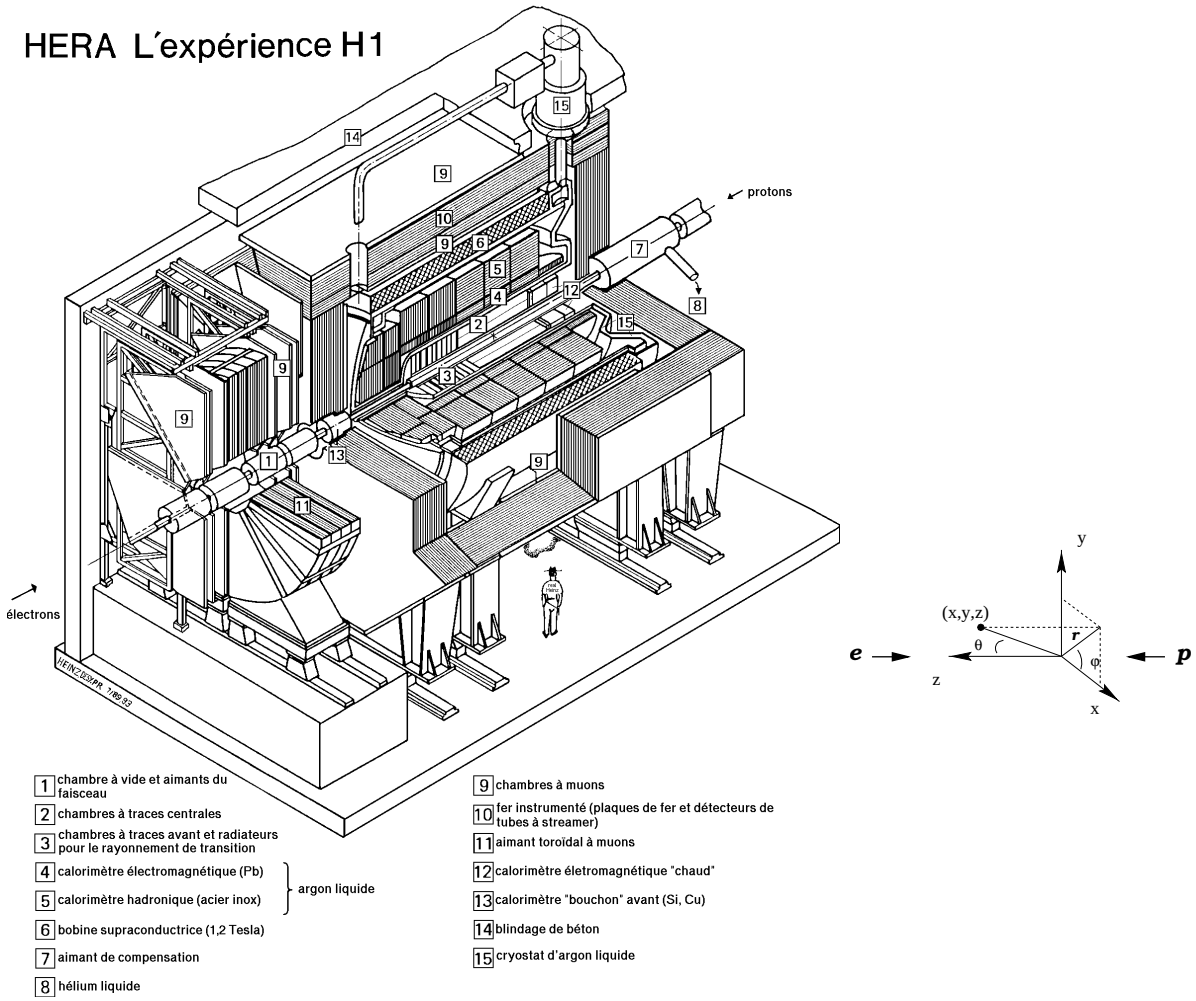

Figure 1.4 : *Vue schématique du détecteur H1 et définition des coordonnées cartésiennes et polaires utilisées. La région $\theta < 90°$, $z > 0$ correspond à l'avant du détecteur.*

Les détecteurs H1 et ZEUS ont été conçus avant tout pour la mesure des interactions profondément inélastiques aux plus grands Q^2 et avec un état final de grande énergie. Les énergies des faisceaux d'électrons et de protons étant fortement différentes, le flot d'énergie se trouve concentré vers la région avant (dans la direction du proton) et les détecteurs doivent donc être asymétriques, avec une couverture accrue de la région avant. Une grande attention a été portée aux calorimètres électromagnétiques et hadroniques. La collaboration ZEUS a choisi d'utiliser des scintillateurs couplés à des absorbeurs en uranium, dans le but d'égaliser la réponse du calorimètre aux électrons et aux hadrons (pions). La collaboration H1 a, quant à elle, choisi d'utiliser l'Argon liquide (LAr) comme matériau actif de son calorimètre principal afin de maximiser sa stabilité sur le long terme et d'obtenir une meilleure résolution sur la mesure de l'énergie des électrons.

Le détecteur H1 occupe un volume d'environ $12 \times 10 \times 15$ m^3 pour une masse de 2800 tonnes. Il est représenté sur la figure 1.4, tel qu'il était lors de la phase HERA I. Ses caractéristiques détaillées sont disponibles dans [Abt97a, Abt97b, App97]. Seules ses caractéristiques principales sont rappelées ici.

Le système de coordonnées utilisé est représenté dans la figure 1.4. L'axe z est défini suivant la direction du faisceau incident de protons. L'avant du détecteur est défini comme étant la région $\theta < 90°$, $z > 0$.

La région arrière ($153° < \theta < 176°$) du détecteur est couverte par un calorimètre spaghetti, le SpaCal [App97], formé de fibres scintillantes avec des absorbeurs en plomb. Sa résolution en énergie pour des gerbes électromagnétiques est de $\sigma(E)/E \simeq 7.1\%/\sqrt{E/\mathrm{GeV}} \oplus 1\%$. Le calorimètre à argon liquide (LAr) [And93a] couvre la région angulaire $4° \leq \theta \leq 154°$. Sa résolution en énergie, mesurée en faisceaux tests [And93b, And94], est de $\sigma(E)/E \simeq 11\%/\sqrt{E/\mathrm{GeV}} \oplus 1\%$ pour des gerbes électromagnétiques et de $\sigma(E)/E \simeq 50\%/\sqrt{E/\mathrm{GeV}} \oplus 2\%$ pour des gerbes hadroniques.

Le détecteur central de traces ($20° < \theta < 160°$) est composé principalement de deux chambres à dérive cylindriques et coaxiales, les chambres à jets (CJC). Un second détecteur interne de traces constitué, dans sa version HERA II, de chambres à dérive couvre également la région avant du détecteur ($7° < \theta < 25°$).

Le calorimètre LAr et les détecteurs de traces internes sont situés dans une bobine supraconductrice fournissant un champ magnétique de 1.16 T. La mesure du moment transverse des particules chargées est effectué à partir de la courbure de leur trajectoire dans le champ magnétique. Le détecteur de traces central permet alors d'obtenir une résolution allant jusqu'à $\sigma_{P_T}/P_T = 0.002 P_T/\mathrm{GeV} \oplus 0.015$.

La partie la plus externe du détecteur est constituée de fer instrumenté assurant le retour du champ magnétique et servant à détecter la fin des gerbes hadroniques les plus énergétiques. Il est équipé de tubes fonctionnant en mode *streamer* et forme ainsi le détecteur central de muons ($4° < \theta < 171°$). Dans la région avant du détecteur ($3° < \theta < 17°$), une série de chambres à dérive permet également de détecter les muons et de mesurer leur moment en utilisant un aimant toroïdal.

La luminosité est déterminée à partir de la mesure du processus Bethe-Heitler dans un calorimètre proche du faisceau situé à $z = -103$ m dans la région arrière.

1.4 Reconstruction des événements et techniques d'analyse

La reconstruction des événements détectés et enregistrés se fait principalement en deux étapes. Une première étape consiste à reconstruire les traces à partir des hits dans les trajectographes et à combiner les cellules touchées des calorimètres en amas d'énergie. Cette première étape de reconstruction utilise des algorithmes écrits en langage fortran. Les traces et amas d'énergie reconstruits sont ensuite combinés et associés à des particules candidates.

Les algorithmes de cette seconde étape ont été entièrement réécrits en langage C^{++} à l'occasion de la transition entre HERA I et HERA II. Cette réécriture a permis de rénover et d'optimiser les algorithmes fortran utilisés jusqu'alors. Ceci a également permis une standardisation des algorithmes d'identification des particules, uniformisant et facilitant les analyses faites par la suite. L'autre avantage principal de ces nouveaux algorithmes d'identification est de fournir une reconstruction complète du flot d'énergie dans le détecteur, sans double comptage de l'énergie. Chaque trace et amas d'énergie est au final associé de manière unique à une particule identifiée. Les particules identifiées peuvent ensuite être utilisées de la même manière par toutes les analyses de physique menées dans H1, quasi-indépendamment du sujet traité.

Ce résultat a pu être obtenu en rassemblant l'expertise acquise dans les différents groupes de physique et en combinant les informations fournies par les différents sous-détecteurs. La compréhension des connections entre les différents identificateurs est éga-

lement importante. Ce travail d'uniformisation et de standardisation des algorithmes de reconstruction du flot d'énergie global dans le détecteur a été crucial, pour faciliter et assurer la qualité des analyses de physique menées par la suite.

L'identification des différents types de particules s'effectue séquentiellement. En premier lieu, les candidats électrons et photons sont identifiés à partir d'un dépôt d'énergie compact et isolé dans les calorimètres électromagnétiques du LAr et du SpaCal. Leur énergie et direction angulaire sont mesurées par les calorimètres. L'association ou non d'une trace au dépôt d'énergie permet alors de distinguer les électrons des photons.

Les candidats muons sont ensuite identifiés à partir d'une trace interne mesurée avec une bonne précision et dont la direction coïncide avec une trace ou un dépôt d'énergie dans les détecteurs externes de muons. L'impulsion du muon est alors mesurée par la courbure de la trace interne dans le champ magnétique.

Enfin, tous les dépôts d'énergie et traces restantes, non associés à des électrons, photons ou muons, mais aussi les candidats électrons, photons ou muons qui ne sont pas suffisamment isolés dans le détecteur par rapport à d'autres traces ou dépôts d'énergie, sont combinés pour former des hadrons. L'état final hadronique est alors reconstruit par un algorithme spécifique, détaillé dans l'annexe A, et qui combine traces et dépôts d'énergie en objets hadroniques afin de permettre une mesure de l'énergie hadronique avec la meilleure résolution possible, sur l'ensemble de la gamme d'énergie. Il est intéressant de noter que, au final, dans la région centrale du détecteur, plus de 60% de l'énergie hadronique totale se trouve être mesurée par les trajectographes, permettant ainsi d'améliorer significativement la résolution de sa mesure.

Les jets hadroniques sont reconstruits à partir de ces objets hadroniques, avec un P_T minimum de 2.5 GeV, en utilisant un algorithme inclusif de k_T [Ell93, Cat93] avec un schéma de recombinaison pondéré en P_T et dans lequel les jets sont traités comme étant sans masse.

Au final, le schéma de reconstruction des différentes particules étant unique et sans double comptage de l'énergie, l'impulsion transverse manquante, P_T^{miss}, de l'événement peut être reconstruite simplement à partir de la somme des quadri-vecteurs de toutes les particules reconstruites.

1.5 Contributions personnelles

A mon arrivée dans la collaboration H1, début 2002, j'ai commencé par m'impliquer dans le projet de réécriture des algorithmes d'identification de particules en langage orienté objet (C^{++} et Root). J'ai pris tout d'abord la responsabilité de la réécriture de l'identificateur d'électrons (photons).

Par le biais du co-encadrement de Matti Peez, étudiant en thèse à Marseille, je me suis ensuite impliqué dans la validation des nouveaux identificateurs ainsi que dans le développement d'une nouvelle reconstruction de l'état hadronique final. J'ai par la suite assumé la responsabilité de cet identificateur de hadrons au sein de la collaboration H1 (voir annexe A).

De façon plus générale, je me suis fortement impliqué dans le développement de ces nouveaux algorithmes d'identification de particules en langage orienté objet, notamment pour pousser à une plus grande stabilité des programmes, indispensable pour toute analyse de physique. J'ai ensuite travaillé à leur validation pour l'obtention de résultats de physique de qualité. Ces identificateurs ont été à la base des analyses de physique menées sur les données de HERA II à partir de 2003.

Dans la continuité de ce travail, j'ai dirigé le développement d'une nouvelle calibration des jets hadroniques, en collaboration avec Benjamin Portheault, étudiant en thèse au LAL, à Orsay (voir annexe A). Cette calibration est devenue le standard des analyses de H1 et j'en ai assuré la mise à jour au fur et à mesure de l'acquisition de nouvelles données lors de la phase HERA II. Elle a notamment permis d'améliorer la précision expérimentale de la mesure de α_s à partir des jets de grande impulsion transverse [Aar09a]. La précision expérimentale de cette mesure est en effet contrainte par l'erreur systématique sur la mesure de l'énergie des jets, qui a pu être réduite à 1.5% (au lieu de 2% précédemment) par cette calibration pour les données HERA II.

En 2006-2007, j'ai mis en place et co-coordonné un groupe de travail de la collaboration H1, en charge de la calibration *offline* de l'ensemble des calorimètres de H1. Le but de ce groupe est de fournir à la collaboration un ensemble cohérent de calibrations et d'alignement de tous les calorimètres de H1, sur l'ensemble du domaine en énergie, pour les électrons et hadrons et pour l'ensemble des données. Dans ce groupe, j'ai, entre autres, été responsable des premières calibrations en énergie du calorimètre électronique arrière (SpaCal), pour les données HERA II. J'ai également contribué plus particulièrement au développement de nouvelles méthodes de calibration des hadrons de basse énergie. Les idées que j'ai introduites alors ont permis d'obtenir maintenant une calibration relative d'une précision de 2% (contre $\sim 4\%$ auparavant) pour les hadrons de basse énergie.

Enfin, au sein du groupe H1 du CPPM, j'ai développé un environnement d'analyse automatisé pour la gestion de larges lots hétérogènes de données et de Monte Carlo et reposant sur l'utilisation du calcul distribué auprès des fermes de processeurs des centres de calcul. Cet environnement a ainsi permis de mener efficacement en parallèle une grande variété d'analyses différentes. Il a ensuite été également utilisé plus largement dans la collaboration H1, notamment pour les analyses de recherche de nouvelle physique.

Chapitre 2

La précision du modèle standard : métrologie de la structure du proton

Un des intérêts majeur de HERA est bien sûr de pouvoir résoudre la structure en quarks et gluons du proton sur un vaste domaine en (x, Q^2), jamais sondé auparavant.

Après quelques brefs rappels sur la description de la structure du proton dans le cadre du modèle standard, nous présenterons les mesures récentes de DIS par courant neutre et chargé à grand Q^2 effectuées à HERA. Nous montrerons leur impact sur la détermination de la structure du proton et principalement son contenu en impulsion longitudinale.

Enfin, nous montrerons que ces données à grand Q^2 permettent également une détermination alternative de certains paramètres et propriétés du secteur électrofaible du modèle standard.

2.1 La structure du proton dans le modèle standard

2.1.1 Le modèle des quarks-partons et les fonctions de structure

La section efficace inclusive des collisions ep inélastiques peut être exprimée en fonction des variables x et Q^2 :

$$\frac{\mathrm{d}^2\sigma^{ep}}{\mathrm{d}x\mathrm{d}Q^2} = \frac{4\pi\alpha_{em}^2}{xQ^4}\left[\frac{y^2}{2}2xF_1(x,Q^2) + (1-y)F_2(x,Q^2) \pm \left(y - \frac{y^2}{2}\right)xF_3(x,Q^2)\right] . \quad (2.1)$$

Les fonctions de structure F_1, F_2, F_3 dépendent du processus considéré et de sa cinématique. La fonction de structure F_3 est non nulle seulement pour les interactions faibles et est générée par les interactions violant la parité.

En diffusion profondément inélastique (DIS), soit $Q^2 \gg 1$ GeV^2, le proton est vu comme composé de constituants libres et ponctuels, les partons. Ainsi dans le modèle des partons, l'interaction ep peut être décrite comme une somme non cohérente de contributions de partons libres.

Les partons constituant le proton ont ensuite été identifiés aux quarks, et nous parlons alors du modèle des quarks-partons. Les fonctions de structure peuvent alors être exprimées en termes de distributions de quarks $q_i(x)$, l'indice i indiquant le type de quark. Dans un modèle naïf de quarks-partons sans interactions entre eux, aucune dépendance en Q^2 de ces distributions n'est attendue. Cette propriété, appelée invariance d'échelle (ou *Bjorken scaling*), est due au caractère ponctuel des quarks.

Comme les bosons de jauge électrofaibles se couplent aux quarks par un mélange de couplages vecteur (v) et axial-vecteur (a), les fonctions de structure peuvent s'exprimer de

manière générale :

$$\begin{aligned} F_1(x) &= \frac{1}{2}\sum_i q_i(x)(v_i^2+a_i^2)\,, \\ F_2(x) &= \sum_i x q_i(x)(v_i^2+a_i^2)\,, \\ F_3(x) &= 2\sum_i q_i(x)(v_i a_i)\,. \end{aligned} \tag{2.2}$$

L'indice i inclut toutes les saveurs de quarks et antiquarks qui, selon les lois de conservation, peuvent participer à l'interaction. Pour des particules de spin 1/2, à partir des formules (2.2) la relation de Callan-Gross [Cal69] permet de relier F_1 et F_2 :

$$2xF_1(x) = F_2(x)\,. \tag{2.3}$$

Ce modèle naïf des quarks-partons ne permet cependant pas d'expliquer les observations expérimentales des violations de l'invariance d'échelle et de la relation de Callan-Gross. En effet, selon les prédictions de la QCD, les quarks sont liés dans le proton par les gluons. Des fluctuations comme l'émission et la réabsorption de gluons, ainsi que la création et l'annihilation de paires $q\bar{q}$ sont donc attendues. Ainsi, selon le pouvoir de résolution de la sonde et le temps caractéristique de l'interaction, certaines de ces fluctuations peuvent être vues, changeant alors la structure partonique du proton. Les fonctions de structure acquièrent donc une dépendance en fonction de Q^2. Cette dépendance en Q^2 est calculable directement en QCD et sa mesure constitue donc un des tests fondamentaux de la QCD perturbative. La violation de la relation de Callan-Gross est quant à elle une conséquence des radiations QCD. Au-delà du modèle naïf des quarks-partons, le proton doit donc être vu comme composé de trois quarks de valence, issus du modèle des quarks-partons, mais aussi, selon l'échelle à laquelle nous regardons, de gluons et d'un ensemble de paires $q\bar{q}$, appelé la mer, provenant de la dynamique QCD.

2.1.2 La structure du proton en QCD

Les distributions de quarks ne peuvent être calculées en QCD. Cependant, le théorème de factorisation [Col85] permet de séparer la section efficace des interactions dures lepton-hadron en une partie dure d'interaction à courte distance, calculable perturbativement, et une partie non perturbative universelle liée aux interactions à longue distance, les fonctions de distribution de partons (PDF). Ce théorème est valable à des corrections en puissance de m^2/Q^2 près, m étant l'échelle de masse des hadrons mis en jeu, et appelées contributions de *twists* supérieurs (*higher twists*). La partie principale factorisée est appelée le *twist* dominant (*leading twist*). Ce théorème permet alors de calculer l'évolution en fonction de Q^2 des distributions de partons dans le cadre de la QCD perturbative.

En QCD, l'émission de gluons est proportionelle à la constante de couplage fort, α_s, qui est prédite décroissante en fonction de l'échelle de renormalisation du processus considéré, μ_R^2. Dans l'approximation des logarithmes dominants (LLA), α_s vaut :

$$\alpha_x(\mu_R^2) = \frac{12\pi}{(33-N_f)\ln\left(\mu_R^2/\Lambda_{QCD}^2\right)}\,, \tag{2.4}$$

où N_f est le nombre de saveurs, Λ_{QCD} est un paramètre d'échelle libre ayant la dimension d'une masse. L'échelle de renormalisation μ_R^2 est prise égale à Q^2 dans le cas de l'étude des

fonctions de structure. Aux petites valeurs de μ_R^2, la constante de couplage α_s est élevée et il est alors impossible d'appliquer une approche perturbative de la QCD. Selon le principe d'incertitude, cette région correspond à de grandes distances de séparation entre les partons en interaction. Aux grandes valeurs de μ_R^2, donc aux très petites distances, la constante de couplage α_s devient petite et les quarks et les gluons sont libres (liberté asymptotique). Une approche perturbative est alors possible, l'ordre zéro correspondant à l'approximation du modèle naïf des quarks-partons.

En considérant les termes d'ordre supérieur par rapport au modèle des quarks-partons, c'est-à-dire les processus de radiation de gluons, l'évolution en Q^2 des fonctions de densité des quarks et des gluons est prédite, dans l'approximation des logarithmes dominant, par les équations de Dokshitzer, Gribov, Lipatov, Altarelli et Parisi (dites équations DGLAP) [Gri72, Lip74, Dok77, Alt77] :

$$\begin{aligned}
\frac{\partial q_i(x,Q^2)}{\partial \log Q^2} &= \frac{\alpha_s(Q^2)}{2\pi}\int_x^1 \frac{\mathrm{d}\xi}{\xi}\left[q_i(\xi,Q^2)P_{qq}\left(\frac{x}{\xi}\right) + g(\xi,Q^2)P_{qg}\left(\frac{x}{\xi}\right)\right], \\
\frac{\partial g(x,Q^2)}{\partial \log Q^2} &= \frac{\alpha_s(Q^2)}{2\pi}\int_x^1 \frac{\mathrm{d}\xi}{\xi}\left[q_i(\xi,Q^2)P_{gq}\left(\frac{x}{\xi}\right) + g(\xi,Q^2)P_{gg}\left(\frac{x}{\xi}\right)\right], \qquad (2.5)
\end{aligned}$$

où $q_i(x,Q^2)$ et $g(x,Q^2)$ sont les fonctions de densité des quarks et des gluons. Les fonctions d'embranchement (*splitting functions*) P_{qq}, P_{qg}, P_{gq} et P_{gg} décrivent la radiation d'un parton et sont calculables perturbativement en QCD, à un ordre donné en $\alpha_s(Q^2)$ (voir figure 2.1).

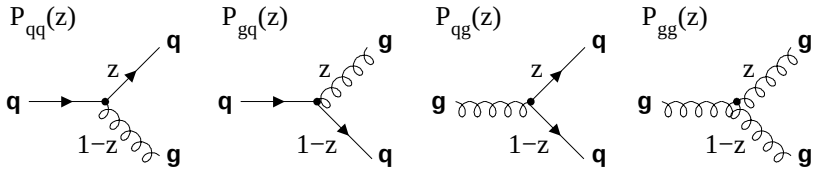

Figure 2.1 : *Fonctions d'embranchement DGLAP à l'ordre dominant.*

2.2 Mesure en collisions ep de la structure du proton

Les événements d'interactions DIS par courant neutre (NC) et chargé (CC) sont les plus utilisés pour déterminer la structure du proton à HERA et mesurer ses fonctions de structure. Les événements de type courant neutre ont comme signature dans le détecteur un électron diffusé (l'électron incident) et un jet de particules hadroniques. Dans les événements de type courant chargé, seul un jet de particules hadroniques est visible, le neutrino diffusé n'étant alors pas détecté. La figure 2.2 présente deux événements NC et CC de grand Q^2 observés dans le détecteur avec H1.

2.2.1 Les interactions par courant neutre

La section efficace de courants neutres peut être exprimée conventionnellement en termes des fonctions de structure :

$$\frac{\mathrm{d}^2\sigma_{NC}^{\pm}}{\mathrm{d}x\mathrm{d}Q^2} = \frac{2\pi\alpha^2}{xQ^4}\left(Y_+\ F_2 \mp Y_-\ xF_3\ -\ y^2\ F_L\right), \qquad (2.6)$$

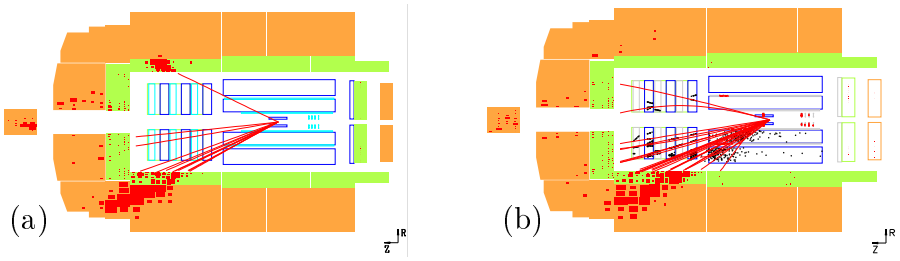

Figure 2.2 : *Evénements typiques de processus NC (a) et CC (b) de grand Q^2 dans le détecteur H1.*

pour les sections efficaces $e^{\pm}p$, avec $Y_{\pm} = 1 \pm (1-y^2)$ donnant la dépendance en hélicité des interactions faibles, et en introduisant la fonction de structure longitudinale $F_L = F_2 - 2xF_1$ qui est non nulle dès que des corrections d'ordre α_s sont prisent en considération. L'introduction des fonctions de structure est indépendante de tout modèle ou hypothèse sur la structure du proton. La section efficace réduite de courants neutres est définie comme :

$$\sigma^{\pm}_{r,NC} = \frac{\mathrm{d}^2\sigma^{\pm}_{NC}}{\mathrm{d}x\mathrm{d}Q^2}\,\frac{xQ^4}{2\pi\alpha^2}\,\frac{1}{Y_+} = F_2 \mp \frac{Y_-}{Y_+}xF_3 \;-\; \frac{y^2}{Y_+}F_L\,. \tag{2.7}$$

Les fonctions de structure F_2 et F_3 peuvent être ensuite décomposées en [Kle84] :

$$F_2 \;=\; F_2^{\gamma} \;-\; v_e\,\kappa\,F_2^{\gamma Z} \;+\; \left(v_e^2 + a_e^2\right)\,\kappa^2\,F_2^{Z}\,, \tag{2.8}$$

$$xF_3 \;=\; -a_e\,\kappa\,xF_3^{\gamma Z} \;+\; 2a_e v_e\,\kappa^2\,xF_3^{Z}\,, \tag{2.9}$$

où κ est le propagateur du boson Z^0 :

$$\kappa = \frac{1}{4\cos^2\theta_W \sin^2\theta_W}\frac{Q^2}{Q^2 + M_Z^2}\,. \tag{2.10}$$

Les variables v_e et a_e sont les couplages vecteur et axial-vecteur de l'électron, ou du positron, au Z^0 [Ams08]. La fonction de structure électromagnétique F_2^{γ} provient de l'échange du photon et domine dans la plupart de l'espace de phase accessible. Les fonctions F_2^Z et xF_3^Z sont les contributions à F_2 et xF_3 provenant de l'échange du Z^0 et les fonctions $F_2^{\gamma Z}$ et $xF_3^{\gamma Z}$ sont les contributions de l'interférence γZ^0. Ces contributions ne sont significative qu'à grand Q^2. Pour des leptons incidents non polarisés longitudinalement, la contribution de F_2 est la même pour des e^- ou e^+ incidents, alors que la contribution de xF_3 change de signe (voir équation (2.6)). La fonction de structure longitudinale F_L peut être décomposée de manière similaire à F_2. Sa contribution est significative uniquement à grand y.

Dans le modèle des quarks-partons, les fonctions de structure F_2^{γ}, $F_2^{\gamma Z}$ et F_2^Z sont reliées à la somme des distributions en moment des quarks et antiquarks, $xq_i(x,Q^2)$ et $x\bar{q}_i(x,Q^2)$:

$$\left[F_2^{\gamma}, F_2^{\gamma Z}, F_2^{Z}\right] = x\sum_i \left[e_{q_i}^2, 2e_{q_i}v_{q_i}, v_{q_i}^2 + a_{q_i}^2\right]\;(q_i + \bar{q}_i)\;. \tag{2.11}$$

La fonction de structure F_2 est ainsi déterminée par la somme des distributions des quarks de valence et de la mer.

Les fonctions de structure $xF_3^{\gamma Z}$ et xF_3^Z sont quant à elles reliées à la différence des distributions d'impulsion des quarks et antiquarks, qui détermine la distribution des quarks

de valence $xq_v(x,Q^2)$:

$$\left[xF_3^{\gamma Z}, xF_3^Z\right] = 2x\sum_i \left[e_{q_i}a_{q_i}, v_{q_i}a_{q_i}\right]\ (q_i - \bar{q}_i) = 2x\sum_{q=u,d}\left[e_q a_q, v_q a_q\right] q_v\,, \tag{2.12}$$

où les variables v_{q_i} et a_{q_i} sont les couplages vecteur et axial-vecteur des quarks au Z^0.

2.2.2 Les interactions par courant chargé

Les interactions par courant chargé, $e^\pm p \to \overset{(-)}{\nu}_e X$, se font par l'échange d'un boson W en voie t. Leur section efficace différentielle peut être paramétrée avec :

$$\frac{\mathrm{d}^2\sigma^\pm_{CC}(e^\pm p)}{\mathrm{d}x\mathrm{d}Q^2} = \frac{G_F^2}{2\pi x}\left[\frac{M_W^2}{M_W^2+Q^2}\right]^2 \sigma^\pm_{r,CC}(x,Q^2)\,, \tag{2.13}$$

$$\tag{2.14}$$

où G_F est la constante de Fermi et M_W la masse du boson W. La section efficace réduite σ_r s'exprime avec les fonctions de structure de courant chargé W_2, xW_3 et W_L :

$$\sigma^\pm_{r,CC}(x,Q^2) = \frac{1}{2}\left[Y_+ W_2^\pm(x,Q^2) \mp Y_- xW_3^\pm(x,Q^2) - y^2 W_L^\pm(x,Q^2)\right]\,. \tag{2.15}$$

Dans le modèle des quarks-partons, $W_L^\pm = 0$ et les fonctions de structure $W_2^\pm$ et $xW_3^\pm$ peuvent être interprétées comme des sommes et différences de distributions de quarks et antiquarks, dépendant de la charge du lepton :

$$\begin{aligned} W_2^+ &= x(\overline{U}+D),\ \ xW_3^+ = x(D-\overline{U})\,,\\ W_2^- &= x(U+\overline{D}),\ \ xW_3^- = x(U-\overline{D})\,. \end{aligned} \tag{2.16}$$

Les termes xU, xD, $x\overline{U}$ et $x\overline{D}$ sont définis comme la somme des distributions de quarks de type u, de type d et de leurs antiquarks. Sous le seuil de la masse du quark b, nous avons alors :

$$xU = x(u+c) \quad \text{et} \quad x\overline{U} = x(\overline{u}+\overline{c})\,, \tag{2.17}$$

$$xD = x(d+s) \quad \text{et} \quad x\overline{D} = x(\overline{d}+\overline{s})\,. \tag{2.18}$$

Nous pouvons déduire des équations (2.15) et (2.16) :

$$\sigma^+_{r,CC} = x\overline{U} + (1-y)^2 xD \quad \text{et} \quad \sigma^-_{r,CC} = xU + (1-y)^2 x\overline{D}\,. \tag{2.19}$$

Ainsi, la section efficace CC est bien plus grande en collisions e^-p que en e^+p, U étant plus grand que D quand x n'est pas trop petit et la section efficace e^+p est, elle, réduite par le facteur cinématique $(1-y)^2$. Nous voyons aussi que les interactions CC apportent une information importante pour séparer les distributions de quarks de types u et d dans le proton.

2.2.3 Mesures expérimentales

Les sections efficaces de NC et CC en fonction de Q^2, mesurées par H1 et ZEUS en collision $e^\pm p$, sont représentées dans la figure 2.3. Ces mesures incluent l'ensemble des données rendues publique par les deux collaborations. A bas Q^2, la section efficace de NC, dominée par l'interaction électromagnétique, est plus grande de deux ordres de grandeur

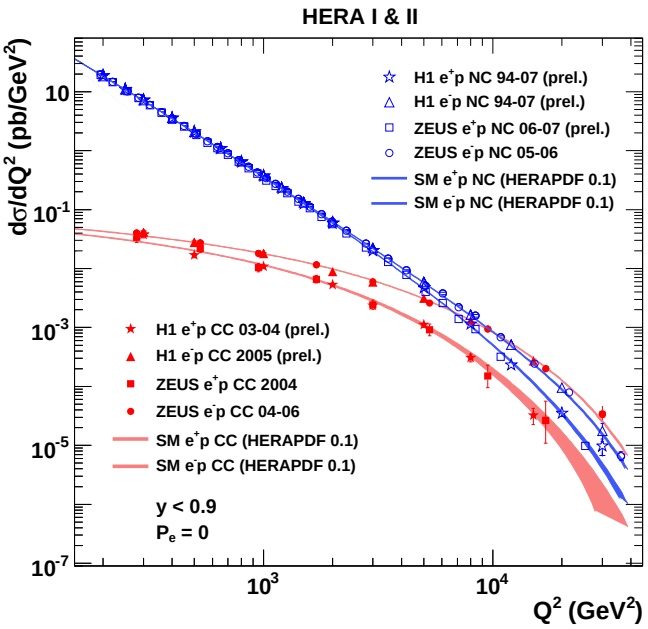

Figure 2.3 : *Sections efficaces de courants neutres et chargés en fonction de Q^2, mesurées à HERA.*

que la section efficace CC, qui correspond quant à elle à une interaction faible pure. A grand Q^2 ($Q^2 \sim M^2_{W,Z}$), par contre, les deux sections efficaces sont similaires, démontrant ainsi l'unification des interactions électromagnétiques et faibles.

Les plus grands Q^2 mesurés correspondent à une résolution de l'ordre de 10^{-18} m, soit 1/1000 de la taille du proton.

La section efficace réduite de courants chargés $\sigma_{r,CC}(x, Q^2)$ est représentée dans la figure 2.4. Les processus CC sont sensibles aux différentes saveurs de quarks dans le proton. Ceci est particulièrement visible à grand Q^2, où les collisions e^+p sondent la distribution de quarks d, alors que les collisions e^-p sont plus sensibles à la distribution de quarks u. Cette propriété des CC est très intéressante, en complément des interactions NC où le pouvoir séparateur des différentes saveurs de quarks est plus faible.

2.2.4 Détermination des fonctions de structure

A HERA, la section efficace de NC est dominée sur un large domaine par la contribution de F_2 (équation (2.6)). Sa mesure permet donc d'accéder directement à F_2. Ceci est illustré par la figure 2.5, qui représente dans le plan (x,Q^2), l'ensemble des mesures de la section efficace réduite de NC $\sigma_{r,NC}(x, Q2)$, équivalente à F_2 si les contributions, faibles, de xF_3 et F_L sont négligées, résultant de la combinaison des données de H1 et de ZEUS de la phase HERA I ainsi que des mesures antérieures effectuées sur cible fixe. Nous pouvons alors observer l'invariance d'échelle de Bjorken dans la région $x \simeq 0.1 - 0.2$, ainsi que sa violation évidente vers les plus bas x, qui provient de la contribution alors grandissante des gluons. Cette figure montre également que les données de HERA ont permis d'étendre considérablement le domaine en (x,Q^2) sondé et de réaliser ainsi une véritable cartographie de précision du contenu en impulsion longitudinale du proton. La large gamme de valeurs de Q^2 accessible permet également de tester avec une grande précision les équations DGLAP.

La fonction de structure xF_3 peut être obtenue en faisant la soustraction des sections

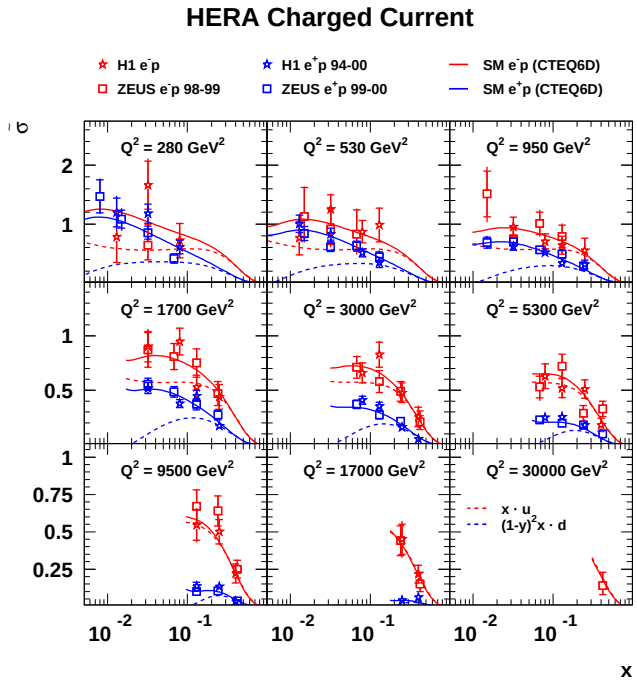

Figure 2.4 : *Sections efficaces réduites de CC $\sigma_{r,CC}$, en fonction de x et de Q^2, mesurées en collisions e^+p et e^-p.*

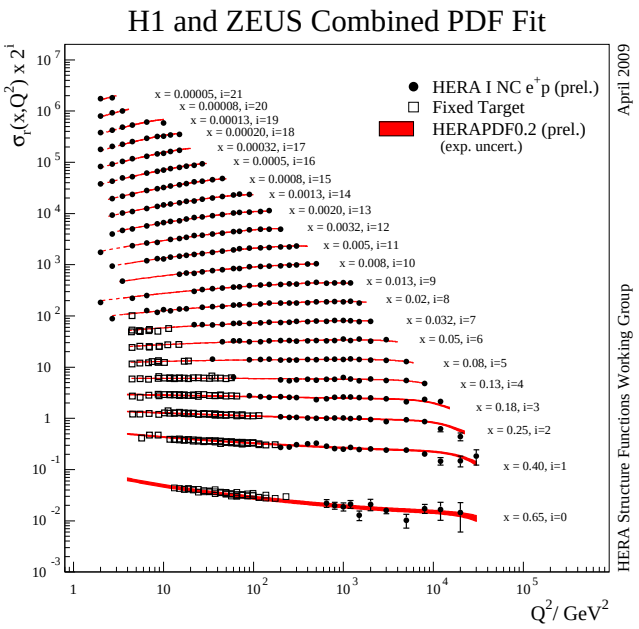

Figure 2.5 : *Section efficace réduite de courants neutres et chargés en fonction de x et de Q^2.*

efficaces NC de collisions e^+p et e^-p, non polarisées (voir équation (2.7)) :

$$xF_3 = \frac{Y_+}{2Y_-}\left[\sigma^-_{r,NC}(x,Q^2) - \sigma^+_{r,NC}(x,Q^2)\right] .$$

Comme le couplage vecteur de l'électron, v_e, est faible, la contribution dominante à xF_3 provient de l'interférence γZ (voir équation (2.9)). En QCD perturbative, à l'ordre dominant LO, la fonction de structure, $xF_3^{\gamma Z}$, peut s'écrire :

$$xF_3^{\gamma Z} = 2x[e_u a_u(U - \overline{U}) + e_d a_d(D - \overline{D})] . \qquad (2.20)$$

La détermination de xF_3 est donc une mesure directe de la distribution des quarks de valence. Sa mesure apporte aussi une information sur les couplages axial-vecteurs des quarks légers au Z^0 (a_u, a_d), ainsi que sur les charges électriques des quarks (e_u, e_d).

Comme seules les interactions NC à grand Q^2 sont sensibles à $xF_3^{\gamma Z}$, la précision de la mesure effectuée lors de la phase HERA I était limitée par la statistique disponible, et principalement par le faible lot de données e^-p (~ 15 pb^{-1}). Le lot important de données e^-p enregistrées lors de la phase HERA II a donc permis d'améliorer la précision statistique de la mesure de $xF_3^{\gamma Z}$. La mesure réalisée par H1 à partir des données de 1997 à 2005 est représentée dans la figure 2.6(a). La mesure est en accord avec la prédiction du modèle standard utilisant les densités de partons déterminées par H1 à partir des données HERA I. La précision de la mesure reste cependant encore limitée par la statistique de données disponibles. Le résultat obtenu ensuite en combinant les données de H1 et de ZEUS est présenté dans la figure 2.6(b). Il s'agit de la mesure de xF_3 la plus précise réalisée à ce jour.

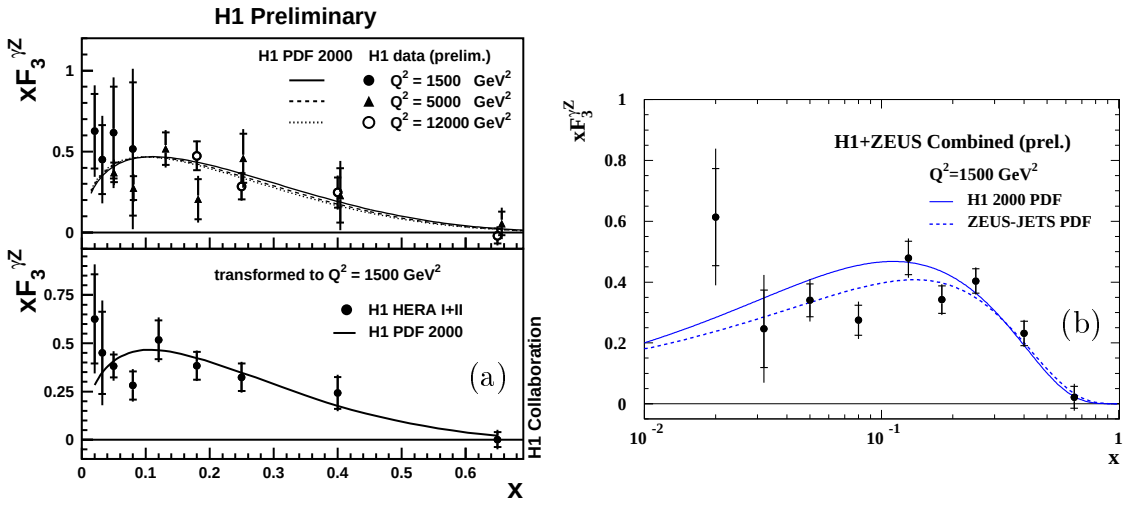

Figure 2.6 : *(a) Fonction de structure $xF_3^{\gamma Z}$ mesurée par H1 à différentes valeurs de Q^2 et transformée à $Q^2 = 1500$ GeV^2. (b) $xF_3^{\gamma Z}$ mesurée en combinant les données de H1 et de ZEUS.*

La fonction de structure F_L est généralement une faible correction visible seulement à grand y. Par définition, F_L contient la déviation à la relation de Callan-Gross et elle est nulle dans le modèle naïf des quarks-partons. Il a été montré que F_L est directement reliée à la densité de gluons dans le proton [Alt78, CS88]:

$$xg(x) = 1.8\left[\frac{3\pi}{2\alpha_s}F_L(0.4x) - F_2(0.8x)\right] \simeq \frac{8.3}{\alpha_s}F_L\,. \tag{2.21}$$

Ainsi, à bas x, la mesure de F_L permet une mesure quasi-directe de la distribution de gluons.

Comme la section efficace de courants neutres $\frac{\mathrm{d}^2\sigma_{NC}}{\mathrm{d}x\mathrm{d}Q^2}$ est proportionelle à $F_2 - y^2F_L/Y_+$ (voir équation (2.6)), une mesure directe de F_L requière la mesure de $\frac{\mathrm{d}^2\sigma_{NC}}{\mathrm{d}x\mathrm{d}Q^2}$ à plusieurs valeurs de y et à x et Q^2 fixés. Les contributions de F_2 et F_L peuvent alors être séparées. Ceci peut être réalisé en variant l'énergie $\sqrt{s}$ dans le centre de masse de la collision, ce qui

nécessite de varier, par exemple, l'énergie du faisceau de protons. Ainsi, durant les trois derniers mois de fonctionnement de HERA, l'énergie du faisceau de protons a été abaissée à 460 et 575 GeV. Les données alors accumulées, combinées à celles prises à 920 GeV, ont permis de mesurer la section efficace $\frac{\mathrm{d}^2\sigma_{NC}}{\mathrm{d}x\mathrm{d}Q^2}$ à deux ou trois valeurs différentes de y et d'extraire ainsi la fonction de structure F_L. Il s'agit de la première mesure directe de F_L dans le domaine des bas x. La mesure la plus précise, effectuée par la collaboration H1, est présentée dans la figure 2.7.

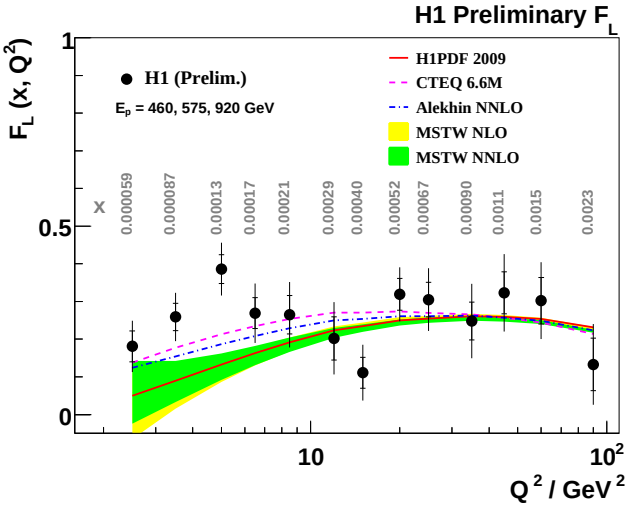

Figure 2.7 : *Fonction de structure longitudinale F_L mesurée par H1 et comparée aux prédictions de différentes distributions de partons.*

2.2.5 Détermination des densités de partons

Les mesures de sections efficaces de NC et de CC sont essentiellement utilisées pour déterminer, à l'aide d'un ajustement global, les densités de partons du proton, alors paramétrées par des fonctions de distributions (PDF). La forme en fonction de x des distributions de quarks et de gluons dans le proton ne peut être obtenue par une approche purement théorique dans le cadre de la QCD. Elles doivent donc être devinées et paramétrées en fonction de x, à une échelle donnée Q_0^2. Ces distributions initiales $q(x, Q_0^2)$ et $g(x, Q_0^2)$ peuvent ensuite être évoluées à n'importe quelle valeur mesurée de x et de Q^2, en utilisant les équations DGLAP. Le nombre total de paramètres utilisés pour décrire ces distributions initiales est de l'ordre de 10. Il est bien inférieur au nombre de points de mesure, de l'ordre de plusieurs centaines. Un ajustement global par minimisation de χ^2 peut alors être réalisé pour déterminer ces paramètres. Cet ajustement, par son faible nombre de degrés de liberté, constitue alors un puissant test de QCD et des équations DGLAP. Un exemple de PDFs obtenues par un ajustement réalisé sur les données HERA I combinées de H1 et de ZEUS est présenté dans la figure 2.8. Nous observons que la distribution des quarks de valence est bien piquée à 1/3, comme attendu dans le modèle naïf des quarks-partons, avec deux fois plus de quarks u que d, et que la distribution de gluons augmente à bas x.

Ce jeu de PDFs présenté est déterminé à partir des seules données de HERA I que sont les sections efficaces de DIS par NC et CC en collisions e^+p et e^-p. Les relativement faibles erreurs obtenues, qui peuvent alors être comparées à celles obtenues dans des fits plus globaux incluant des données d'autres expériences, montre l'importance des données de HERA qui s'avèrent être maintenant l'épine dorsale de toute détermination des PDFs du proton.

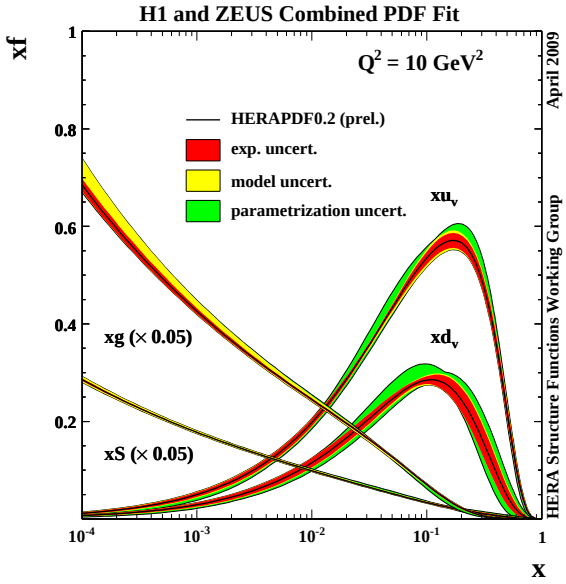

Figure 2.8 : *Fonctions de distribution des quarks de valence* $xu_v = x(U - \overline{U})$ *et* $xd_v = x(D - \overline{D})$*, des quarks de la mer* $xS = 2x(\overline{U} + \overline{D})$ *et gluons* xg*, déterminées à partir des données de HERA I, pour un* $Q^2 = 10\ GeV^2$*.*

Les données de NC de bas Q^2 déterminent les distributions de la mer de quarks et de gluons à bas x. La distribution des quarks de valence est quant à elle déterminée par les sections efficaces de CC à grand Q^2 et la différence entre les sections efficaces NC e^+p et e^-p à grand Q^2. Les CC permettent d'effectuer une distinction entre les saveurs des quarks de type u et de type d. Les NC à grand Q^2, via la contribution de xF_3, apportent, eux, une contrainte, encore faible à cause de la statistique actuellement utilisée, sur les quarks de valence. Les sections efficaces inclusives sont par contre quasiment aveugles vis-à-vis de la saveur, c'est-à-dire que nous ne pouvons pas distinguer les quarks u des quarks c. Le gluon est principalement contraint par les violations d'échelle. L'ajout de sections efficaces de production de jets à HERA permet alors de mieux contraindre le gluon à moyen x.

Dans le futur proche, l'ajout de données de HERA II va permettre de mieux contraindre encore la détermination des PDFs. Notamment, les données de CC en collisions e^-p, limitées statistiquement à HERA I, vont améliorer la détermination de la distribution de quarks à grand x. La mesure plus précise de xF_3 va également permettre d'augmenter la contrainte sur les quarks de valence, et de s'affranchir ainsi un peu plus des mesures faites sur cible de deutérieum, sujettes aux incertitudes sur les corrections nucléaires.

Au-delà des seules données de HERA, lors d'un ajustement global, les données de DIS sur cible fixe permettent de réduire d'un facteur deux l'incertitude sur la distribution des quarks de valence. Les données de jet du Tevatron permettent une meilleure contrainte des densités de quarks et de gluons à grand x.s

2.3 Tests du secteur électrofaible

Les interactions de DIS par NC et CC sont en fait de nature électrofaible, la partie QCD étant incorporée dans les PDFs et les équations DGLAP. Elles peuvent donc être également utilisées pour tester les prédictions du secteur électrofaible du MS.

2.3.1 Dépendance des interactions CC avec la polarisation

La polarisation du faisceau d'électrons disponible à HERA II permet de tester les effets de non-conservation de la parité de l'interaction faible. L'effet le plus important est prédit dans les interactions CC. Dans ce cas, la section efficace de CC dépend linéairement de la polarisation P du lepton incident $e^{\pm}$, $\sigma_{CC}^{e^{\pm}p}(P) = (1 \pm P)\ \sigma_{CC}^{e^{\pm}p}(P = 0)$. Les résultats obtenus, pour la première fois en collision $e^{\pm}p$, par les collaborations H1 et ZEUS sont résumés dans la figure 2.9. La dépendance linéaire attendue de la section efficace CC est confirmée. Ces mesures fournissent une évidence supplémentaire de la structure V-A des courants chargés dans le modèle standard, cette propriété ayant déjà été vérifiée, à plus basse énergie, 25 ans auparavant par la mesure de la polarisation de muons produits lors de diffusions $\nu_\mu - Fe$ [Jon79].

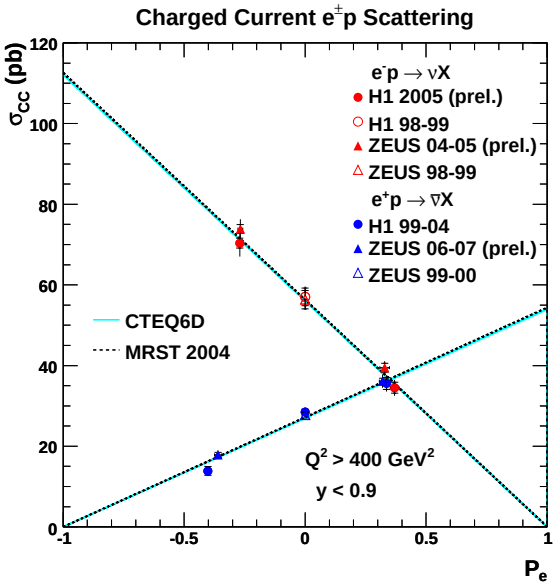

Figure 2.9 : *Sections efficaces de courants chargés en fonction de la polarisation, mesurées par H1 et ZEUS en collisions e^+p et e^-p. Les mesures sont comparées aux prédictions du modèle standard utilisant les distributions de partons CTEQ6D (ligne pleine) et MRST 2004 (ligne en pointillés).*

2.3.2 Dépendance des interactions NC avec la polarisation

De par l'échange du boson Z^0, la polarisation longitudinale du lepton incident affecte aussi la section efficace NC à grand Q^2. Les asymétries de polarisation dépendant de la charge pour la section efficace NC sont définies comme :

$$A^{\pm} = \frac{2}{P_R - P_L} \cdot \frac{\sigma^{\pm}(P_R) - \sigma^{\pm}(P_L)}{\sigma^{\pm}(P_R) + \sigma^{\pm}(P_L)} \simeq \mp \kappa a_e \frac{F_2^{\gamma Z}}{F_2^{\gamma}}\,, \tag{2.22}$$

où P_R et P_L sont respectivement la polarisation moyenne droite et gauche du faisceau de leptons. Elles permettent de mesurer avec une très bonne approximation le rapport des deux fonctions de structure $F_2^{\gamma Z}$ et F_2^{γ}. Ces asymétries sont proportionnelles aux combinaisons $a_e v_q$ et permettent donc une mesure directe de la violation de la parité. Dans le modèle standard, A^+ est positif et égal à $-A^-$.

A grand x, ces asymétries mesurent aussi le rapport d/u des distributions de quarks de valence selon:

$$A^{\pm} \simeq \kappa \frac{1 + d_v/u_v}{4 + d_v/u_v} \tag{2.23}$$

Les mesures récentes de ces asymétries obtenues par H1 et par combinaison des données de H1 et ZEUS sont représentées respectivement dans les figures 2.10(a) et 2.10(b). Nous voyons alors que les mesures sont en accord avec les prédictions du MS et indiquent que les asymétries $A^{\pm}$ sont bien de signe opposé et différentes de zéro, démontrant que la parité est bien violée à des distances aussi faibles que 10^{-18} m.

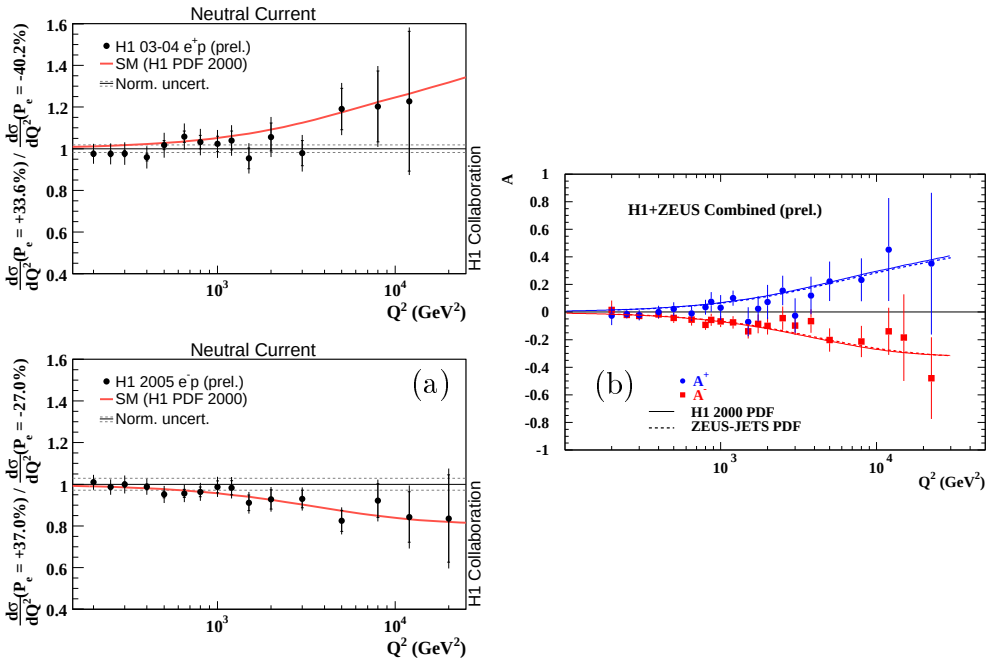

Figure 2.10 : *Asymétrie de polarisation de la section efficace NC en fonction de Q^2, mesurée par H1 (a) et déterminée par combinaison des données de H1 et de ZEUS (b).*

2.3.3 Détermination combinée de paramètres électrofaibles et QCD

Comme nous l'avons vu, par l'intermédiaire des fonctions de structure et grâce à l'échange du boson Z^0 en voie t, les sections efficaces de NC à grand Q^2 dépendent des couplages faibles vecteur, v_q, et axial-vecteur, a_q, des quarks u et d au Z^0. Cette sensibilité peut donc être exploitée pour contraindre ces couplages. La stratégie suivie consiste alors à effectuer un ajustement combiné *EW-QCD* des distributions de partons et de ces paramètres du MS, alors laissés libres dans l'ajustement. Une telle méthode a été proposée pour la première fois par H1 [Akt06a].

La polarisation longitudinale du faisceau de leptons des données de HERA II permet alors d'accroître la sensibilité aux couplages aux quarks. Les résultats de l'ajustement, alors effectué en utilisant les données polarisées de HERA II de H1, sont présentés dans la figure 2.11. Les contraintes alors obtenues sur les couplages aux quarks u et d sont comparées aux résultats similaires obtenus au Tevatron [Aco05] et par les expériences du LEP [LEP04]. Nous voyons alors que la précision obtenue à HERA est meilleure que celle du Tevatron, notamment pour le quark u. Les mesures effectuées à la résonance du Z^0 au LEP, plus précises, permettent seulement d'accéder aux combinaisons av ou $a^2 + v^2$. Ces mesures présentent donc une ambiguïté entre couplages axial et vecteur et seul le signe relatif peut être déterminé. Les mesures effectuées à HERA et au Tevatron permettent de résoudre cette ambiguïté.

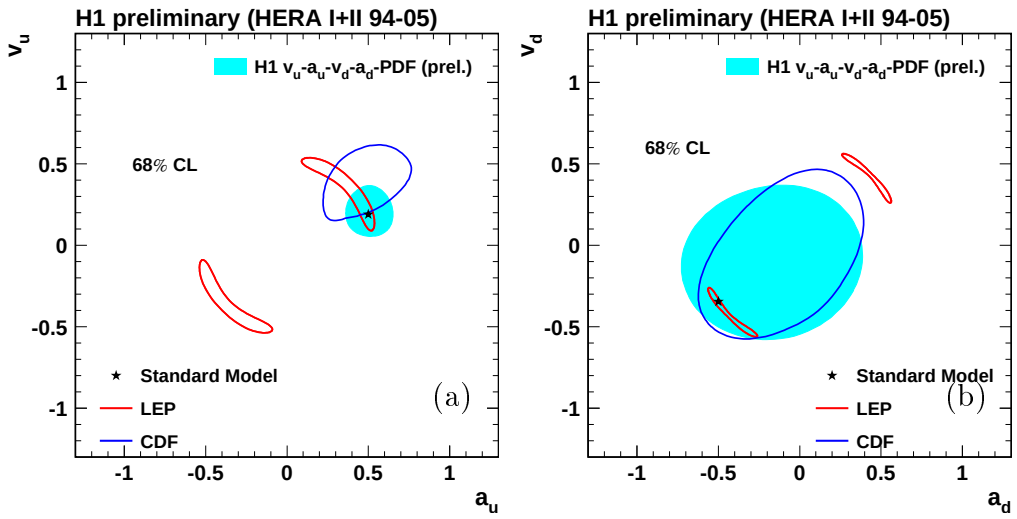

Figure 2.11 : *Contraintes à 68% CL sur les couplages faibles des quarks u (a) et d (b) au boson Z^0.*

2.4 Conclusions

A travers ce chapitre, nous avons vu que les mesures de section efficace de DIS par courant neutre et chargé fournies par HERA sont essentielles pour établir précisément la structure en impulsion longitudinale du proton. Cette connaissance est incorporée dans la détermination des fonctions de distributions des partons dans le proton, les PDFs. Grâce au théorème de factorisation colinéaire, ces PDFs sont devenues un outil indispensable pour le calcul de la section efficace de tout processus physique auprès des grands collisionneurs hadroniques, et notamment au LHC.

Les mesures effectuées à HERA, en exploitant l'ensemble de la statistique disponible et en combinant les données de H1 et de ZEUS, vont ainsi permettre de réduire encore les incertitudes des PDFs actuelles, permettant ainsi une détermination plus précise des sections efficaces des processus du MS au LHC. Ceci pourrait notamment servir à réduire encore l'incertitude théorique sur la section efficace de productin du boson W au LHC et utiliser ainsi ce processus pour mesurer la luminosité.

Les données de HERA permettent également de couvrir une large gamme en x, jusqu'à 10^{-5}, contrairement au Tevatron qui lui ne permet que de sonder le domaine à grand x du proton. Cette connaissance de la dynamique interne du proton à bas x, et notamment de la distribution de gluons, va s'avérer importante pour le LHC dont une grande partie de l'espace de phase est justement située à bas x. Par les équations DGLAP, les mesures de HERA à bas x peuvent en effet être extrapolées à plus grand Q^2, dans le régime du LHC, et fournir ainsi des prédictions.

2.5 Contributions personnelles

Au redémarrage de HERA fin 2003, mes responsabilités dans l'identification des électrons et des hadrons m'ont naturellement conduit à m'impliquer dans les mesures des sections efficaces de courants neutres (NC) et chargés (CC) à grand Q^2.

Pour ces mesures de précision, il est d'usage dans la collaboration H1 d'avoir deux lignes d'analyses indépendantes. J'ai développé une de ces deux lignes d'analyse en collaboration avec Benjamin Portheault, étudiant en thèse à Orsay. En parallèle, une seconde analyse a

été mise en place par des physiciens de DESY et de Munich.

En 2005, j'ai repris l'entière responsabilité de l'analyse *Orsay-Marseille* et participé à la publication de la première mesure à grand Q^2 de la dépendance des processus courants chargés avec la polarisation (voir annexe B). Ceci constitue la première publication alors réalisée avec des données de HERA II.

En collaboration avec les groupes de DESY et de Munich, j'ai ensuite étendu cette analyse aux données de collision $e^- p$, ce qui a conduit en 2006 à une nouvelle mesure préliminaire des sections efficaces NC et CC. Ces mesures ont ainsi permis une nouvelle mesure de la fonction de structure xF_3 ainsi que la mesure de la dépendance des processus NC avec la polarisation (voir section 2.3), auxquelles j'ai participé. Ces mesures ont ensuite été utilisées dans la collaboration H1 pour réaliser un nouvel ajustement combiné EW-QCD et contraindre les valeurs des couplages faibles des quarks au boson Z^0.

En 2007, j'ai également contribué à la mesure préliminaire de la section efficace NC utilisant l'ensemble des données de H1, en assurant le développement complet d'une des deux analyses indépendantes nécessaires. Cette mesure a notamment été utilisée dans la collaboration pour poser une nouvelle contrainte sur la taille des quarks (voir section 4.1.1).

Chapitre 3

La complexité dans le modèle standard : interactions diffractives

Les processus diffractifs à HERA permettent de sonder le proton différemment des réactions de DIS. Ils apportent ainsi des informations supplémentaires sur la structure du proton, comme le contenu en gluons à bas x du proton ou la structure transverse du proton.

L'interaction forte étant à l'origine de ces processus, ils sont également de bons outils pour l'étude des phénomènes complexes liés au secteur de la QCD. Le domaine cinématique accessible à HERA permet ainsi d'étudier, à travers les interactions diffractives, la transition entre régimes perturbatif et non-perturbatif de la QCD. La diffraction à HERA permet également d'accéder aux forces de confinement en QCD. En effet, à de faibles valeurs de x, selon le Q^2 de l'interaction, il est possible de sonder en collisions ep une densité très grande de gluons. Selon le régime cinématique, typiquement pour $x \simeq Q^2/W^2$, la densité de gluons sondée peut devenir si grande que des effets QCD non-linéaires, comme les recombinaisons de gluons, deviennent très importants. Ces effets empêchent alors la densité de gluons de croître et nous parlons alors de phénomène de saturation. Les interactions diffractives sont alors un bon outil pour étudier ces effets de saturation et la dynamique QCD dans le régime des grandes densités de partons, permettant ainsi des connections intéressantes avec la physique des ions lourds.

Après une brève introduction de la diffraction à HERA et des principales approches théoriques utilisées pour décrire ces processus, nous présenterons successivement les mesures inclusives de diffusion diffractive effectuées à HERA et un exemple de processus diffractif exclusif, la diffusion Compton à haute virtualité. Nous discuterons l'intérêt d'étudier ces deux processus et les informations qu'ils nous apportent sur la structure du proton ainsi que sur la dynamique de la QCD dans le cas complexe du régime non-perturbatif.

3.1 Les processus diffractifs à HERA

Un des résultats important du collisionneur HERA est l'observation d'une fraction importante, de l'ordre de 10%, d'événements diffractifs en collisions profondément inélastiques. Ces événements présentent un large intervalle en rapidité entre le proton diffusé, qui reste intact, et le reste de l'état final [Der93, Ahm94]. Dans la description QCD standard du DIS, de tels événements ne sont pas attendus dans une aussi grande proportion, les grands intervalles en rapidité étant supprimés exponentiellement par les cordes de couleurs formées entre les restes du proton et les partons diffusés. Dans ces événements diffractifs, un ensemble de hadrons, neutre de couleur, se fragmente indépendamment du proton diffusé.

Le rapport du nombre d'événements diffractifs sur le nombre total d'événements de DIS dépend seulement faiblement de x et de Q^2. Les événement diffractif correspondent donc à un effet de *twist* dominant avec des violations d'échelle logarithmiques en Q^2, similaires au DIS standard.

La description théorique de ces événements diffractifs reste un réel défi, car elle doit combiner les effets QCD perturbatifs de la diffusion dure avec les phénomènes non perturbatifs liés à la formation de l'intervalle en rapidité. Les événements diffractifs en collision ep offrent alors un environnement unique, de par l'interaction initiale $\gamma^* p$, et mieux contrôlé que les collisions purement hadroniques, pour la compréhension des phénomènes diffractifs en QCD. Ils sont donc un bon outil pour étudier la transition entre régimes durs et mous de la QCD.

En collisions hadron-hadron, les interactions diffractives sont depuis longtemps décrites dans le cadre de la théorie de Regge [Col77]. Dans ce cadre, l'échange de particules en voie t est sommé de manière cohérente pour produire l'échange de ce qui est appelé des *trajectoires de Regge*. La diffraction est alors caractérisée par l'échange d'une trajectoire spécifique, le *pomeron* ($I\!P$), qui possède les nombres quantiques du vide. Un échange en voie t provoquant un intervalle en rapidité doit en effet être neutre de couleur, autrement, toute couleur échangée mènerait à la production de particules supplémentaires, remplissant alors l'intervalle en rapidité. Dans le cadre de la QCD, l'échange d'un pomeron peut être décrit à l'ordre dominant par un échange de deux gluons ayant les nombres quantiques du vide.

Pour les interactions ep, deux grandes approches théoriques sont possibles pour tenter de décrire les interactions diffractives. La première est basée sur une description partonique du proton. La seconde tente une description principalement basée sur des principes fondamentaux de la QCD.

Dans le référentiel où le proton est très rapide, la réaction diffractive peut être vue comme une diffusion profondément inélastique d'un photon virtuel γ^* sur le proton. Le théorème de factorisation colinéaire peut également s'appliquer à ces événements diffractifs [Col98] et le modèle des partons peut alors être utilisé, en analogie avec le DIS standard. La structure spécifique du proton dans ces processus diffractifs peut alors être incorporée dans des fonctions de distribution de partons, diffractives (DPDF).

La diffraction à HERA est alors devenue un outil pour étudier les partons de faible impulsion dans le proton, notamment à travers l'étude des densités diffractives de partons (DPDF) dans les processus inclusifs ou des distributions généralisées de partons (GPD) dans les processus exclusifs. Les densités diffractives de partons peuvent être interprétées comme les probabilités conditionnelles de trouver un parton dans le proton quand l'état final contient un proton rapide sortant, de quadri-impulsion donnée. Les GPDs, quant à elles, à travers leur dépendance combinées aux variables transverses et longitudinales, fournissent une image en trois dimensions du proton dans les réactions à haute énergie.

Si nous nous plaçons par contre dans le référentiel où le proton est au repos, à bas x, le photon virtuel est alors très rapide, avec une impulsion qui peut aller jusqu'à 50 TeV à HERA. Le photon virtuel peut alors fluctuer en une paire quark-antiquark $q\bar{q}$, singulet de couleur appelé dipôle, bien avant d'atteindre le proton. C'est ce dipôle, qui a alors une taille transverse $r \sim 1/Q$, qui va ensuite interagir avec le proton par un processus dur [Mue90, Nik91]. Ce processus est schématisé dans la figure 3.1. Dans le régime purement perturbatif, cette interaction se fait par échange d'un gluon et se transforme en un échange

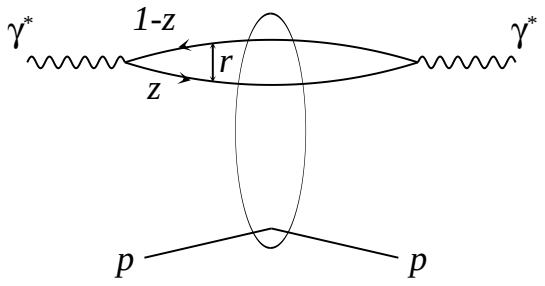

Figure 3.1 : *Représentation schématique du processus d'interaction du dipôle avec le proton (d'après [GB99a]).*

de plusieurs gluons, pour de très faibles valeurs de x, $x \lesssim 0.01$. Dans ce domaine, la densité de gluons du proton devient si large que des effets non-linéaires comme les recombinaisons de gluons vont en limiter l'extension et nous parlons alors de phénomènes de saturation.

Deux grandes catégories de processus diffractifs sont étudiées à HERA : des processus inclusifs et d'autres plus exclusifs comme la production de mésons vecteurs ou la diffusion Compton profondément virtuelle (DVCS). Chacun apporte des informations différentes et permet de sonder différentes facettes de la structure du proton et de la dynamique QCD. Ainsi, les mesures de diffraction inclusive permettent de déterminer les DPDFs et également d'accéder au régime de saturation de la QCD dans le proton. L'étude de la production de mésons vecteurs à HERA et du DVCS permet quant à elle d'accéder aux corrélations entre les partons du proton et d'étudier la structure transverse du proton, informations toutes deux alors encodées dans les GPDs.

Nous présenterons donc deux études concernant respectivement la diffraction inclusive et la mesure d'un processus exclusif, le DVCS.

3.2 La diffraction inclusive

3.2.1 Cinématique

Les collisions ep à HERA permettent de mesurer le processus inclusif de diffraction $ep \to eXY$, Y étant un proton ou une excitation de basse masse du proton. Pour ces processus, l'état hadronique final est alors séparé en deux systèmes X et Y, définis par le plus grand intervalle en rapidité séparant des hadrons dans l'état final. Le système Y est celui étant le plus proche de la direction du proton sortant (voir figure 3.2).

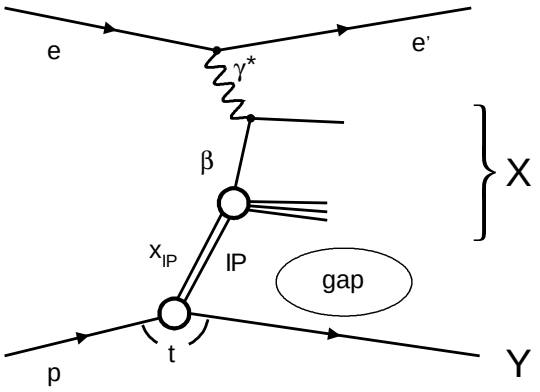

Figure 3.2 : *Schéma de la diffusion diffractive en collision ep.*

La cinématique du processus peut être décrite par les masses invariantes M_X et M_Y

des systèmes X et Y et les scalaires de Lorentz :

$$x = \frac{-q^2}{2P \cdot q} , \qquad y = \frac{P \cdot q}{P \cdot k} , \qquad Q^2 = -q^2 , \qquad t = (P - P_Y)^2 , \tag{3.1}$$

où P et k sont les quadri-vecteurss respectifs du proton et de l'électron incident, P_Y est le quadri-vecteur du système Y et q celui du photon virtuel échangé. La variable t est le carré du quadri-vecteur transféré au vertex du proton.

Les deux variables sans dimensions β et $x_{I\!P}$ peuvent être définies comme :

$$\beta = \frac{-q^2}{2q \cdot (P - P_Y)} = \frac{Q^2}{Q^2 + M_X^2 - t} , \qquad x_{I\!P} = \frac{q \cdot (P - P_Y)}{q \cdot P} = \frac{Q^2 + M_X^2 - t}{Q^2 + W^2 - M_Y^2} , \tag{3.2}$$

où $W^2 = (q + P)^2$ est le carré de l'énergie dans le centre de masse du système photon-proton. Ces variables sont reliées par la formule $x_{I\!P}\beta = x$. La variable $x_{I\!P}$ représente la fraction d'impulsion perdue par le proton incident. La variable β est l'équivalent de la variable de Bjorken x et peut être vue comme la fraction d'impulsion du pomeron portée par le parton diffusé.

Après intégration sur l'angle azimutal du proton diffusé et sur t, la section efficace de DDIS peut être paramétrée par deux fonctions de structure diffractives $F_{2,L}^{D(3)}$, par analogie avec le DIS standard :

$$\frac{\mathrm{d}^3\sigma^{ep\to eXY}}{\mathrm{d}x_{I\!P}\mathrm{d}Q^2\mathrm{d}x} = \frac{2\pi\alpha_{em}^2}{xQ^4} \left[\left(1 + (1-y)^2\right) F_2^{D(3)} - y^2 F_L^{D(3)}\right] . \tag{3.3}$$

La fonction de structure $F_L^{D(3)}$ correspond à la polarisation longitudinale du photon virtuel. Une première mesure en a été faite par la collaboration H1 [Aar09b]. Sa contribution à la section efficace est faible dans la majorité de l'espace de phase accessible expérimentalement, en particulier à bas y, et elle peut donc être négligée par la suite.

3.2.2 Mesures expérimentales

Plusieurs méthodes expérimentales peuvent être utilisées pour sélectionner les événements de DDIS. Une première méthode consiste à détecter le proton dans l'état final à l'aide de détecteurs positionnés très près du faisceau, afin de détecter le proton diffusé à bas angle. L'avantage de cette méthode est que la cinématique complète de la réaction, par la mesure de t, peut être obtenue. Cette méthode est aussi très propre, la détection du proton éliminant tout bruit de fond possible venant de processus où le proton aurait été dissocié. La précision statistique de cette méthode est cependant limitée, due à la faible acceptance des détecteurs de proton.

D'autres méthodes de séparation des événements de DDIS et de DIS qui sont basées sur des caractéristiques différentes du système hadronique X dans ces deux types d'événements sont alors employées. La méthode dite LRG (pour *large rapidity gap*) consiste à sélectionner les événements possédant un système hadronique avec un grand intervalle en rapidité à l'avant. Aucun signal ne doit alors être présent dans la région avant du détecteur. Cette condition impose que les systèmes X et Y soient alors bien séparés, le système X étant contenu dans le détecteur central et le système Y étant non observé et diffusé dans le tube à vide. Une seconde méthode, dite méthode M_X, se base sur la différence de forme du spectre en M_X attendue pour des événements de DDIS et de DIS. Ces deux méthodes permettent de couvrir un large espace de phase avec une bonne précision statistique. Par contre l'estimation du bruit de fond résiduel de DIS est plus difficile, ce qui peut conduire à de grandes incertitudes systématiques.

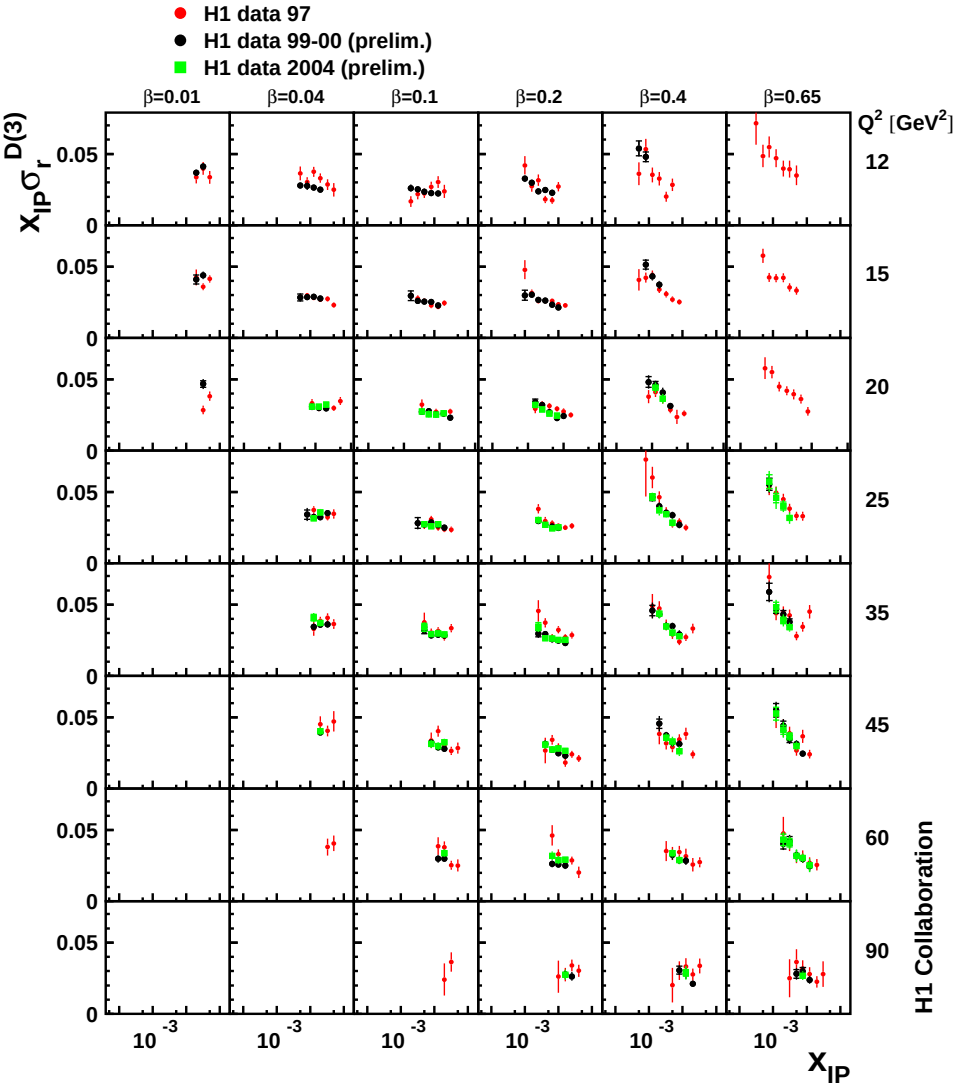

Figure 3.3 : *Sections efficaces réduites $x_{I\!P}\sigma_r^D(3)$ obtenues à partir des données de H1 de* 1997 *[Akt06c] et dans une analyse préliminaire récente des données de* 1999 *à* 2004 *[Akt06b].*

Les sections efficaces mesurées sont habituellement présentées sous la forme de sections efficaces réduites, $\sigma_r^{D(3)}$:

$$\sigma_r^{D(3)}(x, Q^2, x_{I\!P}) = \frac{xQ^4}{2\pi\alpha_{em}^2} \frac{1}{1+(1-y)^2} \frac{\mathrm{d}^3\sigma^{ep\to eXY}}{\mathrm{d}x_{I\!P}\mathrm{d}Q^2\mathrm{d}x}\,. \tag{3.4}$$

La mesure de $\sigma_r^{D(3)}$ effectuée par H1 avec la méthode LRG est présentée dans la figure 3.3, qui compare les résultats obtenus à partir des données enregistrées en 1997 [Akt06c] et de 1999 à 2004 [Akt06b]. Ce lot d'événements diffractifs sélectionnés correspond alors à environ 10% du nombre total d'événements inclusifs. Ceci est illustré dans la figure 3.4 qui présente le rapport $\sigma^{diff}/\sigma^{tot}$ en fonction de x et de Q^2. Nous observons alors que ce rapport reste bien constant en fonction de x et de Q^2.

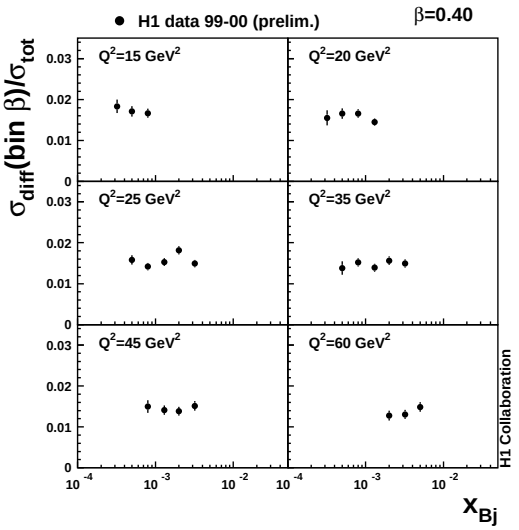

Figure 3.4 : *Evolution du rapport $\sigma^{diff}/\sigma^{tot}$ en fonction de x et de Q^2, à $\beta = 0.4$ fixé.*

3.2.3 Interprétations phénoménologiques

3.2.3.1 Les densités diffractives de partons

La propriété de factorisation colinéaire, prouvée pour le DDIS [Col98], permet d'exprimer $F_2^{D(3)}$ en terme de fonctions de distributions diffractives de partons (DPDF), f_i^D, qui sont indépendantes du processus dur. Les DPDFs s'interprètent, dans le référentiel où l'impulsion du proton est infinie, comme la probabilité conditionnelle de trouver dans le proton un parton ayant une fraction de son impulsion $x = \beta x_{I\!P}$ et sous la condition que le proton reste intact et perde une fraction $x_{I\!P}$ de son impulsion. La dépendance en Q^2 des DPDFs est gouvernée par les équations d'évolution DGLAP. Dans les équations d'évolution, seuls les paramètres (β, Q^2) jouent un rôle, les variables $(x_{I\!P}, t)$ étant des paramètres externes. Ainsi, une modélisation additionnelle de la dépendance en $(x_{I\!P}, t)$ des DPDFs est nécessaire. Pour ceci, l'idée de l'échange d'un pomeron, au sens de la théorie de Regge, pour expliquer la nature diffractive de l'interaction, est encore utilisée. Dans le modèle de la diffraction dure proposé alors par Ingelman et Schlein [Ing85], l'échange d'un pomeron entre le système diffractif et le proton est combiné au concept QCD d'évolution DGLAP de distributions de partons. Les DPDFs sont alors décomposées en un flux de pomeron $f(x_{I\!P}, t)$ et des fonctions de distribution de partons du pomeron, $f_i^{I\!P}(\beta, Q^2)$:

$$f_i^D(x_{I\!P}, t; \beta, Q^2) = f(x_{I\!P}, t)\, f_i^{I\!P}(\beta, Q^2)\,. \tag{3.5}$$

L'échange de pomeron est décrit par un pôle de Regge avec une trajectoire linéaire :

$$\alpha_{I\!P}(t) = \alpha_{I\!P}(0) + \alpha' t\,, \tag{3.6}$$

avec l'intercept $\alpha_{I\!P}(0) \geq 1$.

Le flux de pomeron s'exprime alors :

$$f(x_{I\!P}, t) = \frac{B^2(t)}{8\pi^2}\, x_{I\!P}^{1-2\alpha_{I\!P}(1)}\,, \tag{3.7}$$

$B(t)$ étant le facteur de forme électromagnétique de Dirac du proton. Cette factorisation (3.5), qui reste empirique et non complètement prouvée expérimentalement, est dénommée *factorisation de Regge*. Les deux factorisations, colinéaire et de Regge, sont représentées schématiquement dans la figure 3.5.

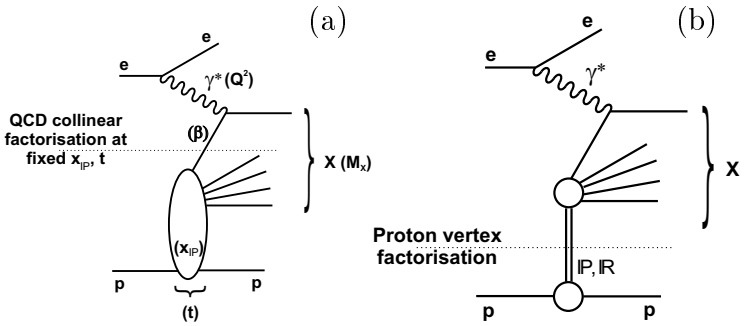

Figure 3.5 : *Diagrammes schématiques représentant les deux factorisations colinéaire (a) et de Regge (b).*

Malgré les problèmes conceptuels de ce modèle, le pomeron n'étant pas une particule, cette idée s'est révélée être bien adaptée pour décrire les données. Cette paramétrisation en termes de DPDFs combinée à un flux de pomeron fournit une des meilleures descriptions des sections efficaces de DDIS sur l'ensemble de l'espace de phase accessible [Roy07].

Un des résultats importants de la détermination des DPDFs est qu'une très grande fraction de l'impulsion échangée dans la réaction est portée par les gluons, de l'ordre de 70 à 80%. Ceci n'est pas surprenant, étant donné que $x = \beta x_{I\!P}$ et que $x_{I\!P} < 0.01$, les partons alors impliqués dans les réactions de diffraction sont de bas x. Une autre façon d'interpréter ce résultat est d'étudier à partir des DPDFs la probabilité d'occurrence de la diffusion diffractive en fonction du type de parton participant à l'interaction dure. Il est alors possible de déterminer que, en fonction du Q^2, environ 60 à 80% des interactions diffractives sont produites par des gluons du proton [Fra99].

La validité de cette définition des DPDFs repose bien sûr sur la factorisation de Regge et donc sur l'absence de dépendance en Q^2 ou β du flux de pomeron. Ceci peut être testé en mesurant l'intercept $\alpha_{I\!P}(0)$ pour différents domaines de Q^2 ou β par un ajustement de la formule (3.5) sur les données, $f_i^{I\!P}(\beta, Q^2)$ étant fixé par les DPDFs. Une telle mesure récente de la dépendance en Q^2 de $\alpha_{I\!P}(0)$ est présentée dans la figure 3.6. Aucune dépendance significative de $\alpha_{I\!P}(0)$ avec Q^2 n'est observée, dans la limite de la précision expérimentale actuelle. Cette mesure a été effectuée à partir du lot de données disposant à l'heure actuelle de la meilleure précision statistique. Nous voyons que celle-ci reste toutefois limitée et il serait donc intéressant d'inclure de nouvelles données, notamment à grand Q^2, afin de mieux contraindre la valeur de $\alpha_{I\!P}(0)$. Ceci pourra se faire par l'analyse des données de la phase HERA II, qui reste encore à réaliser.

Cette approche en termes de DPDFs n'apporte cependant aucune explication sur la nature réelle des interactions diffractives. Son unique intérêt réside dans le fait que les DPDFs, de la même manière que les PDFs, sont des fonctions indépendantes du processus considéré et pourraient donc être utilisées pour la description du tout processus diffractif dans lesquels la factorisation colinéaire dure peut s'appliquer. Ainsi, ceci se vérifie bien en collisions *ep*, où les DPDFs extraites des interactions de DDIS inclusives sont utilisées avec succès pour décrire des processus diffractifs plus exclusifs, comme la production de jets [Akt07b] ou la production diffractive de quarks lourds [Akt07a].

Les DPDFs mesurées à HERA ne sont cependant pas directement utilisables pour décrire les données de collisions diffractives hadron-hadron. En effet, à cause d'interactions entre les partons spectateurs des hadrons en collisions, la factorisation colinéaire ne s'applique pas aux collisions hadrons-hadrons [Wus99]. Ces effets peuvent cependant être mo-

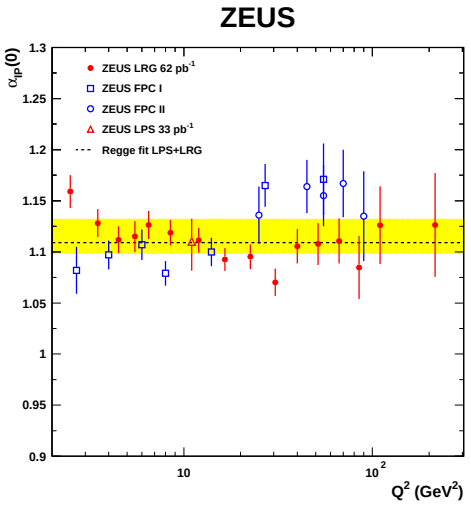

Figure 3.6 : *L'intercept du pomeron, $\alpha_{I\!P}(0)$ en fonction de Q^2 déterminé à partir des différents lots de données existants de l'expérience ZEUS (d'après [Che09a]).*

délisés par l'introduction d'une facteur additionnel de probabilité de survie de l'intervalle en rapidité (*rapidity gap survival probability*). Ainsi, les DPDFs déterminées à HERA pourraient rester un ingrédient essentiel dans l'étude des processus diffractifs au Tevatron puis au LHC.

3.2.3.2 Le modèle de dipôle

Il est possible d'obtenir une bonne description des données de DDIS avec les DPDFs au *twist* dominant. Cependant, cette approche ne permet pas d'expliquer l'observation expérimentale fondamentale que le rapport $\sigma^{diff}/\sigma^{tot}$ reste pratiquement constant en fonction de l'énergie W. La compréhension de ce phénomène est fournie par le modèle de dipôle.

Dans le référentiel du proton au repos, à bas x, le photon fluctue en une paire quark-antiquark qui diffuse ensuite sur le proton par échange de deux gluons, dans la description la plus simple. Le contenu partonique $q\bar{q}$ du photon virtuel est alors décrit en termes de fonctions d'onde dans le cône de lumière.

Ce mécanisme menant à la dissociation du photon, puis à son interaction avec le proton peut être factorisé et décrit par une convolution de la fonction d'onde du photon et d'une section efficace quark-antiquark. Dans le cas du DIS, ceci conduit à l'expression suivante pour la section efficace $\gamma^* p$ et la fonction de structure F_2 :

$$F_2(x,Q^2) = \frac{Q^2}{4\pi^2\alpha_{em}}\left(\sigma_T+\sigma_L\right), \tag{3.8}$$

$$\sigma_{T,L}(x,Q^2) = \int \mathrm{d}z\mathrm{d}^2r \left|\Psi_{L,T}(z,r,Q^2)\right|^2 \hat{\sigma}(x,r), \tag{3.9}$$

où $\Psi_{L,T}$ sont les fonctions d'onde longitudinale et transverse du photon dans le cône de lumière, calculables précisément en QED, r est la taille transverse du dipôle et z la fraction d'impulsion du photon. La section efficace de dipôle $\hat{\sigma}(x,r)$ décrit l'interaction du dipôle avec le proton et dépend principalement d'effets non perturbatifs et doit donc être modélisée.

Pour modéliser la transition vers le régime de saturation de QCD, une première paramétrisation phénoménologique de $\hat{\sigma}(x,r)$ a été proposée [GB99a] :

$$\hat{\sigma}(x,r) = \sigma_0\left(1-e^{(-r^2Q_s^2(x))}\right), \tag{3.10}$$

où $Q_s(x) = Q_0 x^{-\lambda}$ est une échelle de saturation qui caractérise la transition vers le régime de saturation. La transition dans le régime de saturation arrive quand Q devient similaire à $Q_s(x)$. Les paramètres du modèle, σ_0, Q_0 et λ, sont alors définis par un ajustement sur les données de DIS à bas x. Des paramétrisations plus évoluées sont maintenant étudiées [Ian04].

Dans le cas de la diffraction, l'échange neutre de couleur (pomeron) peut être modélisé au premier ordre par l'échange de deux gluons. Lorsque seul le dipôle $q\bar{q}$ contribue à la formation du système diffractif, la section efficace diffractive à $t = 0$ s'écrit :

$$\frac{\mathrm{d}\sigma^{diff}}{\mathrm{d}t}_{|t=0} = \frac{1}{16\pi} \int \mathrm{d}z \mathrm{d}^2 r \left|\Psi_{L,T}(z, r, Q^2)\right|^2 \hat{\sigma}^2(x, r)\,, \tag{3.11}$$

la section efficace $\hat{\sigma}^2(x, r)$ étant la même que celle utilisée pour décrire la section efficace de DIS à bas x (équation (3.9).

Le DDIS est alors un processus idéal pour étudier le phénomène de saturation des partons car il est particulièrement sensible aux contributions de dipôles de grande taille $r > 1/Q_s(x)$. Une modélisation de la section efficace de dipôle incluant la saturation comme dans l'équation(3.10) conduit alors naturellement au rapport [GB99a] :

$$\frac{\sigma^{diff}}{\sigma^{tot}} \sim \frac{1}{\ln(Q^2/Q_s^2(x))}\,. \tag{3.12}$$

Ainsi une même modélisation permet de décrire à la fois la section efficace de DIS à bas x et la section efficace de DDIS. Les paramètres de la section efficace de dipôle, déterminés à partir des données de DIS seule, peuvent en effet être utilisés pour décrire la section efficace de DDIS [GB99b]. Ceci confère donc à cette approche un pouvoir hautement prédictif.

Dans ce cadre du modèle de dipôle, une paramétrisation simple en trois contributions de la fonction de structure diffractive F_2^D a été proposée par J. Bartels *et al.* (BEKW) [Bar99, Che05]. Cette paramétrisation s'est révélée être très efficace pour décrire l'ensemble des données de DDIS [Roy07].

La première contribution $F_2^{D(3)}(q\bar{q}_T)$ correspond à la diffusion diffractive de la composante transverse $q\bar{q}$ du photon par échange de deux gluons (voir figure 3.7(a)). A suffisamment grand M_X^2, la paire $q\bar{q}$ peut rayonner un gluon additionnel avant d'atteindre le proton. La seconde contribution $F_2^{D(3)}(q\bar{q}g_T)$, correspond donc à la composante transverse $q\bar{q}g$ (voir figure 3.7(b)). Enfin, pour de petites masses du système diffractif, il est aussi attendu que la section efficace longitudinale pour la production d'une paire $q\bar{q}$ ne soit pas négligeable par rapport à la section efficace transverse. Ceci est donc pris en compte dans un troisième terme, $F_2^{D(3)}(q\bar{q}_L)$, qui donne une contribution de twist d'ordre supérieur, correspondant à la composante longitudinale $q\bar{q}$.

A titre d'exemple, les sections efficaces de DDIS mesurées par H1 sont comparées au résultat de l'ajustement d'une telle paramétrisation BEKW dans la figure 3.8. L'ajustement a été réalisé en utilisant l'ensemble des données. Nous observons un bon accord entre l'ajustement global et les sections efficaces mesurées, ainsi que l'évolution de chacune des trois composantes en fonction β. Nous voyons aussi que l'ajout de nouvelles données en vue d'augmenter la précision statistique des mesures actuelles permettrait alors d'obtenir des contraintes plus fortes sur les modèles.

D'autres modèles de dipôle, incluant la saturation, permettent également de bien décrire les données de DDIS, et ce, sans aucun ajustement, les paramètres du modèle étant

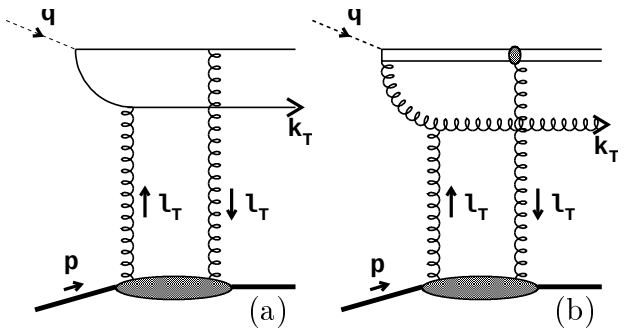

Figure 3.7 : *Contributions $q\bar{q}$ (a) et $q\bar{q}g$ (b) du système diffractif dans le modèle de dipôle.*

déterminés à partir des données de DIS seules [Mar07a], ce qui démontre la force de cette approche. Ces modèles permettent en effet d'unifier la description des interactions de DIS à bas x et de DDIS dans un même cadre théorique fondé sur la QCD. Ils sont ainsi très prometteurs pour améliorer notre compréhension de la transition en régimes dur et mou de la QCD et des effets de saturation. L'apport de nouvelles données de HERA, d'une précision supérieure aux données actuelles, sera alors également nécessaire pour mieux contraindre ces modèles.

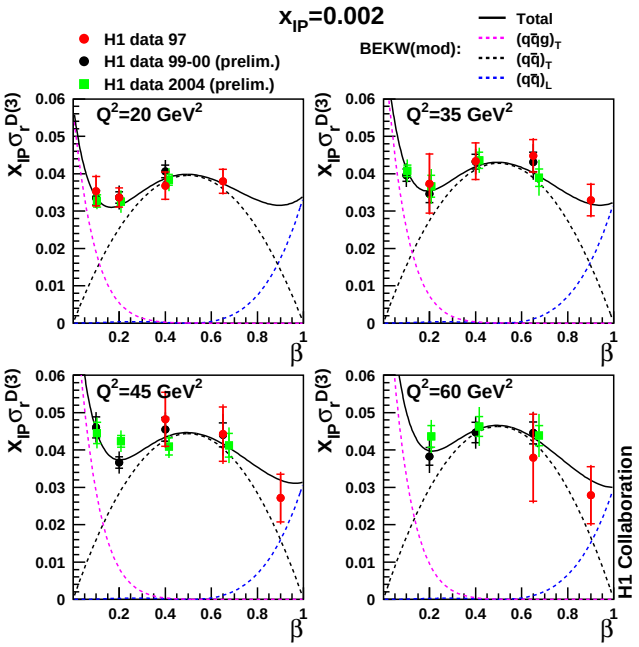

Figure 3.8 : *Comparaisons de la section efficace de DDIS avec le modèle de dipôle BEKW. Les résultats sont présentés en fonction de β, pour différentes valeurs de Q^2 et à une valeur fixe $x_{I\!P} = 0.002$.*

3.3 La diffusion Compton profondément virtuelle

Les processus de DIS et DDIS que nous avons vus jusqu'à présent ont une section efficace qui dépend de la probabilité de diffusion sur un parton dans le proton. Ces processus, conduisant à la destruction de l'objet sondé, permettent donc d'accéder uniquement aux distributions d'impulsion longitudinale des partons et ne peuvent donc fournir une information complète sur la structure du proton. Ils ne sondent ni la distribution spatiale des constituants du proton, ni leurs corrélations.

Les processus de production exclusive de particules, sans excitation ou dissociation du proton, sont alors intéressants pour combler ces déficits. Parmi ceux-ci, la diffusion Compton profondément virtuelle (DVCS), $\gamma^* \rightarrow \gamma p$, est le processus le plus simple. La section efficace de ce processus est proportionnelle à l'amplitude de probabilité d'extraire un parton du proton initial, puis de le remettre pour former à nouveau un proton dans l'état final (voir figure 3.9). La transition d'un photon virtuel à un photon réel force les fractions d'impulsion longitudinale des deux partons participants à être différentes (*skewed*). Cette différence en moment longitudinal contient une information sur les corrélations entre les impulsions des partons du proton, auxquelles le processus de DVCS est donc sensible.

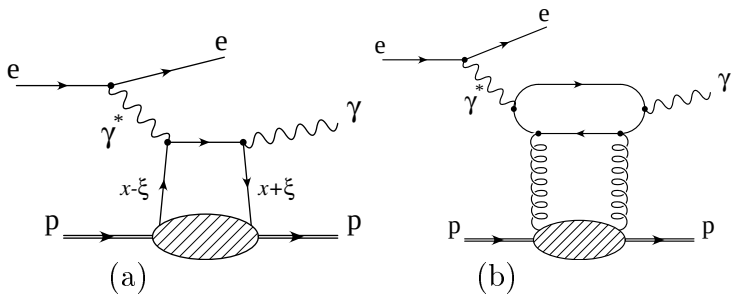

Figure 3.9 : *Exemples de diagrammes pour le processus de DVCS à l'ordre dominant (*leading order*) (a) et à l'ordre suivant (*next-to-leading order*) (b).*

La section efficace du DVCS dépend également du moment transverse transféré au proton, dont le carré est, à haute énergie, égal avec une bonne approximation à $-t$. Par transformée de Fourier de l'espace des moments à celui des paramètres d'impact, cette dépendance en t nous donne une information sur la distribution bidimentionelle dans le plan transverse du parton touché.

A grand Q^2, le théorème de factorisation colinéaire s'applique également au DVCS. Mais, dans ce cas, les PDFs ne peuvent plus être utilisées pour définir l'élément de matrice hadronique et nous devons considérer des fonctions plus complètes, prenant en compte les différences d'impulsion entre les états initial et final du proton. Les distributions généralisées de partons (GPD) sont alors utilisées. Elles dépendent de deux fractions d'impulsion longitudinale, au lieu d'une seule pour les PDFs, de l'impulsion transverse transférée au proton et de l'échelle à laquelle les partons sont sondés. La dépendance des GPDs en fonction de l'échelle est gouvernée par une généralisation des équations DGLAP. La caractérisation des GPDs, dans le régime des bas x et grands Q^2, est donc une des raisons principales pour mesurer le processus de DVCS en collisions ep à HERA.

Le processus DVCS peut, bien sûr, être également interprété dans le cadre du modèle de dipôle [Mar07b].

3.3.1 Mesures expérimentales

Les nouvelles données enregistrées par H1 lors de la phase HERA II ont permis d'améliorer considérablement la précision des mesures de la section efficace du DVCS (voir annexes C et D), par rapport aux mesures antérieures effectuées sur les données HERA I [Akt05, Che03, Che09b]. La section efficace de DVCS mesurée par H1 à partir des données HERA II est présentée dans la figure 3.10, en fonction de Q^2 et de W. Elle est comparée à la mesure la plus récente effectuée par la collaboration ZEUS [Che09b]. Sur cette figure, les évolutions en Q^2 et W prédites par deux modèles basés respectivement sur le formalisme des

GPDs [Kum08, Kum] et des dipôles [Mar07b] sont aussi représentées. Nous observons que ces deux modèles décrivent bien les données. La forte évolution de la section efficace de DVCS en fonction de W, de la forme $W^{0.63}$, indique clairement la présence d'un processus dur sous-jacent. Cette dépendence est constante en fonction de Q^2 dans le domaine cinématique étudié (voir annexe D).

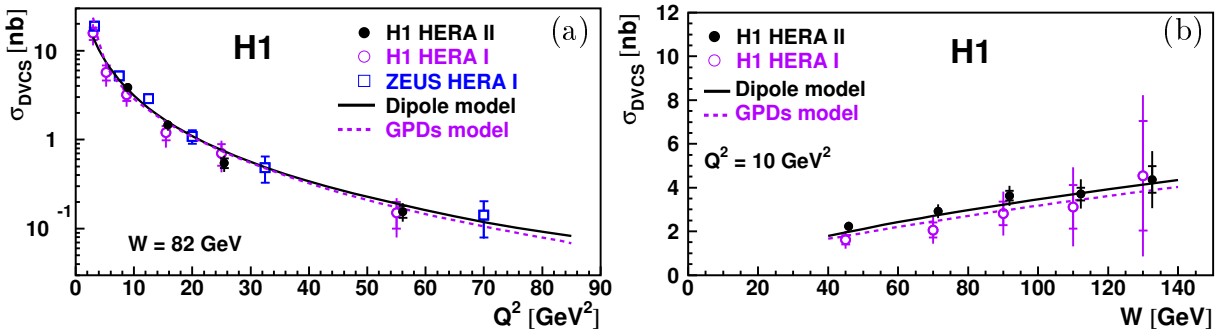

Figure 3.10 : *Section efficace du processus DVCS $\gamma * p \rightarrow \gamma p$ en fonction de Q^2 à $W = 82$ GeV (a) et en fonction de W à $Q^2 = 10$ GeV. Les mesures réalisées par H1 sur les données HERA I [Akt05] et HERA II (annexe D) et par ZEUS [Che09b] sont représentées. Les lignes en pointillés représentent les prédictions d'un modèle de GPDs [Kum08, Kum] et les lignes pleines celles d'un modèle de dipôle [Mar07b].*

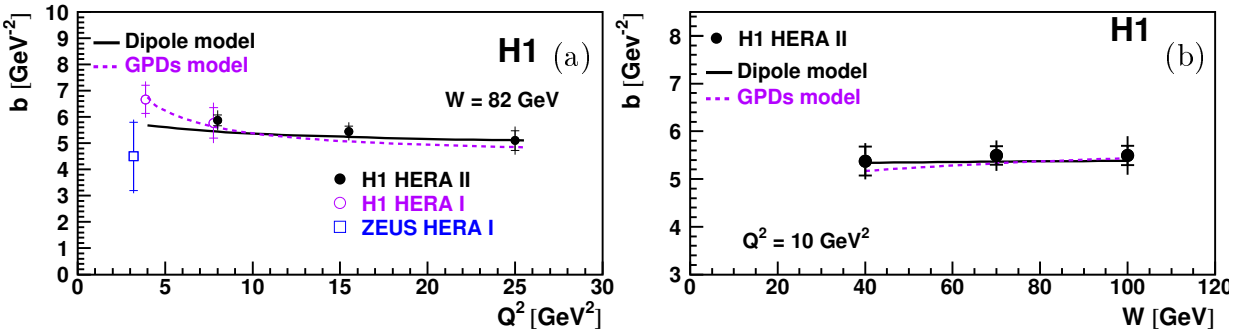

Figure 3.11 : *Evolution de la pente en t, b, du DVCS en fonction de Q^2 (a) et W (b). Dans la figure (a), les mesures récentes de H1 (annexe D) sont comparées aux autres mesures de H1 [Akt05] et ZEUS [Che09b]. Les lignes en pointillés représentent les prédictions d'un modèle de GPDs [Kum08, Kum] et les lignes pleines celles d'un modèle de dipôle [Mar07b]*

La dépendance en t de la section efficace de DVCS peut être paramétrée avec une bonne approximation par une fonction de la forme $e^{-b|t|}$. Le lot de données HERA II a ainsi permis de mesurer la dépendance en t de la section efficace de DVCS, en fonction de Q^2 et, pour la première fois, en fonction de W. Ces mesures sont illustrées par la figure 3.11 qui représente l'évolution de b en fonction de Q^2 et W. Par transformée de Fourier, la variable b peut être reliée à la distance transverse typique entre les objets en collision. A grand Q^2, le dipôle $q\bar{q}$ est quasiment ponctuel et b est donc essentiellement le reflet de l'extension transverse du proton. Le b moyen mesuré sur l'ensemble des données peut donc être converti en un paramètre d'impact moyen de $\sqrt{< r_T^2 >} = 0.64 \pm 0.02$ fm, qui correspond alors à l'extension transverse de la densité de partons. A la valeur moyenne de $x = 1.2 \cdot 10^{-3}$ de notre mesure, cette densité est dominée par les gluons et les quarks de la mer.

Il est alors possible d'étudier l'évolution de l'extension transverse des partons en fonction de x. Ainsi, à de plus larges valeurs de x ($x > 0.1$), une plus faible valeur de $\sqrt{< r_T^2 >}$ est attendue. Elle est alors dominée par les contributions des quarks de valence. Dans ce domaine, seules des déterminations indirectes de $\sqrt{< r_T^2 >}$ existent. Elles donnent une estimation de $\sqrt{< r_T^2 >} \sim 0.4$ fm pour $x > 0.2$ [Bel02]. Ceci nous indique une image en trois dimensions du proton, comme étant composé de partons *rapides* (à grand x) formant un centre de quarks de valence, entouré de partons plus lents (à bas x), que sont les quarks de la mer et les gluons, d'extension spatiale plus grande autour du centre. Les calculs récents de QCD sur réseau semblent ainsi valider une telle image du proton [Neg04].

3.3.2 Caractérisation des GPDs

L'intérêt des données de HERA II est également de disposer de lots de données en collisions e^+p et e^-p de luminosités quasiment égales. Ceci nous a permis de mesurer, pour la première fois en collisions ep, l'asymétrie de la section efficace de la réaction $e^\pm p \to e^\pm \gamma p$ en fonction de la charge du lepton incident. Cette asymétrie provient de l'interférence entre deux processus contribuant à cette réaction, le Bethe-Heitler, un processus purement électromagnétique, et le DVCS, qui lui est purement hadronique (voir annexe D). L'asymétrie dépend de ϕ, l'angle formé par le plan contenant les leptons entrant et sortant avec le plan formé par les photons réels et virtuels [Bel02].

La mesure de cette asymétrie est importante car elle permet d'accéder de manière unique à la partie réelle de l'amplitude du DVCS (voir annexe D). En effet, dans le régime cinématique de HERA, l'amplitude du DVCS est principalement imaginaire [Bel02]. La mesure de la section efficace du DVCS ne permet donc que d'accéder à la partie imaginaire de l'amplitude. Dans le modèle des GPDs, le calcul de la partie réelle de l'amplitude du DVCS nécessite une paramétrisation des GPDs sur l'ensemble du domaine en x [Bel02, Kum08, Kum]. La mesure de cette quantité apporte donc une information nouvelle et est un bon test de la validité des paramétrisations de GPDs employées dans les modèles.

L'asymétrie mesurée est représentée dans la figure 3.12. Elle est comparée à la prédiction d'un modèle de GPDs [Kum08, Kum], qui est en bon accord avec notre mesure. Même si la précision statistique et systématique de cette mesure reste limitée, elle fournit cependant un bon test pour les modèles actuels.

Nous observons aussi que dans le domaine de bas x de notre mesure, la partie réelle de l'amplitude de DVCS est positive. En comparaison, à plus grand x ($x \sim 0.1$) et plus bas Q^2, une partie réelle plus faible et négative a été mesurée par la collaboration HERMES [Air08] [1]. Ce dernier résultat ne semble donc pas indiquer, dans le domaine cinématique de HERMES, une dépendance en énergie dure de la section efficace de DVCS, à l'opposé de notre résultat. Il serait donc intéressant de pouvoir sonder la région intermédiaire en x, de transition entre les deux régimes d'interactions dures et molles, respectivement à bas et grand x. C'est ce que propose le programme futur de l'expérience COMPASS [d'H02] en mesurant la section efficace de DVCS dans le domaine des x intermédiaires et permettant ainsi une étude détaillée de la région de transition.

[1] Il faut noter que la convention pour la définition de l'angle ϕ alors utilisée par HERMES est différente de celle adoptée dans notre analyse.

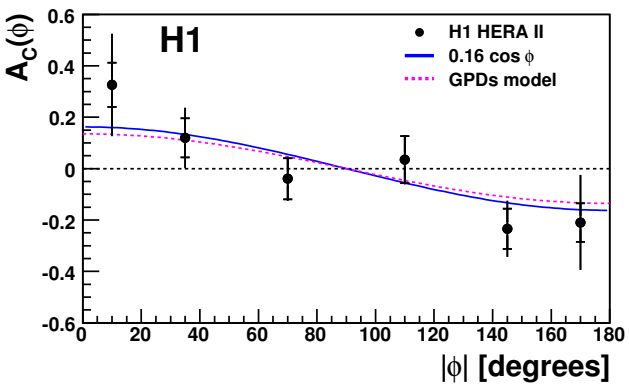

Figure 3.12 : *Asymétrie due à la charge du lepton incident en fonction de l'angle ϕ (voir annexe D). La ligne en pointillés représente la fonction $0.16\cos\phi$ et la courbe pleine la prédiction d'un modèle de GPDs [Kum08, Kum].*

3.3.3 Le DVCS et la saturation

Une propriété importante des modèles de dipôles qui incluent la saturation est que la section efficace totale peut être exprimée comme une fonction d'une seule variable sans dimension τ :

$$\sigma_{tot}^{\gamma^* p}(x, Q^2) = \sigma_{tot}^{\gamma^* p}(\tau), \quad \text{avec} \quad \tau = \frac{Q^2}{Q_s^2(x)}\,. \tag{3.13}$$

Cette propriété est appelée invariance d'échelle géométrique (*geometric scaling*) et est illustrée dans la figure 3.13 pour la section efficace de DIS. Elle est l'indication de l'existence d'une échelle interne (l'échelle de saturation), caractérisant les systèmes de partons denses. Elle a été observée expérimentalement dans le domaine des bas x pour la section efficace de DIS ep [Sta01], pour les réactions profondément inélastiques sur des cibles de nucléons [Fre03] et également pour les processus diffractifs [Mar06].

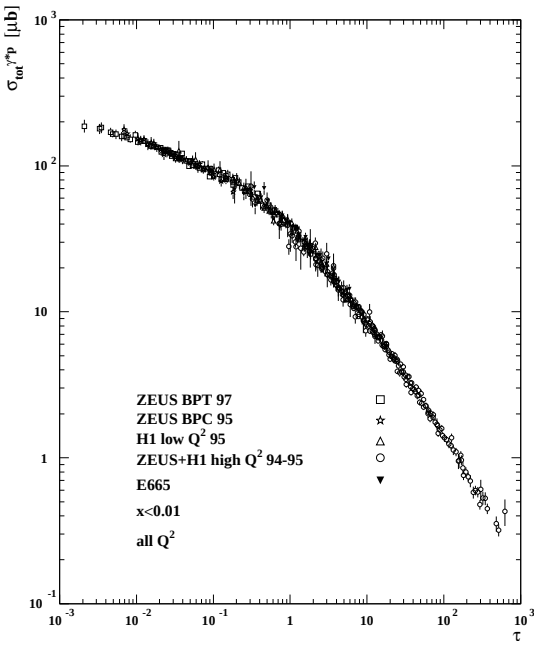

Figure 3.13 : *Mesures expérimentales de $\sigma^{\gamma^* p}$ pour la région $x < 0.01$ représentées en fonction de la variable d'invariance d'échelle τ (d'après [Sta01]).*

Il est donc intéressant d'utiliser ces nouvelles données sur le DVCS pour vérifier avec une meilleure précision cette propriété d'invariance d'échelle géométrique. Ainsi, la section

efficace de DVCS est présentée en fonction de la variable τ dans la figure 3.14. Nous observons que toutes les valeurs s'alignent bien sur une même courbe, ce qui est la manifestation de l'effet de la saturation. La section efficace du DVCS est donc bien compatible avec la loi d'invariance d'échelle géométrique prédite par le modèle utilisé. La dépendance de la section efficace du DVCS en fonction de τ a aussi pu être étudiée pour la première fois (voir annexe C) et cette propriété d'invariance d'échelle géométrique a alors été vérifiée pour différentes valeurs de t.

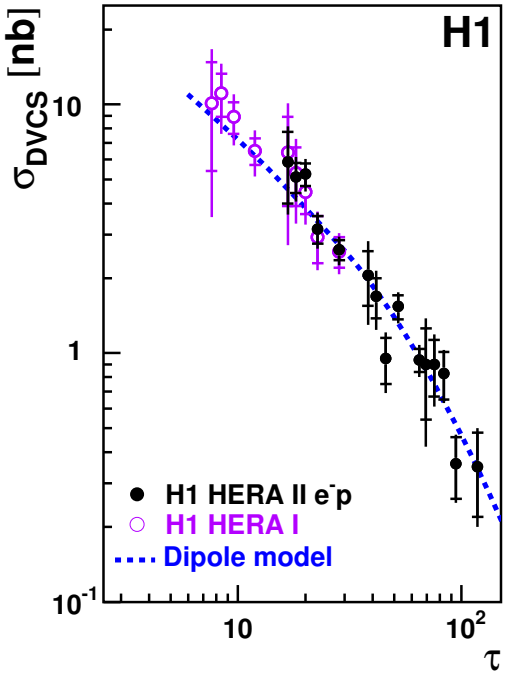

Figure 3.14 : *Section efficace de DVCS en fonction de la variable d'échelle $\tau = Q^2/Q_s^2(x)$. La courbe en pointillés représente les prédictions d'un modèle de dipôles [Ian04, Mar06].*

3.4 Conclusions

Au travers de ce chapitre, nous avons vu que les interactions diffractives à HERA offrent de nouvelles fenêtres pour l'étude de la structure du proton à bas x et de la dynamique QCD.

La diffusion diffractive inclusive permet ainsi de regarder l'interaction de singulets de couleur de petites tailles avec le proton et de sonder ainsi son contenu en partons de bas x, différemment et avec une meilleure sensibilité que les interactions de DIS.

Les interactions diffractives à HERA donnent également accès à des densités très grandes de partons dans le proton. Elles permettent ainsi d'étudier la dynamique de la QCD dans ce régime particulier dit de saturation, avec des connections intéressantes avec les mesures effectuées en collisions d'ions lourds. Ainsi, les estimations de l'échelle de saturation $Q_s^2(x)$ faites à HERA peuvent être utilisées pour décrire certaines caractéristiques des données obtenues au RHIC [Kha01, Kra03].

Les mesures de DVCS, et plus généralement de production de mésons vecteurs, à HERA permettent quant à elles d'obtenir de nouvelles informations sur la structure en trois dimensions du proton et sur son extension transverse. Elles permettent de compléter ainsi l'image en impulsion longitudinale du proton donnée par la mesure des PDFs. Le processus de DVCS permet également d'accéder aux corrélations entre partons dans le proton, apportant ainsi des éléments additionnels pour la détermination des GPDs.

Une meilleure compréhension des corrélations entre la distribution transverse des partons du proton et leur fraction d'impulsion est non seulement intéressante en elle-même pour décrire la structure interne des hadrons, mais elle a aussi des conséquences pratiques pour les collisions hadrons-hadrons. Considérons la production d'un système de grande masse, une particule lourde ou deux jets. Selon la factorisation dure standard, seules les distributions de partons intégrées sur l'ensemble des paramètres d'impact sont utiles pour déterminer sa section efficace de production inclusive. Les distributions de partons en paramètre d'impact (dans le plan transverse) ne jouent alors aucun rôle. Il peut cependant se produire des interactions additionnelles, dans la même collision, tout particulièrement à haute énergie comme au Tevatron ou au LHC. Les effets de ces interactions secondaires s'annulent lorsque nous regardons des observables suffisamment inclusives. Elles affectent cependant les caractéristiques de l'événement et doivent en pratique être prises en compte. La distribution transverse des partons du proton devient alors importante. En effet, la production d'un système lourd requiert que les partons interagissant aient de grandes fractions d'impulsion. La distribution en paramètre d'impact de ces partons, alors étroite, force la collision à être plus centrale, ce qui de ce fait accroît la probabilité d'interactions multiples dans l'événement.

La connaissance des corrélations entre les distributions transverse et en impulsion des partons du proton est donc importante pour pouvoir décrire les interactions multiples au LHC ou au Tevatron [Fra04].

3.5 Contributions personnelles

A partir de 2005, j'ai travaillé en collaboration avec Laurent Schoeffel, physicien au SPP-Irfu du CEA Saclay, pour l'étude des interactions diffractives à HERA.

Nous avons ainsi réalisé une mesure préliminaire de la section efficace de DDIS utilisant des données de HERA I et HERA II, afin d'augmenter la précision statistique de la mesure par rapport aux résultats alors existants. Ce résultat a été présenté en conférences en 2006. A l'époque, deux méthodes différentes étaient employées par les collaborations H1 et ZEUS pour extraire les événements de DDIS des événements de DIS. Les analyses menées dans H1 étaient traditionnellement basées sur la mesure d'un intervalle en rapidité (LRG), alors que ZEUS utilisait la mesure de M_X pour effectuer la séparation. Cette différence était alors source de conflit entre les deux expériences, lors de la comparaison des résultats respectifs.

Nous avons alors appliqué pour la première fois la méthode dite M_X employée par ZEUS aux données de H1, afin de pouvoir comparer les deux méthodes et estimer leurs biais expérimentaux potentiels sur un même lot de données de grande statistique. Nous en avons conclu que les deux méthodes étaient en bon accord sur le domaine cinématique considéré. La démarche inverse d'utiliser la méthode LRG a depuis été reprise par ZEUS pour étudier leurs données. Nous travaillons actuellement à une mesure de F_D^2 basée sur l'ensemble des données de H1 enregistrées entre 1999 et 2007.

Nous avons ensuite étudié le processus de DVCS en réalisant deux publications portant sur les données HERA II (voir annexes C et D). Ces mesures de la section efficace de DVCS en collisions ep à HERA sont les plus précises à ce jour et nous avons mesuré l'asymétrie du processus en fonction de la charge du lepton incident, pour la première fois dans ce domaine cinématique.

Chapitre 4

La frontière à haute énergie du modèle standard

A l'heure actuelle, HERA fait partie, avec le LEP et le Tevatron, des trois plus grands collisionneurs de particules ayant opéré, ou opérant, à la frontière à haute énergie du modèle standard. La luminosité maintenant accumulée à HERA permet de rechercher de nouveaux processus ou de sonder des processus rares du MS ayant une section efficace inférieure à 1 pb.

De manière générale, HERA, à la différence du Tevatron ou du LEP, n'est pas une machine d'annihilation de deux particules. En collisions $p\bar{p}$ ou e^+e^-, toute nouvelle particule peut être produite par paire, en voie s, par couplage à un boson de jauge du MS. A HERA, en revanche, le boson du MS échangé se trouve dans la voie t, ce qui va limiter les recherches principalement à la production simple de nouvelles particules. Seuls de nouveaux bosons, couplant directement aux leptons et aux quarks pourraient être produits en collisions eq, en voie s. Dans ces cas, la section efficace d'une production de nouvelle particule va dépendre de son couplage, non connu, aux champs du MS. Ainsi les recherches à HERA ne peuvent fournir de contraintes absolues sur la masse de nouvelles particules. Cependant, l'observation en collisions ep de toute nouvelle particule fournirait, non seulement une information sur sa masse, mais aussi sur son couplage au MS.

A HERA, le bruit de fond QCD, qui est important au Tevatron, devient moins problématique. Ceci permet alors d'investiguer un plus large spectre de canaux de désintégration et d'étendre la sensibilité de HERA à des régions de l'espace des paramètres inaccessibles au Tevatron. Les recherches menées au LEP bénéficient quant à elles de bas bruits de fond et de grandes luminosités, mais sont limitées par l'énergie disponible dans le centre de masse, plus faible qu'à HERA ou au Tevatron.

Dans la quête de déviations aux prédictions du MS, deux grandes voies s'offrent à nous. La première possibilité est de rechercher, dans les données, les signatures spécifiques prédites par différentes extensions théoriques possibles au MS. La seconde approche, dite modèle indépendante, consiste à s'affranchir de tout à priori théorique, en dehors du MS, et à chercher des déviations lors de comparaisons précises entre données et prédictions du MS, pour certaines topologies d'états finals spécifiques. Ceci peut alors se faire en étudiant des processus rares du MS, ayant une faible section efficace et présentant peu de bruits de fond. La méthode la plus générale consiste à investiguer de manière générique l'ensemble des états finals pouvant être produits.

Bien sûr, toute recherche de nouvelle physique, qu'elle soit modèle indépendante ou initiée par un certain modèle, repose avant tout sur une bonne compréhension, et modélisation par les générateurs Monte Carlo disponibles, des processus du MS, ainsi qu'une

excellente compréhension de la réponse du détecteur sur l'ensemble de l'espace de phase accessible.

4.1 Recherches spécifiques de nouvelle physique

En tant que collisionneur électron-proton, HERA est une machine idéale pour la recherche de particules couplant directement aux quarks et aux leptons, les leptoquarks qui sont prédits dans de nombreuses extensions du MS. Une large variété d'autres extensions possibles du MS peut aussi être testée à HERA, comme, entre autre, l'existence de dimensions supplémentaires ou de particules supersymétriques dans le cas où la R-parité serait violée. Parmi ces différentes recherches possibles, nous allons nous intéresser plus particulièrement à la recherche de nouvelles sous-structures de la matière. Pour ce faire, il est alors possible de rechercher une manifestation indirecte d'une telle sous-structure, comme une modification de la section efficace de diffusion $eq \to eq$, ou bien une manifestation directe par l'observation de nouvelles résonances.

4.1.1 Les quarks sont-ils ponctuels ?

Rappelons que la diffusion de particules est le processus par excellence utilisé pour sonder les sous-structures de la matière. Les interactions de DIS par courant neutre à HERA permettent ainsi de sonder la sous-structure du proton à des distances de l'ordre de 10^{-18} m.

Les mesures de section efficace NC peuvent ainsi être utilisées pour rechercher aux plus grands Q^2 une déviation par rapport à la prédiction du MS, donnée par les densités de quark, déterminées à bas Q^2, et les équations d'évolution DGLAP. Par exemple, un modèle naïf associant une distribution de charge de taille finie, et donc un facteur de forme, aux quarks et considérant l'électron comme une particule ponctuelle, réduirait à grand Q^2 la section efficace NC par rapport aux prédictions du MS selon:

$$\frac{\mathrm{d}\sigma}{\mathrm{d}Q^2} = \frac{\mathrm{d}\sigma^{SM}}{\mathrm{d}Q^2} \left[1 - \frac{R_q^2}{6} Q^2\right]^2 , \tag{4.1}$$

où R_q est alors le rayon de la distribution de charge des quarks.

La mesure de la section efficace NC en fonction de Q^2 sur l'ensemble des données de H1 permet ainsi de poser une limite sur la taille des quarks de $R_q < 0.74 \cdot 10^{-18}$ m à 95% de niveau de confiance (CL) (voir figure 4.1). La limite déduite des données de ZEUS est équivalente, et égale à $R_q < 0.63 \cdot 10^{-18}$ m à 95% CL.

4.1.2 Existence de sous-structures des fermions ?

Au-delà des recherches indirectes par interactions de contact, une signature non-ambiguë d'une nouvelle sous-structure de la matière serait l'observation d'états excités de fermions (f^*), par leur désintégration en un boson de jauge du MS. Une structure composite des fermions permettrait en effet d'expliquer la hiérarchie des masses des particules du MS ainsi que l'agencement des particules en trois familles.

Les interactions de ces fermions excités avec les particules du MS peuvent être décrites de manière très générale dans un modèle effectif [Hag85, Bou93, Bau90]. L'interaction d'un f^* avec un boson de jauge est alors décrite par un couplage magnétique proportionnel à

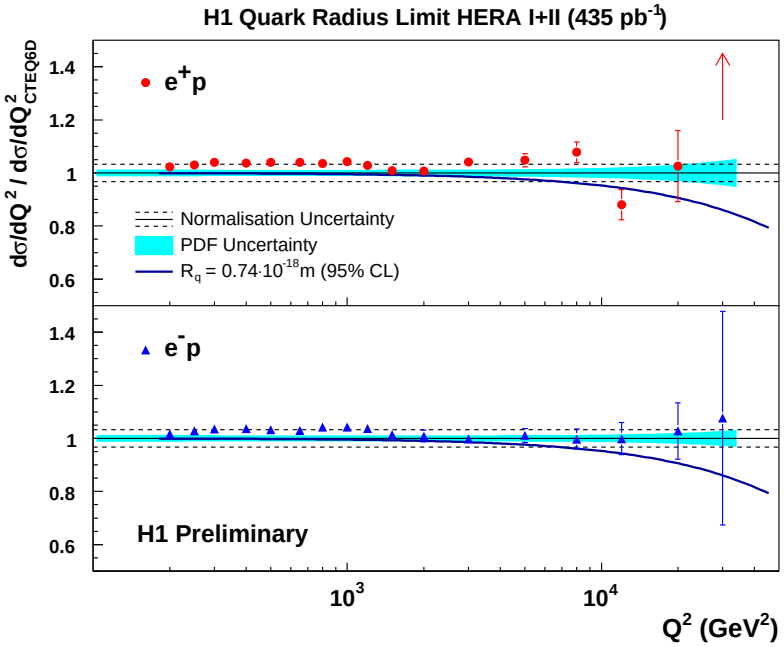

Figure 4.1 : *La section efficace NC $d\sigma/dQ^2$, normalisée à la prédiction du MS déterminée à partir des PDFs CTEQ6D [Pum02], pour des collisions e^+p et e^-p. Les courbes représentent la correction au MS due à un hypothétique rayon de charge fini des quarks de* $0.74 \cdot 10^{-18}$ *m.*

$1/\Lambda$, Λ correspondant alors à une nouvelle échelle de sous-structure. Le Lagrangien effectif utilisé s'écrit [Bou93] :

$$\mathcal{L}_{int.} = \frac{1}{2\Lambda}\bar{F}^*_R\,\sigma^{\mu\nu}\left[gf\frac{\tau^a}{2}W^a_{\mu\nu} + g'f'\frac{Y}{2}B_{\mu\nu} + g_s f_s\frac{\lambda^a}{2}G^a_{\mu\nu}\right]\,F_L + h.c.\,, \qquad (4.2)$$

où $W^a_{\mu\nu}$, $B_{\mu\nu}$ et $G^a_{\mu\nu}$ sont les tenseurs de champs respectivement associés aux champs de jauge $SU(2)_L$, $U(1)_Y$ et $SU(3)_C$, τ^a, Y et λ^a sont les générateurs des groupes de jauge correspondant, soit, respectivement, les matrices de Pauli, l'hypercharge faible et les matrices de Gell-Mann. Les constantes de couplages électrofaible et fort sont notées respectivement g, g' et g_s.

HERA est bien adapté pour la recherche de fermions excités. En effet, leurs signatures en collisions ep sont particulièrement propres, de nombreux canaux de désintégration pouvant être sondés, et les recherches peuvent être menées jusqu'à la limite cinématique, voir légèrement au-delà.

L'ensemble des données de H1 a donc été utilisé pour la recherche de neutrinos (ν^*), électrons (e^*) ou quarks (q^*) excités de première génération (voir annexes E, F et G). Le lot substantiel de données de collisions e^-p enregistrées à HERA II a notamment permis d'augmenter significativement la sensibilité de HERA pour la recherche de ν^*, la section efficace de production de ceux-ci devant être bien plus grande en collisions e^-p que e^+p.

Aucun signal de l'existence de ces fermions excités n'a cependant été observé. Les limites d'exclusion alors obtenues sur leur masse et le couplage f/Λ sont résumées dans la figure 4.2. Les limites obtenues au LEP ou au Tevatron sont aussi représentées. Les limites obtenues à HERA apparaissent comme étant complémentaires des recherches menées au LEP ou au Tevatron.

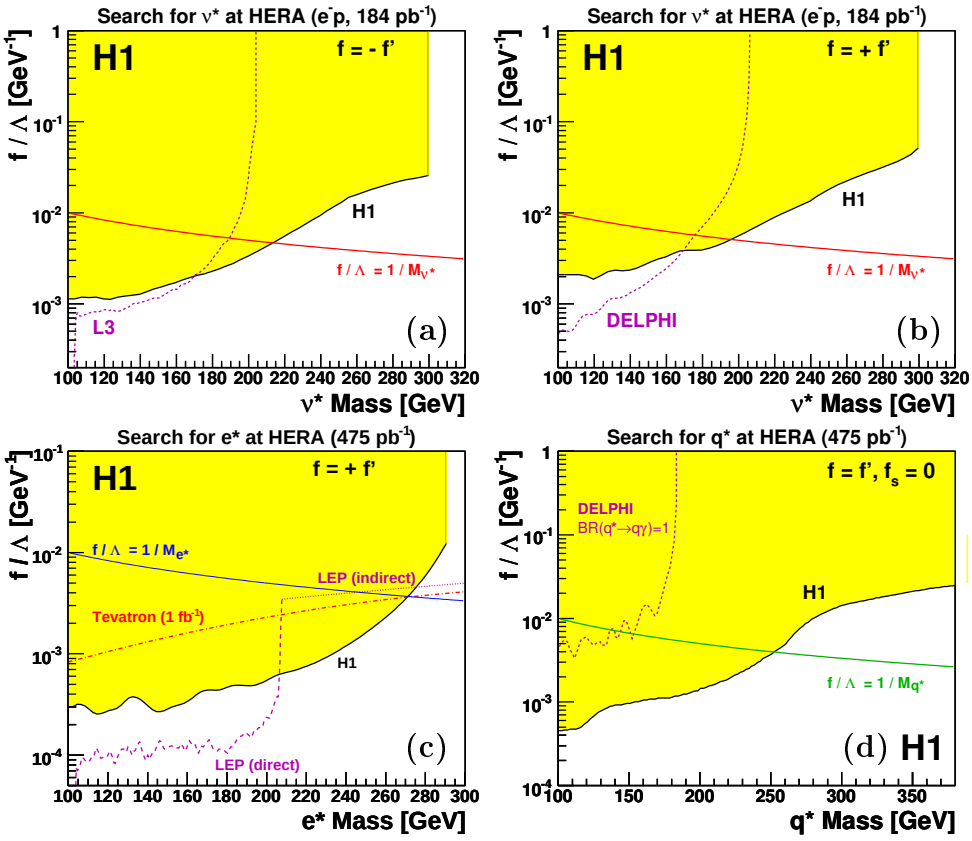

Figure 4.2 : *Limites d'exclusion à 95% CL sur le couplage f/Λ en fonction de la masse des fermions excités, pour des ν^*, sous les hypothèses $f = -f'$ (a) et $f = +f'$ (b), des e^* (c) et des q^* (d). Les valeurs au-dessus des courbes sont exclues. Les limites récentes obtenues par H1 (zone colorée) sont comparées aux limites obtenues au LEP (courbes pointillés) et au Tevatron, d'après [Aba08, Mey07], en supposant que l'acceptance pour des e^* crées par interactions de jauge (GM) ou de contact (CI) est la même (courbe en traits-points figure (b)).*

Pour la recherche de ν^*, HERA permet de sonder une région au-delà de la limite cinématique du LEP. Les limites obtenues à HERA sont alors les plus contraignantes à l'heure actuelle. En effet, aucune limite sur la production de ν^* n'a été obtenue au Tevatron. Des ν^* pourraient cependant y être produits par échange d'un γ ou Z^0 dans la voie s (comme pour un processus de Drell-Yann), donnant lieu à des topologies avec un γ et de l'énergie transverse manquante ou des jets et de l'énergie transverse manquante. Ces états finals ont cependant été déjà étudiés au Tevatron dans le cadre de recherches de dimensions supplémentaires ou de particules supersymétriques et aucune déviation aux prédictions du MS n'y a été détectée..

Pour la production éventuelle de e^*, les limites posées par le LEP sont déjà très contraignantes. Les données de HERA permettent cependant d'exclure une région supplémentaire de masses intermédiaires, $M_{e^*} \sim 200$ à 280 GeV. Le Tevatron reste cependant actuellement le seul à pouvoir exclure les e^* de très grande masse, pour un couplage f/Λ de l'ordre de $4 \cdot 10^{-3}$. Ce cas de la recherche de e^* est une bonne illustration de la complémentarité des trois types principaux de collisionneurs : e^+e^-, $p\bar{p}$ et $e^{\pm}p$. Des études prospectives montrent qu'un collisionneur ep dans la région du TeV resterait la machine idéale pour la recherche de e^*, permettant alors d'obtenir une meilleure sensibilité que le LHC pour des électron excités de masse intermédiaire en accédant à de plus faibles valeurs de couplage f/Λ (voir

figure 4.3).

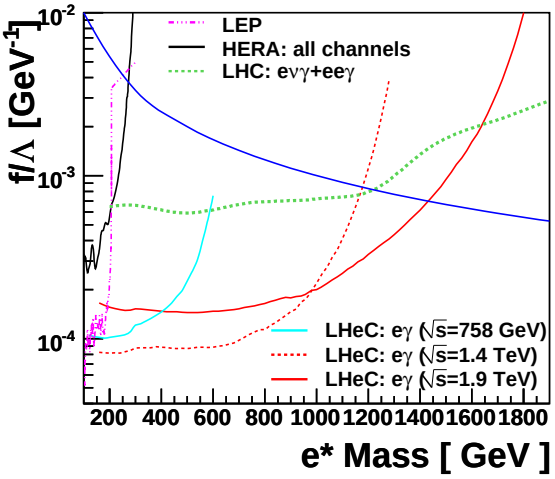

Figure 4.3 : *Sensibilité pour la recherche d'électrons excités estimée pour différents scénarios de collisionneurs électron-proton, LHeC [Dai06] et comparée à la sensibilité attendue au LHC (d'après [Tri08]). Les courbes présentent les limites d'exclusion possibles à 95% CL dans le plan $(M_{e^*}, f/\Lambda)$, les régions au-dessus des courbes étant alors exclues.*

Pour la production de q^*, les recherches menées à HERA sont surtout sensibles aux hypothèses où f_s, définissant le couplage du q^* aux gluons, serait faible. La sensibilité de HERA sous l'hypothèse $f = f' = f_s = 1$ est faible. En effet, dans ce cas, le q^* va décroître de manière prédominante en deux jets, ce qui conduit à un état final où le bruit de fond du modèle standard provenant des processus de photo-production de deux jets est très grand. Sur un collisionneur $p\bar{p}$, les q^* sont produits principalement par fusion de quark et de gluon, sous la condition $f_s \neq 0$. Les limites alors posées par le Tevatron avec l'hypothèse $f = f' = f_s = 1$ sont très bonnes, excluant la production de q^* de masse $M_{q^*} < 870$ GeV [Aba04, Aal09]. La sensibilité du Tevatron à de basses valeurs de f_s reste cependant limitée et, grâce à HERA, les limites dans ce cas ont pu être étendues (voir annexe G).

4.2 Recherches modèle indépendantes

4.2.1 Production d'événements multi-leptons de grande impulsion transverse

Dans le cadre du modèle standard, la production de paires de leptons en collisions ep se fait principalement par interaction photon-photon, $\gamma\gamma \to \ell^+\ell^-$, les photons étant rayonnés par l'électron et le proton incident [Ver83]. Ceci conduit alors à des événements possédant plusieurs leptons dans l'état final. La section efficace de ce processus est calculable précisément et est faible pour des leptons de grande impulsion transverse ($\sim$ 1 pb pour des leptons de P_T entre 5 et 10 GeV). En outre, les états finals résultants présentent très peu de bruit de fond d'autres processus du MS. L'étude de ces événements est donc un moyen de tester avec précision les prédictions du modèle standard à grand moment transverse et ces topologies offrent une grande sensibilité pour la recherche de processus nouveaux susceptibles de produire des états finals à plusieurs leptons.

L'étude de ces événements a été initiée par la collaboration H1, lors d'une première étude de la production d'événements multi-électrons de grand P_T à partir de données HERA I (voir annexe H). Plusieurs événements très énergétiques et possédant une grande masse invariante, M_{12}, des deux leptons de plus grand P_T ont alors été mis en évidence. Trois

événements avec deux électrons et trois événements avec trois électrons ont été observés dans la région $M_{12} > 100$ GeV, pour des prédictions respectives du MS de 0.3 ± 0.04 et 0.23 ± 0.04 événements.

La production de paires de muons de grande impulsion transverse a aussi été étudiée par H1 à partir des données de HERA I, mais aucun excès d'événements de grande masse invariante n'a été observé [Akt04].

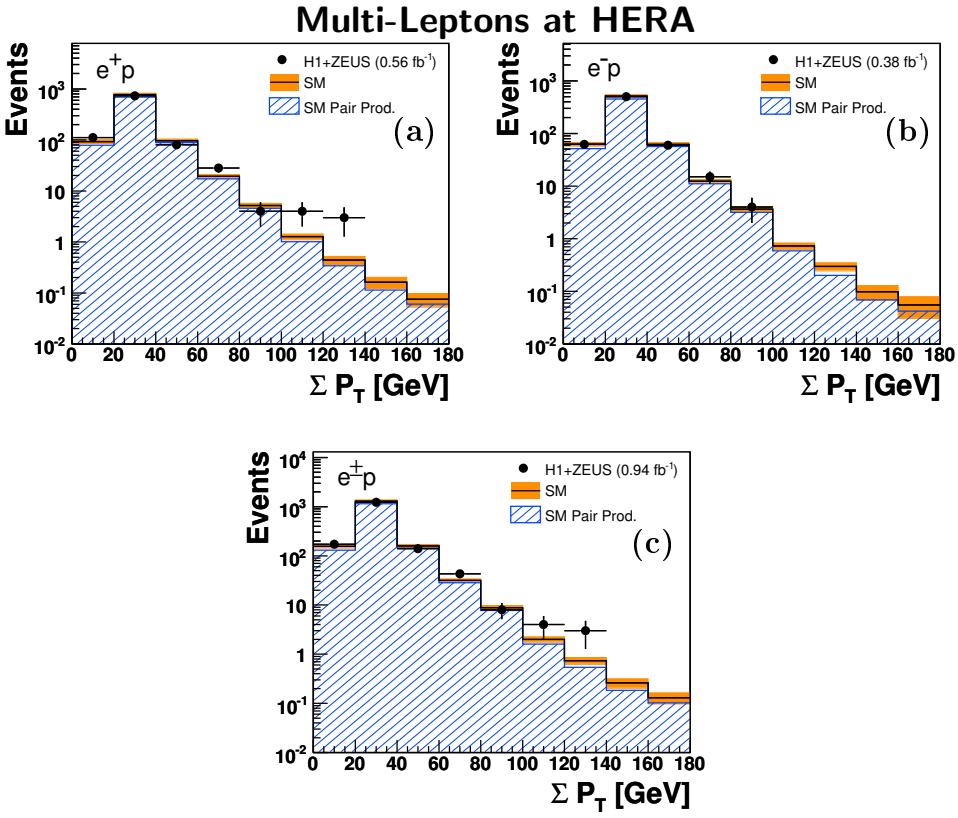

Figure 4.4 : *Distributions de $\sum P_T$ pour l'ensemble des états finals multi-leptons étudiés, pour des événements de collisions e^+p (a) et e^-p (b) et $e^\pm p$ (c) enregistrés par les expériences H1 et ZEUS.*

Hors du MS, la production de bosons de Higgs doublement chargés, $H^{\pm\pm}$, pourrait être à l'origine de tels événements multi-leptons de grand P_T. Ces bosons de Higgs doublement chargés apparaissent quand le secteur de Higgs du MS est étendu par un triplet additionnel, comme par exemple dans des extensions du MS avec une symétrie gauche-droite. Ces bosons $H^{\pm\pm}$ pourraient alors être assez légers pour être produits auprès des accélérateurs actuels, et notamment en collisions ep à HERA [Aul98, Cha98, Dut99]. Nous avons donc testé nos données et les quelques événements de grande masse observés avec les prédictions d'un tel modèle (voir annexe K). Mais cette hypothèse de production de bosons $H^{\pm\pm}$ a été écartée, notamment en regardant les charges des leptons détectés. Nous avons donc conclu en l'absence d'un tel signal et avons posé de nouvelles limites sur la masse du $H^{\pm\pm}$ en fonction de la valeur de leur couplage aux leptons. Ces limites, dans le cas de $H^{\pm\pm}$ couplant aux électrons et muons ou taus, étendent les domaines d'exclusion obtenus au LEP et au Tevatron.

Une analyse combinant les états finals avec électrons et muons a ensuite été développée par H1, de façon à inclure dans une même analyse toutes les topologies multi-leptons

possibles, possédant des électrons ou des muons de grand P_T. L'ensemble des données de H1, des phases HERA I et HERA II, a alors été analysé (voir annexe I).

Afin de doubler le lot de données de cette analyse encore limitée par la faible statistique disponible à grand P_T, une analyse similaire, développée par la collaboration ZEUS, a été combinée à celle de H1. Le résultat est présenté dans l'annexe J, correspondant alors à une luminosité totale analysée de 0.94 fb^{-1}. Les distributions de la somme scalaire des impulsions transverses des leptons, $\sum P_T$, combinant tous les états finals, sont présentées dans la figure 4.4, pour des événements de collisions $e^{\pm}p$ et, séparément, e^+p et e^-p. Nous voyons que sept événements sont observés dans la région $\sum P_T > 100$ GeV, en collision e^+p uniquement. La prédiction correspondante du MS est de 1.94 ± 0.17 événements. La probabilité d'une fluctuation positive au moins égale à celle observée dans les données, par rapport à cette prédiction, est de 0.4% (2.6σ). Cinq de ces événements de grand P_T sont observés par H1 et deux par ZEUS. Pour une prédiction similaire du MS, aucun événement avec $\sum P_T > 100$ GeV n'est observé en collisions e^-p. Des événements de grande masse invariante M_{12} sont également observés par les deux expériences, toujours en collisions e^+p uniquement (voir tableau 2 de l'annexe J).

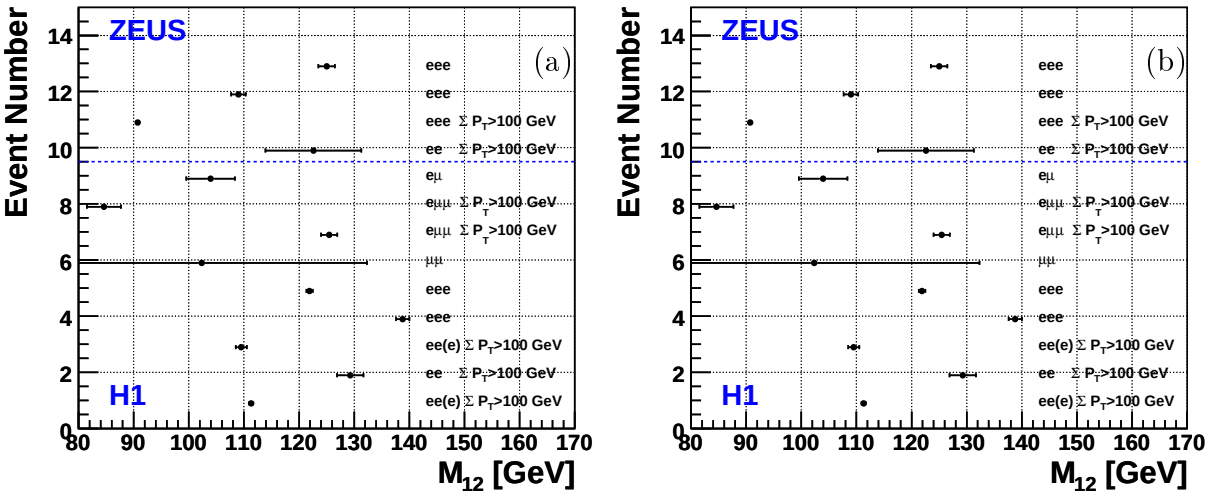

Figure 4.5 : *Masses invariantes des deux leptons de plus grand P_T, M_{12} (a) et des trois leptons, M_{all} (b) après ajustement cinématique pour les événements multi-leptons de H1 et de ZEUS mesurés avec une masse invariante $M_{12} > 100$ GeV ou $\sum P_T > 100$ GeV.*

La cinématique de ces événements a alors été étudiée en détails. Comme dans la majorité des événements, l'ensemble des particules pouvant être présentes dans l'état final a été détecté, des ajustements sous contraintes des caractéristiques cinématiques de ces événements ont été réalisés [Rot05]. Ces ajustements permettent, en imposant la conservation de l'impulsion transverse et longitudinale, une détermination plus précise des masses invariantes des différentes particules, notamment. Pour tous les événements de grande masse invariante et de grand $\sum P_T$, les masses invariantes M_{12}, des deux leptons de plus grand P_T, et M_{all}, des trois leptons quand ceux-ci sont détectés, ainsi obtenues sont présentées dans la figure 4.5. Nous observons alors que ces événements ne semblent pas s'accumuler autour d'une même valeur de M_{12} ou M_{all}.

Les charges des leptons de ces événements ont également été regardées. Cependant, la grande impulsion de ces leptons, et donc la faible courbure de leur trace, rend la mesure

de leur charge difficile, voir impossible. Il n'a donc pas été possible d'établir qu'un ou plusieurs de ces événements présenterait une combinaison de charges incompatible avec les prédictions de MS, d'une production de paires de leptons de signe opposé.

La quantité de données disponible à grand P_T reste cependant limitée et, vu le faible nombre d'événements observés, l'hypothèse d'une fluctuation statistique comme explication à cet apparent excès d'événements par rapport aux prédictions du MS ne peut être exclue. L'observation de ces quelques événements très énergétiques, uniquement en collisions e^+p, et par deux expériences indépendantes, n'en reste pas moins curieuse.

4.2.2 Une recherche générique de nouvelle physique

Les recherches de signaux spécifiques permettent déjà d'étudier un large spectre d'états finals différents, mais souvent dans des régions bien spécifiques de l'espace de phase. Ainsi, même si beaucoup d'états finals peuvent avoir été sondés lors de recherches dédiées, certains types de signaux auxquels nous n'aurions pas pensé peuvent avoir été oubliés. La solution consiste donc à étudier de manière générique tous les états finals de grand P_T expérimentalement accessibles. La méthode de recherche générique va ainsi permettre de sonder un espace de phase plus grand et gagner en généralité, tout en perdant forcément un peu en sensibilité par rapport aux recherches dédiées.

La méthode repose sur une identification peu ambiguë (en minimisant le taux de mauvaise identification) des particules de grand P_T présentes dans chaque événement. Les événements sont alors classifiés de façon exclusive en fonction du nombre et du type de particules contenues dans leur état final. Des quantités cinématiques telles que la masse invariante des particules, M_{all}, ou la somme scalaire de leur impulsion transverse, $\sum P_T$, sont alors définies. La masse invariante est intéressante pour rechercher une éventuelle résonance et $\sum P_T$ est liée à la *dureté* de l'interaction et indique les événements les plus énergétiques. Un algorithme statistique est alors employé pour rechercher les régions de déviations éventuelles des données par rapport aux prédictions du MS, et, surtout, pour en quantifier l'importance.

L'idée d'une telle méthode de recherche générique a tout d'abord été émise par la collaboration H1 [Kra99, Zin98]. Une approche un peu similaire a ensuite été tentée par l'expérience D0 [Abb00, Abb01] en effectuant une réinterprétation statistique de plusieurs analyses indépendantes portant sur différents états finals. L'ensemble des états finals n'y était cependant pas analysé de manière cohérente et l'espace de phase défini pour chaque type de particule était différent. La collaboration H1 a alors effectué une véritable recherche générique, utilisant une seule analyse, de façon à investiguer de façon cohérente tous les états finals possibles (voir annexe L). Dans les collisions ep, le nombre d'états finals peuplés à grand P_T reste plus limité que dans les collisions $p\bar{p}$. Tous les états finals possibles peuvent donc y être analysés.

L'analyse de H1 repose sur la définition d'un espace de phase commun pour toutes les particules identifiées. Les particules considérées sont les électrons (e), photons (γ), muons (μ), jets (j) et neutrinos (ν) (ou bien toute particule n'interagissant pas dans le détecteur). Tous les états finals possédant au moins deux particules identifiées de $P_T > 20$ GeV et dans la région angulaire $10° < \theta < 140°$ sont étudiés. Les événements sélectionnés sont classifiés de manière exclusive en fonction du nombre et du type de particules détectées dans l'état final.

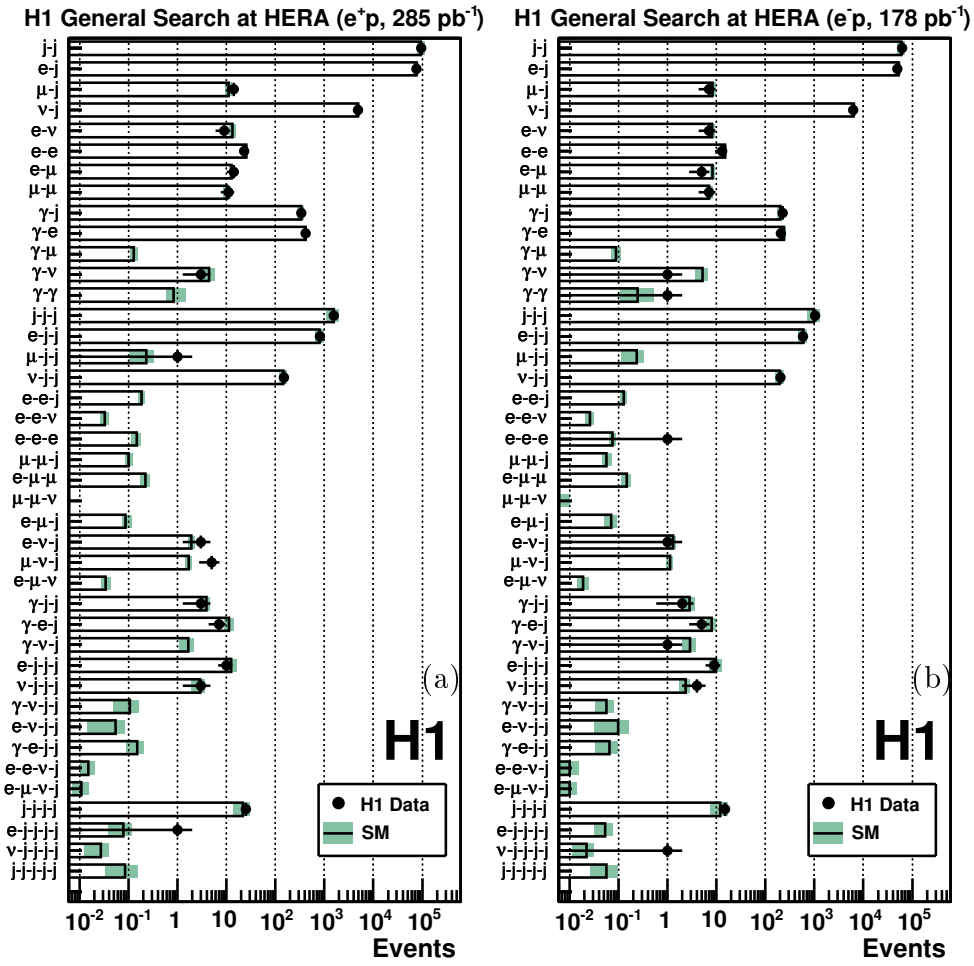

Figure 4.6 : *Nombre d'événements de données et prédictions du MS pour toutes les classes d'événements de la recherche générique, ayant des événements observés ou une prédiction du MS supérieure à* 0.01*, pour des collisions e^+p (a) et e^-p (b).*

Le nombre d'événements alors observés dans chaque classe est comparé aux prédictions du MS dans la figure 4.6. Les données sont présentées séparément pour des collisions e^+p et e^-p. Un très bon accord avec le MS est trouvé pour presque toutes les topologies observées, ce qui est remarquable étant donné la complexité de beaucoup d'états finals analysés. Cette figure permet également d'avoir une vue globale des taux d'événements relatifs en fonction de l'état final.

Ce très bon accord, alors global, entre les données et le MS reste confirmé lorsque nous analysons plus en détails la topologie des différents canaux. Les distributions des variables globales M_{all} et $\sum P_T$ sont alors étudiées, ainsi que des variables topologiques liées aux distributions angulaires des particules ou au partage de l'énergie globale de l'événement entre elles. Ces variables plus topologiques ont ainsi été introduites pour la première fois dans ce genre d'études. Un bon accord avec les prédictions du MS est alors observé dans les grande majorité des cas (voir annexe M).

Un algorithme statistique est ensuite appliqué, afin de rechercher de manière automatique dans ces distributions les régions de plus grande déviation au MS (en excès ou en déficit). Il permet également de quantifier l'importance de la déviation observée, ainsi que sa probabilité statistique d'occurrence d'une fluctuation d'origine statistique lorsque l'on

analyse un grand nombre de distributions ayant un nombre d'événements limité. Dans l'analyse globale sur l'ensemble des données de H1, la plus grande déviation est observée dans la classe e-e , à grande masse invariante. Par rapport à l'analyse multi-leptons (voir section 4.2.1), cette classe d'événements di-électrons couvre une espace de phase étendu à l'avant jusqu'à 10° mais restreint aux électrons de plus grand P_T. La déviation alors observée dans l'espace de phase de la recherche générique a une probabilité d'environ 2.5σ. La probabilité globale d'observer une fluctuation du MS au moins aussi grande dans un des canaux de l'analyse générique parmi l'ensemble des canaux possibles, et pour une luminosité égale à celle des données, est de 12%.

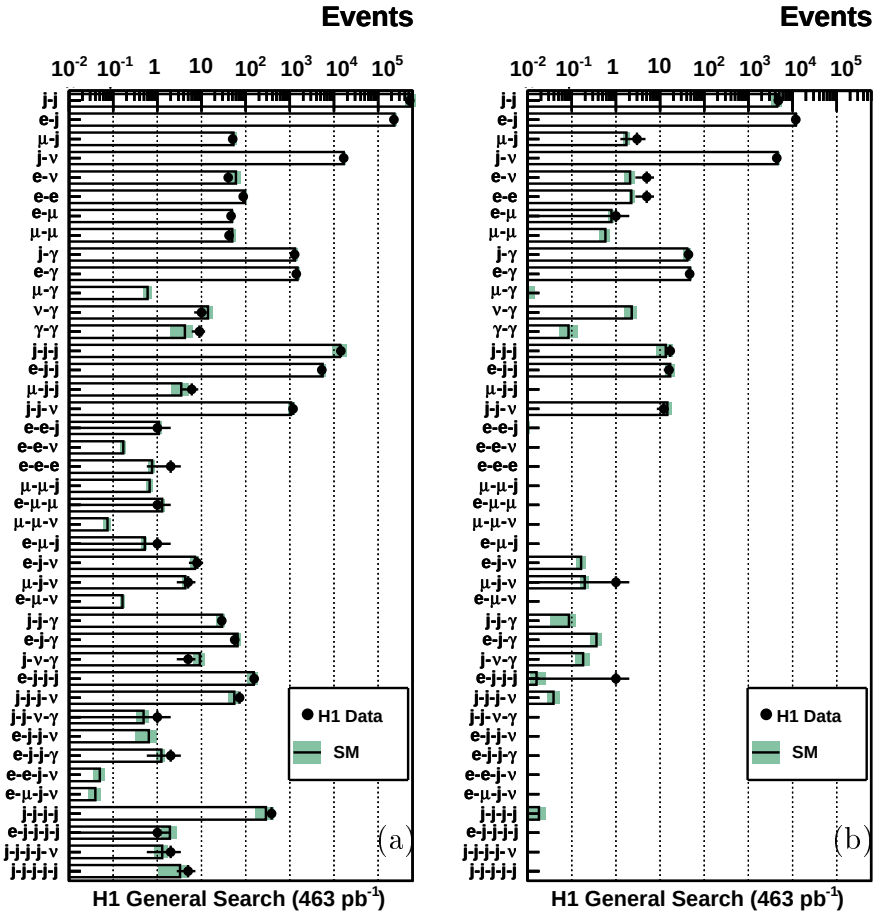

Figure 4.7 : *Nombre d'événements de données et prédictions du MS pour toutes les classes d'événements de la recherche générique, ayant des événements observés ou une prédiction du MS supérieure à* 0.01*, pour des particules de* $P_T > 15$ *GeV (a) et de* $P_T > 40$ *GeV (b).*

Une telle analyse générale nécessite une bonne compréhension à la fois du MS, et du détecteur utilisé. Dans le cas de H1, elle a été rendue possible par l'effort de standardisation des méthodes de reconstruction des particules et par la reconstruction cohérente du flot d'énergie dans l'état final. Elle repose également sur une standardisation des générateurs Monte Carlo utilisés pour la description des processus de grand P_T à HERA. Cette standardisation a été effectuée au cours de ces dernières années et repose sur de nombreux tests effectués dans différents espaces de phase étendus par rapport à l'analyse principale, notamment à plus bas P_T. Tous ces tests ont permis de qualifier les générateurs Monte Carlo alors utilisés pour l'analyse. Ainsi, cette analyse a été reproduite en changeant le

moment transverse minimum des particules identifiées de $P_T > 20$ GeV à $P_T > 15$ GeV ou $P_T > 40$ GeV. Les nombres totaux d'événements alors observés dans les différents canaux dans ces deux cas sont présentés dans la figure 4.7 et comparés aux prédictions du MS. Un bon accord entre données et prédictions du MS est alors observé. Les distributions de M_{all} et $\sum P_T$, ainsi que celles des variables topologiques ont également été étudiées pour ces deux sélections et étaient en bon accord avec les simulations du MS. Aucune déviation significative aux prédictions du MS n'a été observée dans ces deux sélections (voir annexe M).

Ce type de recherche générale, bien qu'obligatoirement moins sensible que des recherches dédiées, est nécessaire dans les programmes de recherche de nouvelle physique auprès des grands collisionneurs actuels et futurs. Face à la multiplicité des possibles théories sur l'au-delà du MS ainsi que des états finals pouvant être produits, de telles analyses peuvent apporter des éléments de réponse à la question *Avons nous vraiment cherché partout ?*. Elles permettent aussi de quantifier la probabilité d'observer une fluctuation des données dans un ou deux canaux parmi tous ceux étudiés.

De plus, outre leur intérêt pour les recherches de nouvelle physique, ce type d'analyse générique, par le grand nombre de distributions étudiées de façon automatique, s'avère être un très bon outil pour détecter des problèmes liés à la réponse du détecteur lors de la prise de données, ou à des déficits flagrants des générateurs Monte Carlo. Les recherches générales effectuées actuellement au Tevatron par les collaboration CDF [Aal08] et D0 sont un bon exemple de ce dernier cas.

Ainsi, pour les premières données du LHC, ce type d'analyse est à l'étude, notamment dans la collaboration CMS. Même si une analyse similaire à celle de H1 n'est pas envisageable à cause de la multitude des états finals possibles, cette approche peut s'avérer intéressante pour le contrôle des données de grand P_T et pour une recherche automatisée, notamment dans des topologies multi-leptons. Un atout supplémentaire serait alors de pouvoir effectuer cette analyse à partir d'un flux dédié de données de grand P_T, sélectionnées au dernier niveau de trigger.

4.3 Conclusions

Au cours de ce chapitre, nous avons vu que HERA a été un bon outil pour la recherche de nouvelle physique à la frontière à haute énergie du modèle standard. En effet, les collisionneurs *ep* s'avèrent être bien adaptés pour la recherche de nouvelles sous-structures de la matière, tentant ainsi de répéter les expériences historiques de particules ponctuelles ayant conduit aux découvertes successives de l'atome, du noyau, des nucléons et des partons. Une des complémentarités des collisionneurs *ep* par rapport aux collisions $p\bar{p}$ ou *pp* serait, par exemple, de pouvoir y mesurer plus facilement les couplages au MS de nouvelles particules, permettant ainsi une caractérisation plus approfondie de la nouvelle physique découverte.

Devant la très grande diversité des scénarios théoriques possibles pour étendre et améliorer le MS, la mise en place de recherches plus générales et indépendantes de toute supposition faite sur la nature des manifestations de nouvelle physique recherchées devient de plus en plus importante. Les analyses effectuées à HERA ont ainsi été pionnières dans la mise en place de recherches modèle indépendantes, basée uniquement sur la mesure de différentes signatures topologiques. Dans ce domaine, la relative simplicité des interactions *ep* par rapport aux collisions *pp*, ainsi que la présence modérée d'interactions de type QCD, a permis d'effectuer à HERA un balayage complet et précis de l'ensemble des états finals

possible de grand P_T. C'est la première analyse complète de ce type effectuée à partir des données d'un grand collisionneur.

Parmi tous les différents états finals étudiés à HERA, la plus importante déviation aux prédictions du MS est observée dans des événements multi-leptons. Même si le nombre d'événements observés reste faible, ce qui empêche toute conclusion quant à leur origine, cette observation effectuée par les deux expériences H1 et ZEUS n'en reste pas moins curieuse.

A l'heure actuelle, le Tevatron reste le seul collisionneur en fonction permettant de repousser encore les limites du champ d'application du MS à haute énergie. L'avènement du LHC dans un futur proche va ouvrir de nouveaux horizons en donnant accès à un vaste territoire aux énergies de l'ordre du TeV, domaine où la structure de la matière n'a jamais été étudiée et où certains arguments théoriques laissent actuellement à penser que de nouveaux processus physiques devraient se manifester.

4.4 Contributions personnelles

J'ai commencé par contribuer à la première publication de H1 sur la production d'événements multi-électrons de grand P_T. J'ai notamment réalisé pour cette publication les analyses de contrôle et développé une procédure d'ajustement cinématique, afin de mieux contraindre la masse invariante des quelques candidats atypiques observés à grand P_T (voir annexe H). J'ai ensuite pris l'entière responsabilité de cette analyse sur les données HERA II. L'extension de cette analyse aux muons et aux topologies combinées électrons-muons a été réalisée par Florian Rothmaier, étudiant de *Diplomarbeit* à Marseille, sous ma direction. J'ai ensuite finalisé et publié seul cette analyse sur l'ensemble des données de H1 (voir annexe I). Un travail commun avec les physiciens de la collaboration ZEUS travaillant sur le sujet a récemment permis de réaliser une combinaison des données de H1 et de ZEUS (voir annexe J). Ceci constitue la première publication combinée H1 et ZEUS.

En relation avec cette étude, j'ai participé à la publication de H1 sur la recherche de boson de Higgs doublement chargé (voir annexe K). Pour cette publication incluant plusieurs canaux, j'ai réalisé la recherche dans le canal $e\mu$.

La recherche générique de nouvelle physique a été développée à partir des données HERA I par Matti Peez, étudiant en thèse à Marseille, que j'ai co-encadré sur ce sujet, et en compétition, puis collaboration, avec un second groupe de physiciens au sein de la collaboration H1 (voir annexe L). J'ai ensuite assumé l'entière responsabilité de cette analyse pour les données HERA II, avec des mises à jour successives présentées en conférences, à mesure de l'accumulation des données. J'ai finalement réalisé seul la publication finale de cette analyse, portant sur l'ensemble des données de H1.

Les recherches successives de neutrinos, électrons et quarks excités ont été réalisées sous ma direction par Thi Nguyet Trinh, étudiante en thèse à Marseille, (voir annexes E, F et G), entre 2005 et 2008. Thi Nguyet Trinh a été récompensée par le prix 2008 jeune chercheur Michelin, de la Société Française de Physique, pour ses travaux.

Depuis juillet 2005, je suis également co-responsable du groupe de travail de la collaboration H1, chargé des analyses de recherches de signaux de physique au-delà du modèle standard. Au cours de ces dernières années, mon travail de coordination de ce groupe de physique a consisté à gérer la réalisation, avant le démarrage du LHC, des publications finales de H1 dans les domaines où les données de HERA sont complémentaires de celles du Tevatron et du LEP. Egalement, dans ce domaine de recherche très prospectif, la réactivité dans l'analyse des nouvelles données à mesure qu'elles sont enregistrées est très important.

Ces deux objectifs ont pu être atteints grâce à la mise en place au sein du groupe d'outils d'analyse communs et d'une standardisation et automatisation des procédures d'analyse, que j'ai réalisées.

Conclusion

Dans ce manuscrit, nous avons discuté certaines des limitations actuelles du modèle standard, qui font que cette description de la structure de la matière que nous avons aujourd'hui reste avant tout un modèle. La précision de ses prédictions dans certains domaines peut encore être améliorée. De nombreux phénomènes, liés principalement à la complexité de la dynamique des interactions fortes, restent encore mal compris. Enfin, le modèle standard n'apporte aucune réponse à de nombreuses questions que nous nous posons sur la structure de la matière. Nous sommes donc à la recherche de nouveaux phénomènes physiques, que nous espérons trouver à haute énergie, pour nous indiquer le chemin vers une théorie plus fondamentale.

Le collisionneur électron-proton HERA s'est révélé être un bon outil pour explorer ces différents problèmes. Aucune évidence de nouvelle physique n'y a cependant été observée, repoussant ainsi la frontière de la validité du MS à haute énergie. Actuellement, la majorité des recherches possibles à HERA dans ce domaine a été finalisée.

HERA fut aussi un outil extraordinaire pour progresser dans notre connaissance de la dynamique interne du proton. Un des résultats majeurs de HERA est ainsi la mesure précise des distributions de partons constituant le proton sur un très grand domaine cinématique. Sur ce sujet, l'analyse des données accumulées à HERA II reste encore à finaliser. Des analyses préliminaires ont montré que ces données vont permettre de réduire encore les incertitudes actuelles sur la détermination des PDFs. La combinaison des mesures finales de H1 et de ZEUS permettra alors d'obtenir la meilleure précision possible à HERA.

Au-delà de la structure en impulsion longitudinale du proton, HERA permet d'apporter de nouvelles informations sur les autres degrés de liberté dans le proton. Ainsi, les interactions de nature diffractive apportent des informations complémentaires sur la distribution spatiale des partons dans le plan transverse et sur leurs corrélations. Dans ce domaine, les nouvelles données de HERA II ont permis d'entrer dans le domaine de la précision. Les résultats expérimentaux, auparavant encore limités en précision statistique, apportent maintenant des contraintes plus importantes sur les différents modèles théoriques.

J'ai ainsi eu la chance de pouvoir participer et d'apporter mes contributions personnelles à plusieurs de ces résultats qui resteront comme partie du legs de HERA à la physique des particules.

Le collisionneur de nouvelle génération, le LHC, va maintenant entrer progressivement en fonctionnement à la fin de l'année 2009. Il va ouvrir une nouvelle fenêtre sur des états de la matière à plus haute énergie, jamais encore explorés. Face à la complexité des interactions hadroniques à haute énergie, comprendre la QCD et la structure du proton sera nécessaire à l'étude des collisions au LHC et à toute découverte de nouvelle physique.

Les mesures effectuées à HERA auront sans nul doute un rôle important à jouer dans ce domaine.

Bibliographie

[Aal08] T. Aaltonen *et al.* [CDF Collaboration]
Model-Independent and Quasi-Model-Independent Search for New Physics at CDF.
Phys. Rev. D **78** (2008) 012002 [arXiv:0712.1311]

[Aal09] T. Aaltonen *et al.* [CDF Collaboration]
Search for new particles decaying into dijets in proton-antiproton collisions at sqrt(s) = 1.96 TeV.
Phys. Rev. D **79** (2009) 112002 [arXiv:0812.4036]

[Aar08] F. D. Aaron *et al.* [H1 Collaboration]
Measurement of the Proton Structure Function F_L at Low x.
Phys. Lett. B **665** (2008) 139 [arXiv:0805.2809]

[Aar09a] F. D. Aaron *et al.* [H1 Collaboration]
Jet Production in ep Collisions at High Q^2 and Determination of α_s.
Submitted to Eur. Phys. J C (2009) [arXiv:0904.3870]

[Aar09b] F.D. Aaron *et al.* [H1 Collaboration]
Measurement of the diffractive longitudinal structure function F_L^D at HERA II.
Preliminary result submitted to DIS 2009 (2009)

[Aba04] V. M. Abazov *et al.* [D0 Collaboration]
Search for new particles in the two-jet decay channel with the DØ detector.
Phys. Rev. D **69** (2004) 111101 [hep-ex/0308033]

[Aba08] V. M. Abazov *et al.* [D0 Collaboration]
Search for excited electrons in ppbar collisions at sqrt(s) = 1.96 TeV.
Phys. Rev. D **77** (2008) 091102(R) [arXiv:0801.0877]

[Abb00] B. Abbott *et al.* [D0 Collaboration]
Search for new physics in eμX data at DØ using Sherlock: A quasi model independent search strategy for new physics.
Phys. Rev. D **62** (2000) 092004 [hep-ex/0006011]

[Abb01] B. Abbott *et al.* [D0 Collaboration]
A quasi-model-independent search for new physics at large transverse momentum.
Phys. Rev. D **64** (2001) 012004 [hep-ex/0011067]

[Abt97a] I. Abt *et al.* [H1 Collaboration]
The H1 detector at HERA.
Nucl. Instr. Meth. A **386** (1997) 310

[Abt97b] I. Abt *et al.* [H1 Collaboration]
The H1 Detector At HERA: The Tracking, calorimeter and muon detectors of the H1 experiment at HERA.
Nucl. Instr. Meth. A **386** (1997) 348

[Aco05] D. E. Acosta *et al.* [CDF Collaboration]
Measurement of the forward-backward charge asymmetry of electron positron pairs in $p\bar{p}$ collisions at $\sqrt{s} = 1.96$ TeV.
Phys. Rev. D **71** (2005) 052002 [hep-ex/0411059]

[Ahm94] T. Ahmed *et al.* [H1 Collaboration]
Deep inelastic scattering events with a large rapidity gap at HERA.
Nucl. Phys. B **429** (1994) 477

[Air08] A. Airapetian *et al.* [HERMES Collaboration]
Measurement of Azimuthal Asymmetries With Respect To Both Beam Charge and Transverse Target Polarization in Exclusive Electroproduction of Real Photons.
JHEP **0806** (2008) 066 [arXiv:0802.2499]

[Akt04] A. Aktas *et al.* [H1 Collaboration]
Muon pair production in e p collisions at HERA.
Phys. Lett. B **583** (2004) 28 [hep-ex/0311015]

[Akt05] A. Aktas *et al.* [H1 Collaboration]
Measurement of deeply virtual Compton scattering at HERA.
Eur. Phys. J. C **44** (2005) 1 [hep-ex/0505061]

[Akt06a] A. Aktas *et al.* [H1 Collaboration]
A determination of electroweak parameters at HERA.
Phys. Lett. B **632** (2006) 35 [hep-ex/0507080]

[Akt06b] A. Aktas *et al.* [H1 Collaboration]
Measurement and interpretation of the diffractive cross section at medium Q^2.
Preliminary result submitted to DIS 2006, H1prelim-06-014 (2006),
http://www-h1.desy.de/psfiles/confpap/DIS2006/H1prelim-06-014.ps

[Akt06c] A. Aktas *et al.* [H1 Collaboration]
Measurement and QCD analysis of the diffractive deep-inelastic scattering cross-section at HERA.
Eur. Phys. J. C **48** (2006) 715 [hep-ex/0606004]

[Akt07a] A. Aktas *et al.* [H1 Collaboration]
Diffractive open charm production in deep-inelastic scattering and photoproduction at HERA.
Eur. Phys. J. C **50** (2007) 1 [hep-ex/0610076]

[Akt07b] A. Aktas *et al.* [H1 Collaboration]
Dijet Cross Sections and Parton Densities in Diffractive DIS at HERA.
JHEP **0710** (2007) 042 [arXiv:0708.3217]

[Alt77] G. Altarelli et G. Parisi
Asymptotic Freedom In Parton Language.
Nucl. Phys. B **126** (1977) 298

[Alt78] G. Altarelli et G. Martinelli
Transverse Momentum Of Jets In Electroproduction From Quantum Chromodynamics.
Phys. Lett. B **76** (1978) 89

[Ams08] C. Amsler *et al.* [Particle Data Group Collaboration]
Review of particle physics.
Phys. Lett. B **667** (2008) 1

[And93a] B. Andrieu *et al.* [H1 Calorimeter Group Collaboration]
The H1 liquid argon calorimeter system.
Nucl. Instr. Meth. A **336** (1993) 460

[And93b] B. Andrieu *et al.* [H1 Calorimeter Group Collaboration]
Results From Pion Calibration Runs For The H1 Liquid Argon Calorimeter And Comparisons With Simulations.
Nucl. Instr. Meth. A **336** (1993) 499

[And94] B. Andrieu *et al.* [H1 Calorimeter Group Collaboration]
Beam tests and calibration of the H1 liquid argon calorimeter with electrons.
Nucl. Instr. Meth. A **350** (1994) 57

[App97] R. D. Appuhn *et al.* [H1 SPACAL Group Collaboration]
The H1 lead/scintillating-fibre calorimeter.
Nucl. Instr. Meth. A **386** (1997) 397

[Aul98] C. S. Aulakh, A. Melfo, et G. Senjanovic
Minimal supersymmetric left-right model.
Phys. Rev. D **57** (1998) 4174 [hep-ph/9707256]

[Bar99] J. Bartels, J. R. Ellis, H. Kowalski, et M. Wusthoff
An analysis of diffraction in deep-inelastic scattering.
Eur. Phys. J. C **7** (1999) 443 [hep-ph/9803497]

[Bau90] U. Baur, M. Spira, et P. M. Zerwas
Excited Quark And Lepton Production At Hadron Colliders.
Phys. Rev. D **42** (1990) 815

[Bel02] A. V. Belitsky, D. Mueller, et A. Kirchner
Theory of deeply virtual Compton scattering on the nucleon.
Nucl. Phys. B **629** (2002) 323 [hep-ph/0112108]

[Blo69] E. D. Bloom *et al.* [SLAC-MIT Collaboration]
High-Energy Inelastic E P Scattering At 6-Degrees And 10-Degrees.
Phys. Rev. Lett. **23** (1969) 930

[Blo79] A. Blondel et F. Jacquet
Proceedings of the Study of an *ep* Facility for Europe, ed. U. Amaldi, DESY **79/48** (1979) 391

[Bou93] F. Boudjema, A. Djouadi, et J. L. Kneur
Excited fermions at e+ e- and e P colliders.
Z. Phys. C **57** (1993) 425

[Bre69] M. Breidenbach *et al.* [SLAC-MIT Collaboration]
Observed Behavior Of Highly Inelastic Electron-Proton Scattering.
Phys. Rev. Lett. **23** (1969) 935

[Cal69] C. G. Callan et D. J. Gross
High-energy electroproduction and the constitution of the electric current.
Phys. Rev. Lett. **22** (1969) 156

[Cat93] S. Catani *et al.*
Longitudinally invariant K(t) clustering algorithms for hadron-hadron collisions.
Nucl. Phys. B **406** (1993) 187

[Cha98] Z. Chacko et R. N. Mohapatra
Supersymmetric left-right models and light doubly charged Higgs bosons and Higgsinos.
Phys. Rev. D **58** (1998) 015003 [hep-ph/9712359]

[Che03] S. Chekanov *et al.* [ZEUS Collaboration]
Measurement of deeply virtual Compton scattering at HERA.
Phys. Lett. B **573** (2003) 46 [hep-ex/0305028]

[Che05] S. Chekanov *et al.* [ZEUS Collaboration]
Study of deep inelastic inclusive and diffractive scattering with the ZEUS forward plug calorimeter.
Nucl. Phys. B **713** (2005) 3 [hep-ex/0501060]

[Che09a] S. Chekanov *et al.* [ZEUS Collaboration]
Deep inelastic scattering with leading protons or large rapidity gaps at HERA.
Nucl. Phys. B **816** (2009) 1 [arXiv:0812.2003]

[Che09b] S. Chekanov *et al.* [ZEUS Collaboration]
A measurement of the Q^2, W and t dependences of deeply virtual Compton scattering at HERA.
JHEP **0905** (2009) 108 [arXiv:0812.2517]

[Col77] P.D.B. Collins
An Introduction to Regge Theory and High-Energy Physics.
Cambridge University Press, Cambridge (1977)

[Col85] J. C. Collins, D. E. Soper, et G. Sterman
Factorization For Short Distance Hadron - Hadron Scattering.
Nucl. Phys. B **261** (1985) 104

[Col98] J. C. Collins
Proof of factorization for diffractive hard scattering.
Phys. Rev. D **57** (1998) 3051 [Erratum–ibid. D **61** (2000) 019902] [hep-ph/9709499]

[CS88] A. M. Cooper-Sarkar *et al.*
Measurement Of The Longitudinal Structure Function And The Small X Gluon Density Of The Proton.
Z. Phys. C **39** (1988) 281

[Dai06] J. B. Dainton *et al.*
Deep inelastic electron nucleon scattering at the LHC.
JINST **1** (2006) P10001 [hep-ex/0603016]

[Der93] M. Derrick *et al.* [ZEUS Collaboration]
Observation of events with a large rapidity gap in deep inelastic scattering at HERA.
Phys. Lett. B **315** (1993) 481

[d'H02] N. d'Hose *et al.*
Feasibility study of deeply virtual Compton scattering using COMPASS.
Nucl. Phys. A **711** (2002) 160

[Dok77] Y. L. Dokshitzer
Calculation Of The Structure Functions For Deep Inelastic Scattering And e^+e^- Annihilation By Perturbation Theory In Quantum Chromodynamics.
Sov. Phys. JETP **46** (1977) 641

[Dut99] B. Dutta et R. N. Mohapatra
Phenomenology of light remnant doubly charged Higgs fields in the supersymmetric left-right model.
Phys. Rev. D **59** (1999) 015018 [hep-ph/9804277]

[Ell93] S. D. Ellis et D. E. Soper
Successive combination jet algorithm for hadron collisions.
Phys. Rev. D **48** (1993) 3160 [hep-ph/9305266]

[Fra99] L. Frankfurt et M. Strikman
Future small x physics with e p and e A colliders.
Nucl. Phys. Proc. Suppl. **79** (1999) 671 [hep-ph/9907221]

[Fra04] L. Frankfurt, M. Strikman, et C. Weiss
Dijet production as a centrality trigger for pp collisions at CERN LHC.
Phys. Rev. D **69** (2004) 114010 [hep-ph/0311231]

[Fre03] A. Freund, K. Rummukainen, H. Weigert, et A. Schäfer
Geometric scaling in inclusive e A reactions and nonlinear perturbative QCD. ((T)).
Phys. Rev. Lett. **90** (2003) 222002 [hep-ph/0210139]

[GB99a] K. J. Golec-Biernat et M. Wusthoff
Saturation effects in deep inelastic scattering at low Q^2 and its implications on diffraction.
Phys. Rev. D **59** (1999) 014017 [hep-ph/9807513]

[GB99b] K. J. Golec-Biernat et M. Wusthoff
Saturation in diffractive deep inelastic scattering.
Phys. Rev. D **60** (1999) 114023 [hep-ph/9903358]

[Gri72] V. N. Gribov et L. N. Lipatov
Deep Inelastic E P Scattering In Perturbation Theory.
Sov. J. Nucl. Phys. **15** (1972) 781

[Hag85] K. Hagiwara, S. Komamiya, et D. Zeppenfeld
Excited Lepton Production at LEP and HERA.
Z. Phys. C **29** (1985) 115

[Hof55] R. Hofstadter et R. W. McAllister
Electron Scattering From The Proton.
Phys. Rev. **98** (1955) 217

[Ian04] E. Iancu, K. Itakura, et S. Munier
Saturation and BFKL dynamics in the HERA data at small x.
Phys. Lett. B **590** (2004) 199 [hep-ph/0310338]

[Ing85] G. Ingelman et P. E. Schlein
Jet Structure In High Mass Diffractive Scattering.
Phys. Lett. B **152** (1985) 256

[Jon79] M. Jonker *et al.*
Polarization Of Positive Muons Produced In High-Energy Anti-Neutrino Interactions.
Phys. Lett. B **86** (1979) 229

[Kha01] D. Kharzeev et E. Levin
Manifestations of high density QCD in the first RHIC data.
Phys. Lett. B **523** (2001) 79 [nucl-th/0108006]

[Kle84] M. Klein et T. Riemann
Electroweak Interactions Probing The Nucleon Structure.
Z. Phys. C **24** (1984) 151

[Kra99] M.W. Krasny et H. Spiesberger
Standard model large-E(T) processes and searches for new physics at HERA.
J. Phys. G **25** (1999) 1428 [hep-ph/9901359]

[Kra03] A. Krasnitz, Y. Nara, et R. Venugopalan
Classical gluodynamics of high energy nuclear collisions: An erratum and an update.
Nucl. Phys. A **727** (2003) 427 [hep-ph/0305112]

[Kum] K. Kumerički, D. Mueller, et K. Passek-Kumerički
Fitting DVCS amplitude in moment-space approach to GPDs.
() [arXiv:0807.0159]

[Kum08] K. Kumerički, D. Mueller, et K. Passek-Kumerički
Sum rules and dualities for generalized parton distributions: Is there a holographic principle ?.
Eur. Phys. J. C **58** (2008) 193 [arXiv:0805.0152]

[LEP04] LEP et SLD Electroweak workin groups
A Combination of Preliminary Electroweak Measurements and Constraints on the Standard Model.
(2004) [hep-ex/0412015]

[Lip74] L. N. Lipatov
The parton model and perturbation theory.
Sov. J. Nucl. Phys. **20** (1974) 181

[Mar06] C. Marquet et L. Schoeffel
Geometric scaling in diffractive deep inelastic scattering.
Phys. Lett. B **639** (2006) 471 [hep-ph/0606079]

[Mar07a] C. Marquet
A unified description of diffractive deep inelastic scattering with saturation.
Phys. Rev. D **76** (2007) 094017 [arXiv:0706.2682]

[Mar07b] C. Marquet, R. B. Peschanski, et G. Soyez
Exclusive vector meson production at HERA from QCD with saturation.
Phys. Rev. D **76** (2007) 034011 [hep-ph/0702171]

[Mey07] A. Meyer, *Communication privée*, (2007)

[Mue90] A. H. Mueller
Small x Behavior and Parton Saturation: A QCD Model.
Nucl. Phys. B **335** (1990) 115

[Neg04] J.W. Negele *et al.*
Insight into nucleon structure from lattice calculations of moments of parton and generalized parton distributions.
Nucl. Phys. B (Proc. Suppl.) **128** (2004) 170

[Nik91] N. N. Nikolaev et B. G. Zakharov
Colour transparency and scaling properties of nuclear shadowing in deep inelastic scattering.
Z. Phys. C **49** (1991) 607

[Pum02] J. Pumplin *et al.*
New generation of parton distributions with uncertainties from global QCD analysis.
JHEP **0207** (2002) 012 [hep-ph/0201195]

[Reg59] T. Regge
Introduction To Complex Orbital Momenta.
Nuovo Cim. **14** (1959) 951

[Reg60] T. Regge
Bound states, shadow states and Mandelstam representation.
Nuovo Cim. **18** (1960) 947

[Rot05] F. Rothmaier
Production of High P_T Multi-Lepton Events at HERA.
Diplomarbeit, Université de Hambourg (2005).
Disponible à http://www-h1.desy.de/psfiles/theses/h1th-401.ps

[Roy07] C. Royon *et al.*
A global analysis of inclusive diffractive cross sections at HERA.
Nucl. Phys. B **781** (2007) 1 [hep-ph/0609291]

[Sta01] A. M. Staśto, K. Golec-Biernat, et J. Kwieciński
Geometric scaling for the total gamma p cross-section in the low x region.*
Phys. Rev. Lett. **86** (2001) 596 [hep-ph/0007192]

[Tri08] T. N. Trinh
Single Production of Ecited Leptons at the LHeC.
Prepared for the 1^{st} ECFA-CERN LHeC Workshop, September 1-*s*3, Divonne, France (2008)

[Ver83] J. A. M. Vermaseren
Two Photon Processes At Very High-Energies.
Nucl. Phys. B **229** (1983) 347

[Wus99] M. Wusthoff et A. D. Martin
The QCD description of diffractive processes.
J. Phys. G **25** (1999) R309 [hep-ph/9909362]

[Zin98] P. Zini
Qualification du calorimètre SpaCal de H1 et étude des événements de très grande énergie transversee.
Thèse, Université de Paris XI (1998).
Disponible à http://www-h1.desy.de/psfiles/theses/h1th-118.ps

Annexe A

An energy flow algorithm for Hadronic Reconstruction in OO: Hadroo2

M. Peez, B. Portheault and E. Sauvan,
H1 internal note H1-01/05-616.

Abstract

This note describes in detail the algorithm performing the identification and measurement of the Hadronic Final State in the OO framework, and the corresponding high P_T jet calibration procedure.

1 Introduction

One of the tasks of the OO framework is to provide to the user reconstructed particles at the μODS level. To achieve this goal physics algorithm now benefit of all the expert knowledge integrated during the HERA I operating phase. Particle identification is made by a set of different finders running sequentially, namely the electron finder, the muon finder, and the hadronic final state (HFS) finder. Additional finders may create so-called composed particles, such as the D^* finder or the jet finder. The input of the jet finder for the "exclusive jets" is the output of the HFS finder.

An energy flow algorithm is characterised by the combination of information coming from different sub-detectors. Following the guideline of a general improvement in the measurement of physical quantities with the H1 detector, the HADROO (for Hadronic Reconstruction in OO) algorithm was developed by M. Peez and C. Vallée [1], introducing the idea of using either the track or the calorimetric information for the creation of a particle candidate, depending on the error of the track measurement. This was the first step toward an energy flow algorithm.

This implementation was then refined, including also a better calorimeter noise rejection and an absolute calibration of the hadronic final state, based on reconstructed jets and suited for high Q^2 analyses. This actual implementation, called Hadroo2, will be described in this note.

The minor conceptual difference between Hadroo2 and a so-called energy flow algorithm — such as for example the D0 one [2] or the ZEUS one [3] — is that a one-to-one attribution of a cluster to a track is not performed[1]. In this view, it is an inclusive oriented algorithm, however it suits also to exclusive analyses because of the detailed track treatment.

This note will be organised in the following way: first, a description of the basic inputs of the algorithm (tracks and clusters) will be done. Particularly, the noise treatment applied to calorimetric objects will be detailed. Then the algorithm itself will be described, and compared with other HFS algorithms developed in H1. Its application to the reconstruction of high P_T jets and a suited calibration procedure is developed in the last part of this document.

2 Selection of the input objects: Tracks and Clusters

2.1 Tracks

As the spirit is to benefit from expert knowledge, the tracks used are the standard "good quality" tracks as defined by the heavy flavour group, the so-called "Lee West" tracks [4]. These tracks, measured with the central and forward tracking detectors (see Fig. 1), are classified in three categories, Central, Combined and Forward, requiring the quality cuts detailed in Table 1. If a track satisfies several sets of cuts, the preference order is Central, Combined, Forward. Both primary and secondary vertex fitted tracks can be selected but preference is given to primary. For HERA II data and MC, pure forward and combined tracks are excluded because their kinematics as well as their error measurement are at the moment not well studied and described. The selected tracks build up the input of the Hadroo2 algorithm.

[1]This problem is not trivial because of combinatorial ambiguities and its difficulty depends crucially on the features of the clustering algorithm.

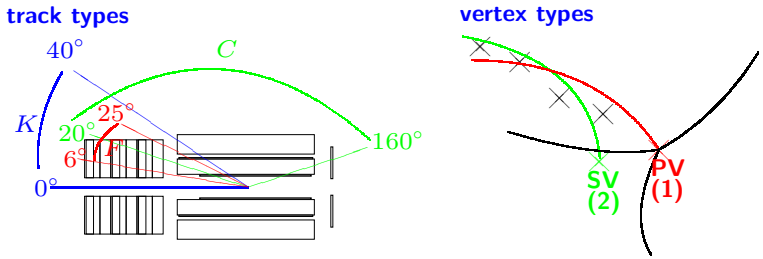

Figure 1: Different track types and their angular domain, and the two vertex hypothesis for a single track. Both primary and secondary vertex fitted tracks can be selected.

combined (K)	**central (C)**
$p_T > 120$ MeV $0° < \theta < 40°$ $\|dca'\| \leq 5$ cm $R_{start} \leq 50$ cm $R_{length} \geq 0$ cm $\Delta p/p \leq 99999.9$ $N_{CJC\ hits} \geq 0$ $\chi^2_{track-vertex fit} \leq 50$ $\chi^2_{cent.-fwd.tracker} \leq 50$	$p_T > 120$ MeV $20° < \theta < 160°$ $\|dca'\| \leq 2$ cm $R_{start} \leq 50$ cm $R_{length} \geq 10$cm for $\theta \leq 150°$ $R_{length} \geq 5$cm for $\theta > 150°$ $N_{CJC\ hits} \geq 0$
forward (F)	
$p_T > 1$ MeV $6° \leq \theta \leq 25°$ $R_0 \leq 10$ cm $\chi^2_{trackfit}/NDOF \leq 10$ $\chi^2_{track-vertex fit} \leq 25$ $nPrimary + nSecondary$ $PlanarSegments \geq 1$ $nPlanar + nRadialSegments \geq 2$ $\Delta p/p \leq 9999.9$ $p \geq 0.5$ GeV	

Table 1: Summary of the different cuts used in the track selection. If a track satisfies several set of cuts, the preference order is Central, Combined, Forward.The dca is the distance of closest approach of the track extrapolation to the vertex and dca' is the distance of closest approach in the x,y plane at $z = z_{vertex}$.

2.2 Clusters

The clusters are aligned and beam tilted in a proper way using run-dependent alignment factors. Calorimetric clusters are made only out of LAr or SpaCal. Iron or Plug cluster are not considered (beside the mediocre energy resolution of the Iron calorimeter, a significant fraction of Iron clusters are noise or background[2]). If a cluster in LAr have cells in Iron or Plug, these cells are removed from the cluster. Note that the negative energy cells in clusters are kept, as it must be to avoid a systematic positive bias in energy measurements.

The cluster energy momentum four-vector is made of the addition of massless cells four vectors (in this way clusters acquire a "mass"). The position of the center of gravity is determined with a linear energy weighting of the cells positions.

2.2.1 Weighting

As the LAr calorimeter has the well-known behaviour of being non-compensating, weighting algorithms are necessary to compensate the lower response to hadrons with respect to electron for a same energy [5]. Such a weighting procedure is already applied at the reconstruction level, in H1REC, identifying clusters as originating from electromagnetic particles or from hadrons.

But in the present algorithm this classification was modified. All clusters with at least 95 % of their energy in electromagnetic part and with also 50 % of it in the first two layers of the electromagnetic calorimeter are taken at the electromagnetic scale. All other clusters are considered as originating from hadrons and the hadronic energy scale, determined by the H1REC weighting algorithm, is considered. It was shown by S. Hellwig and K. Daum that this improves the energy resolution in D^* analysis and that the total reconstructed energy of the HFS was closer to the true level [6].

2.2.2 Noise suppression

The default situation All the measurement relying on the LAr calorimeter are affected by a relatively large amount of noise (few GeV per event). This noise is due to detector effects such as noise in the electronics or pile-up deposition of energy coming from non ep physics like halo or cosmic muons. The impact of this noise on physics analysis is clearly not negligible. For an inclusive analysis, the distribution

$$y_h = \frac{\sum_h E_h - Pz_h}{2E_0} \tag{1}$$

is specially affected. At low y_h (when $E_h \sim Pz_h$) most of the hadrons are produced in the forward direction. Any noisy cluster misidentified as part of the hadronic final state will count in the sum of Eq. (1) with a weight increasing with θ. So even relatively low energy noisy clusters in the barrel part of the LAr will strongly bias the y_h distribution. This situation is depicted in Fig. 2 where the different contribution to the distorsion of the measurement of y_h are depicted. Two first sources of bias in the measurement of y_h are the misidentification

[2]Note that the inclusion of tail catcher clusters with connected activity in the LAr could help to improve the determination of the energy of high P_T jets. This study is therefore planned for further developments of the HFS finder

of part of the energy of the scattered electron as hadrons[3] and the presence of photons due to QED initial state radiation. These two contributions are discussed in details in [11] and will be explicitely removed in the present study. After the removal of such events, the remaining bias introduced by noise can be observed in Fig. 2. On the right plot the difference between the reconstructed and the true value of y_h as a function of the true y_h shows that the events with $y_h \sim 10^{-2}$ have a systematic bias of the order of 60 %, even after the application of noise suppression at the reconstruction level.

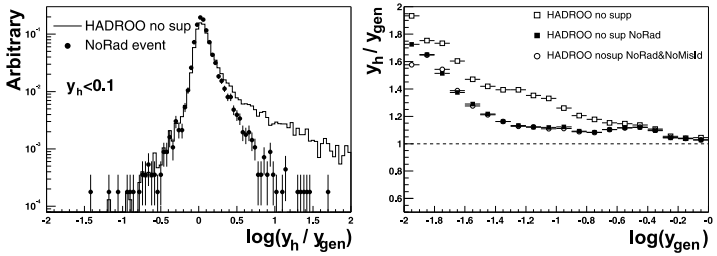

Figure 2: Comparions between the reconstructed and true values of y_h using a neutral current Monte Carlo event sample. The left figure shows the effect of the radiative NC events on the y_h/y_{gen} distribution (Note the logarithmic scales). The right figure shows the mean of y_h/y_{gen} as a function of y_{gen} and the effect of removing explicitely contributions due to radiative events (labeled "NoRad"), and misidentification of the scattered electron ("NoMisId").

Beside topological background finders [9, 10] dedicated to the rejection of an entire event which does not originate from an ep collision, the noise suppression algorithms described here are designed to remove the unphysical clusters while keeping the event. They are specially tuned to remove the previously described high θ background. Note that before all this there is already the so-called topological noise suppression (ETNS) (see Ref. [5]) which is applied at the reconstruction level (H1REC). In Monte Carlo noise is added on top of the simulated energy deposit. This noise come from real data taken during dedicated random trigger runs.

Noise suppression strategy First, all one-cell clusters are considered as not physical and removed, as well as clusters with energy $E_{clu} < 0.2$ GeV in LAr or 0.1 GeV in SpaCal. Then a set of background finders (as developed in [11]) are applied. Now these finders will be described and their performance studied.

[3]The imperfect cluster algorithm can give rise to multiple clusters for the scattered electron in particular when it hits Φ crack between octants

2.2.3 The FSCLUS algorithm

The principle of the FSCLUS algorithm, noise suppression inherited from a fortran algorithm, is the suppression of low energy isolated clusters. If the energy E_{clu} of a cluster is such that $E_{clu} < E_1$ the energy E_{sphere} in a sphere of radius R around the cluster is computed and if $E_{sphere} < E_2$ then the cluster is suppressed. This allows low energy cluster to survive if they are near more energetic ones *e.g.* if they are due to a shower fluctuation. The values for the different thresholds are $E_1 = E_2 = 0.4$ GeV and $R = 40$ cm for $\theta_{clu} > 15°$, $E_1 = E_2 = 0.8$ GeV and $R = 20$ cm for $\theta_{clu} < 15°$. Consistently with the first suppression the threshold E_1 is lowered to 0.2 GeV for clusters in the electromagnetic part of LAr. Clusters near the beam pipe in the SpaCal calorimeter are also suppressed if $\sqrt{x_{clu}^2 + y_{clu}^2} < 9.6$ cm. The performance of the FSCLUS algorithm is shown in Fig. 3: the bias is reduced by 20 % and is now at a level of 40 %. So this noise suppression is clearly not efficient enough and has to be combined with other algorithms.

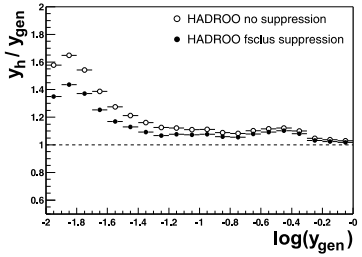

Figure 3: Mean of y_h/y_{gen} distribution as a function of y_{gen} (Note the logarithmic scales). The situation before and after the application of FSCLUS is depicted by open and solid circles, respectively. Neutral current events from a Monte Carlo sample have been used.

2.2.4 The HALOID algorithm

The HALOID algorithm is devoted to the suppression of energy deposit due to halo muons on top of real physics events. The signature is a narrow energy deposit parallel to the beam axis. To suppress such a pattern, for each cluster it is defined two cylinders of radius $R_1 = 25$ cm and $R_2 = 65$ cm. If there is energy deposit in these cylinders in at least 4 wheels including 2 CB wheels, and if at least two of the following criteria are true:

$$E_{cylinder\,1} \geq 0.5 E_{cylinder\,2} \tag{2}$$

$$N_{clusters\,in\,cylinder\,1} \geq 0.5 N_{clusters\,in\,cylinder\,2} \tag{3}$$

$$N_{cells\,in\,cylinder\,1} \geq 0.5 N_{cells\,in\,cylinder\,2} \tag{4}$$

the cluster is flagged as noise and suppressed. The improvement in the measurement of y_h before and after the suppression is shown in Fig. 4 based on a charged current MC sample.

There is a clear improvement in the y_h reconstruction of these very biased events.

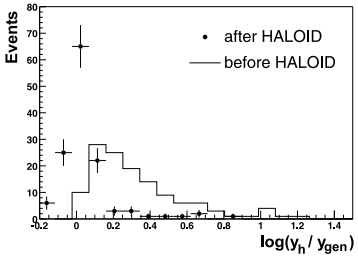

Figure 4: Improvement in y_h reconstruction after the HALOID algorithm for charged current MC events in which there is an overlap halo muon.

2.2.5 The HNOISE algorithm

Contrary to halo muons, cosmic muons or coherent noise do not have a characteristic pattern of energy deposit. However, on general ground, any deposit in the hadronic part of LAr should be connected to activity in the electromagnetic part or linked with tracks. The HNOISE algorithm look for clusters in the hadronic part and suppress them if the following conditions are all fulfilled:

- There is no energy deposit in the first hadronic layer or there is energy deposit in the first hadronic layer and there is no more energetic clusters at a distance less than 75 cm.
- There is no electromagnetic energy in a safety cylinder of 50 cm radius. The axis of this cylinder is defined by the interaction vertex and the barycenter of the considered cluster.
- There is no vertex fitted track with a dca of less than 50 cm.

This finder help again to remove a part of the noise, as shown in [11] . However there is still noise contribution at large angles leading to a bias in the y_h distribution. The NEWSUP algorithm is designed to remove this remaining background.

2.2.6 The NEWSUP algorithm

The NEWSUP algorithm is inspired form FSCLUS: it is designed to suppress low energy isolated clusters. However, to remove completely the noise a threshold higher than previously applied is needed, but only in the central region of LAr where the $E - Pz$ contribution of a false particle candidate biases the y_h of the event by a large value. Contrary to FSCLUS this algorithm care about track-cluster link and if there is a vertex fitted track with $dca \leq 25$ cm for an electromagnetic cluster or $dca \leq 50$ cm in the hadronic part the corresponding cluster is not suppressed. The same thresholds as in FSCLUS are applied, except that now $E_1 = E_2 = 1.5$ GeV for $\theta > \alpha_h$. The angle α_h is chosen to be the maximum between the angle of the most backward track and the inclusive hadronic angle[4] $\tan(\gamma_h/2) = (E_h - Pz_h)/P_T^h$. The algorithm is run iteratively until there is no cluster suppressed. The results are presented in Fig. 5 where situation for charged current events is depicted. The energy reconstructed at

[4] If $\gamma_{h\,LAr} \leq 50°$ or $y_{h\,LAr} \leq 0.1$ the SpaCal clusters do not enter in the calculation of γ_h.

high angles is much greater than the generated one without any noise suppression. After the application of all suppression algorithms developed here the measurement is closer to the true level.

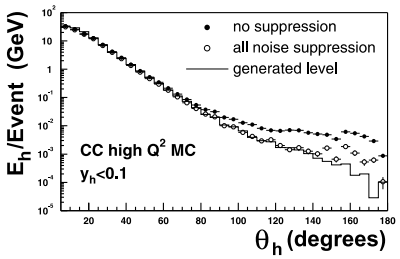

Figure 5: Comparison between the total reconstructed and generated energy distributions for low y_h events with all noise suppressions (open circles) and without (solid circles). The true level is represented by an histogram. Charged current events from a Monte Carlo sample have been used.

All the previous discussions were purely based on MC files. We have now to check that all the noise suppression is applicable to real data. This is done in Fig. 6 where the energy fraction suppressed from data and MC are compared as a function of y_h. A good agreement is observed and the amount of suppressed noise energy is comparable to the previous FORTRAN implementation of the algorithms, as presented in [11]. The conclusion is that the combination of these complementary noise finders allows a good reconstruction of the y_h kinematic variables. A good suppression is also very important in the views of a calibration procedure aiming at the knowledge of the true energy.

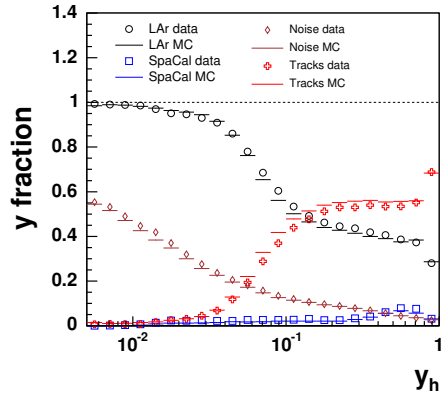

Figure 6: Comparison of the fraction of the suppressed noise energy in data (points) and in MC (histograms). The other components contributing to the final y_h are also displayed. 2003-2004 data and Django MC have been used here.

2.2.7 Safety tests of the noise finders

As these finders are applied by default, careful studies have been performed to see if signal relevant for exclusive studies were not suppressed. Tests were made on different MC samples, namely D^* events in photoproduction and in DIS, and diffractive J/Ψ events.

The principle of the tests was to look if these additional noise suppressions was killing genuine signal. The distance in the η, φ plane between a generated particle (with $P_T^{gen} > 180$ MeV, so that it reaches the calorimeter) and each particle candidate was computed:

$$d = \sqrt{(\eta_{gen} - \eta_{cand})^2 + (\varphi_{gen} - \varphi_{cand})^2}. \quad (5)$$

The minimal distance is supposed to give the corresponding candidate associated to the generated particle. By looking at this minimal distance before noise suppression d_{nosup} and after noise suppression d_{sup} we can see if signal has been suppressed.

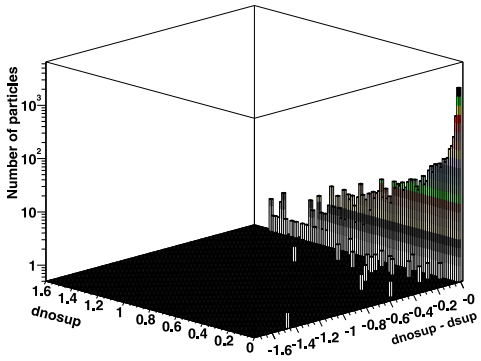

Figure 7: Numbers of entries regarding the minimal distance in η, φ between a generated particle and a particle candidate before d_{nosup} and after d_{sup} noise suppression, in the D^* photoproduction event sample.

The figures 7 and 8 are two dimensional histograms of d_{nosup} versus $d_{nosup} - d_{sup}$. It is straightforward to see that first, most entries are concentrated at $d_{nosup} - d_{sup} = 0$, so the noise suppression was safe, and in the $d_{nosup} - d_{sup} = 0$ plane the region $d_{nosup} \simeq 0$ dominate, so the generated particle was correctly matched to a candidate. The region to look for signal suppressed is the region of $d_{nosup} \simeq 0$ (the particle is well associated to a generated one) and $d_{nosup} - d_{sup} < 0$. We see two such entries on the histogram of Fig. 7, at $d_{nosup} - d_{sup} = -0.5$ and -1.5. The first one is a π^- killed by the NEWSUP algorithm, and the second one a n killed by the HNOISE algorithm. For the histogram of Fig. 8, five particles (two γ, two K_L^0 and a n) are found to be suppressed, this being mainly due to the special topology of photoproduction charm events with a large number of very low energy particles in a large η range. A conclusion can be drawn by looking at the Table 2 where one can see that the loss of genuine signal is at a very low and acceptable rate with respect to the signal suppressed.

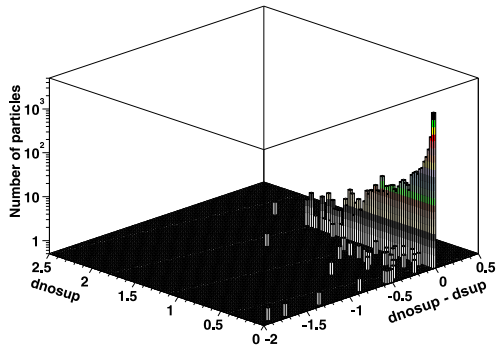

Figure 8: Numbers of entries regarding the minimal distance in η, φ between a generated particle and a particle candidate before d_{nosup} and after d_{sup} noise suppression, in the D^* low Q^2 DIS event sample.

D^* photoproduction sample		Inefficiency
2 signal killed	717 newsup clusters	0.2 %
3 signal killed	114 hnoise clusters	2.6 %
D^* low Q^2 DIS sample		Inefficiency
1 signal killed	562 newsup clusters	0.2 %
1 signal killed	140 hnoise clusters	0.7 %

Table 2: Summary of the signal suppression.

For sake of completeness a test was made on a diffractive J/Ψ sample. It was found that two μ with no tracks associated and not found by the muon finder were suppressed by HNOISE, this for 10^4 J/Ψ events. So the noise suppression is clearly safe for diffractive vector meson production.

To conclude the noise finding achieves a very good compromise between efficiency and safety. The output list of noise suppressed clusters is the input of the Hadroo2 algorithm which is now going to be described in detail. Every noise suppressed cluster is flagged and re-used to calculate the total hadronic LAr four-vector produced by noisy cells. This information is stored on HAT in the variables which start with the string 'HfsClusNoiseXXXX' and allows then to study the impact of the different noise finders.

3 The Hadroo2 algorithm

The Hadroo2 algorithm realises the creation of the HFS particles. Note that if there are identified electrons or muons which are not flagged as isolated[5], they are considered as being part of the Hadronic Final State but their four vector remains unchanged and their associated tracks and clusters are excluded from any additional treatment.

The algorithm starts with the previously described list of selected tracks and clusters. The cornerstone idea of the energy flow algorithm is the combination of the tracks and clusters. As we may have both for a charged particle, we want to keep the best measurement. To achieve this, we propose to compare relative resolutions of the tracker or of the calorimeter for the measurement of the same amount of energy.

3.1 Comparison of tracker and calorimeter resolutions

Each track is supposed to originate from a pion, with energy

$$E^2_{track} = P^2_{track} + m^2_\pi = P^2_{T,track} / \sin^2\theta + m^2_\pi. \tag{6}$$

The error on this energy is obtained by standard error propagation using some of the track fitting error information:

$$\frac{\sigma_{E_{track}}}{E_{track}} = \frac{1}{E_{track}} \sqrt{\frac{P^2_{T,track}}{\sin^4\theta} \cos^2\theta \sigma^2_\theta + \frac{\sigma^2_{P_T}}{\sin^2\theta}} \tag{7}$$

where σ_{P_T} and σ_θ are the corresponding error on P_T and θ and neglecting their correlations. It was checked that the use of the full covariance matrix gave similar results within 2 % at most.

Now we evaluate for each track what would be the corresponding error of this particle as measured with the calorimeter. This decision turns out to be only based on the track, but it is not possible to make any decision based on the calorimeter deposit as this one is a priori unknown due to possible contribution of neutral particles. We made the assumption that the corresponding error on the measurement of this particle in the LAr [5] would lead to the error $\sigma_{E\ LAr\ expect.}$

$$\left(\frac{\sigma_E}{E}\right)_{LAr\ expectation} = \frac{\sigma_{E\ LAr\ expect.}}{E_{track}} = \frac{0.5}{\sqrt{E_{track}}}. \tag{8}$$

The relative resolutions defined by Eqs. (7) and (8) are then compared to determine which of the tracker or the calorimeter provides the best measurement. The track is considered as a "good one" if

$$\frac{\sigma_{E_{track}}}{E_{track}} < \frac{\sigma_{E\ LAr\ expect.}}{E_{track}} \tag{9}$$

The Fig. 9 shows the relative resolutions of the track compared to the LAr expectation. We observe that the tracker measurement is better up to 12 GeV for forward tracks, 25 GeV for

[5] A muon is isolated if the calorimeter energy in a cylinder around the extrapolated muon track is < 5 GeV (cylinder radius of 35 cm in electromagnetic, 75 cm in hadronic LAr section) and if there is no other selected track in a cone of radius $R_{\eta-\varphi} = 0.5$.

An electron is isolated if the calorimeter energy not attributed to any other identified electron in a cone around the electron of radius $R_{\eta-\varphi} = 0.5$ is less than 3 % of the electron energy. All SpaCal electrons are considered as isolated.

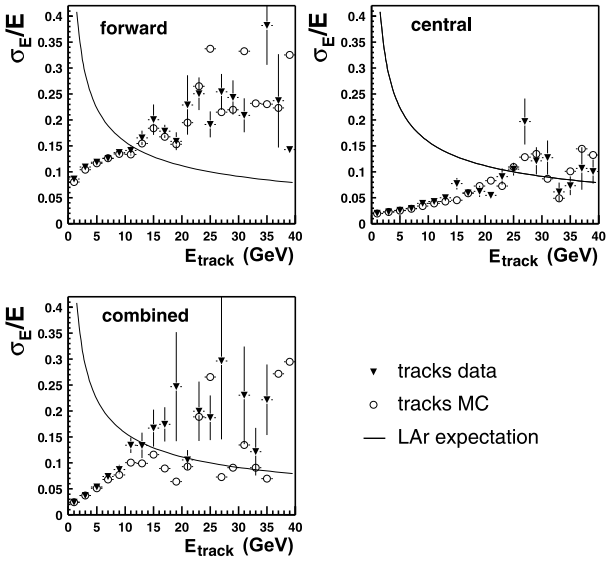

Figure 9: Relative resolution of the different types of tracks compared to the LAr expectation.

central tracks and about 13 GeV for combined tracks. We also observe that the error of the track measurement is reasonably well described by the MC, at least up to the turnaround energy.

To also optimise the global energy measurement, selected charged tracks are ordered by increasing P_T, in order to associate first the clusters to the well measured low P_T tracks. Then the algorithm do a loop over selected tracks and for each track test the Eq. (9) and try to associate calorimetric clusters to the track.

3.2 Track measurement preferred

If Eq. (9) is true, the track measurement is used to make a particle candidate. In this case the calorimetric energy has to be suppressed to avoid double counting. Each track is extrapolated up to the surface of the calorimeter as an helix, and inside LAr as a straight line. The calorimetric energy $E_{cylinder}$ is computed as the sum of all clusters in the overlapping volume of a 67.5° cone and two cylinders of radius 25 cm in the electromagnetic part of LAr and 50 cm in the hadronic part (see Fig. 10). This volume will be referred hereafter as the "cylinder". The numerical values are such that the cylinder reasonably contains the full hadronic shower. Small variations of these values do not lead to significant changes in the performance of the algorithm.

Then the track energy E_{track} is compared to the calorimetric energy inside the cylinder

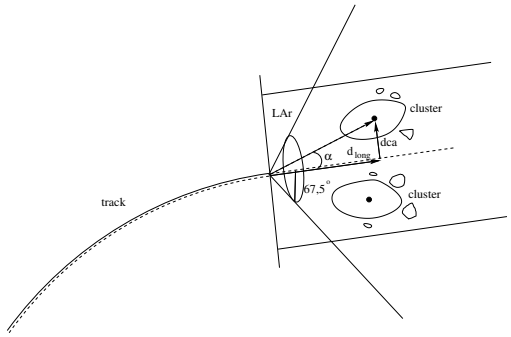

Figure 10: The axis of the cone and the cylinders is the straight line extrapolation of the particle trajectory into the calorimeter. The distance of closest approach (dca) of a cluster is defined with respect to this line. This drawing is courtesy of A. Perieanu.

$E_{cylinder}$, taking into account possible fluctuations of both measurement within their standard errors[6] and if

$$E_{cylinder} < E_{track} \times \left[1 + 1.96\sqrt{\left(\frac{\sigma_{E_{track}}}{E_{track}}\right)^2 + \left(\frac{\sigma_E}{E}\right)^2_{LAr\,expectation}}\right] \qquad (10)$$

an amount of calorimetric energy $E_{suppressed}$ equal to $E_{cylinder}$ has to be suppressed completely. Otherwise only an amount of energy $E_{suppressed} = E_{track}$ is suppressed. Clusters are suppressed one after the other by increasing dca and up to the needed energy. To reach the exact $E_{suppressed}$ energy, some clusters may be only partially removed and their energy is adjusted.

The meaning of Eq. (10) is the following: the calorimeter measurement may have fluctuated, but the well measured track give a constraint on the amount of energy coming from charged particles; so we discard all the calorimeter measurement except if the observed fluctuation is above 95 % C.L. of the error. If Eq. (10) is false the energy difference $E_{cylinder} - E_{track}$ is assumed to originate from neutral particles or other charged tracks. So it is a way of deciding whether there is additional energy not belonging to the primary track or not without always believing the upward fluctuations of the LAr energy measurement.

3.3 Calorimetric measurement preferred

If Eq. (9) is false then the energies $E_{cylinder}$ and E_{track} are compared and if

$$E_{track} \in \left[E_{cylinder} - 1.96\,\sigma_{E_{cylinder}}, E_{cylinder} + 1.96\,\sigma_{E_{cylinder}}\right] \qquad (11)$$

[6] This feature of the algorithm was suggested by K. Daum

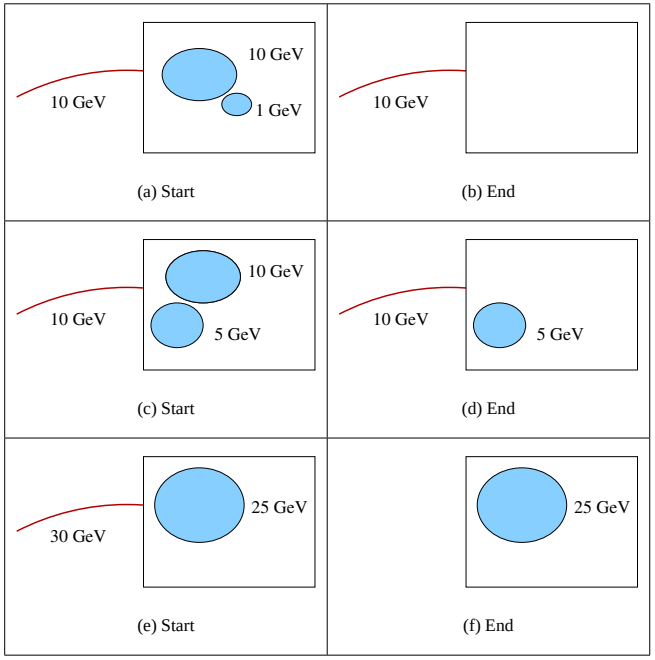

Figure 11: Example: behaviour of the Hadroo2 algorithm given three starting situations involving tracks and clusters. On the first line, a 10 GeV track measured with a 4 % accuracy is kept (Eq. (9)) and all the calorimetric information is removed (Eq. (10)). On the second line the track information is still kept, however the cylinder energy of 15 GeV is determined to contain a neutral component (following the Eq. (10)) and only the track energy is subtracted. On the third line the track is not well measured (15 % accuracy) and the calorimetric information is used.

(with $\sigma_{E_{cylinder}} = 0.5\sqrt{E_{cylinder}}$) the track energy is considered to be compatible with the calorimetric deposit and the calorimetric measurement is used to define a particle candidate. Otherwise, if

- $E_{track} < E_{cylinder} - 1.96\,\sigma_{E_{cylinder}}$, the track measurement is used and calorimetric energy is subtracted as in Sec. 3.2.

- $E_{track} > E_{cylinder} + 1.96\,\sigma_{E_{cylinder}}$, the track is suppressed and an hadron is defined using the calorimetric clusters[7].

Indeed, when the compared energies are compatible, the hadrons are well measured but most of the time the measurement of the calorimeter is more accurate. When the track energy is much larger than the calorimeter energy, it is most of the time due to a bad measurement of an high P_T track.

3.4 Treatment of residual clusters

Once all the tracks have been treated, particles candidates are made out of remaining clusters using the calorimetric energies. The momentum of these clusters is rescaled to obtained massless particles. Thes particles correspond to neutral hadrons with no associated track or to charged particles with a badly measured track.

4 Comparison with other HFS algorithms

The main kinematic variable used in the next sections are defined using the hadronic and double-angle methods. The total hadronic transverse momentum P_T^h is defined by

$$P_T^h = \sqrt{\left(\sum_h P_x^h\right)^2 + \left(\sum_h P_y^h\right)^2} \tag{12}$$

where the summation h extends over all reconstructed hadrons at the μODS level. The quantity θ_h and θ_h^e stand for the hadronic inclusive polar angle calculated respectively with the hadronic and positron variables using:

$$\tan(\theta_h/2) = \frac{\sum_h (E_h - Pz_h)}{P_T^h} \tag{13}$$

and

$$\tan(\theta_h^e/2) = \frac{2E_0^e - (E_e - Pz_e)}{P_T^e} \tag{14}$$

where E_0^e, E_e, Pz_e and P_T^e are respectively the energy of the incident positron, the energy, the longitudinal and transverse momenta of the scattered positron.

The total transverse momentum P_T^{da} is calculated using the double angle method from the angles of the positron and of the hadronic system:

$$P_T^{da} = \frac{2E_0^e}{\tan\frac{\theta_e}{2} + \tan\frac{\theta_h}{2}}. \tag{15}$$

The P_T balance P_T^{bal} stands for the ratio of the hadronic transverse momentum and the double angle transverse momentum:

$$P_T^{bal} = \frac{P_T^h}{P_T^{da}}. \tag{16}$$

[7] Note that technically the four-vector of the particle candidate associated to the track is changed using the calorimeter informations. Only if there is no calorimetric energy behind the track, its particle candidate four-vector is set to zero.

In this note the following area depicted on Fig. 12 will be used. It is an angular division roughly named after the corresponding calorimeter wheels.

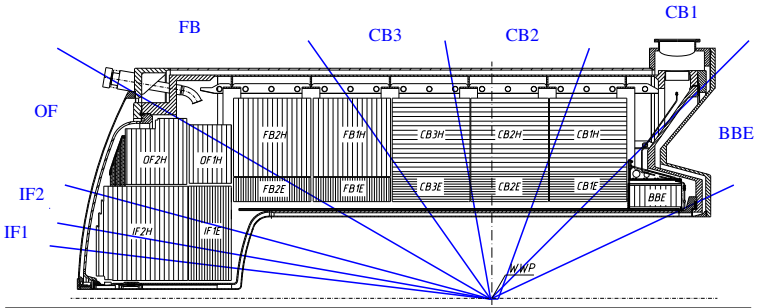

IF1	IF2	OF	FB	CB3	CB2	CB1	BBE
7°-10°	10°-15°	15°-30°	30°-55°	55°-80°	80°-110°	110°-135°	135°-155°

Figure 12: Definition of the different areas of the LAr calorimeter defined for the HFS calibration.

In the past, several other approaches for the reconstruction of the hadronic final state have been used. For inclusive high Q^2 analysis, algorithm using only calorimeter information has been used — this is referred here as the "clusters only" algorithm. This suffers from the drawback that low P_T tracks component is not included in the HFS reconstruction and is therefore missing.

The widely used FSCOMB algorithm has been one of the first attempts to combine tracks and clusters, but tracks were only considered up to[8] a P_T of 2 GeV. In FSCOMB the subtraction also is done in such a way that only E_{track} is suppressed, and never $E_{cylinder}$. So there is no equivalent to Eq. (10) and the energy measurement of LAr is always trusted.

4.1 Composition in tracks and clusters of the HFS particles

Figure 13 shows the relative contribution of clusters to P_T^h for neutral current (NC DIS) events with only one jet and for data and MC events. The details of the event selection used here are given in Sec. 5.2. The fraction of tracks is then the complement to one of the cluster fraction presented in Fig. 13.

A clear pattern of dependencies upon P_T^{da} and θ_{jet} appears. We see that first, the contribution of tracks is decreasing when the transverse energy of the jet is increasing. This is consistent with the fact that more clusters are chosen at high energies. The main dependency is the one with respect to θ_{jet}. For $\theta_{jet} < 15°$ the forward and combined track contributions are rather low, and the HFS particles are clearly cluster-dominated by about 80 %. In the OF region the central track contribution starts to play a role and the cluster contribution decreases. At the end, the cluster contribution in the central region is around 40 %. We can also observe that

[8] When the algorithm was developed, high P_T tracks had not been extensively studied.

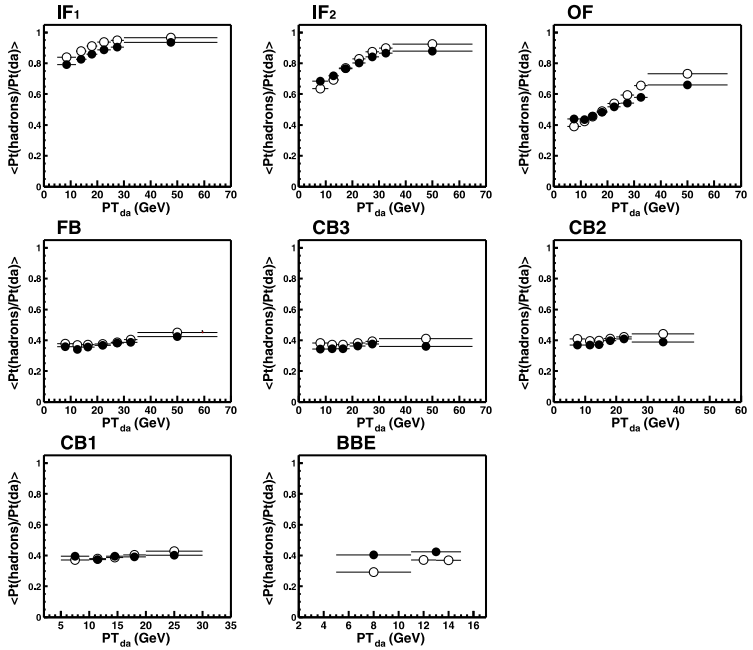

Figure 13: Fraction of the total hadronic P_T due to clusters for high Q^2 NC DIS one jet events, as a function of θ_{jet} and P_T^{da}. Data are presented using solid circles and MC with open circles.

the contributions of tracks and cluster in the data are reasonably well described by the MC, as expected from the good description of the track relative resolution as shown in Fig. 9.

Figure 14 is a comparison of the $P_T^{bal}(\theta_{jet}, P_T^{da}) = P_T^h / P_T^{da}$ for the same high Q^2 NC DIS one jet sample reconstructed with different algorithms. No cluster calibration is applied. In almost all calorimeter wheels, a 10 % shift of the P_T^{bal} mean values of the Hadroo2 algorithm is observed due to the different weighting scheme used (see Sec. 2.2.1). On this plot the contribution of tracks is clear, already for the OF region: the P_T^{bal} is much flatter with respect to P_T^{da}. In the IF1 and IF2 regions, where track contribution is negligible, all the P_T^{bal} have a similar shape.

4.2 Resolution

The evolution of P_T^{bal} distributions as a function of P_T^{da} and θ_{jet} for FSCOMB and Hadroo2 algorithms are compared in Fig. 15. The evolution of mean values of P_T^{bal} distributions are

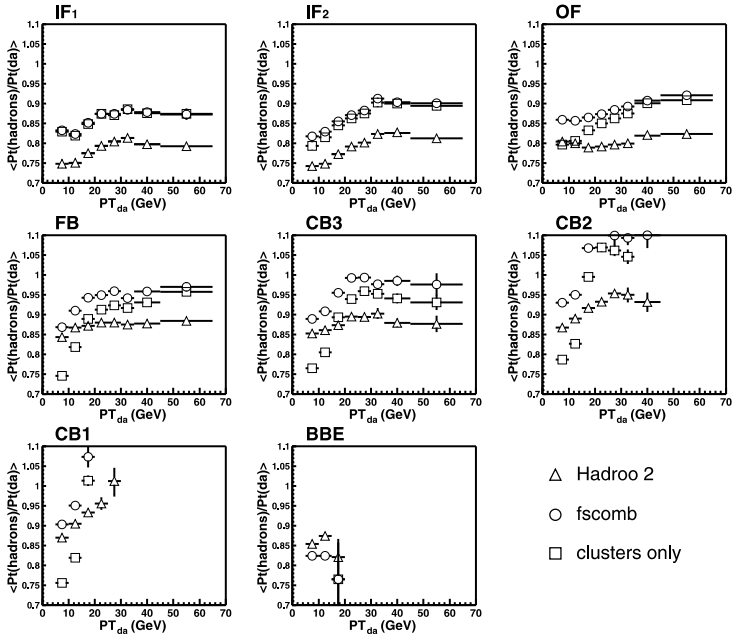

Figure 14: Comparison of the $P_T^{bal} = P_T^h / P_T^{da}$ dependency upon P_T^{da} for different HFS algorithms: FSCOMB, Hadroo2 and clusters only.

depicted on the left figures while the right figures present the evolution of the relative resolution, defined as $\sigma(P_T^{bal}) / < P_T^{bal} >$. NC DIS events with only one jets have again been used (see Sec. 5.2). The mean values corresponding to the Hadroo2 algorithm are shifted down by $\sim$ 10 % due to the weigthing scheme used. Nevertheless the resolution obtained with the Hadroo2 algorithm is comparable to FSCOMB and even better in the backward region of the LAr calorimeter.

Further improvement of the resolution can be obtained by combining the Hadroo2 algorithm with the new energy weighting scheme for hadronic clusters proposed in [7, 8]. This is displayed by blue points on Fig. 15. We can observe that the resolution is improved in all regions of the calorimeter and especially in the central part of the barrel and for 10 GeV $< P_T^{da} <$ 20 GeV. The evolution of the mean values of P_T^{bal} as a function of P_T^{da} is also flat using this new weighting. Therefore it is planned to include this new energy weighting in next developments of the HFS finder.

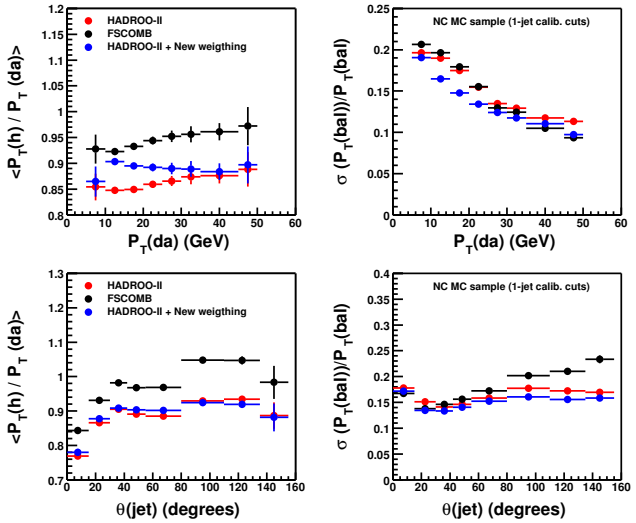

Figure 15: Evolution of mean values (left figures) and relative resolutions (right figures) of P_T^{bal} as a function of P_T^{bal} and θ_{jet}, for FSCOMB and Hadroo2 algorithms. The influence of the "new weighting" [7, 8] (blue dots) is also presented.

5 Jet Calibration procedure

This section is devoted to the calibration of jets for high Q^2 inclusive measurements. The knowledge of the absolute energy scale and its error is a key point for lots of analyses, ranging from searches and "exotic" analyses where we want to reconstruct an invariant mass, to jets and inclusive physics where the understanding of the error on the hadronic energy scale is crucial. This is especially true for the Charged Current analysis where all the kinematics variables are reconstructed using the HFS.

5.1 The principle of calibration

Once the hadron finding algorithm has been fully specified, a suited calibration procedure can be applied. The selected tracks are already calibrated and the calibration procedure must not change their energy. In figure 16 we observe that the K^0 mass peak obtained with the default *H1PartK0Finder* has an accuracy better than 1 %.

The aim is therefore to perform a jet calibration but only changing the energy of calorimeter clusters. The method of jet calibration used here is derived from [12]. The reference quantities used for the calibration are determined with the double angle kinematics. The hadronic trans-

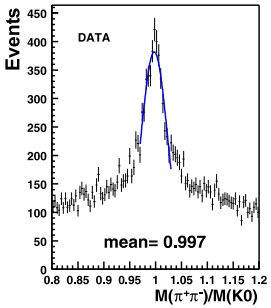

Figure 16: K0 mass spectrum (normalised to the K0 mass) obtained with the μODS standard *H1PartK0Finder*. The invariant mass of the two pions is computed using the good quality tracks. The mean of a Gaussian fit (blue line) is centered to one with less than 1 % deviation.

verse momentum determined with this method is independent of the LAr energy calibration to a good approximation. The calibration is said to be *absolute* if the measured P_T^h coïncides with the P_T^{da} (see Sec. 4 for definition of the variables). The use of the double angle method as a reference has several consequences: first, the calibration sample chosen to determine the calibration constants must be such that the P_T^{da} measurement is well under control. Secondly this method does not rely on MC which is separately calibrated and no relative calibration is needed. Finally the method is also independent of the electron calibration.

5.2 Determination of the calibration constants

The event sample used to determine the calibration coefficients is defined by the following selection:

- Good quality selection (High Voltage, Vertex, background finders, *etc*),
- $Q^2 \geq 100\,GeV^2$,
- 1 electron with $P_T^e \geq 10$ GeV,
- only one jet,
- good P_T^{da} measurement cuts:
  - Anti ISR cut $P_T^e/P_T^{da} > 0.88$
  - Anti leakage cuts : $E_{SpaCal}/E_{total} < 1$ %
  - $P_T^{SpaCal}/P_T^{total} < 1$ %
  - $E_{iron}/E_{total} < 1$ % or $P_T^{iron}/P_T^{total} < 1$ %
  - $d\theta = |\theta_{had} - \theta_{jet}| < 1.5$. This cut was shown to improve the double angle measurement at low P_T^{jet} and θ_{jet} (see [12]).

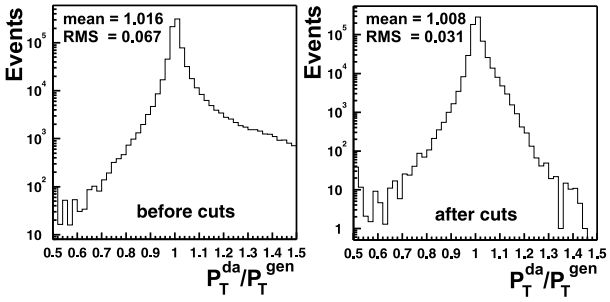

Figure 17: P_T^{da}/P_T^{gen} distributions before and after having applied the good double angle measurement cuts. The bias of P_T^{da} to higher values due to QED ISR is significantly reduced by these cuts.

The figure 17 shows the ratio P_T^{da}/P_T^{gen} before and after the good P_T^{da} measurement cuts for high Q^2 neutral current MC.

The improvement of the P_T^{da} measurement is clear, especially the bias of the P_T^{da} to larger values (due to initial QED radiation) is significantly reduced. Hence we can say that the double angle measurements are well under control. Note that no cut on the hadronic energy is used, because indeed such a cut would bias the distributions used to calibrate. In these one jet events the hadronic final state is entirely contained in a single material region of the LAr and we have an approximation of the difference between the true P_T of the jet (approximated as P_T^{da}) and the response (or lack of response) of the detector.

The evolution of mean values of P_T^{bal} distributions upon P_T^{da} — called F_{ptbal} — is fitted separately for several θ regions. The functional form used for the fit is

$$F_{ptbal}^{\theta}(P_T^{da}) = A_\theta(1 - \exp^{-B_\theta - C_\theta P_T^{da}}) \tag{17}$$

The P_T^{bal} distributions and the result of the fit are shown in Fig. 18.

During the calibration procedure described in the next section each jet will then be corrected by this factor F_{ptbal}. But, as these coefficients are determined using an high P_T (greater than 10 GeV) selection, the extrapolation of F_{ptbal} to low P_T jets cannot be reliably trusted. Therefore, only jets with $P_T^{jet} > 4$ GeV will be calibrated with this method. In very forward region, $\theta_{jet} < 7°$, affected by leakage in the beam-pipe no absolute calibration can be reasonably applied too. Jets reconstructed in the SpaCal calorimeter ($\theta_{jet} > 155°$) are also not calibrated.

In order to also calibrate remaining hadrons which are not part of a jet, or in jets not calibrated using F_{ptbal}, the dependence of the mis-calibration is also determined as a function of θ_h^e only, as presented in Fig. 19. This will be use to determine calibration coefficients D_θ for each θ bin as defined in Fig. 12. The coefficients D_θ will be applied to all remaining hadrons, separately for data and MC to perform an absolute calibration, except in the region $\theta_{hadron} < 7°$ where a relative calibration is applied. Here only data events will be calibrated, to bring the response of the LAr calorimeter to the one simulated in the MC.

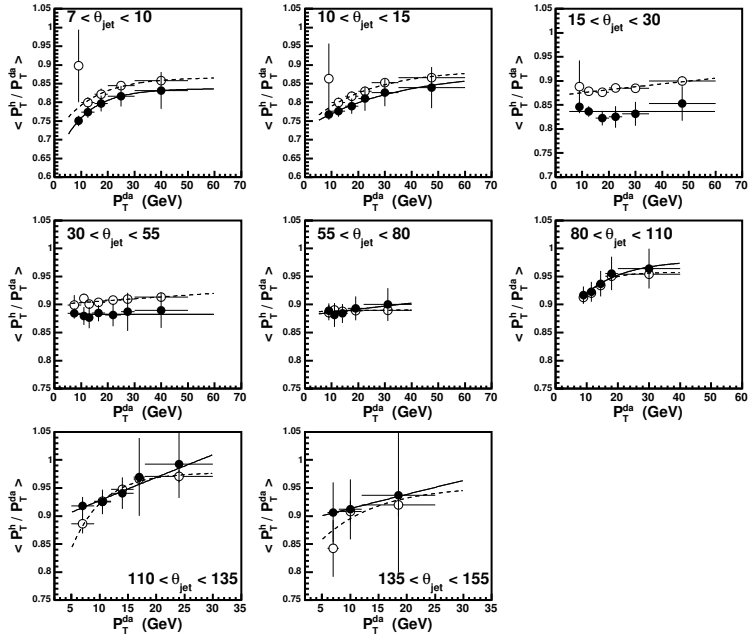

Figure 18: Evolution of the mean values of the P_T^{bal} distributions with P_T^{da} for the calibration sample in the different θ_{jet} regions. Solid and open circles stand for the data and MC, respectively. The plain and dashed lines are fits of the functional form of Eq. (17) to data and MC points, respectively. This example is for 1999p-2000 data and RAPGAP Monte Carlo.

5.3 Application of the calibration

In a first step all hadrons in jets will be calibrated, jet by jet. As the calibration should be applied only to clusters, we have to disentangle for each jet hadrons reconstructed from tracks and from clusters. For each jet we can define the fraction of P_T^{jet} carried by clusters before calibration C_{cls} as

$$C_{cls} = \frac{P_T^{uncalibrated\,clusters}}{P_T^{tracks} + P_T^{uncalibrated\,clusters}}. \tag{18}$$

The fraction of P_T^{jet} carried by tracks is the complement $(1 - C_{cls})$. Note that here the fraction C_{cls} is an approximation because it is determined before any calibration of the energy of clusters. If F_{ptbal} is the absolute correction defined in Sec. 5.2 it is easy to see that the correction

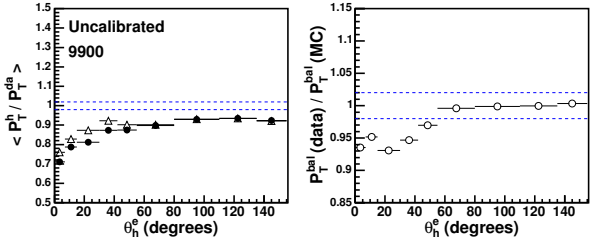

Figure 19: Mean values of P_T^{bal} distributions for each LAr wheel (left figure), for data (solid circles) and MC (open circles). The ratio between data and MC points is presented in the figure on the right. This example is for 1999p-2000 data and RAPGAP Monte Carlo.

factor f we need to apply only to all clusters in the jet is given by

$$f = \frac{1 - F_{ptbal} \times (1 - C_{cls})}{F_{ptbal} \times C_{cls}} \tag{19}$$

For each jet F_{ptbal} which was determined as a function of θ and P_T^{da} (Eq. (17)) will be calculated using instead the mean polar angle of the jet θ_{jet} and its transverse momentum P_T^{jet}. Indeed P_T^{da} can not be used now as, for a general selection, the double angle measurement may not be reliable and the total transverse momentum can be also shared between different jets. In order to have an approximation of the "true" transverse momentum an iterative procedure is used. The uncalibrated P_T^{jet} is used as the argument in Eq. (17) for a first approximation of f. The resulting $P_T^{jet'}$ is then used to compute the final f used to calibrate. For each jet the calibration is performed by multiplying the cluster energy by the f factor. Then in order to be consistent with the kt jet kinematics $\varphi_{jet}, \eta_{jet}, P_T^{jet}$ are properly recomputed and the final jet is massless.

The jets are not calibrated if $P_T^{jet} < 4$ GeV or $\theta^{jet} < 7°$ or $\theta^{jet} > 155°$. The total hadronic final state can be decomposed in hadrons belongings to calibrated jets and remaining hadrons:

$$P_{HFS,Uncalibrated} = \sum_i P_{jet\,i,Uncalibrated} + P_{HFS,not\,in\,jet} \tag{20}$$

where $P_{HFS,not\,in\,jet}$ the part of the HFS not in jets brings a negligible P_T contribution in high Q^2 events[9]. In a second step $P_{HFS,not\,in\,jet}$ will be calibrated using D_θ coefficients depending on the polar angle of each hadron θ_{hadron}. All cluster hadrons will be absolutely calibrated, except for $\theta_{hadron} < 7°$ where the calibration is applied only to data events using $D_{\theta<7°} = D^{data}_{\theta<7°} \,/\, D^{MC}_{\theta<7°}$. The total calibrated hadronic system is then obtained with:

$$P_{HFS,Calibrated} = \sum_i P_{jet\,i,Calibrated} + P_{HFS,not\,in\,jet,calibrated} \tag{21}$$

[9] In the theoretical prescription implemented in the jet finder [13] one end with nothing but only jets in the HFS. However as it is not really reliable to go down to arbitrary low P_T a cut of $P_T^{jet} \geq 2.5$ GeV is introduced for the writing of jets on μODS.

Note that all the calibration coefficients determined here are specific both to Hadroo2 and to the kt jet algorithm.

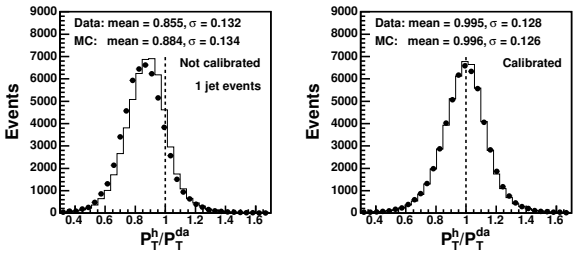

Figure 20: P_T^h/P_T^{da} distribution for one jet events, before (left) and after (right) the application of the jet calibration. The mean and σ values are obtained using a Gaussian fit to the central part of the distributions.

5.4 Tests of the Calibration

The tests are performed with a much larger event sample, requiring the following set of cuts:

- Good quality selection (High Voltage, Vertex, background finders, *etc*),
- $Q^2 \geq 100$ GeV^2,
- 1 electron with $P_T^e \geq 10$ GeV,
- $P_T^h/P_T^e > 0.35$,
- Anti ISR cut $\sum_{h,e}(E - Pz) > 42$ GeV,
- $\theta_{jet} > 7°$, this ensures that the jets are well contained in the calorimeter acceptance.

Now a total $E - Pz$ cut is allowed to reduce the effect of ISR. This different set of cuts will allow to check that the method does not depend on the selection used for the determination of the coefficients. Different NC DIS event sub-samples containing only one, two and three jets will be used for the tests. The two and three jets event samples are independent from the events used for the calibration and therefore provide good tests.

5.4.1 One jet check sample

First the tests with a one jet check sample are performed on 1999p-2000 data and an NC DIS Monte Carlo events generated using RAPGAP. The calibrated and uncalibrated P_T^{bal} distributions are presented in Fig. 20. The distribution is now centered at one and the width is reduced.

The evolution of the mean values of P_T^{bal} distributions as a function of P_T^{da} and θ_h^e is presented in Fig. 21. The ratio $P_T^{bal}(data)/P_T^{bal}(MC)$ is also shown. It is well described within 2 %.

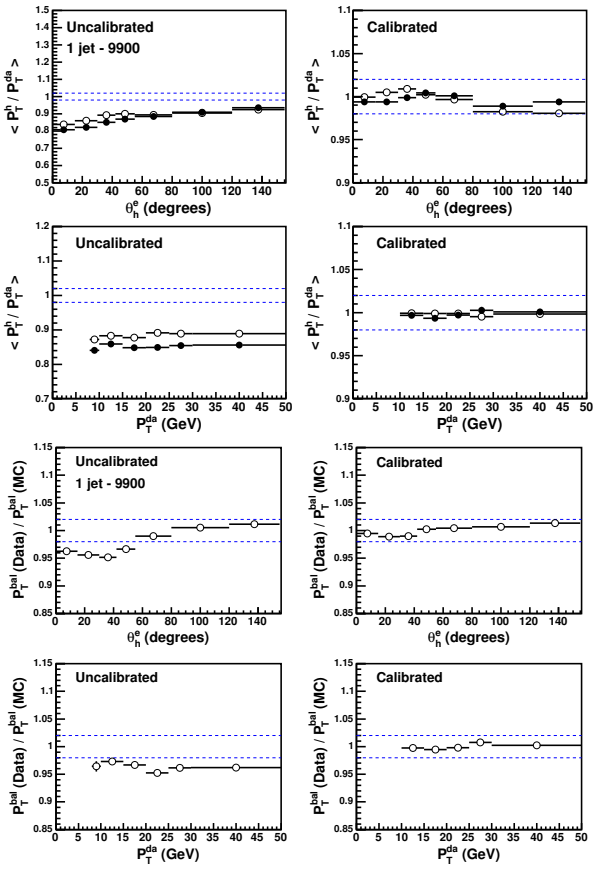

Figure 21: Mean of the P_T^h/P_T^{da} distributions (upper figures) and the ratio $P_T^{bal}(data)/P_T^{bal}(MC)$ (bottom figures) as a function of P_T^{da} and θ_h^e for one jet events, before and after calibrations.

5.4.2 Two and three jets check sample

Especially for cross section measurements of high P_T jets, the minimisation of the hadronic scale uncertainty, and therefore the optimisation of the jet calibration, is necessary. The uncorrected and corrected P_T^{bal} distributions are presented in Fig. 22. Again, after corrections the data and MC agreement is improved and the absolute momentum balances are centered around

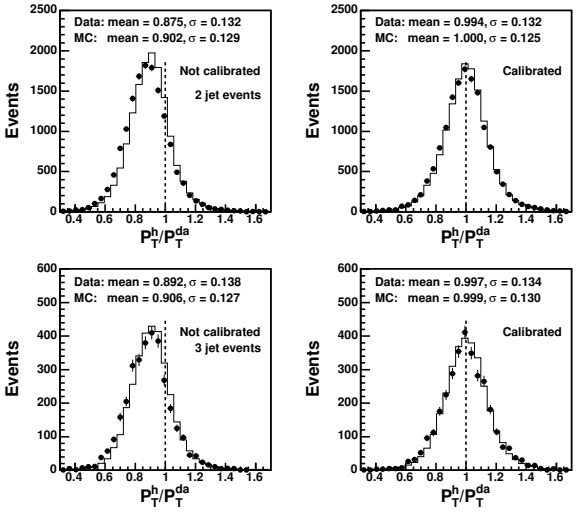

Figure 22: P_T^h/P_T^{da} distributions for two (upper figures) and three (bottom figures) jets events, before (left) and after (right) the application of the jet calibration. The mean and σ values are obtained using a Gaussian fit to the central part of the distributions.

one. The mean values of P_T^{bal} are displayed on Figs. 23 and 24 as a function of P_T^{da} and θ_h^e for two and three jet events.

The results obtained with a two jet sample show that the overall P_T balance is centered around 1.0 and that the systematic shift does not exceed 2 %. We can observe that the absolute hadronic scale is obtained within 2 % after coorection, for the data and the MC. The systematic uncertainties are also of the order of 2 % in all the P_T^{da} and θ_h^e ranges.

5.4.3 Inclusive check sample

With the inclusive check samples which has a larger statistics, the calibration can be tested as a function of P_T^{da} and θ at the same time. The mean values of corrected and uncorrected P_T^{bal} distributions as a function of P_T^{da} and θ_h^e are presented in Fig. 25. This example shows, on data event only, the effect of the jet calibrations. We can observe that after correction the absolute hadronic energy scale is well obtained within 2 %. The effect of the jet calibrations on the agreement between data and MC P_T^{bal} distributions is displayed in Fig. 26. One can see that again after having applied the calibration, the systematic error is well contained within 2 % in all P_T^{da} bins of each θ region.

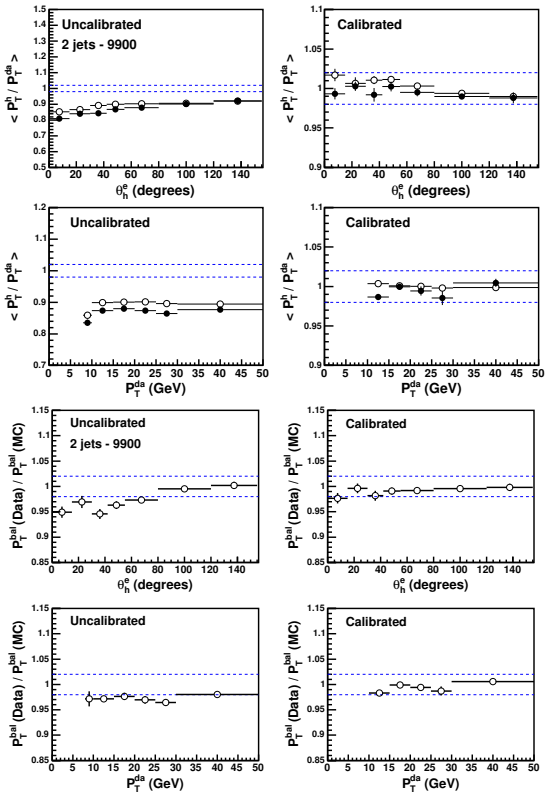

Figure 23: Mean of the P_T^h/P_T^{da} distributions (upper figures) and the ratio $P_T^{bal}(data)/P_T^{bal}(MC)$ (bottom figures) as a function of P_T^{da} and θ_h^e for two jets events.

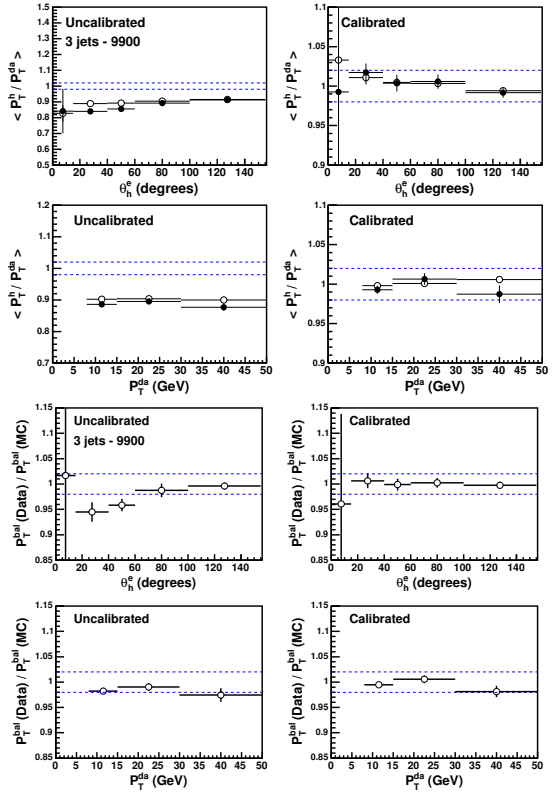

Figure 24: Mean of the P_T^h/P_T^{da} distributions (upper figures) and the ratio $P_T^{bal}(data)/P_T^{bal}(MC)$ (bottom figures) as a function of P_T^{da} and θ_h^e for three jets events.

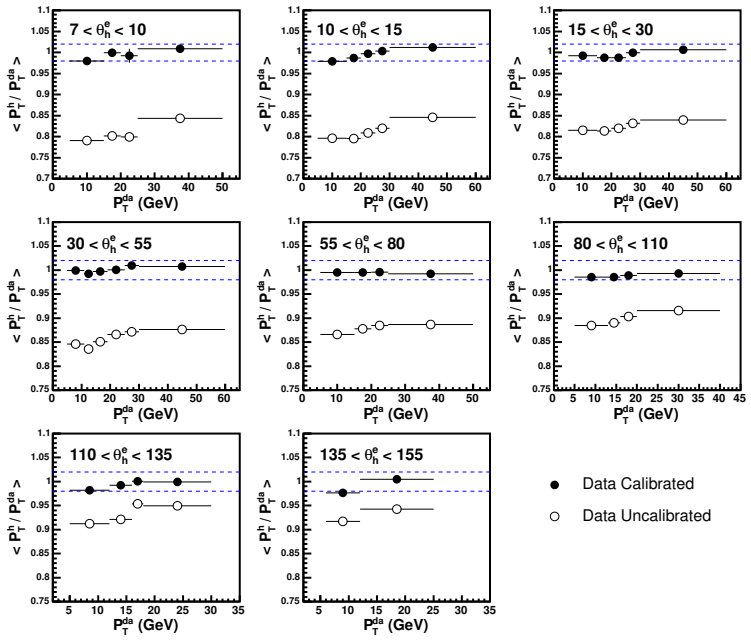

Figure 25: Evolution of the mean values of the P_T^{bal} distributions for data with P_T^{da} for the inclusive check sample in the different θ_h^e regions, before (open circles) and after (solid circles) application of the calibration. This example is for 1999p-2000 data.

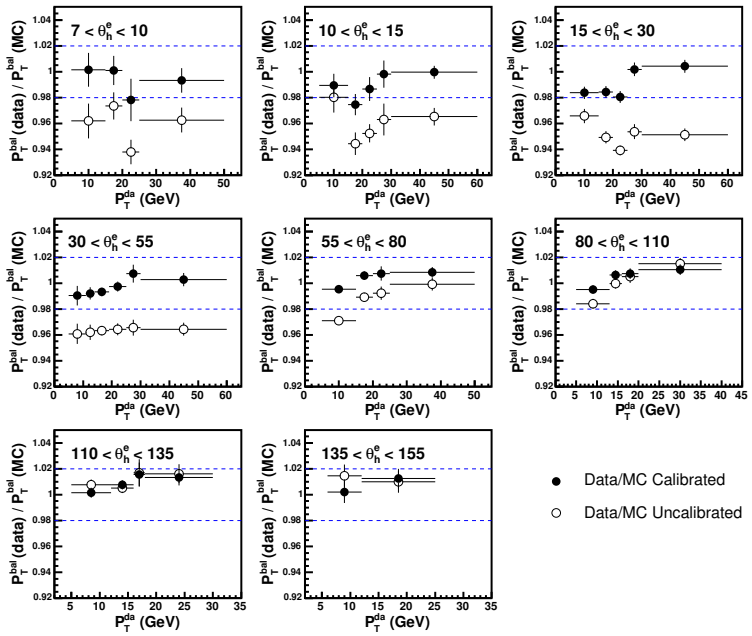

Figure 26: Evolution of the agreement between data and MC P_T^{bal} distributions with P_T^{da} for the inclusive check sample in the different θ_h^e regions. This example is for 1999p-2000 data and RAPGAP Monte Carlo.

5.5 Resolution improvements

Using the inclusive check sample, we can verify the effect of the hadronic calibrations on the resolution of the P_T^h measurement. The evolution of the relative resolutions $\sigma(P_T^{bal})/P_T^{bal}$ as a function of θ_h^e and P_T^{da} is presented in Fig. 27. The resolutions are calculated before and after the application of the jet calibration. In general, the relative resolutions are improved by the calibrations.

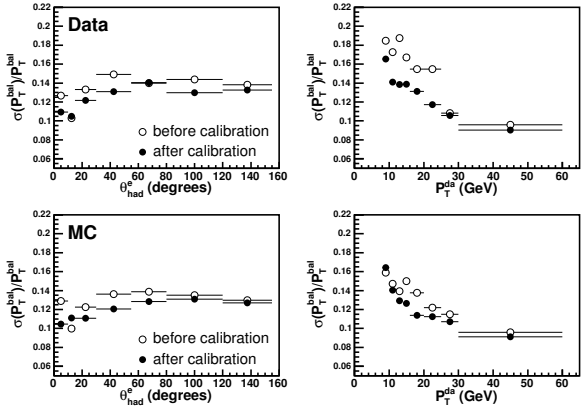

Figure 27: Evolution of the relative resolutions, calculated before and after applying the jet calibrations, as a function of θ_h^e (left) and P_T^{da} (right). The effect on data and MC is presented in upper and bottom figures, respectively.

5.6 Practical implementation in analysis: how to use it ?

This section will be devoted to give an example of the use of the actual jet calibration available in the *H1JetCalibration* package into an H1OO analysis. Indeed the reconstructed hadrons and jets available on μODS are not presently calibrated and each user has to apply by itself the jet calibration in his own analysis. We should here stress that this calibration was only developed for high P_T jets (greater than 10 GeV) and high Q^2 inclusive analyses ($Q^2 > 100$ GeV^2) and it can not be guaranteed that this calibration is working also on low Q^2 events.

The jet calibrations should first be initialised at the beginning of your job (before entering in the event loop) using:

```
H1JetCalibration* JetCalib = new H1JetCalibration;
JetCalib->InitHadroo2KtJetCalibration((int)RunYear,
                                      (int)RunType);
```

The RunType has to be 0 for data and 1 for MC. The available run periods for RunYear are defined as 96-97 = 3, 98-99 = 4 , 99-00 = 5 and 03-04 = 7.

Then inside the event loop, each event has to be calibrated by calling:

```
Int_t nJets=ModsPartJet.GetEntries();
Float_t fPthCalib=0;
Float_t fGammahCalib=0;
Float_t fEmpzhCalib=0;
TLorentzVector* jetscal= new TLorentzVector[nJets];
TLorentzVector HadCalTotVec=
               JetCalib->GetHadroo2KtJetCalibration(fPthCalib,
               fGammahCalib,fEmpzhCalib,jetscal);
delete [] jetscal; //--- after having used it
```

where HadCalTotVec is the four-vector of the calibrated hadronic final state, fPthCalib the calibrated P_T^h, fGammahCalib is θ_h after calibration and fEmpzhCalib the $E - Pz$ of the hadronic system. The calibrated four-vectors of all jets in the events are provided in the array jetscal (note that the user has to take care of deleting properly this array).

The total $E-Pz$ and missing transverse momentum P_T^{miss} of the event (Epz and Ptmiss, respectively) can be re-calculated by adding all isolated identified electrons and muons to the total HFS four-vector with:

```
TLorentzVector TotalVec=HadCalTotVec;
H1PartEmArrayPtr   ModsPartEm;
H1PartMuonArrayPtr ModsPartMuon;
for(Int_t i=0;i<ModsPartEm->GetEntries();i++){
 if(ModsPartEm[i]->IsIsolatedLepton())
     TotalVec+=ModsPartEm[i]->GetFourVector();
}
for(Int_t i=0;i<ModsPartMuon->GetEntries();i++){
 if(ModsPartMuon[i]->IsIsolatedLepton())
     TotalVec+=ModsPartMuon[i]->GetFourVector();
}
Float_t Epz=TotalVec.E()-TotalVec.Pz();
Float_t Ptmiss=TotalVec.Pt();
```

The hadronic kinematic variables can be also re-calculated:

```
Eh =  HadTotVec.E();
Pzh = HadTotVec.Pz();
Pth = HadTotVec.Pt();
Phh = HadTotVec.Phi();
if (Pth>0) Thh = 2*TMath::ATan((Eh-Pzh)/Pth);
Gammah = Thh;
yh  = (Eh-Pzh)/(2*GenPl);
Q2h = (Pth*Pth)/(1-yh);
if(yh!=0) xh = Q2h/(yh*GenS);
```


as well as the kinematic variables from the double angle method:

```
Q2da = 4*pow(GenPl,2)*sin(Gammah)*(1+TMath::Cos(The))
     /(TMath::Sin(Gammah)+TMath::Sin(The)-TMath::Sin(Gammah+The));
xda = (GenPl/GenPp)*(TMath::Sin(Gammah)+TMath::Sin(The)
    +TMath::Sin(Gammah+The))/(TMath::Sin(Gammah)+TMath::Sin(The)
    -TMath::Sin(Gammah+The));
yda = Q2da / (xda*GenS);
Ptda = 2*GenPl/(TMath::Tan(The/2)+((Eh-Pzh)/Pth));
Eda = 2*GenPl*sin(Gammah)/(sin(Gammah)+sin(The)-sin(Gammah+The));
```

where The is the polar angle of the scattered electron and GenPl = 27.598 and GenPp = 919.971 the energies of the incoming lepton and proton beams, respectively.

6 Conclusion

Along this note the motivations and details implemented in the actual Hadroo2 HFS finder have been described. Firstly the distortion in the measurement of the kinematic variables in the low y region was investigated. Inspired by previous FORTRAN implementations, dedicated noise suppression algorithm have been implemented into Hadroo2 to correct this distortion. Detailed checks have shown that these algorithms are working properly and that no signal important to exclusive analyses is suppressed. In a second part, details of the Hadroo2 algorithm and the way track and clusters measurements are chosen and combined were explained. Results of comparisons of Hadroo2 with other HFS reconstruction algorithms were presented. They show that Hadroo2 improves effectively the HFS reconstruction and the resolution, especially in the high P_T domain. Finally, the method of jet calibration available in *H1JetCalibration* was presented. This calibration is applicable for any event samples provided the transverse momentum of either the scattered electron or the hadronic system is larger than 10 GeV. It is available for all running periods, from 1994 to 2004 and checks have shown that the absolute hadronic scale is reached within 2 % and that the systematic errors are of the order of 2 %. Concerning future developments of the HFS reconstruction, it was shown that the application of the new weighting scheme presented in [7, 8] can help for additional improvement of the resolution. Work is also ongoing to extend the actual hadronic calibrations to all events, including low Q^2 ones and to apply it directly to each μODS hadron.

References

[1] M. Peez, "Recherche de déviations au Model Standard dans les processus de grande énergie transverse sur le collisionneur électron - proton HERA", Ph.D. thesis, Université de Lyon (2003), DESY-THESIS-2003-023. (available at http://www-h1.desy.de/psfiles/theses/).

[2] M. Ridel, "Reconstruction of the energy flow and search for squarks and gluinos in the D0 experiment. (In French)," FERMILAB-THESIS-2002-08 (available at http://www.slac.stanford.edu/spires/find/hep/www?r=fermilab-thesis-2002-08).

[3] G.M. Briskin, "Diffractive Dissociation in ep Deep Inelastic Scattering", DESY-THESIS-1998-036.

[4] QHQTRK manual, (Heavy Flavor Working Group track selection code by Lee West).

[5] I. Abt *et al.* [H1 Collaboration], "The H1 detector at HERA," Nucl. Instrum. Meth. A **386** (1997) 310.

[6] S. Hellwig, "Untersuchung der $D^{\star} - \pi_{slow}$ Double Tagging Methode in Chamanalysen", Diplomarbeit, Universität Hamburg (2004).
(available at http://www-h1.desy.de/psfiles/theses/).

[7] C. Issever, K. Borras, D. Wegener, "An Improved Weighting Algorithm to Achieve Software Compensation in a Fine Grained LAr Calorimeter", H1-03/03-608.

[8] M. Ellerbrock, "An Improved Weighting Algorithm to Achieve Software Compensation in a Fine Grained LAr Calorimeter", Ph.D. thesis, Phys. Inst. der Univ. Heidelberg, DESY-THESIS-2004-015. (available at http://www-h1.desy.de/psfiles/theses/).

[9] E. Chabert *et al.*, "QBGFMAR, an updated PHAN package for cosmic and halo muon topological rejection in high P_T physics analysis", H1-11/98-556.

[10] C. Veelken, "H1NonepBgFinder - Rejection of cosmic muon and beam-halo events in the H1OO framework", H1-09/02-603.

[11] J. Cao and Z. Zhang, "Towards an Unbiased Measurement of Kinematic Variables at Low y Region", H1-12/99-580.

[12] M. Jacquet, Z. Zhang *et al.*, "Absolute hadronic jet calibration of the H1 Liquid Argon calorimeter", H1-04/99-571.

[13] S. D. Ellis and D. E. Soper, "Successive Combination Jet Algorithm For Hadron Collisions," Phys. Rev. D **48** (1993) 3160, [arXiv:hep-ph/9305266].

Annexe B

First Measurement of Charged Current Cross Sections at HERA with Longitudinally Polarised Positrons

A. Aktas *et al.* [H1 Collaboration],
Phys. Lett. B **634** (2006) 173,
arXiv:hep-ex/0512060

Abstract

Data taken with positrons of different longitudinal polarisation states in collision with unpolarised protons at HERA are used to measure the total cross sections of the charged current process, $e^+p \to \overline{\nu}X$, for negative four-momentum transfer squared $Q^2 > 400\,\mathrm{GeV}^2$ and inelasticity $y < 0.9$. Together with the corresponding cross section obtained from the previously published unpolarised data, the polarisation dependence of the charged current cross section is measured for the first time at high Q^2 and found to be in agreement with the Standard Model prediction.

1 Introduction

In autumn 2003 the HERA accelerator started operation of the second phase of its ep collider programme. The e^+p data collected by the H1 and ZEUS experiments since then were taken with a longitudinally polarised positron beam for the first time. Measurements of deep inelastic scattering (DIS) with polarised leptons on protons allow the parton distribution functions (PDFs) of the proton to be further constrained through polarisation asymmetries [1] and specific tests of the electroweak (EW) parts of the Standard Model to be performed [2, 3]. In particular, the measurements presented here extend the tests of the $\mathrm{V}-\mathrm{A}$ structure of charged current interactions from low Q^2 [4] into the high Q^2 regime, where Q^2 is the negative four-momentum transfer squared.

At HERA DIS proceeding via charged currents (CC), $ep \to \nu X$, and neutral currents (NC), $ep \to eX$, can be measured accurately [5, 6]. The polarisation dependence of the CC and NC cross sections is fixed within the Standard Model framework. Specifically, the Standard Model predicts, from the absence of right handed charged currents, that the CC e^+p cross section is directly proportional to the fraction of right handed positrons in the beam.

In this paper first measurements of the charged current total cross sections, $\sigma^{\mathrm{tot}}_{\mathrm{CC}}$, are reported for two values of longitudinal polarisation, $P_e = (N_R - N_L)/(N_R + N_L)$, with N_R (N_L) being the number of right (left) handed positrons in the beam. The corresponding data sets are termed the R and L data sets respectively. The R data set has a luminosity weighted mean polarisation value of $(33.6 \pm 0.7)\,\%$ and an integrated luminosity value of $26.9 \pm 0.6\,\mathrm{pb}^{-1}$. The corresponding numbers for the L data set are $(-40.2 \pm 1.1)\,\%$ and $20.7 \pm 0.5\,\mathrm{pb}^{-1}$. In both data sets the incident positron beam energy is $27.5\,\mathrm{GeV}$, whilst the unpolarised proton beam energy is $920\,\mathrm{GeV}$. This yields a centre-of-mass energy of $\sqrt{s} = 318\,\mathrm{GeV}$.

The measurements presented here, as well as the corresponding one obtained using the published unpolarised data, are compared to Standard Model expectations and a linear fit to $\sigma^{\mathrm{tot}}_{\mathrm{CC}}$ as a function of P_e is performed. The result of the fit is used to derive a cross section for a fully left handed positron beam corresponding to $P_e = -1$.

2 Charged Current Cross Section

The measured double differential CC cross section for collisions of polarised positrons with unpolarised protons, corrected for QED radiative effects, may be expressed as

$$\frac{\mathrm{d}^2\sigma_{\mathrm{CC}}}{\mathrm{d}x\mathrm{d}Q^2} = (1+P_e)\frac{G_F^2}{4\pi x}\left[\frac{M_W^2}{M_W^2+Q^2}\right]^2 \left(Y_+ W_2 - Y_- x W_3 - y^2 W_L\right)\cdot(1+\delta^{\mathrm{CC}}_{\mathrm{weak}})\,, \qquad (1)$$

where x is the Bjorken x variable and y characterises the inelasticity of the interaction. The Fermi constant G_F is defined [7] using the weak boson masses. Other quantities in Eq.(1) include M_W, the mass of the W boson, W_2, xW_3 and W_L, CC structure functions, and $\delta^{\mathrm{CC}}_{\mathrm{weak}}$, the weak radiative corrections. The helicity dependences of the weak interaction are contained in $Y_\pm = 1 \pm (1-y)^2$. In the quark parton model (QPM), where $W_L \equiv 0$, the structure functions

W_2 and xW_3 for e^+p scattering may be expressed as the sum and difference of the quark and anti-quark momentum distributions, $xq(x,Q^2)$ and $x\overline{q}(x,Q^2)$:

$$W_2 = x(\ \overline{u} + \overline{c} + d + s)\,, \qquad (2)$$
$$xW_3 = x(-\overline{u} - \overline{c} + d + s)\,. \qquad (3)$$

The total cross section, $\sigma^{\mathrm{tot}}_{\mathrm{CC}}$, is defined as the integrated cross section in the kinematic region $Q^2 > 400\,\mathrm{GeV}^2$ and $y < 0.9$. From Eq.(1) it can be seen that the cross section has a linear dependence on the polarisation of the positron beam P_e. For a fully left handed positron beam, $P_e = -1$, the cross section is identically zero in the Standard Model.

3 Experimental Technique

At HERA transverse polarisation of the positron beam arises naturally through synchrotron radiation via the Sokolov-Ternov effect [8]. In 2000 a pair of spin rotators was installed in the beamline on either side of the H1 detector, allowing transversely polarised positrons to be rotated into longitudinally polarised states and back again. The degree of polarisation is constant around the HERA ring and is continuously measured using two independent polarimeters LPOL [9] and TPOL [10]. The polarimeters are situated in beamline sections in which the beam leptons have longitudinal and transverse polarisations respectively. Both measurements rely on an asymmetry in the energy spectrum of left and right handed circularly polarised photons undergoing Compton scattering with the positron beam. The TPOL measurement uses in addition a spatial asymmetry. The LPOL polarimeter measurements are used when available and TPOL measurements otherwise.

The H1 detector components most relevant to this analysis are the liquid argon (LAr) calorimeter, which measures the positions and energies of charged and neutral particles over the polar[1] angular range $4^\circ < \theta < 154^\circ$, and the inner tracking detectors, which measure the angles and momenta of charged particles over the range $7^\circ < \theta < 165^\circ$. A full description of the detector can be found in [11].

Simulated DIS events are used in order to determine acceptance corrections. DIS processes are generated using the DJANGO [12] Monte Carlo (MC) simulation program, which is based on LEPTO [13] for the hard interaction and HERACLES [14] for single photon emission and virtual EW corrections. LEPTO combines $\mathcal{O}(\alpha_s)$ matrix elements with higher order QCD effects using the colour dipole model as implemented in ARIADNE [15]. The JETSET program [16] is used to simulate the hadronisation process. In the event generation the DIS cross section is calculated using the H1 PDF 2000 [5] parametrisation for the proton PDFs.

The dominant ep background contribution arises from photoproduction processes. These are simulated using the PYTHIA [17] MC with leading order PDFs for the proton taken from CTEQ [18] and for the photon from GRV [19]. Further backgrounds from NC DIS, QED-Compton scattering, lepton pair production, prompt photon production and heavy gauge boson ($W^\pm, Z^0$) production are also simulated; their final contribution to the analysis sample is small. Further details are given in [5].

[1] The polar angle θ is defined with respect to the positive z axis, the direction of the incident proton beam.

The detector response to events produced by the generation programs is simulated in detail using a program based on GEANT [20]. These simulated events are then subjected to the same reconstruction and analysis chain as the data.

The selection of CC interactions follows closely that of the previously published analysis of unpolarised data from H1 [5] and is briefly described below. The CC events are characterised as having large unbalanced transverse momentum, $P_{T,h}$, attributed to the undetected neutrino. The quantity $P_{T,h}$ is determined from $P_{T,h} = \sqrt{(\sum_i p_{x,i})^2 + (\sum_i p_{y,i})^2}$, where the summation is performed over all particles of the hadronic final state. The hadronic final state particles are reconstructed using a combination of tracks and calorimeter deposits in an energy flow algorithm that avoids double counting [21].

The CC kinematic quantities are determined from the hadonic final state [22] using the relations

$$y_h = \frac{E_h - p_{z,h}}{2\,E_e}\,, \qquad Q^2_h = \frac{P^2_{T,h}}{1-y_h}\,, \qquad x_h = \frac{Q^2_h}{s\,y_h}\,, \tag{4}$$

where $E_h - p_{z,h} \equiv \sum_i (E_i - p_{z,i})$ and E_e is the incident positron beam energy.

NC interactions are also studied as they provide an accurate and high statistics data sample with which to check the detector response. The selection of NC interactions is based mainly on the requirement of an identified scattered positron in the LAr calorimeter, with an energy $E'_e > 11\,\mathrm{GeV}$. The NC sample is used to carry out an *in-situ* calibration of the electromagnetic and hadronic energy scales of the LAr calorimeter using the method described in [5]. The hadronic calibration procedure is based on the balance of the transverse energy of the positrons with that of the hadronic final state. The calibration procedure gives good agreement between data and simulation within an estimated uncertainty of 2%.

In addition, NC events are used for studies of systematic uncertainties in the charged current analysis. The data are processed such that all information from the scattered positron is suppressed, providing the so-called *pseudo-CC* sample [21, 23, 24]. This sample mimics CC interactions allowing trigger and selection efficiencies to be checked with high statistical precision and independently of the MC simulation.

4 Measurement Procedure

Candidate CC interactions are selected by requiring $P_{T,h} > 12\,\mathrm{GeV}$ and a reconstructed vertex within $35\,\mathrm{cm}$ in z of the nominal interaction point. In order to ensure high efficiency of the trigger and good kinematic resolution the analysis is further restricted to the domain of $0.03 < y_h < 0.85$. The ep background is dominantly due to photoproduction events, in which the scattered positron escapes undetected in the backward direction and transverse momentum is missing due to fluctuations in the detector response or undetected particles. This background is suppressed exploiting the correlation between $P_{T,h}$ and the ratio V_{ap}/V_p of transverse energy flow anti-parallel and parallel to the hadronic final state transverse momentum vector [21, 23, 24]. The suppression cuts are different for the R and L data sets as the relative photoproduction contributions differ in the two samples. The residual ep background is negligible for most of the measured kinematic domain. The simulation is used to estimate this contribution, which is

subtracted statistically from the CC data sample. Non-ep background is rejected by searching for typical cosmic ray and beam-induced background event topologies [21, 23, 24]. The final R (L) CC data sample amounts to $\simeq 700$ ($\simeq 200$) events.

The $P_{T,h}$ and $E_h - p_{z,h}$ distributions of the selected events are shown in Fig. 1a,b for the R sample and in Fig. 1c,d for the L sample. The simulation provides a good description of the data. The contribution of background photoproduction processes is small and has the largest influence at low $P_{T,h}$.

Events with $Q^2_h > 400\,\mathrm{GeV}^2$ are used to measure the cross sections, which correspond to the kinematic region $Q^2 > 400\,\mathrm{GeV}^2$ and $y < 0.9$ and thus are corrected for the effects of the analysis cuts. The correction factor is calculated to be 1.067 using the H1 PDF 2000 parametrisation.

The systematic uncertainties on the cross section measurements are discussed briefly below (see [21, 23, 24] and references therein for more details). Positive and negative variations of one standard deviation of each error source are found to yield errors which are symmetric to a good approximation. The systematic uncertainties of each source are taken to be fully correlated between the cross section measurements unless stated otherwise.

- An uncertainty of 2% is assigned to the hadronic energy measured in the LAr calorimeter, of which 1% is considered as a correlated component to the uncertainty. This results in a total uncertainty of 1.3% on the cross section measurements.
- A 10% uncertainty is assigned to the amount of energy in the LAr calorimeter attributed to noise, which gives rise to a systematic error of 0.3% on the cross section measurements.
- The variation of cuts against photoproduction on V_{ap}/V_p and $P_{T,h}$ has an effect on the cross sections of 0.6%.
- A 30% uncertainty on the subtracted ep background is determined from a comparison of data and simulation after relaxing the anti-photoproduction cuts, such that the sample is dominated by photoproduction events. This results in a systematic error of 0.5% (1%) on the cross section of the R (L) data.
- The non-ep background finders introduce an inefficiency for CC events. The associated uncertainty is estimated using pseudo-CC data and found to depend on y. An uncertainty of 2% is applied for $y < 0.1$ and 1% for $y > 0.1$. This yields an uncertainty of 1% on the cross section measurements.
- A y-dependent error is assigned to the vertex finding efficiency: 15% for $y < 0.06$, 7% for $0.06 < y < 0.1$, 4% for $0.1 < y < 0.2$ and 1% for $y > 0.2$. This efficiency is estimated using pseudo-CC data yielding an uncertainty of 2.4% on the cross section measurements.
- An uncertainty of 0.5% accounts for the dependence of the acceptance correction on the PDFs used in the MC simulation.
- A 1.8% uncertainty on the trigger efficiency is determined based on the pseudo-CC data sample. The uncorrelated component of this uncertainty is 1%.

- An error of 0.8% is estimated for the QED radiative corrections. This accounts for missing contributions in the simulation of the lowest order QED effects and for the uncertainty on the higher order QED and EW corrections.
- In addition, there is a global uncertainty of 1.3% on the luminosity measurement for both the R and L data samples, of which 0.5% is considered as correlated.

The total systematic error is formed by adding the individual uncertainties in quadrature and amounts to about 4% on the cross section measurements.

The polarisation measurements have a relative uncertainty of 3.5% for the TPOL [25] and 1.6% for the LPOL [9] polarimeter and yield an absolute uncertainty on the mean polarisation of $\pm 0.7\,\%$ for the R sample and $\pm 1.1\,\%$ for the L sample. These are not included in the total systematic error on the cross section measurements, but are considered as independent uncertainties in a linear fit to the data.

5 Results

The measured integrated CC cross sections are quoted in the range $Q^2 > 400\,\mathrm{GeV}^2$ and $y < 0.9$ and are given in Table 1 and shown in Fig. 2. The measurement of the unpolarised total cross section in the same phase space based on $65.2\,\mathrm{pb}^{-1}$ of data collected in 1999 and 2000 is also given. This measurement follows identically the procedure described in [5] but with the Q^2 cut adopted in this analysis. The systematic uncertainties of this unpolarised measurement are taken to be the same as in [5], with the exception of the QED radiative correction uncertainty, which has been reduced from 3% to 0.8%. The measurements are compared to expectations of the Standard Model using the H1 PDF 2000 parametrisation. The uncertainty on the Standard Model expectations combines the uncertainties from experimental data used in the H1 PDF 2000 fit as well as model uncertainties [5].

P_e (%)	$\sigma^{\mathrm{tot}}_{\mathrm{CC}}$ (pb)	SM expectation (pb)
$+33.6$	$35.6 \pm 1.5_{\mathrm{stat}} \pm 1.4_{\mathrm{sys}}$	35.1 ± 0.6
0.0	$28.4 \pm 0.8_{\mathrm{stat}} \pm 0.8_{\mathrm{sys}}$	26.3 ± 0.4
-40.2	$13.9 \pm 1.1_{\mathrm{stat}} \pm 0.6_{\mathrm{sys}}$	15.7 ± 0.3

Table 1: *Measured cross section values for $\sigma^{\mathrm{tot}}_{\mathrm{CC}}(e^+p \to \overline{\nu} X)$ in the region $Q^2 > 400\,\mathrm{GeV}^2$ and $y < 0.9$ compared to the Standard Model (SM) expectation.*

A linear fit to the polarisation dependence of the measured cross sections is performed taking into account the correlated systematic uncertainties between the measurements and is shown in Fig. 2. The fit provides a reasonable description of the data with a $\chi^2 = 4.4$ for one degree of freedom (dof). The result of the fit extrapolated to the point $P_e = -1$ yields a fully left handed charged current cross section of

$$\sigma^{\mathrm{tot}}_{\mathrm{CC}}(P_e = -1) = -3.9 \pm 2.3_{\mathrm{stat}} \pm 0.7_{\mathrm{sys}} \pm 0.8_{\mathrm{pol}}\ \mathrm{pb}\,, \qquad (5)$$

where the quoted errors correspond to the statistical (stat), experimental (sys) and polarisation-related (pol) systematic uncertainties. This extrapolated cross section is consistent with the Standard Model prediction of a vanishing cross section and corresponds to an upper limit on $\sigma^{\mathrm{tot}}_{\mathrm{CC}}(P_e = -1)$ of $1.9\,\mathrm{pb}$ at 95% confidence level (CL), as derived according to [26]. This result excludes the existence of charged currents involving right handed fermions mediated by a boson of mass below $208\,\mathrm{GeV}$ at 95% CL, assuming Standard Model couplings and a massless right handed ν_e.

It is also possible to fit the measured cross sections by constraining the cross section at $P_e = -1$ to zero. This yields a cross section at $P_e = 0$ of $27.5 \pm 0.6_{\mathrm{stat}} \pm 0.9_{\mathrm{sys}}\,\mathrm{pb}$ with a $\chi^2/\mathrm{dof} = 3.5$ and a negligible error due to the uncertainty on the polarisation measurement. The fitted value agrees well with the Standard Model expectation of $26.3 \pm 0.4\,\mathrm{pb}$.

6 Summary

The first measurement has been performed of polarised e^+p total charged current cross sections in the kinematic region of $Q^2 > 400\,\mathrm{GeV}^2$ and $y < 0.9$. The results presented here are based on data collected from collisions of unpolarised protons with unpolarised positrons and, for the first time, with longitudinal polarised positrons in left and right helicity states. The polarisation dependence of the charged current cross section has thus been established at HERA, extending previous tests of the chiral structure of the charged current interaction into the region of large, space-like Q^2. The data are found to be consistent with the absence of right handed charged currents as predicted by the Standard Model.

Acknowledgements

We are grateful to the HERA machine group whose outstanding efforts have made this experiment possible. We thank the engineers and technicians for their work in constructing and maintaining the H1 detector, our funding agencies for financial support, the DESY technical staff for continual assistance and the DESY directorate for support and for the hospitality which they extend to the non DESY members of the collaboration.

References

[1] M. Klein and T. Riemann, Z. Phys. C **24** (1984) 151.

[2] A. Aktas *et al.* [H1 Collaboration], Submitted to Phys. Lett. B [hep-ex/0507080], DESY-05-093.

[3] R. Beyer *et al.*, Proceedings of the Workshop "Future Physics at HERA", vol. 1, eds. W. Buchmüller, G. Ingelman, A. De Roeck and R. Klanner, DESY (1996) 142; R. Cashmore *et al.*, ibid., 163.

[4] M. Jonker *et al.* [CHARM Collaboration], Phys. Lett. B **86** (1979) 229.

[5] C. Adloff *et al.* [H1 Collaboration], Eur. Phys. J. C **30** (2003) 1 [hep-ex/0304003].

[6] C. Adloff *et al.* [H1 Collaboration], Eur. Phys. J. C **21** (2001) 33 [hep-ex/0012053].

[7] A. Arbuzov, D.Y. Bardin, J. Bluemlein, L. Kalinovskaya and T. Riemann, Comput. Phys. Commun. **94**, 128 (1996) [hep-ph/9511434].

[8] A.A. Sokolov and I.M. Ternov, Sov. Phys. Dokl. **8** No. 12 (1964) 1203.

[9] M. Beckmann *et al.*, Nucl. Instrum. Meth. A **479** (2002) 334.

[10] D.P. Barber *et al.*, Nucl. Instrum. Meth. A **329** (1993) 79.

[11] I. Abt *et al.* [H1 Collaboration], Nucl. Instrum. Meth. A **386** (1997) 310 and 348; R.D. Appuhn *et al.* [H1 SPACAL Group], Nucl. Instrum. Meth. A **386** (1997) 397.

[12] G.A. Schuler and H. Spiesberger, Proceedings of the Workshop "Physics at HERA", vol. 3, eds. W. Buchmüller, G. Ingelman, DESY (1992) 1419.

[13] G. Ingelman, Proceedings of the Workshop "Physics at HERA", vol. 3, eds. W. Buchmüller, G. Ingelman, DESY (1992) 1366.

[14] A. Kwiatkowski, H. Spiesberger and H.-J. Möhring, Comput. Phys. Commun. **69** (1992) 155.

[15] L. Lönnblad, Comput. Phys. Commun. **71** (1992) 15.

[16] T. Sjöstrand and M. Bengtsson, Comput. Phys. Commun. **43** (1987) 367.

[17] T. Sjöstrand, Comput. Phys. Commun. **82** (1994) 74.

[18] H.L. Lai *et al.* [CTEQ Collaboration], Eur. Phys. J. C **12** (2000) 375 [hep-ph/9903282].

[19] M. Glück, E. Reya and A. Vogt, Phys. Rev. D **46** (1992) 1973.

[20] R. Brun *et al.*, GEANT3 User's Guide, CERN-DD/EE-84-1 (1987).

[21] B. Portheault, Ph.D. thesis (March 2005), LAL 05-05 (IN2P3/CNRS), Université de Paris-Sud XI, Orsay, available at http://www-h1.desy.de/publications/theses_list.html.

[22] A. Blondel and F. Jacquet, Proceedings of the Study of an ep Facility for Europe, ed. U. Amaldi, DESY (1979) 391.

[23] A. Aktas, Ph.D. thesis (August 2005), Hamburg University, available at http://www-h1.desy.de/publications/theses_list.html.

[24] R. Plačakytė, Ph.D. thesis (*in preparation)*, Max-Planck-Institut für Physik, Munich, will be available at http://www-h1.desy.de/publications/theses_list.html.

[25] W. Lorenzon [HERMES Collaboration], DESY-HERMES-97-68, *7th International Workshop on Polarized Gas Targets and Polarized Beams*, Urbana, IL, 18-22 Aug 1997; F. Corriveau *et al.* [TPOL Polarimeter Group], "A Calibration of the HERA Transverse Polarimeter for the 2003/2004 Data", available at http://www.desy.de/∼pol2000/documents/documents.html.

[26] G.J. Feldman and R.D. Cousins, Phys. Rev. D **57** (1998) 3873 [physics/9711021].

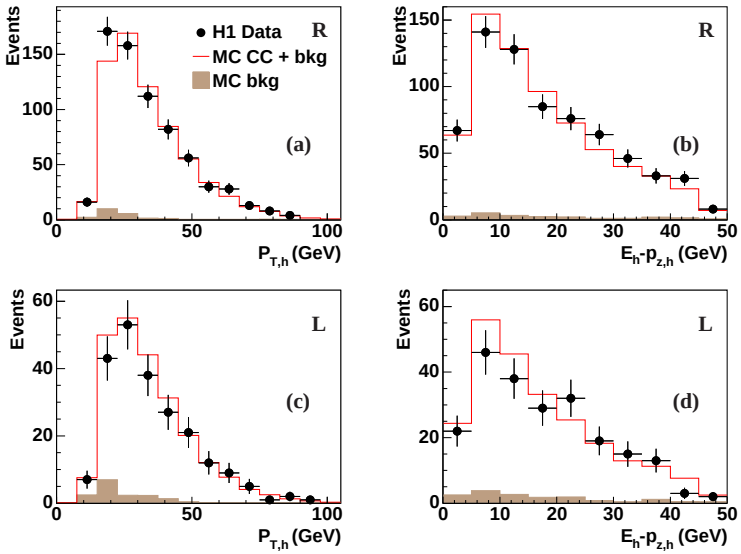

Figure 1: Distributions of $P_{T,h}$ (a,c) and $E_h - p_{z,h}$ (b,d) for the selected events in the right handed (R) and left handed (L) data sets. The Monte Carlo (MC) contributions from the charged current (CC) process and the ep background (bkg) processes are shown as open histograms with the latter contribution alone being shown as shaded histograms.

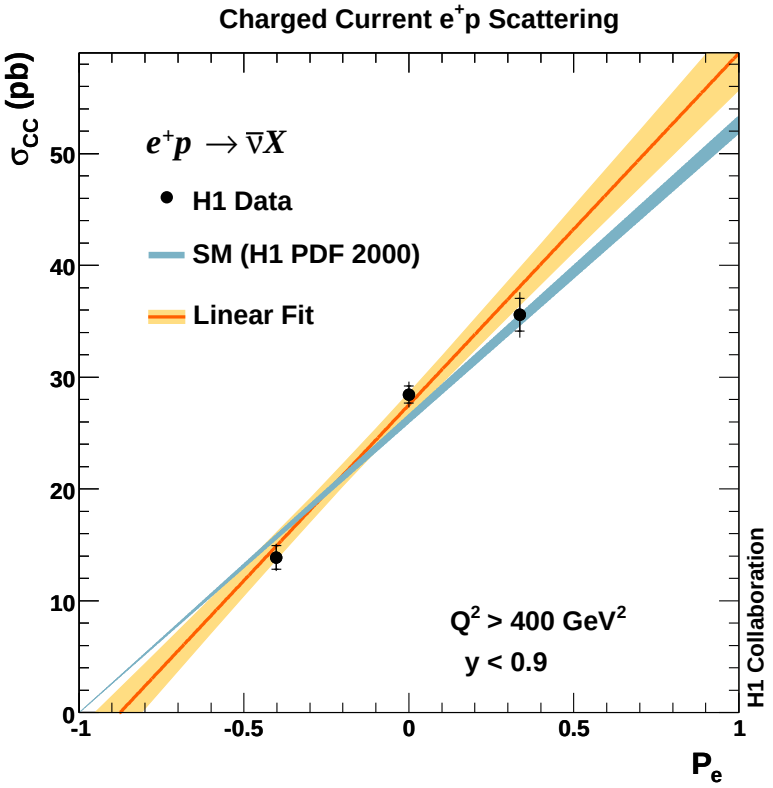

Figure 2: The dependence of the e^+p CC cross section on the lepton beam polarisation P_e. The inner and outer error bars represent respectively the statistical and total errors. The uncertainties on the polarisation measurement are smaller than the symbol size. The data are compared to the Standard Model prediction based on the H1 PDF 2000 parametrisation (dark shaded band). The light shaded band corresponds to the resulting one-sigma contour of a linear fit to the data shown as the central line.

Annexe C

Measurement of Deeply Virtual Compton Scattering and its t-dependence at HERA

F.D. Aaron *et al.* [H1 Collaboration],
Phys. Lett. B **659** (2008) 796,
arXiv:0709.4114

Abstract

A measurement of elastic deeply virtual Compton scattering $\gamma^* p \to \gamma p$ using $e^- p$ collision data recorded with the H1 detector at HERA is presented. The analysed data sample corresponds to an integrated luminosity of 145 pb^{-1}. The cross section is measured as a function of the virtuality Q^2 of the exchanged photon and the centre-of-mass energy W of the $\gamma^* p$ system in the kinematic domain $6.5 < Q^2 < 80$ GeV^2, $30 < W < 140$ GeV and $|t| < 1$ GeV^2, where t denotes the squared momentum transfer at the proton vertex. The cross section is determined differentially in t for different Q^2 and W values and exponential t-slope parameters are derived. The measurements are compared to a NLO QCD calculation based on generalised parton distributions. In the context of the dipole approach, the geometric scaling property of the DVCS cross section is studied for different values of t.

1 Introduction

Measurements of inclusive deep-inelastic scattering (DIS) of leptons and nucleons allow the extraction of Parton Distribution Functions (PDFs) which describe the fraction of the longitudinal momentum of the nucleon carried by the quarks, anti-quarks and gluons. A shortfall of this approach is that the PDFs contain information neither on the correlations between partons nor on their transverse distributions. This missing information can be provided by measurements of processes in which the nucleon remains intact and the four momentum transfer squared at the nucleon vertex, t, is non-zero [1–6]. The simplest such reaction is deeply virtual Compton scattering (DVCS), the diffractive scattering of a virtual photon off a proton $\gamma^* p \to \gamma p$. In high energy electron-proton collisions at HERA, DVCS is accessed through the reaction $ep \to e\gamma p$ [7–9]. This reaction also receives a contribution from the purely electromagnetic Bethe-Heitler (BH) process, where the photon is emitted from the electron. The BH cross section is precisely calculable in QED and can be subtracted from the total process rate to extract the DVCS cross section.

Perturbative QCD calculations assume that the DVCS reaction involves two partons in the proton which carry different longitudinal and transverse momenta. The difference in longitudinal momentum of the two involved partons, also called skewing, is a consequence of the mass difference between the incoming virtual photon and the outgoing real photon. The skewing can be described by introducing generalised parton distributions (GPDs) [1–5], which are functions of the two unequal momenta and thus encode information on the longitudinal momentum correlations of partons. Information on the transverse momentum of partons is incorporated in the t-dependence of GPDs [2–5]. The t-dependent functions follow particular equations for their evolution as a function of the four momentum transfer squared Q^2 of the exchanged virtual photon [3–5]. These evolution equations still need to be tested.

The DVCS cross section can also be interpreted within the dipole model [10–12]. In this picture the virtual photon fluctuates into a colour singlet $q\bar{q}$ pair (or dipole) of a transverse size $r \sim 1/Q$, which subsequently undergoes hard scattering with the gluons in the proton [13]. At very small values of the Bjorken scaling variable x the saturation regime of QCD can be reached. In this domain, the gluon density in the proton is so large that non-linear effects like gluon recombination tame its growth. In the dipole model approach, the transition to the saturation regime is characterised by the so-called saturation scale parametrised here as $Q_s(x) = Q_0(x_0/x)^{-\lambda/2}$, where Q_0, x_0 and λ are parameters [14]. The transition to saturation occurs when Q becomes comparable to $Q_s(x)$. An important feature of dipole models that incorporate saturation is that the total cross section can be expressed as a function of the single variable τ:

$$\sigma_{tot}^{\gamma^* p}(x, Q^2) = \sigma_{tot}^{\gamma^* p}(\tau), \quad \text{with} \quad \tau = \frac{Q^2}{Q_s^2(x)}. \tag{1}$$

This property, called geometric scaling, has already been observed to hold for the total ep DIS cross section [15, 16] as well as in DIS on nuclear targets [17] and in diffractive processes [12]. It has also recently been addressed in the context of exclusive processes including DVCS [12] and extended to cases with non-zero momentum transfer to the proton [18].

This paper presents a new measurement of single and double differential DVCS cross sections as a function of Q^2 and the $\gamma^* p$ centre-of-mass energy W. The single differential cross section $d\sigma/dt$ is also extracted. The data were recorded in the years 2005 and 2006 with the H1 detector when HERA collided protons of 920 GeV energy with 27.6 GeV electrons. The sample corresponds to an integrated luminosity of 145 pb^{-1}, four times larger than the previous H1 measurement [8] of DVCS in positron-proton collisions. The measurement is carried out in the kinematic range $6.5 < Q^2 < 80$ GeV^2, $30 < W < 140$ GeV and $|t| < 1$ GeV^2. The t-dependence of the DVCS cross section, $d\sigma/dt$, is found to be well approximated by an exponential form $e^{-b|t|}$; this parametrisation is used throughout the paper. The Q^2 and W dependences of b are studied. A parametrisation of the observed Q^2 dependence of b is used to constrain the normalisation of the pQCD predictions based on GPDs. The validity of the skewed evolution equations is tested. The geometric scaling property of DVCS is also investigated and the cross section is compared with dipole model predictions. The scaling property is studied for the first time for different values of t.

2 Experimental Conditions and Monte Carlo Simulation

A detailed description of the H1 detector can be found in [19]. Here, only the detector components relevant for the present analysis are described. H1 uses a right-handed coordinate system with the z axis along the beam direction, the $+z$ or "forward" direction being that of the outgoing proton beam. The polar angle θ is defined with respect to the z axis and the pseudo-rapidity is given by $\eta = -\ln\tan\theta/2$. The SpaCal [20], a lead scintillating fibre calorimeter, covers the backward region ($153^\circ < \theta < 176^\circ$). Its energy resolution for electromagnetic showers is $\sigma(E)/E \simeq 7.1\%/\sqrt{E/\text{GeV}} \oplus 1\%$. The liquid argon (LAr) calorimeter ($4^\circ \leq \theta \leq 154^\circ$) is situated inside a solenoidal magnet. The energy resolution for electromagnetic showers is $\sigma(E)/E \simeq 11\%/\sqrt{E/\text{GeV}}$ as obtained from test beam measurements [21]. The main component of the central tracking detector is the central jet chamber CJC ($20^\circ < \theta < 160^\circ$) which consists of two coaxial cylindrical drift chambers with wires parallel to the beam direction. The measurement of charged particle transverse momenta is performed in a magnetic field of 1.16 T, which is uniform over the full tracker volume. The innermost proportional chamber CIP ($9^\circ < \theta < 171^\circ$) is used in this analysis to complement the CJC in the backward region for the reconstruction of the interaction vertex. The forward muon detector (FMD) consists of a series of drift chambers covering the range $1.9 < \eta < 3.7$. Primary particles produced at larger η can be detected indirectly in the FMD if they undergo a secondary scattering with the beam pipe or other adjacent material. Therefore, the FMD is used in this analysis to provide an additional veto against inelastic or proton dissociative events. The luminosity is determined from the rate of Bethe-Heitler processes measured using a calorimeter located close to the beam pipe at $z = -103$ m in the backward direction.

A dedicated event trigger was set up for this analysis. It is based on topological and neural network algorithms and uses correlations between electromagnetic energy deposits of electrons or photons in both the LAr and the SpaCal [26]. The combined trigger efficiency is close to 100%.

Monte Carlo (MC) simulations are used to estimate the background contributions and the corrections that must be applied to the data to account for the finite acceptance and the resolution of the detectors. Elastic DVCS events in ep collisions are generated using the Monte Carlo

generator MILOU [22], based on the cross section calculation from [23] and using a t-slope parameter $b = 5.45$ GeV^{-2}, as determined in this analysis (see section 5.1). Inelastic DVCS events in which the proton dissociates into a baryonic system Y are also simulated with MILOU setting the t-slope b_{pdiss} to 1.2 GeV^{-2}, as determined in a dedicated study (see section 3). The Monte Carlo program COMPTON 2.0 [24] is used to simulate elastic and inelastic BH events. The background source of diffractive meson events is simulated using the DIFFVM Monte Carlo [25]. All generated events are passed through a detailed simulation of the H1 detector and are subject to the same reconstruction and analysis chain as the data.

3 Event Selection

In elastic DVCS events, the scattered electron and the photon are the only particles that should give signals in the detector [8]. The scattered proton escapes undetected through the beam pipe. The selection of the analysis event sample requires the scattered electron to be detected in the SpaCal and the photon in the LAr. The energy of the scattered electron candidate must be greater than 15 GeV. The photon is required to have a transverse momentum P_T above 2 GeV and a polar angle between 25° and 145°. Events are selected if there are either no tracks at all or a single central track which is associated with the scattered electron. In order to reject inelastic and proton dissociation events, no further energy deposit in the LAr calorimeter larger than 1 GeV is allowed and no activity above the noise level should be present in the FMD. The influence of QED radiative corrections is reduced by the requirement that the longitudinal momentum balance $E - P_z$ be greater than 45 GeV. Here, E denotes the energy and P_z the momentum along the beam axis of all measured final state particles. To enhance the DVCS signal with respect to the BH contribution and to ensure a large acceptance, the kinematic domain is restricted to $6.5 < Q^2 < 80$ GeV^2 and $30 < W < 140$ GeV.

The selected analysis sample contains 2538 events. It is dominated by elastic DVCS events, but also contains contributions from the elastic BH process and from the BH and DVCS processes with proton dissociation, $e^- p \to e^- \gamma Y$, where the baryonic system Y of mass M_Y is undetected. These background contributions are studied in further detail. A control sample of BH events is selected. For this sample, it is required that the electron be detected in the LAr and the photon in the SpaCal (see [8] for more details). The COMPTON MC describes accurately the normalisation and the shapes of the distributions of the kinematic variables for these events. The deviations are within 3%, and this value is used subsequently as an estimate for the systematic uncertainty on this contribution. A second control sample dominated by inelastic BH and DVCS processes is obtained by selecting events with a signal in the FMD. After subtracting the inelastic BH contribution, as estimated from the COMPTON MC, this sample allows the normalisation of the inelastic DVCS process to be determined. Within the model used in MILOU [22], the normalisation of the inelastic contribution is directly related to the exponential t-slope parameter. The measured event yield corresponds to an exponential t distribution with a slope of 1.2 GeV^{-2} which is subsequently used in the simulation of inelastic DVCS events. The corresponding contribution of proton dissociation in the analysis event sample is found to be 16 ± 5%. Other backgrounds from diffractive ω and ϕ production with decay modes to final states including photons are estimated to be negligible in the kinematic range of the analysis.

Contamination from processes with low multiplicity π^0 production was also investigated and found to be negligible.

The reconstruction method for the kinematic variables Q^2, x and W relies on the measured polar angles of the final state electron and photon (double angle method) [8]. The variable t is approximated by the negative square of the transverse momentum of the outgoing proton. The latter is computed from the vector sum of the transverse momenta of the final state photon $\vec{P}_{T_\gamma}$ and of the scattered electron $\vec{P}_{T_e}$: $t \simeq -|\vec{P}_{T_\gamma} + \vec{P}_{T_e}|^2$. The resolution of the t reconstruction lies in the range 0.08 to 0.22 GeV^2.

Distributions of selected kinematic variables are presented in figure 1 for the analysis sample. The MC expectations of the different processes are also displayed. Each source is normalised to the data luminosity. A good description of the shape and normalisation of the measured distributions is observed.

4 Cross Section Determination and Systematic Uncertainties

The DVCS and BH contributions dominate in the analysis phase space. In addition, an interference term contributes to the cross section due to the identical final states of both processes. In the leading twist approximation, the main contribution resulting from the interference of the BH and DVCS processes is proportional to the cosine of the azimuthal angle of the photon[1] [1, 27]. Since the present measurement is integrated over this angle, the contribution of the interference term is estimated to be small (below 1%). The DVCS cross section, $\gamma^* p \to \gamma p$, is evaluated in each bin i with the bin centre values Q_i^2, W_i, t_i, from the total number $N_i^{\rm obs}$ of data events in the analysis sample using the expression

$$\sigma_{DVCS}(Q_i^2, W_i, t_i) = \frac{(N_i^{\rm obs} - N_i^{\rm BH} - N_i^{\rm p-diss})}{N_i^{\rm DVCS}} \cdot \sigma^{\rm th}_{DVCS}(Q_i^2, W_i, t_i). \qquad (2)$$

The other numbers in this equation are calculated using the MC simulations described in section 2. $N_i^{\rm BH}$ denotes the number of BH events (elastic and inelastic) reconstructed in bin i, $N_i^{\rm p-diss}$ the number of inelastic DVCS background events, $N_i^{\rm DVCS}$ the number of DVCS events computed from the elastic DVCS MC and $\sigma^{\rm th}_{DVCS}$ is the theoretical DVCS cross section used for the generation of DVCS MC events. The measured cross section is thus directly corrected for detector inefficiencies and acceptances and is expressed at each bin centre value.

The mean value of the acceptance, defined as the number of MC events reconstructed in a bin divided by the number of events generated in the same bin, is 45% over the whole kinematic range and reaches 78% for the highest t bin. The systematic errors of the measured DVCS cross section are determined by repeating the analysis after applying to the MC appropriate variations for each systematic source. The main contribution comes from the acceptance correction factors calculated by varying the t-slope parameter set in the elastic DVCS MC by ± 8%. The uncertainty on the number of elastic DVCS events lost by the application of the FMD veto is

[1] The azimuthal angle of the photon is defined in the proton rest frame as the angle between the plane formed by the incoming and scattered electron and that formed by the virtual photon and the scattered proton.

modelled by a 4% variation of the FMD efficiency. Both error sources together result in an error of 10% on the measured elastic DVCS cross section. The uncertainty related to the inelastic DVCS background is estimated from the variation of its t-slope parameter by 25% around the nominal value of $b = 1.2$ GeV^{-2}. The resulting error on the cross section amounts to 5% on average and reaches 15% at high t. The uncertainties related to trigger efficiency, photon identification efficiency, radiative corrections and the subtraction of BH background and luminosity measurement are each in the range of 2 to 4%. The total systematic uncertainty of the cross section amounts to about 15% and is dominated by correlated errors.

5 Results and Interpretations

5.1 Cross Sections and t-dependence

The complete DVCS sample is used to extract the W dependence of the DVCS cross section expressed at $Q^2 = 8$ GeV^2 as well as the Q^2 dependence at $W = 82$ GeV. The results are displayed in figure 2 and are in agreement within errors with the previous measurements [8, 9]. The steep rise of the cross section with W is an indication of the presence of a hard underlying process [28]. The corresponding cross section measurements are shown in table 1.

Next, the W dependence of the DVCS cross section is determined for three separate ranges of Q^2 and shown in figure 3(a). The corresponding cross section measurements are given in table 2. A fit of the form W^δ is performed to the cross section in each Q^2 range. Figure 3(b) presents the δ values obtained as a function of Q^2. It is observed that δ is independent of Q^2 within the errors. Using the complete analysis sample, the value of δ expressed at $Q^2 = 8$ GeV^2 is found to be $0.74 \pm 0.11 \pm 0.16$, where the first error is statistical and the second systematic.

The differential cross section as a function of t is displayed in figures 4(a) and (b) for three values of Q^2 and W, respectively. Fits of the form $d\sigma/dt \sim e^{-b|t|}$ are performed taking into account the statistical and correlated systematic errors; they describe the data well. The derived t-slope parameters $b(Q^2)$ and $b(W)$ are displayed in figures 4(c) and (d), respectively. The cross section values and the results for b in each Q^2 and W bin are given in table 3. This analysis extends the study of the evolution of b with Q^2 to larger values than in the previous H1 measurement [8]. This Q^2 dependence can be parametrised [30] as

$$b(Q^2) = A\left(1 - B\log(Q^2/(2\text{ GeV}^2))\right). \tag{3}$$

Fitting this function to the measured b values of the present data and to the value obtained at $Q^2 = 4$ GeV^2 in the previous H1 publication [8] yields $A = 6.98 \pm 0.54$ GeV^2 and $B = 0.12 \pm 0.03$. The systematic errors and their point to point correlations were taken into account in the fit, resulting in a correlation coefficient between A and B of $\rho_{AB} = 0.92$. As shown in figure 4(c) the fit function provides a good description of the measured b values over the whole Q^2 range. The values of b as a function of W are measured for the first time and shown in figure 4(d). No significant variation of b with W is observed.

Using the complete analysis sample, the value of b expressed at $Q^2 = 8$ GeV^2 is found to be $5.45 \pm 0.19 \pm 0.34$ GeV^{-2}, where the first error is statistical and the second systematic. Following [2, 6], this t-slope value can be converted to an average impact parameter of

$\sqrt{< r_T^2 >} = 0.65 \pm 0.02$ fm. It corresponds to the transverse extension of partons, dominated by sea quarks and gluons for an average value $x = 1.2\ 10^{-3}$, in the plane perpendicular to the direction of motion of the proton. This value is related to the size of the core of the proton with no account of the peripheral soft structure.

5.2 QCD Interpretation in Terms of GPDs

The determination of $b(Q^2)$ described above can be used to study the Q^2 evolution of the GPDs. The DVCS cross section integrated over the momentum transfer t can be written [23] as

$$\sigma_{DVCS}(Q^2, W) \equiv \frac{\left[\mathcal{I}mA(\gamma^* p \to \gamma p)_{t=0}(Q^2, W)\right]^2 (1+\rho^2)}{16\pi\, b(Q^2, W)}\,, \tag{4}$$

where $\mathcal{I}mA(\gamma^* p \to \gamma p)_{t=0}(Q^2, W)$ is the imaginary part of the $\gamma^* p \to \gamma p$ scattering amplitude at $t = 0$ and ρ^2 is a small correction due to the real part of the amplitude. In the following, ρ is determined from dispersion relations [11] to be $\rho = \tan(\frac{\pi}{2}\omega(Q^2))$. The coefficient $\omega(Q^2)$ describes the power governing the W dependence of DVCS at a given Q^2. It is taken from the corresponding power of the rapid rise of the proton structure function F_2 at low x ($F_2 \sim x^{-\omega}$) [31], assuming that it is sufficiently close to the one in DVCS. In the GPD formalism, the amplitude $A(\gamma^* p \to \gamma p)_{t=0}$ is directly proportional to the GPDs. As shown in the previous section, the Q^2 dependence of the t-slope b is non-negligible. Therefore, the Q^2 evolution of the GPDs themselves is accessed by removing this variation of $b(Q^2)$. For this purpose, the dimensionless observable S is defined as

$$S = \sqrt{\frac{\sigma_{DVCS}\, Q^4\, b(Q^2)}{(1+\rho^2)}}\,. \tag{5}$$

Using the parametrisation (3) for $b(Q^2)$, S is then calculated for each Q^2 bin from the cross section measurements of this analysis (table 1) and from those of the previous H1 publication [8]. The uncertainties on the parameters A and B of (3) are directly propagated to determine the error on $b(Q^2)$ at any given Q^2 value. The results for S are presented in figure 5(a) together with the prediction of a GPD model [30], based on the PDFs parametrisation given in [32]. It is observed that the pQCD skewed evolution equations [3–5] provide a reasonable description of the measured weak rise of S with Q^2.

The magnitude of the skewing effects present in the DVCS process can be extracted by constructing the ratio of the imaginary parts of the DVCS and DIS amplitudes. At leading order in α_s, this ratio $R \equiv \mathcal{I}m\, A\,(\gamma^* p \to \gamma p)_{t=0} / \mathcal{I}m\, A\,(\gamma^* p \to \gamma^* p)_{t=0}$ is equal to the ratio of the GPDs to the PDFs. The virtual photon is assumed to be mainly transversely polarised in the case of the DVCS process due to the real photon in the final state and therefore has to be taken as transversely polarised in the DIS amplitude too. The expression for R as a function of the measured observables can be written as

$$R = \frac{4\sqrt{\pi\, \sigma_{DVCS}\, b(Q^2)}}{\sigma_T(\gamma^* p \to X)\sqrt{(1+\rho^2)}} = \frac{\sqrt{\sigma_{DVCS}\, Q^4\, b(Q^2)}}{\sqrt{\pi^3}\,\alpha_{EM} F_T(x, Q^2)\sqrt{(1+\rho^2)}}\,, \tag{6}$$

using the relation $\sigma_T(\gamma^* p \to X) = 4\pi^2 \alpha_{EM} F_T(x,Q^2)/Q^2$ with $\alpha_{EM} = 1/137$. R is evaluated taking $F_T = F_2 - F_L$ from the QCD analysis presented in [33] and using the parametrisation (3) for $b(Q^2)$. The measured values of the ratio R for each Q^2 bin are shown in figure 5(b) and compared with the calculation based on the GPD model proposed in [30]. The typical values of R are around 2, whereas in a model without skewing R would be equal to unity. Therefore, the present measurement confirms the large effect of skewing. In GPD models, two different effects contribute to skewing [3–5]: the kinematics of the DVCS process and the Q^2 evolution of the GPDs. The data are compared to a model which takes only the former effect into account. The result of this incomplete model is represented by a dotted line in figure 5(b). The present measurements show that such an approximation is not sufficient to reproduce the total skewing effects observed in the data.

5.3 Geometric Scaling

As discussed in section 1, the dipole model represents another possible theoretical approach to describe the DVCS reaction. It is therefore interesting to test if the present DVCS measurements obey the geometric scaling laws predicted by such models.

In the following study parameters of the dipole model are taken from an analysis of the total DIS cross section [14, 18]. The saturation scale $Q_s(x) = Q_0(x_0/x)^{-\lambda/2}$ is evaluated using $Q_0 = 1$ GeV, $\lambda = 0.25$ and $x_0 = 2.7\ 10^{-5}$. The DVCS cross section measurements listed in table 2 and those from the previous H1 publication [8] which are measured at different Q^2 and $x = Q^2/W^2$ values can be represented as a function of the single variable τ (see equation (1)). The result is shown in figure 6(a). All of the cross section measurements appear to be well aligned on a single curve as a function of τ. Therefore the DVCS data are compatible with the geometric scaling law. The dipole model of [12, 14] is also represented in figure 6(a) and gives a good description of the cross section measurements over the complete range of τ.

The dependence of the DVCS cross section on τ is also studied at four different values of t. For this purpose, the cross section is measured differentially in t for three values of W and two ranges of Q^2 ($6.5 < Q^2 < 11$ GeV^2 and $11 < Q^2 < 80$ GeV^2), as listed in table 4. Keeping the same parameters Q_0, λ and x_0 as previously defined, each value of the differential cross section is again represented as a function of τ. The results are shown in figure 6(b), together with the predictions of the dipole model [12, 14]. For these predictions, the t-dependence is factorised out as $e^{-b|t|}$, where the global t-slope parameter b measured in section 5.1 is used. A reasonable description of the DVCS cross section values in the four t bins is observed, with the same saturation scale $Q_s(x)$ used in all cases.

6 Conclusion

The cross section for deeply virtual Compton scattering $\gamma^* p \to \gamma p$ has been measured with the H1 detector at HERA. The analysis uses the $e^- p$ data recorded in 2005 and 2006 corresponding to a luminosity of 145 pb^{-1}, four times larger than in the previous H1 publication [8]. The measurement is performed in the kinematic range $6.5 < Q^2 < 80$ GeV^2, $30 < W < 140$ GeV and $|t| < 1$ GeV^2.

The W dependence of the cross section is well described by a function W^δ. No significant variation of the exponent δ as a function of Q^2 is observed. For the total sample a value $\delta = 0.74 \pm 0.11 \pm 0.16$ is determined. The steep rise of the cross section with W indicates a hard underlying process. The t-dependence of the cross section is well described by the form $e^{-b|t|}$ with an average slope of $b = 5.45 \pm 0.19 \pm 0.34$ GeV^{-2}. This value corresponds to a transverse extension of sea quarks and gluons in the proton of $\sqrt{< r_T^2 >} = 0.65 \pm 0.02$ fm. The t-slopes are determined for the first time differentially in W with no significant dependence observed. The study of the Q^2 dependence of b is extended to significantly larger Q^2 values compared to previous measurements. The slopes found in the present analysis and in the previous H1 publication are in agreement with a slow decrease of b as a function of Q^2.

The measurement of $b(Q^2)$ obtained in the present analysis is used to constrain the normalisation and Q^2 dependence of theoretical predictions based on GPDs. It is found that a GPD model reproduces well both the DVCS amplitude and its weak rise with Q^2. The skewing effects have been investigated and are found to be large, as expected in GPD models. Another approach based on a dipole model including saturation effects predicts that the cross section can be approximated by a function of the single variable, $\tau = Q^2/Q_s^2(x)$ where $Q_s(x)$ is the saturation scale. The present measurement of the DVCS cross section is found to be compatible with such a geometric scaling using the same parameters as derived from inclusive DIS. For the first time, this scaling property is observed for different values of t.

Acknowledgements

We are grateful to the HERA machine group whose outstanding efforts have made this experiment possible. We thank the engineers and technicians for their work in constructing and maintaining the H1 detector, our funding agencies for financial support, the DESY technical staff for continual assistance and the DESY directorate for the hospitality which they extend to the non DESY members of the collaboration. We would like to thank Markus Diehl for helpful discussions.

References

[1] M. Diehl, T. Gousset, B. Pire and J. P. Ralston, Phys. Lett. B **411** (1997) 193 [hep-ph/9706344].

[2] M. Burkardt, Int. J. Mod. Phys. A **18** (2003) 173 [hep-ph/0207047].

[3] M. Diehl, Eur. Phys. J. C **25** (2002) 223 [Erratum-ibid. C **31** (2003) 277] [hep-ph/0205208].

[4] K. Kumerički, D. Müller and K. Passek-Kumerički, hep-ph/0703179.

[5] V. Guzey and T. Teckentrup, Phys. Rev. D **74** (2006) 054027 [hep-ph/0607099].

[6] L. Frankfurt, M. Strikman and C. Weiss, Ann. Rev. Nucl. Part. Sci. **55** (2005) 403 [hep-ph/0507286].

[7] C. Adloff *et al.* [H1 Collaboration], Phys. Lett. B **517** (2001) 47 [hep-ex/0107005].

[8] A. Aktas *et al.* [H1 Collaboration], Eur. Phys. J. C **44** (2005) 1 [hep-ex/0505061].

[9] S. Chekanov *et al.* [ZEUS Collaboration], Phys. Lett. B **573** (2003) 46 [hep-ex/0305028].

[10] A. Donnachie and H. G. Dosch, Phys. Lett. B **502** (2001) 74 [hep-ph/0010227].

[11] L. Favart and M. V. T. Machado, Eur. Phys. J. C **29** (2003) 365 [hep-ph/0302079].

[12] C. Marquet and L. Schoeffel, Phys. Lett. B **639** (2006) 471 [hep-ph/0606079].

[13] A. H. Mueller, Nucl. Phys. B **335** (1990) 115;
N. N. Nikolaev and B. G. Zakharov, Z. Phys. C **49** (1991) 607.

[14] E. Iancu, K. Itakura and S. Munier, Phys. Lett. B **590** (2004) 199 [hep-ph/0310338].

[15] K. Golec-Biernat and M. Wüsthoff, Phys. Rev. D **59** (1999) 014017 [hep-ph/9807513].

[16] A. M. Staśto, K. Golec-Biernat and J. Kwieciński, Phys. Rev. Lett. **86** (2001) 596 [hep-ph/0007192].

[17] A. Freund, K. Rummukainen, H. Weigert and A. Schäfer, Phys. Rev. Lett. **90** (2003) 222002 [hep-ph/0210139].

[18] C. Marquet, R. Peschanski and G. Soyez, hep-ph/0702171.

[19] I. Abt *et al.* [H1 Collaboration], Nucl. Instrum. Meth. A **386** (1997) 310;
I. Abt *et al.* [H1 Collaboration], Nucl. Instrum. Meth. A **386** (1997) 348.

[20] R. D. Appuhn *et al.* [H1 SPACAL Group], Nucl. Instrum. Meth. A **386** (1997) 397.

[21] B. Andrieu *et al.* [H1 Calorimeter Group], Nucl. Instrum. Meth. A **350** (1994) 57.

[22] E. Perez, L. Schoeffel and L. Favart, hep-ph/0411389.

[23] L. L. Frankfurt, A. Freund and M. Strikman, Phys. Rev. D **58** (1998) 114001 [Erratum-ibid. D **59** (1999) 119901] [hep-ph/9710356].

[24] A. Courau, S. Kermiche, T. Carli and P. Kessler, *Quasi-Real QED Compton Monte Carlo, Proceedings of the Workshop on Physics at HERA*, Vol. 2: 902-915, Hamburg 1991.

[25] B. List, A. Mastroberardino, *DIFFVM: A Monte Carlo generator for diffractive processes in ep scattering, Proceedings of the Monte Carlo Generators for HERA physics*, DESY-PROC-1999-02, p. 396.

[26] B. Roland, "Mesure de la Diffusion Compton à Haute Virtualité à HERA II", Ph.D. thesis, Université libre de Bruxelles (2007) (in preparation, to appear at http://www-h1.desy.de/psfiles/theses/).

[27] A. V. Belitsky, D. Müller and A. Kirchner, Nucl. Phys. B **629** (2002) 323 [hep-ph/0112108].

[28] I. P. Ivanov, N. N. Nikolaev and A. A. Savin, Phys. Part. Nucl. **37** (2006) 1 [hep-ph/0501034].

[29] W. M. Yao *et al.* [Particle Data Group], J. Phys. G **33** (2006) 1.

[30] A. Freund, Phys. Rev. D **68** (2003) 096006 [hep-ph/0306012].

[31] C. Adloff *et al.* [H1 Collaboration], Phys. Lett. B **520** (2001) 183 [hep-ex/0108035].

[32] J. Pumplin, D. R. Stump, J. Huston, H. L. Lai, P. Nadolsky and W. K. Tung, JHEP **0207** (2002) 012 [hep-ph/0201195].

[33] C. Adloff *et al.* [H1 Collaboration], Eur. Phys. J. C **21** (2001) 33 [hep-ex/0012053].

Q^2 [GeV^2]	σ_{DVCS} [nb]		
8.75	3.59	$\pm$ 0.21	$\pm$ 0.41
15.5	1.38	$\pm$ 0.10	$\pm$ 0.21
25	0.58	$\pm$ 0.09	$\pm$ 0.09
55	0.13	$\pm$ 0.03	$\pm$ 0.04

W [GeV]	σ_{DVCS} [nb]		
45	2.91	$\pm$ 0.20	$\pm$ 0.25
70	3.96	$\pm$ 0.32	$\pm$ 0.37
90	4.78	$\pm$ 0.41	$\pm$ 0.57
110	5.55	$\pm$ 0.57	$\pm$ 0.88
130	6.56	$\pm$ 1.17	$\pm$ 1.77

Table 1: The DVCS cross section $\gamma^* p \to \gamma p$, σ_{DVCS}, as a function of Q^2 for $W = 82\,\mathrm{GeV}$ and as a function of W for $Q^2 = 8\,\mathrm{GeV}^2$, both for $|t| < 1\,\mathrm{GeV}^2$. The first errors are statistical, the second systematic.

	σ_{DVCS} [nb]								
W [GeV]	$Q^2 = 8$ GeV^2			$Q^2 = 15.5$ GeV^2			$Q^2 = 25$ GeV^2		
45	2.60	$\pm$ 0.24	$\pm$ 0.24	0.94	$\pm$ 0.10	$\pm$ 0.10	0.35	$\pm$ 0.13	$\pm$ 0.07
70	3.15	$\pm$ 0.40	$\pm$ 0.33	1.54	$\pm$ 0.17	$\pm$ 0.14	0.36	$\pm$ 0.10	$\pm$ 0.05
90	5.25	$\pm$ 0.55	$\pm$ 0.55	0.95	$\pm$ 0.20	$\pm$ 0.17	0.83	$\pm$ 0.18	$\pm$ 0.09
110	5.11	$\pm$ 0.71	$\pm$ 0.76	1.69	$\pm$ 0.31	$\pm$ 0.33	0.90	$\pm$ 0.23	$\pm$ 0.18
130	5.88	$\pm$ 1.89	$\pm$ 1.26	2.06	$\pm$ 0.51	$\pm$ 0.56	0.90	$\pm$ 0.36	$\pm$ 0.32

Table 2: The DVCS cross section $\gamma^* p \to \gamma p$, σ_{DVCS}, as a function of W for three Q^2 values. The first errors are statistical, the second systematic.

	$d\sigma_{DVCS}/dt$ [nb/GeV^2]								
	$W = 82$ GeV								
$\lvert t\rvert$ [GeV^2]	Q^2 =8 GeV^2			Q^2 =15.5 GeV^2			Q^2 =25 GeV^2		
0.10	13.1	$\pm$ 1.10	$\pm$ 1.85	4.37	$\pm$ 0.47	$\pm$ 0.86	1.41	$\pm$ 0.40	$\pm$ 0.43
0.30	4.69	$\pm$ 0.45	$\pm$ 0.55	1.02	$\pm$ 0.16	$\pm$ 0.18	0.71	$\pm$ 0.16	$\pm$ 0.08
0.50	1.37	$\pm$ 0.21	$\pm$ 0.23	0.49	$\pm$ 0.08	$\pm$ 0.08	0.28	$\pm$ 0.07	$\pm$ 0.04
0.80	0.19	$\pm$ 0.04	$\pm$ 0.06	0.12	$\pm$ 0.02	$\pm$ 0.02	0.04	$\pm$ 0.01	$\pm$ 0.02
b [GeV^{-2}]	5.84	$\pm$ 0.30	$\pm$ 0.35	5.16	$\pm$ 0.26	$\pm$ 0.30	5.09	$\pm$ 0.55	$\pm$ 0.60
	$Q^2 = 10$ GeV^2								
$\lvert t\rvert$ [GeV^2]	$W = 40$ GeV			$W = 70$ GeV			$W = 100$ GeV		
0.10	4.99	$\pm$ 0.66	$\pm$ 0.54	7.78	$\pm$ 0.69	$\pm$ 0.87	10.9	$\pm$ 1.14	$\pm$ 2.36
0.30	1.45	$\pm$ 0.29	$\pm$ 0.18	2.74	$\pm$ 0.31	$\pm$ 0.30	3.47	$\pm$ 0.42	$\pm$ 0.53
0.50	0.49	$\pm$ 0.14	$\pm$ 0.08	0.81	$\pm$ 0.14	$\pm$ 0.11	1.49	$\pm$ 0.21	$\pm$ 0.24
0.80	0.12	$\pm$ 0.03	$\pm$ 0.03	0.19	$\pm$ 0.03	$\pm$ 0.03	0.19	$\pm$ 0.04	$\pm$ 0.06
b [GeV^{-2}]	5.40	$\pm$ 0.40	$\pm$ 0.25	5.34	$\pm$ 0.25	$\pm$ 0.27	5.48	$\pm$ 0.31	$\pm$ 0.45

Table 3: The DVCS cross section $\gamma^* p \to \gamma p$, differential in t, $d\sigma_{DVCS}/dt$, for three values of Q^2 at $W = 82$ GeV, and for three values of W at $Q^2 = 10$ GeV^2. Results for the corresponding t-slope parameters b are given. The first errors are statistical, the second systematic.

	$d\sigma_{DVCS}/dt$ [nb/GeV^2]								
	$Q^2 = 8$ GeV^2								
$\lvert t\rvert$ [GeV^2]	$W = 40$ GeV			$W = 70$ GeV			$W = 100$ GeV		
0.10	8.10	$\pm$ 1.22	$\pm$ 0.82	10.0	$\pm$ 1.30	$\pm$ 1.27	16.0	$\pm$ 2.11	$\pm$ 2.74
0.30	2.30	$\pm$ 0.54	$\pm$ 0.28	4.35	$\pm$ 0.63	$\pm$ 0.46	5.45	$\pm$ 0.80	$\pm$ 0.73
0.50	0.45	$\pm$ 0.22	$\pm$ 0.10	1.08	$\pm$ 0.27	$\pm$ 0.17	1.96	$\pm$ 0.41	$\pm$ 0.35
0.80	0.16	$\pm$ 0.06	$\pm$ 0.03	0.13	$\pm$ 0.06	$\pm$ 0.04	0.21	$\pm$ 0.09	$\pm$ 0.08
	$Q^2 = 20$ GeV^2								
$\lvert t\rvert$ [GeV^2]	$W = 40$ GeV			$W = 70$ GeV			$W = 100$ GeV		
0.10	1.06	$\pm$ 0.28	$\pm$ 0.28	2.38	$\pm$ 0.29	$\pm$ 0.26	2.98	$\pm$ 0.49	$\pm$ 0.85
0.30	0.33	$\pm$ 0.07	$\pm$ 0.07	0.67	$\pm$ 0.12	$\pm$ 0.07	0.89	$\pm$ 0.17	$\pm$ 0.17
0.50	0.22	$\pm$ 0.06	$\pm$ 0.06	0.24	$\pm$ 0.05	$\pm$ 0.03	0.44	$\pm$ 0.08	$\pm$ 0.08
0.80	0.04	$\pm$ 0.01	$\pm$ 0.01	0.07	$\pm$ 0.01	$\pm$ 0.02	0.06	$\pm$ 0.02	$\pm$ 0.02

Table 4: The DVCS cross section $\gamma^* p \to \gamma p$, differential in t, $d\sigma_{DVCS}/dt$, for three values of W extracted in two Q^2 intervals: $6.5 < Q^2 < 11$ GeV^2 and $11 < Q^2 < 80$ GeV^2, corrected to the central values of $Q^2 = 8$ GeV^2 and 20 GeV^2, respectively. The first errors are statistical, the second systematic.

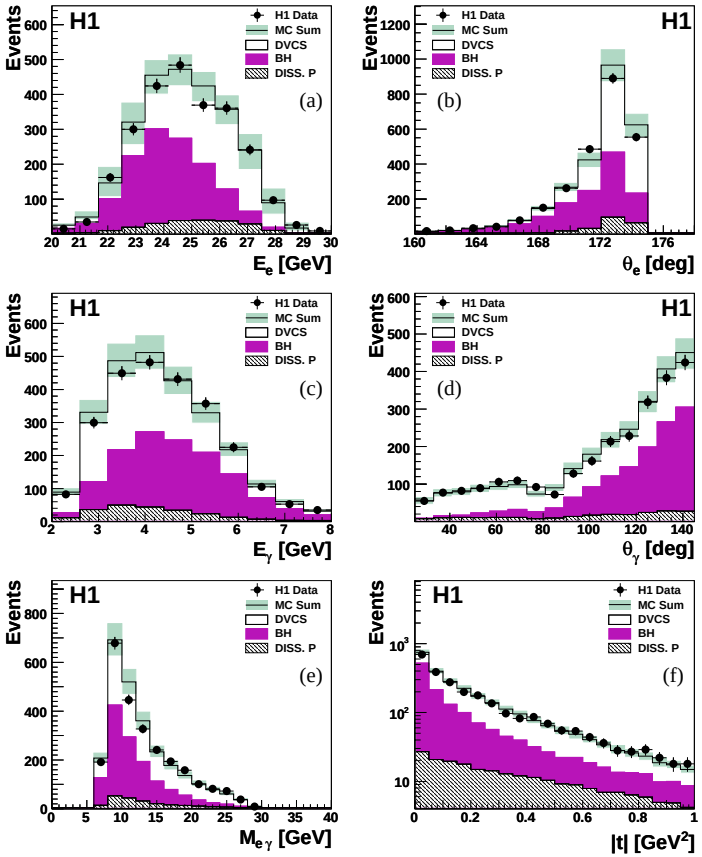

Figure 1: Distributions of the energy (a) and polar angle (b) of the scattered electron, the energy (c) and polar angle (d) of the photon, the electron-photon invariant mass (e) and the proton four momentum transfer squared $|t|$ (f). The data are compared with Monte Carlo expectations for elastic DVCS, elastic and inelastic BH and inelastic DVCS (labelled DISS. p). All Monte Carlo simulations are normalised according to the luminosity of the data. The open histogram shows the total prediction and the shaded band its estimated uncertainty.

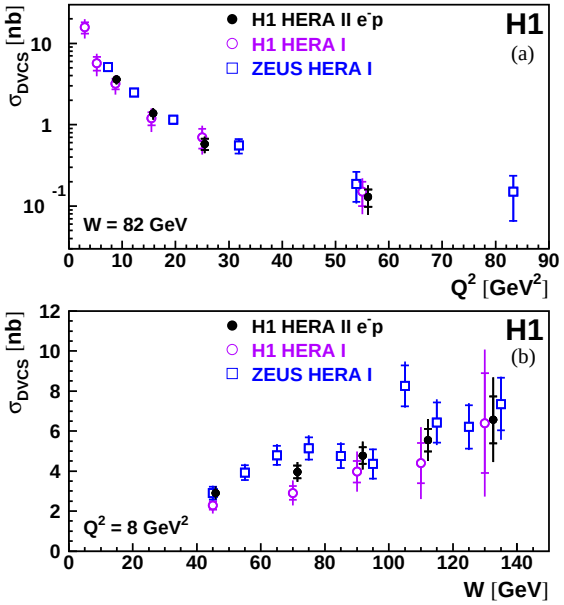

Figure 2: The DVCS cross section as a function of Q^2 at $W = 82$ GeV (a) and as a function of W at $Q^2 = 8$ GeV^2 (b). The results from the previous H1 and ZEUS publications [8, 9] based on HERA I data are also displayed. The inner error bars represent the statistical errors, the outer error bars the statistical and systematic errors added in quadrature.

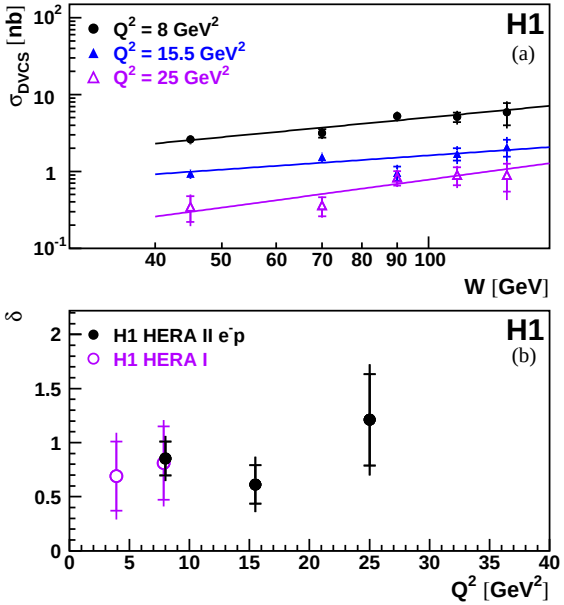

Figure 3: The DVCS cross section as a function of W at three values of Q^2 (a). The solid lines represent the results of fits of the form W^{δ}. The fitted values of $\delta(Q^2)$ are shown in (b). The inner error bars represent the statistical errors, the outer error bars the statistical and systematic errors added in quadrature.

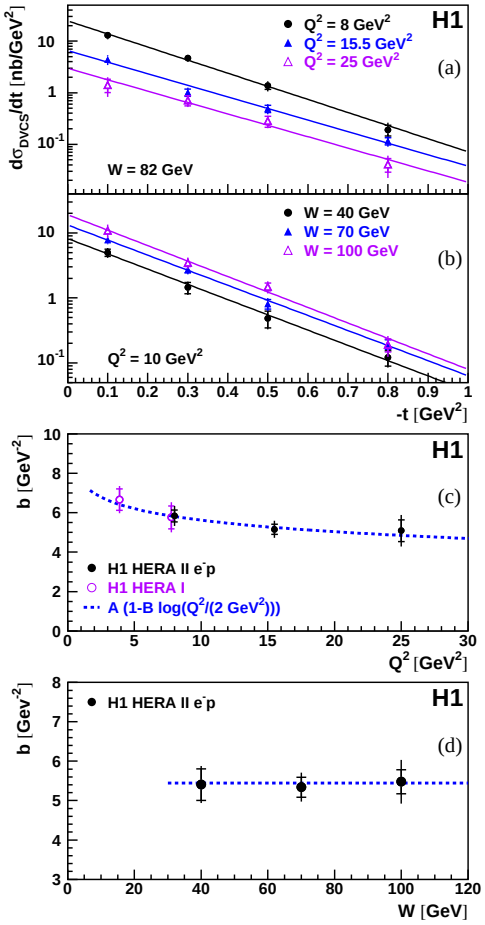

Figure 4: The DVCS cross section, differential in t, for three values of Q^2 expressed at $W = 82$ GeV (a) and for three values of W at $Q^2 = 10$ GeV^2 (b). The solid lines in (a) and (b) represent the results of fits of the form $e^{-b|t|}$. The fitted t-slope parameters $b(Q^2)$ are shown in (c) together with the t-slope parameters from the previous H1 publication [8]. The dashed curve in (c) represents the result of a fit to the $b(Q^2)$ values using a phenomenological function as described in the text. In (d) the fitted t-slope parameters $b(W)$ are shown. The dashed line in (d) corresponds to the average value $b = 5.45$ GeV^{-2}, obtained from a fit to the complete data sample of the present measurement. The inner error bars represent the statistical errors and the outer error bars the statistical and systematic errors added in quadrature.

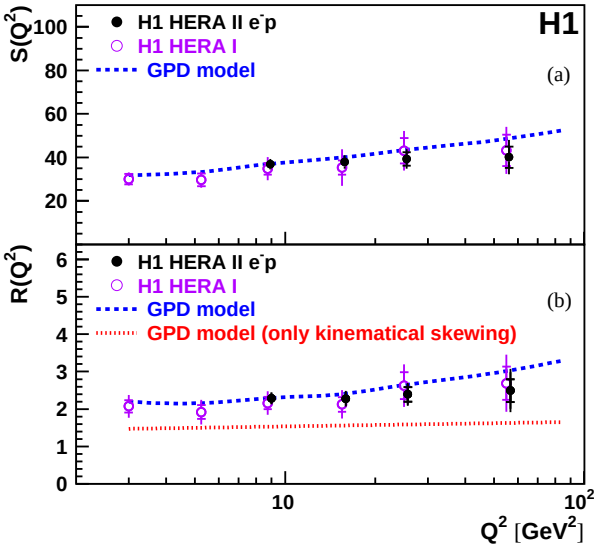

Figure 5: The observables S and R (see text), shown as a function of Q^2 in (a) and (b), respectively. The results from the previous H1 publication [8] based on HERA I data are also displayed. The inner error bars represent the statistical errors, the outer error bars the statistical and systematic errors added in quadrature. The dashed curves show the predictions of the GPD model [30, 32]. In (b), the dotted curve shows the prediction of a GPD model based on an approximation where only the kinematical part of the skewing effects are taken into account (see text).

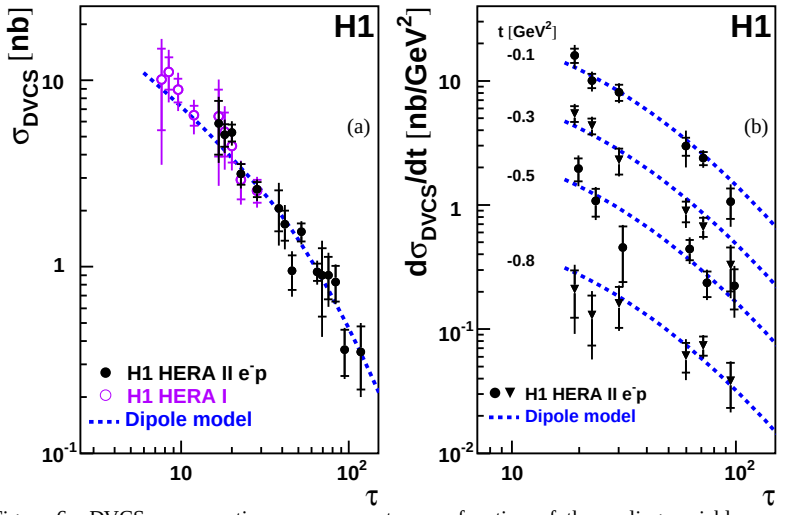

Figure 6: DVCS cross section measurements as a function of the scaling variable $\tau = Q^2/Q_s^2(x)$. In (a) the results are shown for the full t range $|t| < 1$ GeV^2 and in (b) at four values of t. The cross section measurements from the previous H1 publication [8] are also shown in (a). The inner error bars indicate the statistical errors, the outer error bars the statistical and systematic errors added in quadrature. The dashed curves represent the predictions of the dipole model [12, 14].

Annexe D

Deeply Virtual Compton Scattering and its Beam Charge Asymmetry in $e^{\pm}p$ Collisions at HERA

F.D. Aaron *et al.* [H1 Collaboration],
Phys. Lett. B **681** (2009) 391,
arXiv:0907.5289

Abstract

A measurement of elastic deeply virtual Compton scattering $\gamma^* p \to \gamma p$ using e^+p and e^-p collision data recorded with the H1 detector at HERA is presented. The analysed data sample corresponds to an integrated luminosity of 306 pb^{-1}, almost equally shared between both beam charges. The cross section is measured as a function of the virtuality Q^2 of the exchanged photon and the centre-of-mass energy W of the γ^*p system in the kinematic domain $6.5 < Q^2 < 80$ GeV^2, $30 < W < 140$ GeV and $|t| < 1$ GeV^2, where t denotes the squared momentum transfer at the proton vertex. The cross section is determined differentially in t for different Q^2 and W values and exponential t-slope parameters are derived. Using e^+p and e^-p data samples, a beam charge asymmetry is extracted for the first time in the low Bjorken x kinematic domain. The observed asymmetry is attributed to the interference between Bethe-Heitler and deeply virtual Compton scattering (DVCS) processes. Experimental results are discussed in the context of two different models, one based on generalised parton distributions (GPDs) and one based on the dipole approach.

1 Introduction

Measurements of the deep-inelastic scattering (DIS) of leptons and nucleons allow the extraction of Parton Distribution Functions (PDFs). While these functions provide crucial input to perturbative Quantum Chromodynamic (QCD) calculations, they do not provide a complete picture of the partonic structure of nucleons. In particular, PDFs contain neither information on the correlations between partons nor on their transverse spatial distribution.

Hard exclusive particle production, without excitation or dissociation of the nucleon, have emerged in recent years as prime candidates to address these issues [1–7]. Among them, deeply virtual Compton scattering (DVCS) on the proton ($\gamma^* p \to \gamma p$) is the simplest. The DVCS reaction can be regarded as the elastic scattering of the virtual photon off the proton via a colourless exchange, producing a real photon in the final state. In the Bjorken scaling regime, corresponding to large virtuality Q^2 of the exchanged photon and $|t|/Q^2 \ll 1$, where t is the squared momentum transfer at the proton vertex, QCD calculations assume that the exchange involves two partons in a colourless configuration, having different longitudinal and transverse momenta. These unequal momenta, or skewing, are a consequence of the mass difference between the incoming virtual photon and the outgoing real photon and may be interpreted in the contexts of generalised parton distributions (GPDs) or dipole amplitudes, respectively. In basic terms, a GPD (off-diagonal parton distribution) is the transition amplitude for removing a parton from the fast moving proton and reabsorbing it with a different momentum, thereby imparting a certain momentum transfer to the proton. In the dipole approach the virtual photon fluctuates into a colour singlet $q\bar{q}$ pair (or dipole) of a transverse size $r \sim 1/Q$, which subsequently undergoes hard scattering with the gluons in the proton. The t-dependence of the DVCS cross section carries information on the transverse momentum of partons.

In the kinematic range of the HERA collider, where DVCS is accessed through the reaction $e^{\pm}p \to e^{\pm}\gamma p$ [8–12], the DVCS amplitude is mainly imaginary [2], while the change of the amplitude with energy gives rise to a small real part. This reaction also receives a contribution from the purely electromagnetic Bethe-Heitler (BH) process, where the photon is emitted from the electron. The interference between DVCS and BH processes allows the extraction of the real part of the amplitude. In addition, the real part of the DVCS amplitude can be related to its imaginary part using dispersion relations. In the high energy limit at low momentum fraction x, the dispersion relations take a simple form [13] which can therefore be used for the DVCS process to verify the consistency between measurements of the real and imaginary parts of the amplitude.

This paper presents a measurement of DVCS cross sections as a function of Q^2 and the $\gamma^* p$ centre-of-mass energy W. The single differential cross section $d\sigma/dt$ is also extracted. The data were recorded with the H1 detector in the years 2004 to 2007, during which period HERA collided protons of 920 GeV energy with 27.6 GeV electrons and positrons. The total integrated luminosity of the data is 306 pb^{-1}. The data comprise 162 pb^{-1} recorded in e^+p and 144 pb^{-1} in e^-p collisions. During this HERA II running period, the electron[1] beam was longitudinally polarised, at a level of typically 35%. For this analysis, the periods with left-handed and right-handed beams are combined and the analysed data samples have a left-handed residual polarisation of 1% and 5% for e^+p and e^-p collisions, respectively. Cross section measurements are carried out in the kinematic range $6.5 < Q^2 < 80$ GeV^2, $30 < W < 140$ GeV and $|t| < 1$ GeV^2. The range in $x \simeq Q^2/W^2$ of the present measurement extends from $5 \cdot 10^{-4}$ to 10^{-2}. The cross section measurements of this analysis supersede those of a previous H1 publication [8], in which less than half of the present HERA II data was used. It is complementary to measurements performed at lower Q^2 using HERA I data [10]. In addition, using both beam charges, the beam charge asymmetry of the interference between the BH and DVCS processes is measured for the first time at a collider.

[1] In this paper the term "electron" is used generically to refer to both electrons and positrons, unless otherwise stated.

2 Theoretical Framework

In this paper, cross section measurements are compared to predictions based either on GPDs or on a dipole approach. At the present level of understanding, the pure GPDs approach and dipole models, based on the proton-dipole amplitude, are not connected. However, in the low x domain, dipole amplitudes could be used to provide parameterisations for GPDs at a certain scale [14]. In this context, the DVCS process is interesting as calculations are simplified by the absence of an unknown vector meson wave function. The GPDs model [6] used here has been shown to describe previous data. It is based on partial wave expansions of DVCS amplitudes and is a first attempt to parametrise all GPDs over the full kinematic domain. The dipole model [15], with a limited number of parameters, describes a large panel of low x measurements at HERA, from inclusive to exclusive processes. In this model, mainly using the gluon density extracted from fits to F_2 data, the DVCS cross section is computed using a universal dipole amplitude.

For GPDs models, a direct measurement of the real part of the DVCS amplitude is an important issue, as it gives an increased sensitivity to the parameterisation of the GPDs [2, 6]. Indeed, a calculation of the real part of the DVCS amplitude requires a parametrisation of the GPDs over the full x range. Considering the large flexibility in GPDs parameterisation, this is an important quantity to qualify the correct approach with GPDs. In the dipole approach, as the dipole amplitude refers only to the imaginary part, the magnitude of the real part can be predicted using a dispersion relation.

In high energy electron-proton collisions at HERA, DVCS and BH processes contribute to the reaction $e^{\pm}p \to e^{\pm}\gamma p$. The BH cross section is precisely calculable in QED. Since these two processes have an identical final state, they interfere. The squared photon production amplitude is then given by

$$|A|^2 = |A_{BH}|^2 + |A_{DVCS}|^2 + \underbrace{A_{DVCS}\, A^*_{BH} + A^*_{DVCS}\, A_{BH}}_{I}, \qquad (1)$$

where A_{BH} is the BH amplitude, A_{DVCS} represents the DVCS amplitude and I denotes the interference term. In the leading twist approximation, the interference term can be written quite generally as a linear combination of harmonics of the azimuthal angle ϕ. As defined in [2], ϕ is the angle between the plane containing the incoming and outgoing leptons and the plane formed by the virtual and real photons. For an unpolarised proton beam and if only the first harmonic

in $\cos\phi$ and $\sin\phi$, which are dominant at low x [6], are considered, the interference term I can be written as

$$I \propto -C\,[a_1 \cos\phi\, \mathrm{Re}A_{DVCS} + a_2 P_l \sin\phi\, \mathrm{Im}A_{DVCS}], \tag{2}$$

where $C = \pm 1$ is the charge of the lepton beam, P_l its longitudinal polarisation and a_1 and a_2 are functions of the ratio of longitudinal to transverse virtual photon flux [1–6]. Cross section measurements which are integrated over ϕ are not sensitive to the interference term. The measurement of the cross section asymmetry with respect to the beam charge as a function of ϕ allows to access the interference term. The beam charge asymmetry (BCA) of the cross section is defined as

$$A_C(\phi) = \frac{d\sigma^+/d\phi - d\sigma^-/d\phi}{d\sigma^+/d\phi + d\sigma^-/d\phi}, \tag{3}$$

where $d\sigma^+/d\phi$ and $d\sigma^-/d\phi$ are the differential $ep \to ep\gamma$ cross sections measured in e^+p and e^-p collisions, respectively.

Considering the low residual polarisation of the data and the theoretical expression of a_1 and a_2 [2], $a_1 \gg a_2 P_l$ and the contribution of the $\sin\phi$ term is neglected. Therefore, $A_C(\phi)$ can be expressed as

$$A_C(\phi) = p_1 \cos\phi = 2A_{BH}\frac{\mathrm{Re}A_{DVCS}}{|A_{DVCS}|^2 + |A_{BH}|^2}\cos\phi. \tag{4}$$

The term $|A_{DVCS}|^2$ can be derived directly from the DVCS cross section measurement $\sigma_{DVCS} = |A^2_{DVCS}|/(16\pi b)$, where b is the slope of the exponential t-dependence $e^{-b|t|}$ of the DVCS cross section. As the BH amplitude is precisely known, the measured asymmetry is directly proportional to the real part of the DVCS amplitude and the ratio between real and imaginary parts of the DVCS amplitude, $\rho = \mathrm{Re}A_{DVCS}/\mathrm{Im}A_{DVCS}$, can be extracted. This ratio ρ can also be derived using a dispersion relation [6, 16]. In the high energy limit, at low x and when the W dependence of the cross section is parameterised by a single term $W^{\delta(Q^2)}$, the dispersion relation can be written as [13]

$$\rho = \mathrm{Re}A_{DVCS}/\mathrm{Im}A_{DVCS} = \tan\left(\frac{\pi\delta(Q^2)}{8}\right). \tag{5}$$

The ratio ρ can therefore be determined directly from the energy dependence of the DVCS cross section parameterised by $\delta(Q^2)$. Comparison between the ρ values calculated from the energy dependence of the DVCS amplitude and from its real part therefore provides an important consistency test of the measured BCA.

3 Experimental Conditions and Monte Carlo Simulation

A detailed description of the H1 detector can be found in [17]. Here, only the detector components relevant for the present analysis are described. H1 uses a right-handed coordinate system with the z axis along the beam direction, the $+z$ or "forward" direction being that of the outgoing proton beam. The polar angle θ is defined with respect to the z axis and the pseudo-rapidity is given by $\eta = -\ln\tan\theta/2$.

The SpaCal [18], a lead scintillating fibre calorimeter, covers the backward region ($153^\circ < \theta < 176^\circ$). Its energy resolution for electromagnetic showers is $\sigma(E)/E \simeq 7.1\%/\sqrt{E/\mathrm{GeV}} \oplus 1\%$. The liquid argon (LAr) calorimeter ($4^\circ \leq \theta \leq 154^\circ$) is situated inside a solenoidal magnet. The energy resolution for electromagnetic showers is $\sigma(E)/E \simeq 11\%/\sqrt{E/\mathrm{GeV}}$ as obtained from test beam measurements [19]. The main component of the central tracking detector is the central jet chamber CJC ($20^\circ < \theta < 160^\circ$) which consists of two coaxial cylindrical drift chambers with wires parallel to the beam direction. The measurement of charged particle transverse momenta is performed in the magnetic field of 1.16 T, with a resolution of $\sigma_{P_T}/P_T = 0.002P_T/\mathrm{GeV} \oplus 0.015$. The innermost proportional chamber CIP [20] ($9^\circ < \theta < 171^\circ$) is used in this analysis to complement the CJC in the backward region for the reconstruction of the interaction vertex. The forward muon detector (FMD) consists of a series of drift chambers covering the range $1.9 < \eta < 3.7$. Primary particles produced at larger η can be detected indirectly in the FMD if they undergo a secondary scattering with the beam pipe or other adjacent material. Therefore, the FMD is used in this analysis to provide an additional veto against inelastic or proton dissociative events. The luminosity is determined from the rate of Bethe-Heitler processes measured using a calorimeter located close to the beam pipe at $z = -103$ m in the backward direction.

A dedicated event trigger was set up for this analysis. It is based on topological and neural network algorithms and uses correlations between electromagnetic energy deposits of electrons or photons in both the LAr and the SpaCal [21]. The combined trigger efficiency is 98%.

Monte Carlo (MC) simulations are used to estimate the background contributions and the corrections for the QED radiative effects and for the finite acceptance and the resolution of the detectors. Elastic DVCS events in ep collisions are generated using the Monte Carlo generator MILOU [22], based on the cross section calculation from [23] and using a t-slope parameter $b = 5.4$ GeV^{-2}, as measured in this analysis (see section 6.1). The photon flux is taken from [24]. Inelastic DVCS events in which the proton dissociates into a baryonic system Y are also simulated with MILOU setting the t-slope b_{inel} to 1.5 GeV^{-2}, as determined in a dedicated study (see section 6.2). The Monte Carlo program COMPTON 2.0 [25] is used to simulate elastic and inelastic BH events. In the generated MC events, no interference between DVCS and BH processes is included. Background from diffractive meson events is simulated using the DIFFVM MC generator [26]. All generated events are passed through a detailed, GEANT [27] based simulation of the H1 detector and are subject to the same reconstruction and analysis chain as are the data.

4 Event Selection

In elastic DVCS events, the scattered electron and the photon are the only particles that are expected to give signals in the detector. The scattered proton escapes undetected through the beam pipe. The selection of the analysis event sample requires a scattered electron and a photon identified as compact and isolated electromagnetic showers in the SpaCal and in the LAr, respectively. The electron candidate is required to have an energy above 15 GeV. The photon is required to have a transverse momentum P_T above 2 GeV and a polar angle between 25° and 145°. Events are selected if there are either no tracks at all or a single central track which is associated with the scattered electron. In order to reject inelastic and proton dissociation events, no further energy deposit in the LAr calorimeter larger than 0.8 GeV is allowed and no activity above the noise level should be present in the FMD. The influence of QED radiative corrections is reduced by the requirement that the longitudinal momentum balance $E - P_z$ be greater than 45 GeV. Here, E denotes the energy and P_z the momentum along the beam axis of all measured final state particles. To enhance the DVCS signal with respect to the BH contribution and to ensure a large acceptance, the kinematic domain is restricted to $6.5 < Q^2 < 80$ GeV^2 and $30 < W < 140$ GeV.

The reconstruction method for the kinematic variables Q^2, x and W relies on the measured polar angles of the final state electron and photon (double angle method) [8]. The variable t is approximated by the negative square of the transverse momentum of the outgoing proton, computed from the vector sum of the transverse momenta of the final state photon and the scattered electron. The resolution of the t reconstruction varies from 0.06 at low $|t|$ to 0.20 GeV^2 at high $|t|$.

The selected event sample contains 2643 events in e^+p and 2794 events in e^-p collisions, respectively. Distributions of selected kinematic variables are presented in figure 1 for the full sample from $e^{\pm}p$ collisions and compared to MC expectation normalised to the data luminosity. A good description of the shape and normalisation of the measured distributions is observed. The analysis sample contains contributions from the elastic DVCS and BH processes, as well as backgrounds from the BH and DVCS processes with proton dissociation, $ep \to e\gamma Y$, where the baryonic system Y of mass M_Y is undetected. The latter contribute to $14 \pm 4\%$ of the analysis sample, as estimated from MC predictions. Backgrounds from diffractive ω and ϕ production decaying to final states with photons are estimated to be negligible in the kinematic range of the analysis. Contamination from processes with low multiplicity π^0 production was also investigated and found to be negligible.

5 Cross Section and Beam Charge Asymmetry Measurements

The full $e^{\pm}p$ data sample is used to measure the DVCS cross section integrated over ϕ. The separate e^+p and e^-p data samples are used to measure the beam charge asymmetry as a function of ϕ.

The DVCS cross section, $\gamma^*p \to \gamma p$, is evaluated in each bin i at the bin centre values Q_i^2, W_i, t_i using the expression

$$\sigma_{DVCS}(Q_i^2, W_i, t_i) = \frac{(N_i^{\rm obs} - N_i^{\rm BH} - N_i^{\rm DVCS-inel})}{N_i^{\rm DVCS-el}} \cdot \sigma^{\gamma^*{\rm p}}_{DVCS-el}(Q_i^2, W_i, t_i)\,, \qquad (6)$$

where $N_i^{\rm obs}$ is the number of data events observed in bin i. The other numbers in this equation are calculated using the MC simulations described in section 3. $N_i^{\rm BH}$ denotes the number of BH events (elastic and inelastic) reconstructed in bin i and normalised to the data luminosity, $N_i^{\rm DVCS-inel}$ the number of inelastic DVCS background events, $N_i^{\rm DVCS-el}$ the number of elastic DVCS events and $\sigma^{\gamma^*{\rm p}}_{DVCS-el}$ is the theoretical $\gamma^*p \to \gamma p$ cross section used for the generation of DVCS events. The mean value of the acceptance, defined as the number of DVCS MC events reconstructed in a bin divided by the number of events generated in the same bin, is 60% over the whole kinematic range, for both beam charges.

The systematic errors of the measured DVCS cross section are determined by repeating the analysis after applying to the MC samples appropriate variations for each error source. The main contribution comes from the variation of the t-slope parameter set in the elastic DVCS MC by $\pm 6\%$, as constrained by this analysis, and the 4% uncertainty of the FMD veto efficiency. These error sources result in an error of 10% on the measured cross section. The 20% uncertainty of the t-slope parameter needed to estimate the inelastic DVCS background (see section 6.2) translates into an error on the elastic cross section of 4% on average, but reaches 12% at high t. The contribution from BH processes is controlled using the method detailed in [8]. It induces an uncertainty of 3%. The uncertainties related to subtraction of the BH background, trigger efficiency, photon identification efficiency, radiative corrections and luminosity measurement are each in the range of 1 to 3%. The total systematic uncertainty of the cross section amounts to about 12%. A fraction of about 85% of this error is correlated among bins.

For the BCA measurement, the angle ϕ is calculated from the reconstructed four-vectors of the electron and of the photon. MC studies indicates that the resolution of ϕ is in the range from 20° to 40°. The resolution of ϕ is limited mainly by the resolution on the photon energy in the LAr and the resolution on the electron polar angle. In addition there are large migrations between the true and the reconstructed $|\phi|$ from 0° to 180°, and vice versa. The asymmetry $A_C(\phi)$ is then determined from the differential $ep \to ep\gamma$ cross sections $d\sigma^+/d\phi$ and $d\sigma^-/d\phi$ using the formula (3). The cross sections $d\sigma/d\phi$ are evaluated similarly to $\gamma^*p \to \gamma p$ cross section at bin centre values ϕ_i using the expression

$$d\sigma/d\phi(\phi_i) = \frac{(N_i^{\rm obs} - N_i^{\rm BH-inel} - N_i^{\rm DVCS-inel})}{(N_i^{\rm DVCS-el} + N_i^{\rm BH-el})} \cdot (\sigma^{\rm ep}_{DVCS-el}(\phi_i) + \sigma^{\rm ep}_{BH-el}(\phi_i)), \qquad (7)$$

where $N_i^{\rm BH-el}$ and $N_i^{\rm BH-inel}$ are the numbers of elastic and inelastic MC BH events, respectively, and $\sigma^{\rm ep}_{DVCS-el}(\phi_i) + \sigma^{\rm ep}_{BH-el}(\phi_i)$ denotes the sum of the theoretical DVCS and BH $ep \to ep\gamma$ cross sections. Since a $\cos\phi$ dependence is expected, events with $\phi < 0$ and $\phi > 0$ are combined, in order to increase the statistical significance and to remove effects on the asymmetry of any possible $\sin\phi$ contribution from the residual lepton beam polarisation. The systematic error on the BCA measurement mainly arises from the part of the LAr photon energy scale uncertainty which is correlated between the e^+p and e^-p samples, estimated to be 0.5%.

In order to simulate the interference term, an asymmetry of the form $p_1 \cos\phi$ is added to the MC generation and passed through the full detector simulation and analysis chain to account for all acceptance and migration effects from true to reconstructed ϕ values. To determine the value of p_1, a χ^2 minimisation is performed as a function of p_1 to adjust the reconstructed asymmetry in the MC to the measured one. MC events generated using this p_1 value are then used to correct the measured asymmetry for the effect of migrations. Bin by bin correction factors are determined from the difference between the true and the reconstructed asymmetry in the MC.

6 Results and Interpretations

6.1 Cross Sections and t-dependence

The measured DVCS cross sections as a function of W for $|t| < 1$ GeV^2 and at $Q^2 = 10$ GeV^2 as well as the Q^2 dependence at $W = 82$ GeV are displayed in figure 2 and given in table 1. They agree within errors with the previous measurements [8, 10–12]. The data agree also with models based on GPDs [6] or the dipole approach [15]. DVCS cross sections for e^+p and e^-p data are also found in good agreement with each other. As already discussed in [8], the steep rise of the cross section with W is an indication of the presence of a hard underlying process.

The W dependence of the cross section for three separate bins of Q^2 is shown in figure 3(a) and given in table 2. A fit of the function W^δ is performed in each Q^2 bin. Figure 3(b) shows the obtained δ values. It is observed that δ is independent of Q^2 within the errors. The average value[2] $\delta = 0.63 \pm 0.08 \pm 0.14$ is in agreement with the previous measurement [8], as well as with the value of $\delta = 0.52 \pm 0.09$ (stat.) measured by the ZEUS Collaboration at a lower Q^2 of 3.2 GeV^2 [12].

Differential cross sections are measured as a function of t for three values of Q^2 and W and presented in table 3. Fits of the form $d\sigma/d|t| \sim e^{-b|t|}$, which describe the data well [8], are performed taking into account the statistical and correlated systematic errors. The derived t-slope parameters $b(Q^2)$ and $b(W)$ are displayed in figures 4(a) and (b), respectively. They confirm the result obtained in a previous analysis [8] and no significant variation of b with W is observed. Experimental results are compared with calculations from GPDs and dipole models [6, 15]. A good agreement is obtained for both W and Q^2 dependences of the t-slopes. It should be noted that in the GPDs model previous data of [8, 10] are used to derive the Q^2 and W dependences of b, while no DVCS data enter in the determination of parameters of the dipole model. If b is parametrised as $b = b_0 + 2\alpha' \ln \frac{1}{x}$, with $x = Q^2/W^2$, the obtained α' value is compatible with 0 and an upper limit on α' of 0.20 GeV^{-2} at 95% confidence level (CL) is derived. This value is compatible with results obtained for J/ψ exclusive electroproduction [28, 29], for which the measured α' is below 0.17 GeV^{-2} at 95% CL. An increase of the slope with decreasing x (shrinkage) is therefore not observed. Such a behaviour is expected for hard processes and confirms that perturbative QCD can be used to describe DVCS processes.

Using the complete analysis sample, the value of b is found to be $5.41 \pm 0.14 \pm 0.31$ GeV^{-2} at $Q^2 = 10$ GeV^2. This corresponds to a total uncertainty of 6% on the (elastic) t-slope measurement for the full data sample. As in [8], this t-slope value can be converted to an average impact parameter of $\sqrt{< r_T^2 >} = 0.64 \pm 0.02$ fm. It corresponds to the transverse extension of the parton density, dominated by sea quarks and gluons for an average value $x = 1.2 \cdot 10^{-3}$, in the plane perpendicular to the direction of motion of the proton. At larger values of x ($x > 0.1$), a smaller value of $\sqrt{< r_T^2 >}$, dominated by the contribution of valence quarks, is estimated [4].

[2]Here and in all other places where results are given the first error is statistical and the second systematic.

6.2 Inelastic DVCS t-dependence

The increased statistical precision compared to previous analyses allows a first measurement of the t-slope of the inelastic DVCS process. A sample of events with a signal in the FMD is selected. It corresponds to events with the mass of the proton dissociation system $M_Y \gtrsim 1.4$ GeV, as derived from MC studies. The contribution of inelastic DVCS events is extracted by subtracting the BH (elastic and inelastic) and elastic DVCS contributions, as estimated from the respective MC expectations. The measured differential cross section as a function of t is presented in figure 5. A fit of the form $d\sigma/d|t| \sim e^{-b_{inel}|t|}$ yields $b_{inel} = 1.53 \pm 0.26 \pm 0.44$ GeV^{-2}. This value is compatible with previous determinations for inelastic exclusive production of ρ, ϕ [30] and J/ψ [29]. No indication of a dependence of b_{inel} with Q^2 or W is observed.

6.3 Beam Charge Asymmetry

The contributions of elastic DVCS and BH processes to the analysis sample are of similar size, as can be observed in figure 1. This is a favourable situation for the beam charge asymmetry measurement, with a maximum sensitivity for the interference term. The measured BCA integrated over the kinematic range of the analysis and corrected for detector effects, as detailed in section 5, is presented in figure 6 and table 4. Bins in ϕ with a size of the order of the experimental resolution on ϕ are used.

The χ^2 minimisation procedure leads to a p_1 value of $p_1 = 0.16 \pm 0.04 \pm 0.06$. The resulting function $0.16 \cos\phi$ is displayed in figure 6 and is seen to agree with the prediction of the GPDs model for the first $\cos\phi$ harmonic [6]. The measured asymmetry is in good agreement with the model prediction within experimental errors.

As detailed in section 2, from the measured BCA and the p_1 value determined above, together with the DVCS cross section, the ratio ρ of the real to imaginary parts of the DVCS amplitude can be calculated as $\rho = 0.20 \pm 0.05 \pm 0.08$. This is the first measurement of this ratio. The dispersion relation of equation (5) and our measurement of $\delta(Q^2)$ on the other hand leads to $\rho = 0.25 \pm 0.03 \pm 0.05$, in good agreement with the direct determination. While in the low x domain of the present measurement, the real part of the DVCS amplitude is positive, in contrast, at larger x ($x \sim 0.1$) and lower Q^2, a smaller and negative real part was measured[3] by the HERMES Collaboration [31].

[3]The convention used in [31] for the definition of the ϕ angle is different from the one of [2] adopted in the present paper.

7 Conclusion

The elastic DVCS cross section $\gamma^* p \to \gamma p$ has been measured with the H1 detector at HERA. The measurement is performed in the kinematic range $6.5 < Q^2 < 80$ GeV^2, $30 < W < 140$ GeV and $|t| < 1$ GeV^2. The analysis uses e^+p and e^-p data recorded from 2004 to 2007, corresponding to a total integrated luminosity of 306 pb^{-1}, almost equally shared between both beam charges. The W dependence of the DVCS cross section is well described by a function W^δ. No significant variation of the exponent δ as a function of Q^2 is observed. For the total sample a value $\delta = 0.63 \pm 0.08 \pm 0.14$ is determined. The steep rise of the cross section with W indicates a hard underlying process. The t-dependence of the cross section is well described by the form $e^{-b|t|}$ with an average slope of $b = 5.41 \pm 0.14 \pm 0.31$ GeV^{-2}. The t-slopes are determined differentially in Q^2 and W and are compatible with previous observations. The t-slope is also measured for the inelastic DVCS. The measured elastic DVCS cross section is compared to the predictions of two different models based on GPDs or on a dipole approach, respectively. Both approaches describe the data well. The use of e^+p and e^-p collision data allows the measurement of the beam charge asymmetry of the interference between the BH and DVCS processes, for the first time at a collider. The ratio ρ of the real to imaginary part of the DVCS amplitude is then derived, directly from the measurements of the BCA and of the DVCS cross section to be $\rho = 0.20 \pm 0.05 \pm 0.08$. This ratio can also be calculated from a dispersion relation using only the DVCS energy dependence, leading to $\rho = 0.25 \pm 0.03 \pm 0.05$. Both results are in good agreement. The GPDs model considered here [6] correctly describes the measured BCA as well as ρ. The measurements presented here show that a combined analysis of DVCS observables, including cross section and charge asymmetry, allows the extraction of the real part of the DVCS amplitude and subsequently a novel understanding of the correlations of parton momenta in the proton.

Acknowledgements

We are grateful to the HERA machine group whose outstanding efforts have made this experiment possible. We thank the engineers and technicians for their work in constructing and maintaining the H1 detector, our funding agencies for financial support, the DESY technical staff for continual assistance and the DESY directorate for the hospitality which they extend to the non DESY members of the collaboration. We would like to thank Dieter Mueller, Kresimir Kumerički and Gregory Soyez for helpful discussions and for providing theory predictions.

References

[1] M. Diehl *et al.*, Phys. Lett. B **411** (1997) 193 [hep-ph/9706344].

[2] A. V. Belitsky, D. Mueller and A. Kirchner, Nucl. Phys. B **629** (2002) 323 [hep-ph/0112108].

[3] M. Burkardt, Int. J. Mod. Phys. A **18** (2003) 173 [hep-ph/0207047].

[4] M. Diehl, Eur. Phys. J. C **25** (2002) 223 [Erratum-ibid. C **31** (2003) 277] [hep-ph/0205208].

[5] L. Frankfurt, M. Strikman and C. Weiss, Ann. Rev. Nucl. Part. Sci. **55** (2005) 403 [hep-ph/0507286].

[6] K. Kumerički, D. Mueller and K. Passek-Kumerički, Eur. Phys. J. C **58** (2008) 193 [arXiv:0805.0152];
K. Kumerički, D. Mueller and K. Passek-Kumerički, arXiv:0807.0159;
K. Kumerički and D. Mueller, private communication.

[7] M. Diehl *et al.*, Eur. Phys. J. C **39** (2005) 1 [hep-ph/0408173].

[8] F. D. Aaron *et al.* [H1 Collaboration], Phys. Lett. B **659** (2008) 796 [arXiv:0709.4114].

[9] C. Adloff *et al.* [H1 Collaboration], Phys. Lett. B **517** (2001) 47 [hep-ex/0107005].

[10] A. Aktas *et al.* [H1 Collaboration], Eur. Phys. J. C **44** (2005) 1 [hep-ex/0505061].

[11] S. Chekanov *et al.* [ZEUS Collaboration], Phys. Lett. B **573** (2003) 46 [hep-ex/0305028].

[12] S. Chekanov *et al.* [ZEUS Collaboration], JHEP **0905** (2009) 108 [arXiv:0812.2517].

[13] A. Hebecker and T. Teubner, Phys. Lett. B **498** (2001) 16 [hep-ph/0010273].

[14] M. McDermott, R. Sandapen and G. Shaw, Eur. Phys. J. C **22** (2002) 655 [hep-ph/0107224].

[15] C. Marquet, R. B. Peschanski and G. Soyez, Phys. Rev. D **76** (2007) 034011 [hep-ph/0702171].

[16] M. Diehl and D. Y. Ivanov, Eur. Phys. J. C **52** (2007) 919 [arXiv:0707.0351].

[17] I. Abt *et al.* [H1 Collaboration], Nucl. Instrum. Meth. A **386** (1997) 310;
I. Abt *et al.* [H1 Collaboration], Nucl. Instrum. Meth. A **386** (1997) 348.

[18] R. D. Appuhn *et al.* [H1 SPACAL Group], Nucl. Instrum. Meth. A **386** (1997) 397.

[19] B. Andrieu *et al.* [H1 Calorimeter Group], Nucl. Instrum. Meth. A **350** (1994) 57.

[20] J. Becker *et al.*, Nucl. Instrum. Meth. A **586** (2008) 190.

[21] B. Roland, "Mesure de la Diffusion Compton à Haute Virtualité à HERA II", Ph.D. thesis, Université libre de Bruxelles (2007), available at http://www-h1.desy.de/psfiles/theses/.

[22] E. Perez, L. Schoeffel and L. Favart, "MILOU: A Monte-Carlo for deeply virtual Compton scattering", hep-ph/0411389.

[23] L. L. Frankfurt, A. Freund and M. Strikman, Phys. Rev. D **58** (1998) 114001 [Erratum-ibid. D **59** (1999) 119901] [hep-ph/9710356].

[24] L. N. Hand, Phys. Rev. **129** (1963) 1834.

[25] A. Courau *et al.*, "Quasi-Real QED Compton Monte Carlo", Proceedings of the Workshop "Physics at HERA", eds. W. Buchmüller and G. Ingelman, DESY (1991), vol. 2, p. 902.

[26] B. List and A. Mastroberardino, "DIFFVM: A Monte Carlo generator for diffractive processes in ep scattering", Proceedings of the Workshop "Monte Carlo Generators for HERA Physics", eds. A. T. Doyle *et al.*, DESY (1998), p. 396.

[27] R. Brun *et al.*, "GEANT3", CERN-DD/EE/84-1.

[28] A. Aktas *et al.* [H1 Collaboration], Eur. Phys. J. C **46** (2006) 585 [hep-ex/0510016].

[29] S. Chekanov *et al.* [ZEUS Collaboration], Nucl. Phys. B **695** (2004) 3 [hep-ex/0404008].

[30] C. Adloff *et al.* [H1 Collaboration], Z. Phys. C **75** (1997) 607 [hep-ex/9705014].

[31] A. Airapetian *et al.* [HERMES Collaboration], JHEP **0806** (2008) 066 [arXiv:0802.2499].

Q^2 [GeV^2]	σ_{DVCS} [nb]		
8.75	3.87	$\pm$ 0.15	$\pm$ 0.41
15.5	1.46	$\pm$ 0.07	$\pm$ 0.18
25	0.55	$\pm$ 0.07	$\pm$ 0.08
55	0.16	$\pm$ 0.02	$\pm$ 0.03

W [GeV]	σ_{DVCS} [nb]		
45	2.23	$\pm$ 0.11	$\pm$ 0.19
70	2.92	$\pm$ 0.16	$\pm$ 0.27
90	3.63	$\pm$ 0.22	$\pm$ 0.40
110	3.71	$\pm$ 0.29	$\pm$ 0.61
130	4.37	$\pm$ 0.60	$\pm$ 1.16

Table 1: The DVCS cross section $\gamma^* p \to \gamma p$, σ_{DVCS}, as a function of Q^2 for $W = 82\,\mathrm{GeV}$ and as a function of W for $Q^2 = 10\,\mathrm{GeV}^2$, both for $|t| < 1\,\mathrm{GeV}^2$. The first errors are statistical, the second systematic.

	σ_{DVCS} [nb]								
W [GeV]	$Q^2 = 8\,\mathrm{GeV}^2$			$Q^2 = 15.5\,\mathrm{GeV}^2$			$Q^2 = 25\,\mathrm{GeV}^2$		
45	3.06	$\pm$ 0.18	$\pm$ 0.25	0.98	$\pm$ 0.07	$\pm$ 0.08	0.31	$\pm$ 0.11	$\pm$ 0.05
70	3.54	$\pm$ 0.29	$\pm$ 0.34	1.46	$\pm$ 0.12	$\pm$ 0.12	0.52	$\pm$ 0.08	$\pm$ 0.06
90	4.93	$\pm$ 0.39	$\pm$ 0.52	1.41	$\pm$ 0.16	$\pm$ 0.17	0.81	$\pm$ 0.13	$\pm$ 0.09
110	5.16	$\pm$ 0.51	$\pm$ 0.74	1.66	$\pm$ 0.23	$\pm$ 0.28	0.63	$\pm$ 0.17	$\pm$ 0.15
130	5.62	$\pm$ 1.34	$\pm$ 1.19	2.00	$\pm$ 0.37	$\pm$ 0.47	0.80	$\pm$ 0.26	$\pm$ 0.29
δ	0.61	$\pm$ 0.10	$\pm$ 0.15	0.61	$\pm$ 0.13	$\pm$ 0.15	0.90	$\pm$ 0.36	$\pm$ 0.27

Table 2: The DVCS cross section $\gamma^* p \to \gamma p$, σ_{DVCS}, as a function of W for three Q^2 values and for $|t| < 1\,\mathrm{GeV}^2$. The values of $\delta(Q^2)$ obtained from fits of the form W^δ are given. The first errors are statistical, the second systematic.

	$d\sigma_{DVCS}/d\|t\|$ $\left[\text{nb/GeV}^2\right]$								
	$W = 82\,\text{GeV}$								
$\|t\|$ $\left[\text{GeV}^2\right]$	$Q^2 = 8\,\text{GeV}^2$			$Q^2 = 15.5\,\text{GeV}^2$			$Q^2 = 25\,\text{GeV}^2$		
0.10	13.3	$\pm$ 0.80	$\pm$ 1.73	4.33	$\pm$ 0.35	$\pm$ 0.65	1.68	$\pm$ 0.31	$\pm$ 0.42
0.30	4.82	$\pm$ 0.32	$\pm$ 0.50	1.24	$\pm$ 0.13	$\pm$ 0.16	0.49	$\pm$ 0.10	$\pm$ 0.08
0.50	1.26	$\pm$ 0.14	$\pm$ 0.18	0.45	$\pm$ 0.06	$\pm$ 0.05	0.18	$\pm$ 0.04	$\pm$ 0.03
0.80	0.21	$\pm$ 0.03	$\pm$ 0.04	0.10	$\pm$ 0.01	$\pm$ 0.02	0.05	$\pm$ 0.01	$\pm$ 0.01
b $[\text{GeV}^{-2}]$	5.87	$\pm$ 0.20	$\pm$ 0.32	5.45	$\pm$ 0.20	$\pm$ 0.29	5.10	$\pm$ 0.38	$\pm$ 0.37

	$Q^2 = 10\,\text{GeV}^2$								
$\|t\|$ $\left[\text{GeV}^2\right]$	$W = 40\,\text{GeV}$			$W = 70\,\text{GeV}$			$W = 100\,\text{GeV}$		
0.10	4.77	$\pm$ 0.50	$\pm$ 0.49	7.81	$\pm$ 0.51	$\pm$ 0.85	11.0	$\pm$ 0.85	$\pm$ 2.23
0.30	1.62	$\pm$ 0.23	$\pm$ 0.18	2.88	$\pm$ 0.22	$\pm$ 0.28	3.71	$\pm$ 0.31	$\pm$ 0.49
0.50	0.69	$\pm$ 0.11	$\pm$ 0.07	0.91	$\pm$ 0.10	$\pm$ 0.10	1.18	$\pm$ 0.13	$\pm$ 0.16
0.80	0.10	$\pm$ 0.02	$\pm$ 0.01	0.16	$\pm$ 0.02	$\pm$ 0.02	0.24	$\pm$ 0.03	$\pm$ 0.04
b $[\text{GeV}^{-2}]$	5.38	$\pm$ 0.30	$\pm$ 0.23	5.49	$\pm$ 0.19	$\pm$ 0.26	5.49	$\pm$ 0.20	$\pm$ 0.35

Table 3: The DVCS cross section $\gamma^* p \to \gamma p$, differential in t, $d\sigma_{DVCS}/dt$, for three values of Q^2 at $W = 82\,\text{GeV}$, and for three values of W at $Q^2 = 10\,\text{GeV}^2$. Results for the corresponding t-slope parameters b are given. The first errors are statistical, the second systematic.

ϕ [deg.]	$A_C(\phi)$		
10	0.326	$\pm$ 0.086	$\pm$ 0.180
35	0.119	$\pm$ 0.076	$\pm$ 0.090
70	$-$0.039	$\pm$ 0.080	$\pm$ 0.030
110	0.035	$\pm$ 0.092	$\pm$ 0.028
145	$-$0.234	$\pm$ 0.079	$\pm$ 0.076
170	$-$0.210	$\pm$ 0.075	$\pm$ 0.169

Table 4: The DVCS beam charge asymmetry $A_C(\phi)$ as a function of ϕ and integrated over the kinematic range $6.5 < Q^2 < 80\,\text{GeV}^2$, $30 < W < 140\,\text{GeV}$ and $|t| < 1\,\text{GeV}^2$. The first errors are statistical, the second systematic.

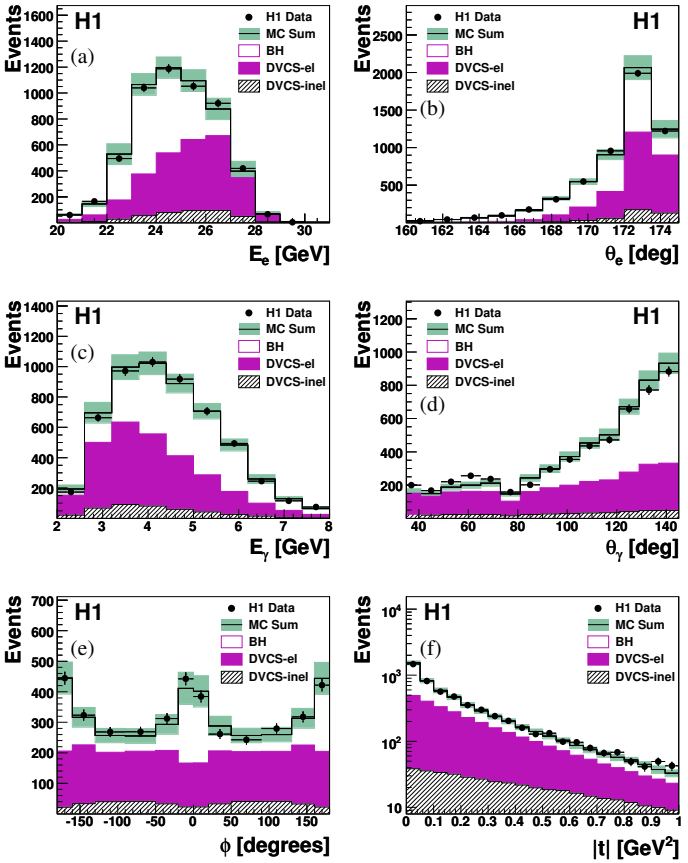

Figure 1: Distributions of the energy (a) and polar angle (b) of the scattered electron, the energy (c) and polar angle (d) of the photon, the ϕ azimuthal angle between the plane of incoming and outgoing lepton and the plane of virtual and real photon [2] (e) and the proton four momentum transfer squared $|t|$ (f). The data correspond to the full $e^{\pm}p$ sample and are compared to Monte Carlo expectations for elastic DVCS, elastic and inelastic BH and inelastic DVCS. All Monte Carlo simulations are normalised according to the luminosity of the data. The open histogram shows the total prediction and the shaded band its estimated uncertainty.

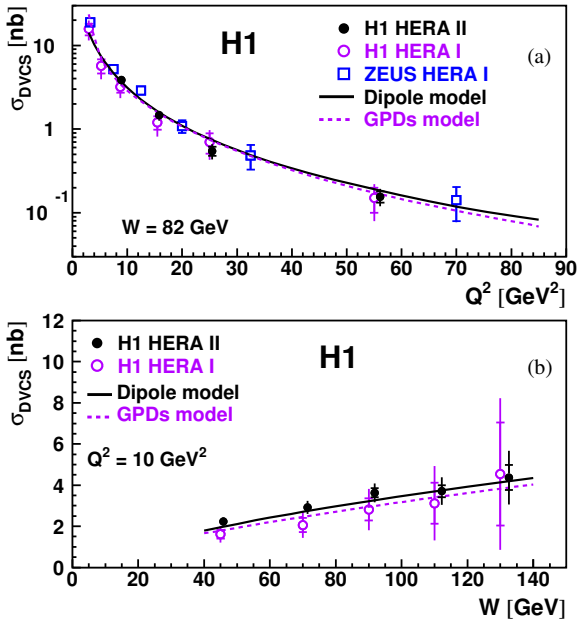

Figure 2: The DVCS cross section $\gamma^* p \to \gamma p$ as a function of Q^2 at $W = 82$ GeV (a) and as a function of W at $Q^2 = 10$ GeV^2 (b). The results from the previous H1 [10] and ZEUS [12] publications based on HERA I data are also displayed. ZEUS measurements are propagated from $W = 104$ GeV to 82 GeV using a W dependence $W^{0.52}$. The inner error bars represent the statistical errors, the outer error bars the statistical and systematic errors added in quadrature. The dashed line represents the prediction of the GPDs model [6] and the solid line the prediction of the dipole model [15].

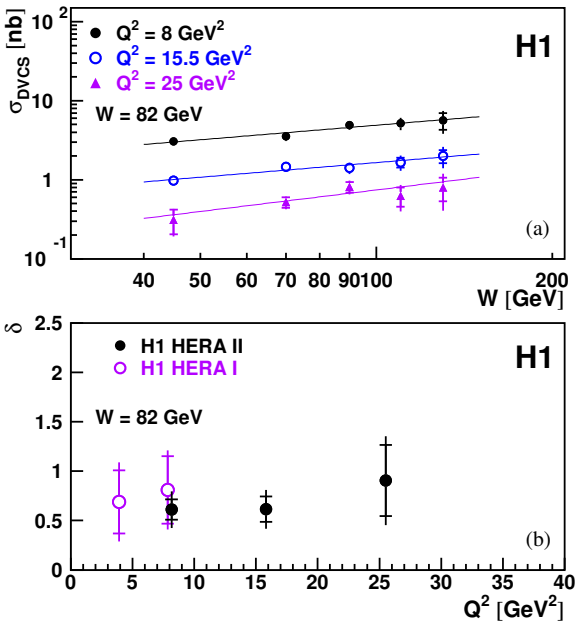

Figure 3: The DVCS cross section $\gamma^* p \to \gamma p$ as a function of W at three values of Q^2 (a). The solid lines represent the results of fits of the form W^{δ}. The fitted values of $\delta(Q^2)$ are shown in (b) together with the values obtained using HERA I data [10]. The inner error bars represent the statistical errors, the outer error bars the statistical and systematic errors added in quadrature.

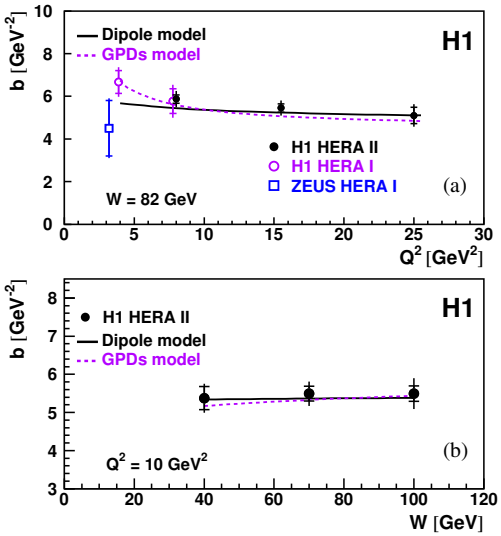

Figure 4: The fitted t-slope parameters $b(Q^2)$ are shown in (a) together with the t-slope parameters from the previous H1 [10] and ZEUS [12] publications based on HERA I data. In (b) the fitted t-slope parameters $b(W)$ are shown. The inner error bars represent the statistical errors and the outer error bars the statistical and systematic errors added in quadrature. The dashed line represents the prediction of the GPDs model [6] and the solid line the prediction of the dipole model [15].

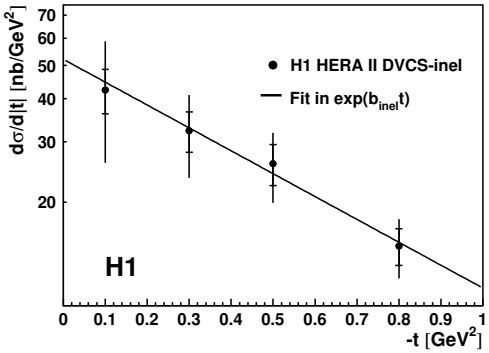

Figure 5: The inelastic DVCS cross section differential in t at $W = 82$ GeV and $Q^2 = 10$ GeV^2. The inner error bars represent the statistical errors, the outer error bars the statistical and systematic errors added in quadrature.

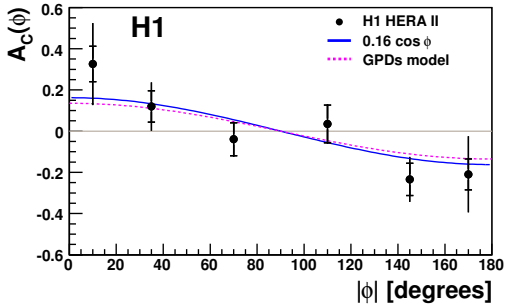

Figure 6: Beam charge asymmetry as a function of the angle ϕ as defined in [2], integrated over the kinematic range of the analysis. The inner error bars represent the statistical errors, the outer error bars the statistical and systematic errors added in quadrature. The function $0.16\cos\phi$ is also shown (solid line), together with the GPDs model prediction (dashed line).

Annexe E

A Search for Excited Neutrinos in e^-p Collisions at HERA

F.D. Aaron *et al.* [H1 Collaboration],
Phys. Lett. B **663** (2008) 382,
arXiv:0802.1858

Abstract

A search for first generation excited neutrinos is performed using the full e^-p data sample collected by the H1 experiment at HERA at a centre-of-mass energy of 319 GeV, corresponding to a total luminosity of 184 pb^{-1}. The electroweak decays of excited neutrinos $\nu^*\to\nu\gamma$, $\nu^*\to\nu Z$ and $\nu^*\to eW$ with subsequent hadronic or leptonic decays of the W and Z bosons are considered. No evidence for excited neutrino production is found. Mass dependent exclusion limits on ν^* production cross sections and on the ratio of the coupling to the compositeness scale f/Λ are derived within gauge mediated models. A limit on f/Λ, independent of the relative couplings to the SU(2) and U(1) gauge bosons, is also determined. These limits extend the excluded region to higher masses than has been possible in previous excited neutrino searches.

1 Introduction

The three-family structure and mass hierarchy of the known fermions is one of the most puzzling characteristics of the Standard Model (SM) of particle physics. Attractive explanations are provided by models assuming composite quarks and leptons [1]. The existence of excited states of leptons and quarks is a natural consequence of these models and their discovery would provide convincing evidence of a new scale of matter. Electron-proton interactions at very high energies provide a good environment in which to search for excited states of first generation fermions. In particular, excited neutrinos (ν^*) could be singly produced through the exchange of a W boson in the t-channel.

In this letter a search for excited neutrinos using the complete e^-p HERA collider data of the H1 experiment is presented. Electroweak decays into a SM lepton (e, ν_e) and a SM gauge boson (γ, W and Z) are considered and hadronic as well as leptonic decays of the W and Z are analysed.

The data, collected at electron and proton beam energies of 27.6 GeV and 920 GeV, respectively, correspond to a total integrated luminosity of 184 pb^{-1}. During the HERA II running period, the electron beam was longitudinally polarised, at a level of typically 35%. For this analysis the periods with left-handed and right-handed beams are combined and the analysed data sample has a residual polarisation of 5% left-handed. With more than a ten-fold increase in statistics, this analysis supersedes the result of the previous H1 search for excited neutrinos based on a data sample corresponding to a luminosity of 15 pb^{-1} [2].

2 Phenomenology

In the present study a model [3–5] is considered in which excited fermions are assumed to have spin $1/2$ and isospin $1/2$. Both left-handed and right-handed components of the excited fermions form weak iso-doublets F_L^* and F_R^*. In order to prevent the light leptons from radiatively acquiring a large anomalous magnetic moment [6, 7], only the right-handed component of the excited fermions takes part in the generalised magnetic de-excitation. The interaction between excited fermions, gauge bosons and ordinary fermions is then described by the effective Lagrangian [4]:

$$\mathcal{L}_{int.} = \frac{1}{2\Lambda}\bar{F_R^*}\,\sigma^{\mu\nu}\left[gf\frac{\tau^a}{2}W^a_{\mu\nu} + g'f'\frac{Y}{2}B_{\mu\nu} + g_s f_s\frac{\lambda^a}{2}G^a_{\mu\nu}\right]\,F_L + h.c.\,. \qquad (1)$$

The matrix $\sigma^{\mu\nu}$ is the covariant bilinear tensor, $W^a_{\mu\nu}$, $B_{\mu\nu}$ and $G^a_{\mu\nu}$ are the field-strength tensors of the SU(2), U(1) and SU(3)$_C$ gauge fields, τ^a, Y and λ^a are the Pauli matrices, the weak hypercharge operator and the Gell-Mann matrices, respectively. The standard electroweak and strong gauge couplings are denoted by g, g' and g_s, respectively. The parameter Λ has units of energy and can be regarded as the compositeness scale which reflects the range of a new confinement force. The constants f, f' and f_s are form factors associated to the three gauge groups. They can be interpreted as parameters setting different scales $\Lambda_i = \Lambda/f_i$ for the different gauge groups, thus allowing the composite fermion to have arbitrary coupling strengths with the three gauge bosons.

Following this model, single production of excited neutrinos in ep collisions may result from the t-channel exchange of a W boson. Due to the helicity dependence of the weak interaction and given the valence quark composition and density distribution of the proton, the ν^* production cross section is predicted to be much larger for e^-p collisions than for e^+p. For a ν^* mass M_{ν^*} of 200 GeV the ratio of the production cross sections is of order 100. The ν^* production cross section is expected to scale linearly with the polarisation of the incident electron beam, similarly to the SM charged current process. The excited neutrino may decay into a lepton and an electroweak gauge boson via $\nu^* \to \nu\gamma$, $\nu^* \to eW$ and $\nu^* \to \nu Z$. For a given M_{ν^*} value and assuming a numerical relation between f and f', the ν^* branching ratios are fixed and the production cross section depends only on f/Λ. The ν^* is expected not to have strong interactions and therefore this search is insensitive to f_s. Two complementary coupling assignments $f = +f'$ and $f = -f'$ are studied in detail. For $f = +f'$ the excited neutrino has no tree-level electromagnetic coupling [8] and therefore the photonic decay of the ν^* is forbidden whereas for $f = -f'$ decays into $\nu\gamma$, νZ and eW are allowed. In addition, arbitrary ratios of f'/f are considered in the range -5 to $+5$.

3 Simulation of Signal and Background Processes

A Monte Carlo (MC) program developed for this analysis is used for the calculation of the ν^* production cross section and the simulation of signal events. The events are simulated using the cross section calculated from the Lagrangian described in equation (1) using the CompHEP package [9]. Initial state radiation from the incident electron is included using the Weizsäcker-Williams approximation [10]. The proton parton densities are taken from the CTEQ5L [11] parametrisation and are evaluated at the scale $\sqrt{Q^2}$, where Q^2 is the four-momentum transfer squared. The parton shower approach [12] is applied to simulate Quantum Chromodynamics (QCD) corrections in the initial and final states. The hadronisation is performed using Lund string fragmentation as implemented in PYTHIA [12].

In the MC generator the full transition matrix including the production and the decay is implemented. This is important if the natural width of the ν^* is large, which is typically the case at high mass where factorisation of the ν^* production and its decay no longer holds. Events used in the determination of signal efficiencies are generated with the coupling f/Λ corresponding, for each ν^* mass, to the expected boundary of the probed domain in the plane defined by M_{ν^*} and f/Λ.

The Standard Model background processes that may mimic a ν^* signal are neutral current (NC) and charged current (CC) deep-inelastic scattering (DIS) and to a lesser extent photoproduction, lepton pair production and real W boson production.

The RAPGAP [13] event generator, which implements the Born, QCD Compton and Boson Gluon Fusion matrix elements, is used to model NC DIS events. The QED radiative effects arising from real photon emission from both the incoming and outgoing electrons are simulated using the HERACLES [14] program. Direct and resolved photoproduction of jets and prompt

photon production are simulated using the PYTHIA event generator. The simulation is based on Born level hard scattering matrix elements with radiative QED corrections. In RAPGAP and PYTHIA, jet production from higher order QCD radiation is simulated using leading logarithmic parton showers and hadronisation is modelled with Lund string fragmentation. The leading order MC prediction of NC DIS and photoproduction processes with two or more high transverse momentum jets is scaled by a factor of 1.2 in order to normalise to next-to-leading order QCD calculations [15]. Charged current DIS events are simulated using the DJANGO [16] program, which includes first order leptonic QED radiative corrections based on HERACLES. The production of two or more jets in DJANGO is accounted for using the colour-dipole-model [17].

Contributions from elastic and quasi-elastic QED Compton scattering are simulated with the WABGEN [18] generator. Contributions arising from the production of W bosons and multi-lepton events are modelled using the EPVEC [19] and GRAPE [20] event generators, respectively.

All processes are generated with an integrated luminosity significantly higher than that of the data sample. Generated events are passed through the full GEANT [21] based simulation of the H1 apparatus, which takes into account the running conditions of the different data taking periods, and are reconstructed and analysed using the same program chain as for the data.

4 Experimental Conditions

A detailed description of the H1 experiment can be found in [22]. Only the detector components relevant to the present analysis are briefly described here. The origin of the H1 coordinate system is the nominal ep interaction point, with the direction of the proton beam defining the positive z-axis (forward region). Transverse momentum (P_T) is measured in the xy plane. The pseudorapidity η is related to the polar angle θ by $\eta = -\ln\tan(\theta/2)$. The Liquid Argon (LAr) calorimeter [23] is used to measure electrons, photons and hadrons. It covers the polar angle range $4^\circ < \theta < 154^\circ$ with full azimuthal acceptance. Electromagnetic shower energies are measured with a precision of $\sigma(E)/E = 12\%/\sqrt{E/\text{GeV}} \oplus 1\%$ and hadronic energies with $\sigma(E)/E = 50\%/\sqrt{E/\text{GeV}} \oplus 2\%$, as measured in test beams [24, 25]. In the backward region, energy measurements are provided by a lead/scintillating-fiber (SpaCal) calorimeter [26] covering the angular range $155^\circ < \theta < 178^\circ$. The central ($20^\circ < \theta < 160^\circ$) and forward ($7^\circ < \theta < 25^\circ$) tracking detectors are used to measure charged particle trajectories, to reconstruct the interaction vertex and to complement the measurement of hadronic energy. The LAr and inner tracking detectors are enclosed in a super-conducting magnetic coil with a field strength of 1.16 T. The return yoke of the coil is the outermost part of the detector and is equipped with streamer tubes forming the central muon detector ($4^\circ < \theta < 171^\circ$). In the forward region of the detector ($3^\circ < \theta < 17^\circ$) a set of drift chambers detects muons and measures their momenta using an iron toroidal magnet. The luminosity is determined from the rate of the Bethe-Heitler process $ep \to ep\gamma$, measured using a photon detector located close to the beam pipe at $z = -103$ m, in the backward direction.

5 Data Analysis

The triggers used in this analysis are based on the detection of energy deposits in the LAr calorimeter [27]. Events containing an electromagnetic deposit (electron or photon) with an energy greater than 10 GeV are triggered with an efficiency close to 100%. For events with missing transverse energy above 20 GeV, the trigger efficiency is $\sim 90\%$.

In order to remove background events induced by cosmic showers and other non-ep sources, the event vertex is required to be reconstructed within 35 cm in z of the nominal interaction point. In addition, topological filters and timing vetoes are applied.

The identification of electrons or photons relies on the measurement of a compact and isolated electromagnetic shower in the LAr calorimeter. In addition, the hadronic energy within a distance in the pseudorapidity-azimuth $(\eta - \phi)$ plane $R = \sqrt{\Delta\eta^2 + \Delta\phi^2} < 0.5$ around the electron (photon) is required to be below 3% of the electron (photon) energy. Muon identification is based on a track measured in the inner tracking systems associated with signals in the muon detectors [28]. A muon candidate should have no more than 5 GeV deposited in a cylinder, centred on the muon track direction, of radius 25 cm and 50 cm in the electromagnetic and hadronic sections of the LAr calorimeter, respectively. Calorimeter energy deposits and tracks not previously identified as electron, photon or muon candidates are used to form combined cluster-track objects, from which the hadronic energy is reconstructed [29, 30]. Jets are reconstructed from these combined cluster-track objects using an inclusive k_T algorithm [31, 32] with a minimum transverse momentum of 2.5 GeV. The missing transverse momentum P_T^{miss} of the event is derived from all identified particles and energy deposits in the event. The P_T^{miss} is assumed to originate from a single neutrino. The four-vector of this neutrino candidate is reconstructed assuming transverse momentum conservation and the relation $\sum_i (E^i - P_z^i) + (E^\nu - P_z^\nu) = 2E_e^0 = 55.2$ GeV, where the sum runs over all detected particles; P_z is the momentum along the beam axis and E_e^0 is the electron beam energy.

Specific selection criteria applied in each decay channel are presented in the following subsections. A detailed description of the analysis can be found in [33].

5.1 $\nu\gamma$ Resonance Search

The signature of the decay channel $\nu^* \to \nu\gamma$ consists of an isolated electromagnetic cluster in events with missing transverse momentum. Background arises from CC DIS events with an isolated π^0 or a radiated photon. Events with substantial missing transverse momentum $P_T^{\text{miss}} > 20$ GeV are selected. In each event, a photon candidate with transverse momentum $P_T^\gamma > 20$ GeV in a polar angle range $5^\circ < \theta^\gamma < 120^\circ$ is required. This polar angle range is restricted to $\theta^\gamma < 60^\circ$ in events with P_T^{miss} below 30 GeV, in order to reduce background from NC DIS. The photon is required to be isolated from jets by a distance $R > 0.5$ to any jet axis. In the central region ($\theta^\gamma > 20^\circ$), photon candidates are selected only if no well measured track points to the electromagnetic cluster within a distance of closest approach (DCA) of 12 cm. For events with P_T^{miss} below 50 GeV, this condition is tightened by accepting only photon candidates having no track with a DCA to the cluster below 24 cm or within $R < 0.5$. The energy and polar angle of the photon are combined into one discriminant variable $\xi^\gamma = E^\gamma \cos^2(\theta^\gamma/2)$.

Radiative CC DIS events are suppressed by requiring that $\xi^\gamma > 45$ GeV. For signal events, in most cases the final state contains a recoil jet, due to ν^* production via t-channel W boson exchange. Hence, in the final selection the presence of at least one jet with $P_T^{\rm jet} > 5$ GeV is also required.

Seven events are selected in the data, compared to a SM expectation of 12.3 ± 3.0, which is dominated by CC DIS events. The invariant mass of the excited neutrino candidate is calculated from the four-vectors of the neutrino and the photon. The invariant mass distributions of the ν^* candidates and of the expected SM background are presented in figure 1(a). The resulting selection efficiency is 50% for $M_{\nu^*} = 120$ GeV, increasing to 55% for $M_{\nu^*} = 260$ GeV. From Monte Carlo studies, the total width of the reconstructed ν^* mass distribution is 11 GeV for a generated ν^* mass of 120 GeV, increasing to 41 GeV for a ν^* mass of 260 GeV.

5.2 $\nu q\bar{q}$ Resonance Search

The signature of the $\nu^*\to\nu Z\to\nu q\bar{q}$ decay channel consists of two jets with high transverse momentum in events with large $P_T^{\rm miss}$. The SM background is dominated by multi-jet CC DIS events and contains a moderate contribution from photoproduction. Events with missing transverse momentum $P_T^{\rm miss} > 20$ GeV are selected. In each event at least two jets are required in the polar angle range $5^\circ < \theta^{\rm jet} < 130^\circ$ with transverse momenta larger than 20 and 15 GeV, respectively. Additionally, the hadronic final state must exhibit a polar angle γ_h, as defined in [34], larger than 20°, in order to remove photoproduction events. Events with $P_T^{\rm miss} < 30$ GeV are selected if the ratio V_{ap}/V_p of transverse energy flow anti-parallel and parallel to the hadronic final state [34] is above 0.1. This condition reduces the contribution of CC DIS processes. Photoproduction and NC DIS backgrounds typically have low volues of x_h, the Bjorken scaling variable calculated from the hadronic system using the Jacquet-Blondel method [34, 35], and are thus suppressed by requiring $x_h > 0.04$. Finally, to further reduce the background from CC DIS, a jet multiplicity greater than or equal to three is required for events with $P_T^{\rm miss} < 50$ GeV. In each event, a Z candidate is reconstructed from the combination of the two jets with an invariant mass closest to the nominal Z boson mass. The reconstructed Z candidate is required to have an invariant mass above 60 GeV.

After this selection, 89 events are found in the data compared to a SM expectation of 95 ± 21 events. The invariant mass of the ν^* candidate is calculated from the neutrino and Z candidate four-vectors. For this calculation, the Z candidate four-vector is scaled such that its mass is set equal to the nominal Z boson mass. The invariant mass distributions of the ν^* candidates and of the expected SM background are presented in figure 1(b). The selection efficiency in this channel is 25% for $M_{\nu^*} = 120$ GeV, increasing to 55% for $M_{\nu^*} = 260$ GeV. From Monte Carlo studies, the total width of the reconstructed ν^* mass distribution is 31 GeV for a generated ν^* mass of 120 GeV, increasing to 41 GeV for a ν^* mass of 260 GeV.

5.3 $eq\bar{q}$ Resonance Search

The signature of the $\nu^*\to eW\to eq\bar{q}$ decay channel consists of one electron and two high P_T jets. Multi-jet NC DIS events constitute the main background contribution from SM processes.

Events are selected with an isolated electron in the LAr calorimeter in the polar angle range $5^\circ < \theta^e < 90^\circ$. The electron variable[1] $\xi^e = E^e \cos^2(\theta^e/2)$ is required to be above 23 GeV or the electron should have a transverse momentum P_T^e greater than 25 GeV. These conditions remove a large part of the NC DIS contribution. In addition, the electron should be isolated from jets by a distance $R > 0.5$ to any jet axis. The events are required to have at least two jets in the polar angle range $5^\circ < \theta^{\rm jet} < 130^\circ$ with transverse momenta larger than 20 and 15 GeV, respectively. In each event, a W candidate is reconstructed from the combination of the two jets with an invariant mass closest to the nominal W boson mass. The reconstructed mass of the W candidate is required to be larger than 40 GeV. To further reduce the NC DIS background it is required that the polar angle of the jet with the highest P_T associated to the W candidate be less than 80° and that events with $P_T^e < 65$ GeV contain at least three jets with a P_T larger than 5 GeV.

After the selection, 220 events are observed compared to a SM expectation of 223 ± 47. The invariant mass of the ν^* candidate is calculated from the electron and W candidate four-vectors. For this calculation, the W candidate four-vector is scaled such that its mass is set equal to the nominal W boson mass. The invariant mass distributions of the ν^* candidates and of the expected SM background are presented in figure 1(c). The selection efficiency in this channel is 40% for $M_{\nu^*} = 120$ GeV, increasing to 65% for $M_{\nu^*} = 260$ GeV. From Monte Carlo studies, the total width of the reconstructed ν^* mass distribution is 15 GeV for a generated ν^* mass of 120 GeV, increasing to 38 GeV for a ν^* mass of 260 GeV.

5.4 $e\nu\mu$ and $e\nu e$ Resonance Searches

In the search for $\nu^*\to eW\to e\nu\mu$, events with $P_T^{\rm miss} > 15$ GeV, one electron with $P_T^e > 20$ GeV and one muon with $P_T^\mu > 10$ GeV are selected. The electron and the muon have to be detected in the polar angle ranges $5^\circ < \theta^e < 100^\circ$ and $10^\circ < \theta^\mu < 160^\circ$, respectively. Furthermore, the electron and the muon must be isolated from jets by minimum distances of $R^e > 0.5$ and $R^\mu > 1$, respectively. The contribution from NC DIS processes is reduced by requiring $\xi^e > 9$ GeV. After this selection no data event remains, while 0.40 ± 0.05 SM background events are expected. The selection efficiency for ν^* with masses above 120 GeV is $\sim 35\%$.

The signatures of the $\nu^*\to eW\to e\nu e$ and $\nu^*\to\nu Z\to\nu ee$ channels are similar and consist of two high P_T electrons in events with large missing transverse momentum. Events with $P_T^{\rm miss} > 20$ GeV are selected. In each event two isolated electromagnetic clusters are required, with a transverse momentum larger than 20 and 15 GeV, respectively. The highest P_T electron should be detected in the polar angle range $5^\circ < \theta^{e1} < 100^\circ$ and the second electron in the range $5^\circ < \theta^{e2} < 120^\circ$. To reduce the background from Compton processes, a track has to be associated to each electromagnetic cluster in the central region ($\theta^e > 35^\circ$). Events in which the invariant mass of the two electromagnetic clusters is within 10 GeV of the nominal Z boson mass are attributed to the $Z\to ee$ decay channel. Events from the $W\to\nu e$ decay channel are selected by requiring the invariant mass of the ν and one of the electromagnetic clusters to be compatible with the W boson mass within 20 GeV. In this channel, the variable ξ^e defined from the highest P_T electron is required to be above 29 GeV. No data candidate is observed in

[1] This variable is proportional to the four-momentum transfer squared Q^2 for NC DIS.

either the Z or W decay channels compared to SM expectations of 0.19 ± 0.05 and 0.7 ± 0.1, respectively. In both channels, the selection efficiency for ν^* with masses above 120 GeV is $\sim 35\%$.

5.5 Systematic Uncertainties

The following experimental systematic uncertainties are considered:

- The uncertainty on the electromagnetic energy scale varies between 1% and 3% depending on the polar angle. The polar angle measurement uncertainty of electromagnetic clusters is 3 mrad.
- The efficiency to identify photons is known with a precision of 10% for high P_T photons.
- The scale uncertainty on the transverse momentum of high P_T muons amounts to 5%. The uncertainty on the reconstruction of the muon polar angle is 3 mrad.
- The hadronic energy scale is known within 2%. The uncertainty on the jet polar angle determination is 10 mrad.
- The uncertainty on the trigger efficiency is 3%.
- The luminosity measurement has an uncertainty of 2.5%.

The effect of the above systematic uncertainties are determined by varying the experimental quantities by ± 1 standard deviation in the MC samples and propagating these variations through the whole analysis chain.

Additional model systematic uncertainties are attributed to the SM background MC generators described in section 3. An error of 20% on the simulation of NC DIS, CC DIS and photoproduction processes with at least two high P_T jets is considered to account for the uncertainty on higher order QCD corrections. An uncertainty of 30% on the simulation of radiative CC DIS events is considered to account for the lack of QED radiation from the quark line in the DJANGO generator. This uncertainty is estimated in the specific phase space of the analysis by a comparison of the DJANGO result to the calculated cross section of the $e^-p \to \nu_e \gamma X$ process [36]. The error on the QED Compton cross section is estimated to be 10%. The errors attributed to multi-lepton and W production are 3% and 15%, respectively. The total error on the SM background prediction is determined by adding the effects of all model and experimental systematic uncertainties in quadrature.

The theoretical uncertainty on the ν^* production cross section is dominated by the uncertainty on the scale at which the proton parton densities are evaluated. It is estimated by varying this scale from $\sqrt{Q^2}/2$ to $2\sqrt{Q^2}$. The resulting uncertainty depends on the ν^* mass and is 10% at $M_{\nu^*} = 100$ GeV, increasing to 30% at $M_{\nu^*} = 300$ GeV.

6 Interpretation

The event yields observed in all decay channels are in agreement with the corresponding SM expectations and are summarised in table 1. The SM predictions are dominated by NC DIS processes for the $eq\bar{q}$ resonance search and by CC DIS for the $\nu\gamma$ and $\nu q\bar{q}$ resonance searches. The distributions of the invariant mass of the data events are in agreement with those of the expected SM background as shown in figure 1. No data event is observed in channels corresponding to leptonic decays of the W or Z bosons, in agreement with the low SM expectations.

Since no evidence for the production of excited neutrinos is observed, upper limits on the ν^* production cross section and on the coupling f/Λ are derived as a function of the mass of the excited neutrino. Limits are presented at the 95% confidence level (CL) and are obtained from the mass spectra using a modified frequentist approach which takes statistical and systematic uncertainties into account [37].

Upper limits on the product of the ν^* production cross section and decay branching ratio are shown in figure 2. The analysed decay channels of the W and Z gauge bosons are combined. The resulting limits on f/Λ after combination of all ν^* decay channels are displayed as a function of the ν^* mass in figure 3, for the conventional assumptions $f = -f'$ and $f = +f'$. Limits are derived for ν^* masses up to 300 GeV. The total fraction of ν^* decays covered in this analysis is $\sim 92\%$ and $\sim 84\%$ in the two cases $f = -f'$ and $f = +f'$, respectively. In the case $f = -f'$, the limit on f/Λ is dominated at low mass by the $\nu^* \to \nu\gamma$ channel, while the $\nu^* \to eW$ channel starts to contribute significantly for masses above 200 GeV. Under the assumption $f = +f'$, the limit on f/Λ is driven mainly by the $\nu^* \to eW$ channel. These new results improve significantly the previously published limits by H1 [2] and ZEUS [38]. For comparison, the most stringent limits obtained in e^+e^- collisions at LEP for the two cases $f = -f'$ and $f = +f'$, determined by L3 [39] and DELPHI [40], respectively, are also shown in figure 3. The H1 measurement provides the most stringent constraints for masses larger than ~ 170 GeV. With the assumption $f/\Lambda = 1/M_{\nu^*}$ excited neutrinos with masses up to 213 GeV (196 GeV) are excluded for $f = -f'$ ($f = +f'$).

Limits with less model dependence can be derived if arbitrary ratios f'/f are considered. The dependence of the limits on this ratio for different ν^* masses is displayed in figure 4(a). Limits which are independent of f'/f are derived for $f'/f \in [-5; 5]$ by choosing in figure 4(a) the point with the weakest limit for each mass hypothesis. The result is shown in figure 4(b) and is found to be almost equal to the limit obtained under the assumption $f = +f'$.

7 Conclusion

Using the full e^-p data sample collected by the H1 experiment at HERA with an integrated luminosity of 184 pb^{-1} a search for the production of excited neutrinos is performed. The excited neutrino decay channels $\nu^* \to \nu\gamma$, $\nu^* \to \nu Z$ and $\nu^* \to eW$ with subsequent hadronic or leptonic decays of the W and Z bosons are considered and no indication of a ν^* signal is found. New limits on the production cross section of excited neutrinos are obtained. Previous HERA results are improved by a factor three to four. Upper limits on the coupling f/Λ as a function of

the excited neutrino mass are established for specific relations between the couplings ($f = +f'$ and $f = -f'$) and independent of the ratio f'/f. Assuming $f = -f'$ and $f/\Lambda = 1/M_{\nu^*}$, excited neutrinos with a mass lower than 213 GeV are excluded at 95% confidence level. The results presented in this letter greatly extend the previously excluded domain and demonstrate the unique sensitivity of HERA to excited neutrinos with masses beyond the LEP reach.

Acknowledgements

We are grateful to the HERA machine group whose outstanding efforts have made this experiment possible. We thank the engineers and technicians for their work in constructing and maintaining the H1 detector, our funding agencies for financial support, the DESY technical staff for continual assistance and the DESY directorate for the hospitality which they extend to the non DESY members of the collaboration. We would like to thank M. Spira for helpful discussions.

References

[1] H. Harari, Phys. Rept. **104** (1984) 159.

[2] C. Adloff *et al.* [H1 Collaboration], Phys. Lett. B **525** (2002) 9 [hep-ex/0110037].

[3] K. Hagiwara, D. Zeppenfeld and S. Komamiya, Z. Phys. C **29** (1985) 115.

[4] F. Boudjema, A. Djouadi and J. L. Kneur, Z. Phys. C **57** (1993) 425.

[5] U. Baur, M. Spira and P. M. Zerwas, Phys. Rev. D **42** (1990) 815.

[6] S. J. Brodsky and S. D. Drell, Phys. Rev. D **22** (1980) 2236.

[7] F. M. Renard, Phys. Lett. B **116** (1982) 264.

[8] F. Boudjema and A. Djouadi, Phys. Lett. B **240** (1990) 485.

[9] E. Boos *et al.* [CompHEP Collaboration], Nucl. Instrum. Meth. A **534** (2004) 250 [hep-ph/0403113];
A. Pukhov *et al.*, "CompHEP - a package for evaluation of Feynman diagrams and integration over multi-particle phase space", hep-ph/9908288
(available at http://theory.sinp.msu.ru/comphep).

[10] C. Berger and W. Wagner, Phys. Rept. **146** (1987) 1.

[11] J. Pumplin *et al.*, JHEP **0207** (2002) 012 [hep-ph/0201195].

[12] T. Sjöstrand *et al.*, PYTHIA version 6.1, Comput. Phys. Commun. **135** (2001) 238 [hep-ph/0010017].

[13] H. Jung, RAPGAP version 3.1, Comput. Phys. Commun. **86** (1995) 147.

[14] A. Kwiatkowski, H. Spiesberger and H. J. Möhring, Comput. Phys. Commun. **69** (1992) 155.

[15] C. Adloff *et al.* [H1 Collaboration], Eur. Phys. J. C **25** (2002) 13 [hep-ex/0201006].

[16] G. A. Schuler and H. Spiesberger, DJANGOH version 1.4, "Django: The Interface for The Event Generators Heracles and Lepto", Proc. of the Workshop "Physics at HERA" (1991), Eds. W. Buchmüller and G. Ingelman, Vol. 3, p. 1419.

[17] L. Lönnblad, Comput. Phys. Commun. **71** (1992) 15.

[18] C. Berger and P. Kandel, "A New Generator For Wide Angle Bremsstrahlung", Prepared for Workshop on Monte Carlo Generators for HERA Physics Hamburg, Germany, 27-30 April 1998.

[19] U. Baur, J. A. Vermaseren and D. Zeppenfeld, EPVEC version 1.1, Nucl. Phys. B **375** (1992) 3.

[20] T. Abe, GRAPE-Dilepton version 1.1, Comput. Phys. Commun. **136** (2001) 126 [hep-ph/0012029].

[21] R. Brun *et al.*, "Geant3", CERN-DD/EE/84-1.

[22] I. Abt *et al.* [H1 Collaboration], Nucl. Instrum. Meth. A **386** (1997) 310;
I. Abt *et al.* [H1 Collaboration], Nucl. Instrum. Meth. A **386** (1997) 348.

[23] B. Andrieu *et al.* [H1 Calorimeter Group Collaboration], Nucl. Instrum. Meth. A **336** (1993) 460.

[24] B. Andrieu *et al.* [H1 Calorimeter Group Collaboration], Nucl. Instrum. Meth. A **336** (1993) 499.

[25] B. Andrieu *et al.* [H1 Calorimeter Group Collaboration], Nucl. Instrum. Meth. A **350** (1994) 57.

[26] R. D. Appuhn *et al.* [H1 SPACAL Group Collaboration], Nucl. Instrum. Meth. A **386** (1997) 397.

[27] C. Adloff *et al.* [H1 Collaboration], Eur. Phys. J. C **30** (2003) 1 [hep-ex/0304003].

[28] V. Andreev *et al.* [H1 Collaboration], Phys. Lett. B **561** (2003) 241 [hep-ex/0301030].

[29] M. Peez, "Recherche de déviations au Modèle Standard dans les processus de grande énergie transverse sur le collisionneur électron - proton HERA", Ph.D. thesis, Université de Lyon (2003), DESY-THESIS-2003-023
(available at http://www-h1.desy.de/psfiles/theses/).

[30] B. Portheault, "Première mesure des sections efficaces de courant chargé et neutre avec le faisceau de positrons polarisé à HERA II et analyses QCD-électrofaibles", Ph.D. thesis, Université Paris XI (2005), LAL-05-05
(available at http://www-h1.desy.de/psfiles/theses/).

[31] S. D. Ellis and D. E. Soper, Phys. Rev. D **48** (1993) 3160 [hep-ph/9305266].

[32] S. Catani *et al.*, Nucl. Phys. B **406** (1993) 187.

[33] T. N. Trinh, "Recherche de leptons excités sur le collisionneur HERA avec le détecteur H1", Ph.D. thesis, Université de la Méditerranée Aix-Marseille II (2008) (in preparation, to appear at http://www-h1.desy.de/psfiles/theses/).

[34] C. Adloff *et al.* [H1 Collaboration], Eur. Phys. J. C **13** (2000) 609 [hep-ex/9908059].

[35] A. Blondel, F. Jacquet, Proceedings of the Study of an ep Facility for Europe, ed. U. Amaldi, DESY 79/48 (1979) 391.

[36] T. Helbig and H. Spiesberger, Nucl. Phys. B **373** (1992) 73.

[37] T. Junk, Nucl. Instrum. Meth. A **434** (1999) 435 [hep-ex/9902006].

[38] S. Chekanov *et al.* [ZEUS Collaboration], Phys. Lett. B **549** (2002) 32 [hep-ex/0109018].

[39] P. Achard *et al.* [L3 Collaboration], Phys. Lett. B **568** (2003) 23 [hep-ex/0306016].

[40] J. Abdallah *et al.* [DELPHI Collaboration], Eur. Phys. J. C **46** (2006) 277 [hep-ex/0603045].

Search for ν^* at HERA (e^-p, 184 pb^{-1})

Channel	Data	SM	Signal Efficiency [%]
$\nu^*\to\nu\gamma$	7	12.3 ± 3.0	50–55
$\nu^*\to eW\to eq\bar{q}$	220	223 ± 47	40–65
$\nu^*\to eW\to e\nu\mu$	0	0.40 ± 0.05	35
$\nu^*\to eW\to e\nu e$	0	0.7 ± 0.1	45
$\nu^*\to\nu Z\to\nu q\bar{q}$	89	95 ± 21	25–55
$\nu^*\to\nu Z\to\nu ee$	0	0.19 ± 0.05	45

Table 1: Observed and predicted event yields for the studied ν^* decay channels. The analysed data sample corresponds to an integrated luminosity of 184 pb^{-1}. The error on the SM predictions includes model and experimental systematic errors added in quadrature. Typical selection efficiencies for ν^* masses ranging from 120 to 260 GeV are also indicated.

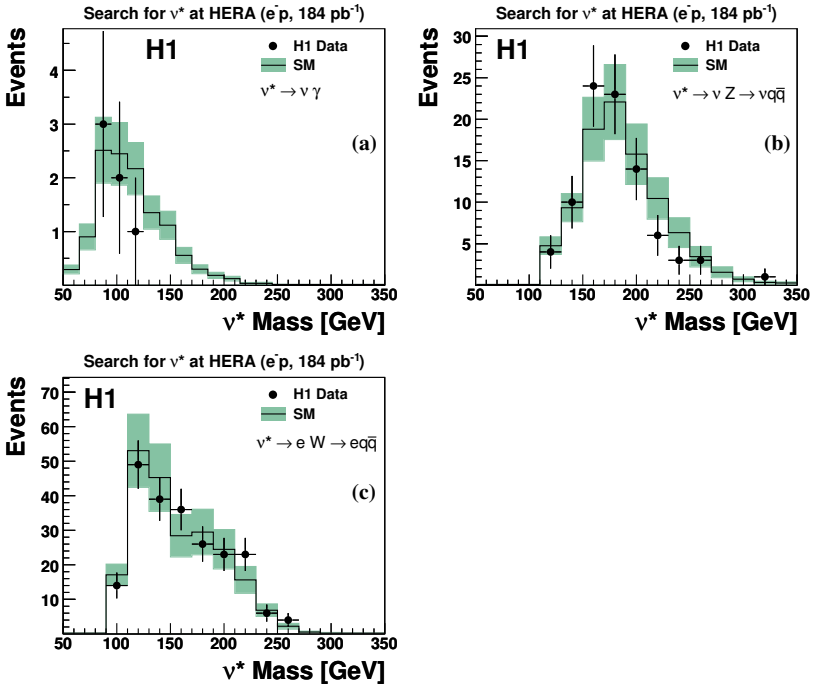

Figure 1: Invariant mass distribution of the ν^* candidates for the $\nu^* \to \nu\gamma$ (a), $\nu^* \to \nu Z \to \nu q\bar{q}$ (b) and $\nu^* \to eW \to eq\bar{q}$ (c) searches. The points correspond to the observed data events and the histogram to the SM expectation after the final selections. The error bands on the SM prediction include model and experimental systematic errors added in quadrature.

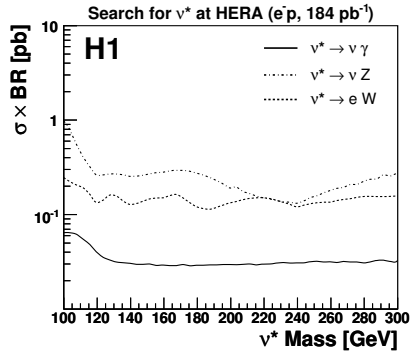

Figure 2: Upper limits at 95% CL on the product of the ν^* production cross section and decay branching ratio, $\sigma \times$ BR, in the three decay channels as a function of the excited neutrino mass. The different decay channels of the W and Z gauge bosons are combined. Areas above the curves are excluded.

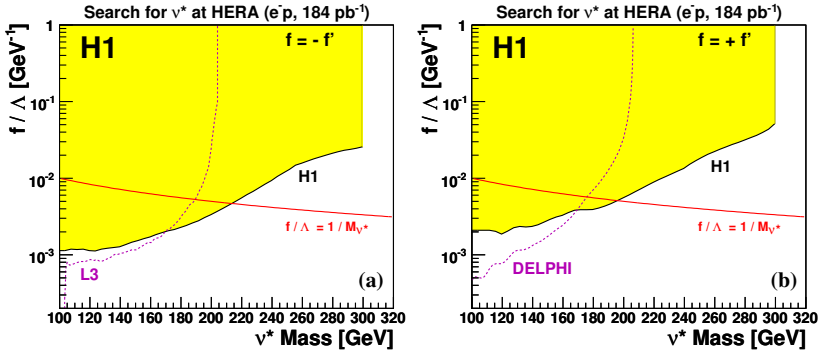

Figure 3: Exclusion limits at 95% CL on the coupling f/Λ as a function of the mass of the excited neutrino with the assumptions (a) $f = -f'$ and (b) $f = +f'$. The excluded domain based on all H1 e^-p data is represented by the shaded area. Values of the couplings above the curves are excluded. The dashed line corresponds to the exclusion limit obtained at LEP by the L3 Collaboration [39] in (a) and by the DELPHI Collaboration [40] in (b).

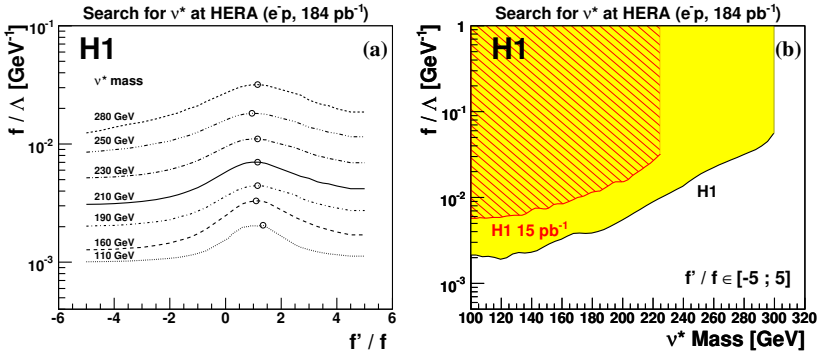

Figure 4: (a) Exclusion limits at 95% CL on the coupling f/Λ as a function of the ratio f'/f. Each curve corresponds to a different ν^* mass. The circle indicates the weakest limit for each mass. (b) Exclusion limit at 95% CL on the coupling f/Λ as a function of the mass of the excited neutrino (shaded area). This limit corresponds to the weakest limit on f/Λ for f'/f values in the interval $[-5; +5]$. The hatched area corresponds to the exclusion domain obtained by H1 in a previous analysis [2]. The regions above the lines are excluded.

Annexe F

Search for Excited Electrons in ep Collisions at HERA

F.D. Aaron *et al.* [H1 Collaboration],
Phys. Lett. B **666** (2009) 131,
arXiv:0805.4530

Abstract

A search for excited electrons is performed using the full $e^{\pm}p$ data sample collected by the H1 experiment at HERA, corresponding to a total luminosity of 475 pb^{-1}. The electroweak decays of excited electrons $e^* \to e\gamma$, $e^* \to eZ$ and $e^* \to \nu W$ with subsequent hadronic or leptonic decays of the W and Z bosons are considered. No evidence for excited electron production is found. Mass dependent exclusion limits on e^* production cross sections and on the ratio f/Λ of the coupling to the compositeness scale are derived within gauge mediated models. These limits extend the excluded region compared to previous excited electron searches. The e^* production via contact interactions is also addressed for the first time in ep collisions.

1 Introduction

The three-family structure and mass hierarchy of the known fermions is one of the most puzzling characteristics of the Standard Model (SM) of particle physics. Attractive explanations are provided by models assuming composite quarks and leptons [1]. The existence of excited states of leptons and quarks is a natural consequence of these models and their discovery would provide convincing evidence of a new scale of matter. Electron[1]-proton interactions at very high energies provide good conditions to search for excited states of first generation fermions. For instance, excited electrons (e^*) could be singly produced through the exchange of a γ or a Z boson in the t-channel.

In this letter a search for excited electrons using the complete $e^{\pm}p$ HERA collider data of the H1 experiment is presented. Electroweak decays into a SM lepton (e, ν_e) and a SM gauge boson (γ, W and Z) are considered and hadronic as well as leptonic decays of the W and Z are analysed.

The data are recorded at electron beam energy of 27.6 GeV and proton beam energies of 820 GeV and 920 GeV, corresponding to centre-of-mass energies $\sqrt{s}$ of 301 GeV and 319 GeV, respectively. The total integrated luminosity of the data is 475 pb^{-1}. The data comprise 184 pb^{-1} recorded in e^-p collisions and 291 pb^{-1} in e^+p collisions, of which 35 pb^{-1} were recorded at $\sqrt{s} = 301$ GeV. With a four-fold increase in statistics, this analysis supercedes the result of the previous H1 search for excited electrons [2]. It complements the search for excited neutrinos [3].

2 Excited Electron Models

In the present study a model [4–6] is considered in which excited fermions are assumed to have spin $1/2$ and isospin $1/2$. The left-handed and right-handed components of the excited fermions form weak iso-doublets F_L^* and F_R^*.

Interactions between excited and ordinary fermions may be mediated by gauge bosons, as described by the effective Lagrangian [5, 6]:

$$\mathcal{L}_{GM} = \frac{1}{2\Lambda}\bar{F}_R^*\,\sigma^{\mu\nu}\left[gf\frac{\tau^a}{2}W^a_{\mu\nu} + g'f'\frac{Y}{2}B_{\mu\nu} + g_s f_s\frac{\lambda^a}{2}G^a_{\mu\nu}\right]F_L + h.c.\,. \qquad (1)$$

Only the right-handed component of the excited fermion F_R^* is allowed to couple to light fermions, in order to protect the light leptons from radiatively acquiring a large anomalous magnetic moment [7, 8]. The matrix $\sigma^{\mu\nu}$ is the covariant bilinear tensor, $W^a_{\mu\nu}$, $B_{\mu\nu}$ and $G^a_{\mu\nu}$ are the field-strength tensors of the SU(2), U(1) and SU(3)$_C$ gauge fields, τ^a, Y and λ^a are the Pauli matrices, the weak hypercharge operator and the Gell-Mann matrices, respectively. The standard electroweak and strong gauge couplings are denoted by g, g' and g_s, respectively. The parameter Λ has units of energy and can be regarded as the compositeness scale which reflects the range of the new confinement force. The constants f, f' and f_s are coupling parameters associated to the three gauge groups and are determined by the yet unknown composite dynamics.

[1] In this letter the term "electron" refers to both electron and positrons, if not otherwise stated.

Following this model of gauge mediated (GM) interactions, single e^* production in ep collisions may result from the t-channel exchange of a γ or Z boson. Since the e^* is expected not to have strong interactions, the present search is insensitive to f_s. The produced e^* may decay into a lepton and an electroweak gauge boson via $e^*\to e\gamma$, $e^*\to\nu W$ and $e^*\to eZ$. For a given e^* mass value M_{e^*} and assuming a numerical relation between f and f', the e^* branching ratios are fixed and the production cross section depends only on f/Λ. In most analyses the assumption is made that the coupling parameters f and f' are of comparable strength and only the relationships $f = -f'$ and $f = +f'$ are considered. In the case $f = -f'$, the excited electron does not couple to the photon and therefore the e^* production cross section at HERA is small. Therefore, only the case $f = +f'$ is considered in this analysis.

In addition to GM interactions, novel composite dynamics may be visible as contact interactions (CI) between excited fermions and SM quarks and leptons. Such interactions can be described by the effective four-fermion Lagrangian [5]:

$$\mathcal{L}_{CI} = \frac{4\,\pi}{2\,\Lambda^2}\,j^\mu j_\mu\,, \qquad (2)$$

where Λ is assumed to be the same parameter as in the Lagrangian (1) and j_μ is the fermion current

$$j_\mu = \eta_L\bar{F}_L^*\gamma_\mu F_L + \eta'_L\bar{F}_L\gamma_\mu F_L + \eta''_L\bar{F}_L^*\gamma_\mu F_L^* + h.c. + (L\to R)\,. \qquad (3)$$

Conventionally, the η factors are set to one for the left-handed and to zero for the right-handed current.

Contact interactions may induce changes in the cross section of neutral current (NC) deep-inelastic scattering (DIS) $ep \to eX$. Searches for deviations from the SM cross section at the highest squared momentum transfers Q^2 in NC DIS processes have excluded values of Λ between 1.6 TeV and 5.5 TeV, depending on the chiral structure considered [9]. Contact interactions may also mediate the resonant production of excited electrons in ep collisions as well as their decays into an electron and a pair of SM fermions. The e^* production and decay by both gauge and contact interactions is also considered in this analysis. In this case the total e^* production cross section σ_{GM+CI} is the sum of pure GM and CI cross sections and of the interference between the two processes [10]. For simplicity, the relative strength of gauge and contact interactions are fixed by setting the parameters f and f' of the gauge interaction to one. The ratio of the GM+CI and GM cross sections $\sigma_{GM+CI}/\sigma_{GM}$ then depends only on Λ and on the e^* mass. For $M_{e^*} = 150$ GeV and $\Lambda = 1$ TeV, $\sigma_{GM+CI}/\sigma_{GM}$ is equal to 8.4, but reduces to 1.3 for $\Lambda = 4$ TeV. Relative branching ratios of GM and CI decays are determined by the e^* partial widths in each decay channel [5]. In the sensitive domain of the present analysis ($\Lambda \simeq 4$ TeV and 100 GeV $< M_{e^*} < 200$ GeV), more than 95% of e^* decays are gauge mediated. Therefore, only GM decay channels are used for the present search.

3 Simulation of Signal and Background Processes

The Monte Carlo (MC) event generator COMPOS [11] is used for the calculation of the e^* production cross section and to determine the signal detection efficiencies. It is based on the cross section formulae for gauge mediated interactions [4, 5]. Cross section formulae for contact interaction production and for the interference between contact and gauge interactions [10] have also been incorporated into COMPOS. Only e^* decays via gauge mediated interactions are simulated. Initial state radiation of a photon from the incident electron is included using the Weizsäcker–Williams approximation [12]. The proton parton densities are taken from the CTEQ5L [13] parametrisation and are evaluated at the scale $\sqrt{Q^2}$. The parton shower approach [14] is applied in order to simulate Quantum Chromodynamics (QCD) corrections in the initial and final states. Hadronisation is performed using Lund string fragmentation as implemented in PYTHIA [14]. The COMPOS generator uses the narrow width approximation (NWA) for the calculation of the production cross section and takes into account the natural width of the excited electron for the e^* decay. The NWA is valid for e^* masses below 290 GeV and the couplings f/Λ relevant to this analysis, as the total e^* width is less than 10% of the e^* mass.

The Standard Model (SM) processes which may mimic the e^* signal are QED Compton scattering, neutral current and charged current (CC) deep-inelastic scattering and to a lesser extent photoproduction, lepton pair production and real W boson production.

The RAPGAP [15] event generator, which implements the Born, QCD Compton and Boson Gluon Fusion matrix elements, is used to model NC DIS events. The QED radiative effects arising from real photon emission from both the incoming and outgoing electrons are simulated using the HERACLES [16] program. Direct and resolved photoproduction of jets and prompt photon production are simulated using the PYTHIA event generator. The simulation is based on Born level hard scattering matrix elements with radiative QED corrections. In RAPGAP and PYTHIA, jet production from higher order QCD radiation is simulated using leading logarithmic parton showers and hadronisation is modelled with Lund string fragmentation. The leading order MC prediction of NC DIS and photoproduction processes with two or more high transverse momentum jets is scaled by a factor of 1.2 to account for missing higher order QCD contributions in the MC generators [19,20]. Charged current DIS events are simulated using the DJANGO [17] program, which includes first order leptonic QED radiative corrections based on HERACLES. The production of two or more jets in DJANGO is accounted for using the colour-dipole-model [18]. Contributions from elastic and quasi-elastic QED Compton scattering are simulated with the WABGEN [21] generator. Contributions arising from the production of W bosons and multi-lepton events are modelled using the EPVEC [22] and GRAPE [23] event generators, respectively.

Generated events are passed through the full GEANT [24] based simulation of the H1 apparatus, which takes into account the actual running conditions of the data taking, and are reconstructed and analysed using the same program chain as for the data.

4 Experimental Conditions

A detailed description of the H1 experiment can be found in [25]. Only the detector components relevant to the present analysis are briefly described here. The origin of the H1 coordinate system is the nominal ep interaction point, with the direction of the proton beam defining the positive z-axis (forward region). Transverse momentum (P_T) is measured in the xy plane. The pseudorapidity η is related to the polar angle θ by $\eta = -\ln\tan(\theta/2)$. The Liquid Argon (LAr) calorimeter [26] is used to measure electrons, photons and hadrons. It covers the polar angle range $4^\circ < \theta < 154^\circ$ with full azimuthal acceptance. Electromagnetic shower energies are measured with a precision of $\sigma(E)/E = 12\%/\sqrt{E/\text{GeV}} \oplus 1\%$ and hadronic energies with $\sigma(E)/E = 50\%/\sqrt{E/\text{GeV}} \oplus 2\%$, as measured in test beams [27, 28]. In the backward region, energy measurements are provided by a lead/scintillating-fiber (SpaCal) calorimeter [29] covering the angular range $155^\circ < \theta < 178^\circ$. The central ($20^\circ < \theta < 160^\circ$) and forward ($7^\circ < \theta < 25^\circ$) tracking detectors are used to measure charged particle trajectories, to reconstruct the interaction vertex and to complement the measurement of hadronic energy. The LAr and inner tracking detectors are enclosed in a super-conducting magnetic coil with a field strength of 1.16 T. The return yoke of the coil is the outermost part of the detector and is equipped with streamer tubes forming the central muon detector ($4^\circ < \theta < 171^\circ$). In the forward region of the detector ($3^\circ < \theta < 17^\circ$) a set of drift chambers detects muons and measures their momenta using an iron toroidal magnet. The luminosity is determined from the rate of the Bethe-Heitler process $ep \to ep\gamma$, measured using a photon detector located close to the beam pipe at $z = -103$ m, in the backward direction.

5 Data Analysis

The triggers employed for collecting the data used in this analysis are based on the detection of electromagnetic deposits or missing transverse energy in the LAr calorimeter [30]. The trigger efficiency is $\sim 90\%$ for events with missing transverse energy of 20 GeV, and increases above 95% for missing transverse energy above 30 GeV. Events containing an electromagnetic deposit (electron or photon) with an energy greater than 10 GeV are triggered with an efficiency close to 100%.

In order to remove background events induced by cosmic showers and other non-ep sources, the event vertex is required to be reconstructed within 35 cm in z of the nominal interaction point. In addition, topological filters and timing vetoes are applied.

The identification of electrons or photons relies on the measurement of a compact and isolated electromagnetic shower in the LAr calorimeter. The hadronic energy within a distance in the pseudorapidity-azimuth $(\eta - \phi)$ plane $R = \sqrt{\Delta\eta^2 + \Delta\phi^2} < 0.5$ around the electron (photon) is required to be below 3% of the electron (photon) energy. Furthermore, each electron (photon) candidate must be isolated from jets by a minimum distance in pseudorapidity-azimuth of $R > 0.5$ to any jet axis. The electron and photon energy and angular direction are measured by the calorimeters. Muon identification is based on a track measured in the inner tracking systems associated with signals in the muon detectors [31]. A muon candidate is required to have no more than 5 GeV deposited in a cylinder, centred on the muon track direction,

of radius 25 cm and 50 cm in the electromagnetic and hadronic sections of the LAr calorimeter, respectively. Additionally, the muon candidate is required to be separated from the closest jet and from any track by $R > 1$ and $R > 0.5$, respectively. Calorimeter energy deposits and tracks not previously identified as electron, photon or muon candidates are used to form combined cluster-track objects, from which the hadronic energy is reconstructed [32, 33]. Jets are reconstructed from these combined cluster-track objects using an inclusive k_T algorithm [34,35] with a minimum transverse momentum of 2.5 GeV. The missing transverse momentum $P_T^{\rm miss}$ of the event is derived from all detected particles and energy deposits in the event. In events with large $P_T^{\rm miss}$, the only non-detected particle in the event is assumed to be a neutrino. The four-vector of this neutrino candidate is reconstructed assuming transverse momentum conservation and the relation $\sum_i (E^i - P_z^i) + (E^\nu - P_z^\nu) = 2E_e^0 = 55.2$ GeV, where the sum runs over all detected particles, P_z is the momentum along the proton beam axis and E_e^0 is the electron beam energy.

Specific selection criteria applied in each decay channel are presented in the following subsections. A detailed description of the analysis can be found in [36].

5.1 $e\gamma$ Resonance Search

The signature of the $e^* \to e\gamma$ decay channel consists of two high P_T isolated electromagnetic clusters. SM background arises mainly from elastic and inelastic QED Compton events. Two isolated electromagnetic clusters are required, each with transverse momentum $P_T > 15$ GeV and polar angle $5^\circ < \theta < 130^\circ$. No explicit electron and photon identification based on tracking conditions is performed in order to retain a high selection efficiency. To reduce contributions from QED Compton processes, the sum of the energies of the two electromagnetic clusters is required to be greater than 110 GeV and the sum of their total transverse momenta has to be larger than 75 GeV.

After this selection, the SM background from elastic QED Compton events is smaller than that from inelastic QED Compton processes. Since about half of the e^* production cross section is expected from elastic e^* production [4], the analysis is separated into two parts. Events with a total hadronic energy $E_h < 5$ GeV are used to search for elastic e^* production, whereas the other events are attributed to possible inelastic e^* production.

In the elastic channel 42 events are selected in the data compared to a SM expectation of 48 ± 4. In the inelastic channel 65 events are found for 65 ± 8 expected. The errors on the SM prediction include model and experimental systematic errors added in quadrature (see section 5.5). The invariant mass of the e^* candidate is calculated from the four-vectors of the electron and photon candidates. The invariant mass distribution of the e^* candidates and the SM background expectations are presented in figure 1(a) and (b) for the elastic and inelastic channels, respectively. The selection efficiency is 60% for $M_{e^*} = 120$ GeV, increasing to 70% for $M_{e^*} = 260$ GeV. From Monte Carlo studies, the experimental resolution on the reconstructed e^* mass distribution is 3 GeV for a generated e^* mass of 120 GeV, increasing to 6 GeV for an e^* mass of 260 GeV.

5.2 $\nu q\bar{q}$ Resonance Search

The signature of the $e^* \to \nu W \to \nu q\bar{q}$ decay channel consists of two high transverse momentum jets in events with large $P_T^{\rm miss}$. The SM background is dominated by multi-jet CC DIS events and contains moderate contributions from NC DIS and photoproduction. Events with missing transverse momentum $P_T^{\rm miss} > 20$ GeV are selected. In each event at least two jets with transverse momenta larger than 20 and 15 GeV, respectively, are required in the polar angle range $5^\circ < \theta < 130^\circ$.

The ratio V_{ap}/V_p of transverse energy flow anti-parallel and parallel to the hadronic final state [37] is used to suppress photoproduction events. Events with $V_{ap}/V_p > 0.3$ are rejected. Photoproduction and NC DIS backgrounds typically have low values of x_h, the Bjorken scaling variable calculated from the hadronic system using the Jacquet-Blondel method [37, 38], and are thus suppressed by requiring $x_h > 0.04$. In each event, a W candidate is reconstructed from the combination of those two jets with invariant mass closest to the nominal W boson mass. The reconstructed W candidate is required to have an invariant mass above 60 GeV. In order to further reduce the background from CC DIS, the invariant mass of all jets and hadrons in the event not associated to the decay of the W boson candidate is required to be below 15 GeV.

After this selection, 129 events are found compared to a SM expectation of 133 ± 32 events which is dominated by CC DIS events. The CC DIS cross section is smaller in e^+p collisions than in e^-p, in contrast to the e^* cross section which is comparable in both collision modes. Therefore, e^+p data have a larger sensitivity to a potential e^* signal in this channel than e^-p data. In the e^+p (e^-p) data sample, 33 (96) events are observed compared to a SM expectation of 51 ± 13 (82 ± 19). A significant excess is observed neither in e^+p nor in e^-p data. The invariant mass of the e^* candidate is calculated from the neutrino and W candidate four-vectors. For this calculation, the W candidate four-vector is scaled such that its mass is set to the nominal W boson mass. The invariant mass distribution of the e^* candidates and the SM background is presented in figure 1(c). The selection efficiency in this channel is 20% for $M_{e^*} = 120$ GeV, increasing to 55% for $M_{e^*} = 260$ GeV. From Monte Carlo studies, the experimental resolution on the reconstructed e^* mass distribution is 9 GeV for a generated e^* mass of 120 GeV, increasing to ~ 20 GeV for an e^* mass of 260 GeV.

5.3 $eq\bar{q}$ Resonance Search

The signature of the $e^* \to eZ \to eq\bar{q}$ decay channel consists of one electron and two high P_T jets. Multi-jet NC DIS events constitute the main background contribution from SM processes. Events are selected with an isolated electron in the LAr calorimeter in the polar angle range $5^\circ < \theta^e < 90^\circ$. The electron should have either a transverse momentum P_T^e greater than 25 GeV or the variable[2] $\xi^e = E^e \cos^2(\theta^e/2)$ above 23 GeV. These conditions remove a large part of the NC DIS contribution. The events are required to have at least two jets in the polar angle range $5^\circ < \theta^{\rm jet} < 130^\circ$ with transverse momenta larger than 20 and 15 GeV, respectively. In each event, a Z candidate is reconstructed from the combination of those two jets with invariant mass closest to the nominal Z boson mass. The reconstructed mass of the Z candidate is required to

[2] For NC DIS events, this variable is proportional to the four-momentum transfer squared Q^2.

be larger than 70 GeV. To further reduce the NC DIS background the polar angle of the jet with the highest P_T associated to the Z candidate is required to be less than 80°. The polar angle of the second jet is required to be greater than 10° in events with $P_T^{\text{jet}_2} < 25$ GeV.

After this selection, 286 events are observed while 277 ± 62 are expected from the SM. The invariant mass of the e^* candidate is calculated from the electron and Z candidate four-vectors. For this calculation, the Z candidate four-vector is scaled such that its mass is set to the nominal Z boson mass. The invariant mass distribution of the e^* candidates and the SM background is presented in figure 1(d). The selection efficiency in this channel is 20% for $M_{e^*} = 120$ GeV, increasing to 55% for $M_{e^*} = 260$ GeV. From Monte Carlo studies, the experimental resolution on the reconstructed e^* mass distribution is 2 GeV for a generated e^* mass of 120 GeV, increasing to 8 GeV for an e^* mass of 260 GeV.

5.4 eee, $e\mu\mu$ and $e\nu\nu$ Resonance Searches

In the search for $e^* \to eZ \to eee$, events with three electrons of high transverse momenta are selected. The electrons must be detected in the polar angle range $5^\circ < \theta^e < 150^\circ$ and have transverse momenta larger than 25, 20 and 15 GeV, respectively. To reduce the background from QED Compton processes, each electron in the central region ($\theta^e > 35^\circ$) must be associated to a charged track. A Z candidate is reconstructed from the combination of the two electrons with an invariant mass closest to the nominal Z boson mass. The reconstructed mass of the Z candidate is required be compatible with the nominal Z boson mass within 7 GeV. After this selection no data event remains, while 0.72 ± 0.06 SM background events are expected. The selection efficiency for e^* with masses above 120 GeV is $\sim 60\%$.

In the search for $e^* \to eZ \to e\mu\mu$, events are selected with one electron with transverse momentum above 20 GeV and two muons with transverse momenta above 15 and 10 GeV, respectively. The electron and the muons must be detected in the polar angle ranges $5^\circ < \theta^e < 150^\circ$ and $10^\circ < \theta^\mu < 160^\circ$, respectively. A Z candidate is reconstructed from the combination of the two muons and its reconstructed mass is required to be larger than 60 GeV. After this selection no data event remains, while 0.52 ± 0.05 SM background events are expected. The selection efficiency in this channel is $\sim 40\%$ for $M_{e^*} = 120$ GeV, decreasing to 15% for $M_{e^*} = 260$ GeV.

The signatures of the $e^* \to \nu W \to \nu e \nu$ and $e^* \to eZ \to e\nu\nu$ channels are similar and consist of one high P_T electron in events with large missing transverse momentum. Events with $P_T^{\text{miss}} > 25$ GeV and one electron with $P_T > 20$ GeV are selected. The electron is detected in the polar angle range $5^\circ < \theta^e < 100^\circ$ and is required to be isolated from jets by a minimum distance of $R > 1$. To reduce the background from radiative CC DIS processes, a track must be associated to the electron in the central region ($\theta^e > 35^\circ$). Events from photoproduction are suppressed by requiring $V_{ap}/V_p < 0.1$. Remaining NC DIS events are removed by requiring that the longitudinal momentum balance of the event be $\sum_i (E_i - P_{z,i}) < 45$ GeV, where the sum runs over all visible particles. In order to remove background arising from SM W production, the hadron system is required to have a total transverse momentum $P_T^h < 20$ GeV and to exhibit a polar angle γ_h, as defined in [37], below 80°. In each event, only one neutrino candidate can be reconstructed, from the total missing transverse momentum, as explained at the beginning of section 5. The invariant mass of the e^* candidate in the $e\nu\nu$ final state is therefore estimated from

the four-vectors of the neutrino candidate and the electron candidate. To further remove background from W production, only events in which the reconstructed e^* mass is above 90 GeV are considered. After this selection four data events remain, while 4.5 ± 0.7 SM background events are expected. The selection efficiency for the $e^* \to \nu W \to \nu e \nu$ ($e^* \to eZ \to e\nu\nu$) signature is $\sim 60\%$ ($\sim 35\%$) for e^* with masses above 120 GeV.

5.5 Systematic Uncertainties

The following experimental systematic uncertainties are considered:

- The uncertainty on the electromagnetic energy scale varies between 0.7% and 2% depending on the polar angle. The polar angle measurement uncertainty is 3 mrad for electromagnetic clusters.
- The scale uncertainty on the transverse momentum of high P_T muons amounts to 2.5%. The uncertainty on the reconstruction of the muon polar angle is 3 mrad.
- The hadronic energy scale is known within 2%. The uncertainty on the jet polar angle determination is 10 mrad.
- The uncertainty on the trigger efficiency is 3%.
- The luminosity measurement has an uncertainty of 3%.

The effect of the above systematic uncertainties on the SM expectation and the signal efficiency are determined by varying the experimental quantities by ± 1 standard deviation in the MC samples and propagating these variations through the whole analysis chain.

Additional model systematic uncertainties are attributed to the SM background MC generators described in section 3. An error of 20% on the normalisation of NC DIS, CC DIS and photoproduction processes with at least two high P_T jets is considered to account for the uncertainty on higher order QCD corrections. The error on the elastic and quasi-elastic QED Compton cross sections is conservatively estimated to be 5%. The error on the inelastic QED Compton cross section is 10%. The errors attributed to lepton pair and W production are 3% and 15%, respectively. The total error on the SM background prediction is determined by adding the effects of all model and experimental systematic uncertainties in quadrature.

The theoretical uncertainty on the e^* production cross section is dominated by the uncertainty on the scale at which the proton parton densities are evaluated. It is estimated by varying this scale from $\sqrt{Q^2}/2$ to $2\sqrt{Q^2}$. The resulting uncertainty depends on the e^* mass and is 10% at $M_{e^*} = 100$ GeV, increasing to 15% at $M_{e^*} = 300$ GeV.

6 Interpretation

The event yields observed in all decay channels are in agreement with the corresponding SM expectations and are summarised in table 1. The SM predictions are dominated by QED Compton for the $e\gamma$ resonance search, by CC DIS in the $\nu q\bar{q}$ resonance search and by NC DIS processes for the $eq\bar{q}$ resonance search. The distributions of the invariant mass of the data events are in agreement with those of the expected SM background as shown in figure 1. Few or no data events are observed in channels corresponding to leptonic decays of the W or Z bosons, in agreement with the low SM expectations.

Since no evidence for the production of excited electrons is observed, upper limits on the e^* production cross section and on the model parameters are derived as a function of the mass of the excited electron. Limits are presented at the 95% confidence level (CL) and are obtained from the mass spectra using a modified frequentist approach which takes statistical and systematic uncertainties into account [39].

Upper limits on the product of the e^* production cross section and of the e^* decay branching ratio are shown in figure 2. The analysed decay channels of the W and Z gauge bosons are combined. Considering pure gauge interactions, the resulting limit on f/Λ after combination of all decay channels is displayed as a function of the e^* mass in figure 3, for the conventional assumption $f = +f'$. The total fraction of all possible e^* gauge decay channels covered in this analysis is $\sim 88\%$. The limit extends up to e^* masses of 290 GeV. Considering the assumption $f/\Lambda = 1/M_{e^*}$ excited electrons with masses up to 272 GeV are excluded. The relative contributions of the e^* decay channels to the combined limit are shown in figure 3(a). At low mass, the combined limit on f/Λ is dominated by the $e^*{\rightarrow}e\gamma$ channel, while the $e^* \rightarrow \nu W$ channel starts to contribute to the limit for masses above 200 GeV. These new results extend the previously published limits by H1 [2] and ZEUS [40] by more than a factor of two in f/Λ. Figure 3(b) shows direct and indirect limits on e^* production obtained in e^+e^- collisions at LEP by the OPAL Collaboration [41] and DELPHI Collaboration [42], respectively. The result of the most recent search for e^* production within gauge mediated models obtained at the Tevatron by the CDF Collaboration is also indicated [43]. The limit from the present analysis extends at high mass beyond the kinematic reach of LEP searches and to lower f/Λ values than are reached by Tevatron searches.

If e^* production is considered via gauge and contact interactions together, an upper limit on $1/\Lambda$ is also obtained, under the assumption $f = f' = 1$. Possible e^* decays by either gauge or contact interactions are taken into account and the efficiency of the analysis to e^* CI decays is conservatively assumed to be zero. The limit on $1/\Lambda$ as a function of the e^* mass is displayed in figure 4. For e^* masses below 250 GeV, the additional contribution of CI to e^* production changes the limit on Λ by a factor of 1.15 to 1.2. A limit on Λ as a function of the e^* mass is also obtained at the Tevatron by considering single e^* production via contact interactions only, followed by its gauge decay into an electron and a photon [44].

7 Conclusion

Using the full $e^{\pm}p$ data sample collected by the H1 experiment at HERA with an integrated luminosity of 475 pb^{-1} a search for the production of excited electrons is performed. The excited electron decay channels $e^*{\rightarrow}e\gamma$, $e^*{\rightarrow}eZ$ and $e^*{\rightarrow}\nu W$ with subsequent hadronic or leptonic decays of the W and Z bosons are considered and no indication of a signal is found. New limits on the production cross section of excited electrons are obtained. Within gauge mediated models, an upper limit on the coupling f/Λ as a function of the excited electron mass is established for the specific relation $f = +f'$ between the couplings. Assuming $f = +f'$ and $f/\Lambda = 1/M_{e^*}$ excited electrons with a mass lower than 272 GeV are excluded at 95% confidence level. For the first time in ep collisions, gauge and four-fermion contact interactions are also considered together for e^* production and decays. In this scenario and assuming the same Λ parameter in contact and gauge interactions as well as $f = +f' = 1, \eta_L = 1$ and $\eta_R = 0$, the limit on $1/\Lambda$ improves only slightly, demonstrating that the gauge interaction mechanism is dominant for excited electron processes at HERA. The results presented in this paper extend previously excluded domain at HERA, LEP or Tevatron.

Acknowledgements

We are grateful to the HERA machine group whose outstanding efforts have made this experiment possible. We thank the engineers and technicians for their work in constructing and maintaining the H1 detector, our funding agencies for financial support, the DESY technical staff for continual assistance and the DESY directorate for the hospitality which they extend to the non DESY members of the collaboration. We also wish to thank M. Spira for many useful discussions and for providing the cross section calculation for excited electron production including contact interactions in ep collisions.

References

[1] H. Harari, Phys. Rept. **104** (1984) 159.

[2] C. Adloff *et al.* [H1 Collaboration], Phys. Lett. B **548** (2002) 35 [hep-ex/0207038].

[3] F. D. Aaron *et al.* [H1 Collaboration], Accepted by Phys. Lett. B, in press, arXiv:0802.1858 [hep-ex].

[4] K. Hagiwara, S. Komamiya and D. Zeppenfeld, Z. Phys. C **29** (1985) 115.

[5] U. Baur, M. Spira and P. M. Zerwas, Phys. Rev. D **42** (1990) 815.

[6] F. Boudjema, A. Djouadi and J. L. Kneur, Z. Phys. C **57** (1993) 425.

[7] S. J. Brodsky and S. D. Drell, Phys. Rev. D **22** (1980) 2236.

[8] F. M. Renard, Phys. Lett. B **116** (1982) 264.

[9] C. Adloff *et al.* [H1 Collaboration], Phys. Lett. B **568** (2003) 35 [hep-ex/0305015].

[10] M. Spira, private communication.

[11] T. Köhler, "Exotic Processes At Hera: The Event Generator COMPOS", Proceedings of the Workshop "Physics at HERA", eds. W. Buchmüller and G. Ingelman, DESY (1991), vol. 3, p. 1526.

[12] C. Berger and W. Wagner, Phys. Rept. **146** (1987) 1.

[13] J. Pumplin *et al.*, JHEP **0207** (2002) 012 [hep-ph/0201195].

[14] T. Sjöstrand *et al.*, PYTHIA version 6.1, Comput. Phys. Commun. **135** (2001) 238 [hep-ph/0010017].

[15] H. Jung, RAPGAP version 3.1, Comput. Phys. Commun. **86** (1995) 147.

[16] A. Kwiatkowski, H. Spiesberger and H. J. Möhring, Comput. Phys. Commun. **69** (1992) 155.

[17] G. A. Schuler and H. Spiesberger, DJANGOH version 1.4, "Django: The Interface for The Event Generators Heracles and Lepto", Proceedings of the Workshop "Physics at HERA", eds. W. Buchmüller and G. Ingelman, DESY (1991), vol. 3, p. 1419.

[18] L. Lönnblad, Comput. Phys. Commun. **71** (1992) 15.

[19] C. Adloff *et al.* [H1 Collaboration], Eur. Phys. J. C **25** (2002) 13 [hep-ex/0201006].

[20] A. Aktas *et al.* [H1 Collaboration], Phys. Lett. B **602** (2004) 14 [hep-ex/0408044].

[21] C. Berger and P. Kandel, "A New Generator For Wide Angle Bremsstrahlung," Proceedings of the Workshop "Monte Carlo Generators for HERA Physics", eds. A. T. Doyle, G. Grindhammer, G. Ingelman and H. Jung, DESY (1998).

[22] U. Baur, J. A. Vermaseren and D. Zeppenfeld, Nucl. Phys. B **375** (1992) 3.

[23] T. Abe, GRAPE-Dilepton version 1.1, Comput. Phys. Commun. **136** (2001) 126 [hep-ph/0012029].

[24] R. Brun, *et al.*, "GEANT3", CERN-DD/EE/84-1.

[25] I. Abt *et al.* [H1 Collaboration], Nucl. Instrum. Meth. A **386** (1997) 310;
I. Abt *et al.* [H1 Collaboration], Nucl. Instrum. Meth. A **386** (1997) 348.

[26] B. Andrieu *et al.* [H1 Calorimeter Group Collaboration], Nucl. Instrum. Meth. A **336** (1993) 460.

[27] B. Andrieu *et al.* [H1 Calorimeter Group Collaboration], Nucl. Instrum. Meth. A **350** (1994) 57.

[28] B. Andrieu *et al.* [H1 Calorimeter Group Collaboration], Nucl. Instrum. Meth. A **336** (1993) 499.

[29] R. D. Appuhn *et al.* [H1 SPACAL Group Collaboration], Nucl. Instrum. Meth. A **386** (1997) 397.

[30] C. Adloff *et al.* [H1 Collaboration], Eur. Phys. J. C **30** (2003) 1 [hep-ex/0304003].

[31] V. Andreev *et al.* [H1 Collaboration], Phys. Lett. B **561** (2003) 241 [hep-ex/0301030].

[32] M. Peez, "Recherche de déviations au Modèle Standard dans les processus de grande énergie transverse sur le collisionneur électron - proton HERA", Ph.D. thesis, Université de Lyon (2003), DESY-THESIS-2003-023
(available at http://www-h1.desy.de/psfiles/theses/).

[33] B. Portheault, "Première mesure des sections efficaces de courant chargé et neutre avec le faisceau de positrons polarisé à HERA II et analyses QCD-électrofaibles", Ph.D. thesis, Université Paris XI (2005), LAL-05-05
(available at http://www-h1.desy.de/psfiles/theses/).

[34] S. D. Ellis and D. E. Soper, Phys. Rev. D **48** (1993) 3160 [hep-ph/9305266].

[35] S. Catani *et al.*, Nucl. Phys. B **406** (1993) 187.

[36] T. N. Trinh, "Recherche de leptons excités sur le collisionneur HERA avec le détecteur H1", Ph.D. thesis, Université de la Méditerranée Aix-Marseille II (2008)
(in preparation, to appear at http://www-h1.desy.de/psfiles/theses/).

[37] C. Adloff *et al.* [H1 Collaboration], Eur. Phys. J. C **13** (2000) 609 [hep-ex/9908059].

[38] A. Blondel and F. Jacquet, Proceedings of the Study of an ep Facility for Europe, ed. U. Amaldi, DESY 79/48 (1979) 391.

[39] T. Junk, Nucl. Instrum. Meth. A **434** (1999) 435 [hep-ex/9902006].

[40] S. Chekanov *et al.* [ZEUS Collaboration], Phys. Lett. B **549** (2002) 32 [hep-ex/0109018].

[41] G. Abbiendi *et al.* [OPAL Collaboration], Phys. Lett. B **544** (2002) 57 [hep-ex/0206061].

[42] J. Abdallah *et al.* [DELPHI Collaboration], Eur. Phys. J. C **37** (2004) 405 [hep-ex/0409058].

[43] D. Acosta *et al.* [CDF Collaboration], Phys. Rev. Lett. **94** (2005) 101802, [hep-ex/0410013].

[44] V. M. Abazov *et al.* [DØ Collaboration], Accepted by Phys. Rev. D Rapid Comm., arXiv:0801.0877 [hep-ex].

Search for e^* at HERA (475 pb^{-1})

Channel	Data	SM	Signal Efficiency [%]
$e^*\to e\gamma$ (ela.)	42	48 ± 4	60–70
$e^*\to e\gamma$ (inel.)	65	65 ± 8	60–70
$e^*\to \nu W\to \nu q\bar{q}$	129	133 ± 32	20–55
$e^*\to \nu W\to \nu e\nu$	4	4.5 ± 0.7	60
$e^*\to eZ\to e\nu\nu$			35
$e^*\to eZ\to eq\bar{q}$	286	277 ± 62	20–55
$e^*\to eZ\to eee$	0	0.72 ± 0.06	60
$e^*\to eZ\to e\mu\mu$	0	0.52 ± 0.05	40–15

Table 1: Observed and predicted event yields for the studied e^* decay channels. The analysed data sample corresponds to an integrated luminosity of 475 pb^{-1}. The errors on the SM predictions include model and experimental systematic errors added in quadrature. Typical selection efficiencies for e^* masses ranging from 120 to 260 GeV are also indicated.

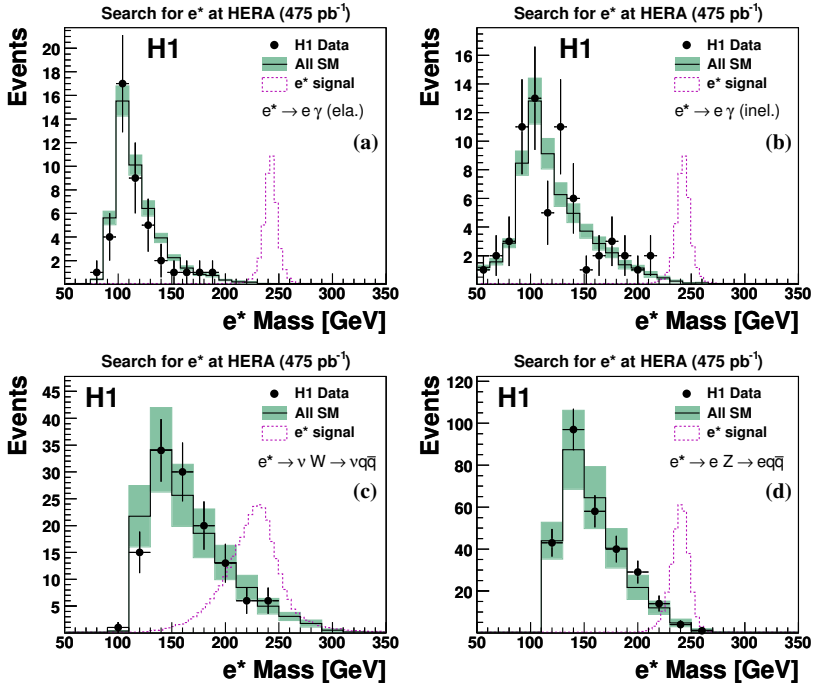

Figure 1: Invariant mass distribution of the e^* candidates in the elastic $e^*\to e\gamma$ (a), inelastic $e^*\to e\gamma$ (b), $e^*\to \nu W\to \nu q\bar{q}$ (c), and $e^*\to eZ\to eq\bar{q}$ (d) search channels. The points correspond to the observed data events and the histograms to the SM expectation after the final selections. The error bands on the SM prediction include model uncertainties and experimental systematic errors added in quadrature. The dashed line represents with an arbitrary normalisation the reconstructed mass distribution of e^* events with $M_{e^*} = 240$ GeV.

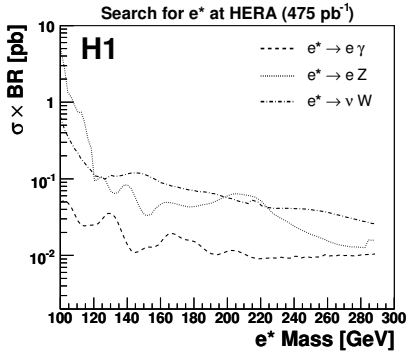

Figure 2: Upper limits at 95% CL on the product of the e^* cross section and decay branching ratio, $\sigma \times$ BR, in the three e^* decay channels as a function of the excited electron mass. The decay channels of the W and Z gauge bosons are combined. Areas above the curves are excluded.

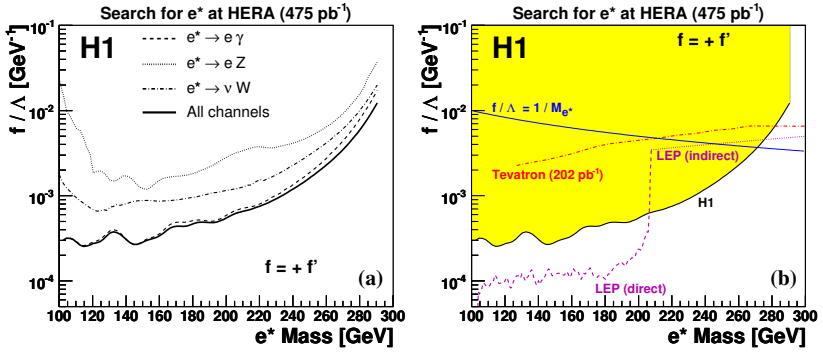

Figure 3: Exclusion limits at 95% CL on the coupling f/Λ as a function of the mass of the excited electron considering gauge mediated interactions only, with the assumption $f = +f'$. The separate contributions of the different e^* decay channels are presented in (a). Values of the couplings above the curves are excluded. The excluded domain based on all H1 $e^{\pm}p$ data is represented in (b) by the shaded area. It is compared to the direct (dashed line) and indirect (dotted line) exclusion limits obtained at LEP by the OPAL Collaboration [41] and by the DELPHI Collaboration [42], respectively. The result from the Tevatron obtained by the CDF experiment [43] is also shown (dashed-dotted line). The curve $f/\Lambda = 1/M_{e^*}$ is indicated in (b).

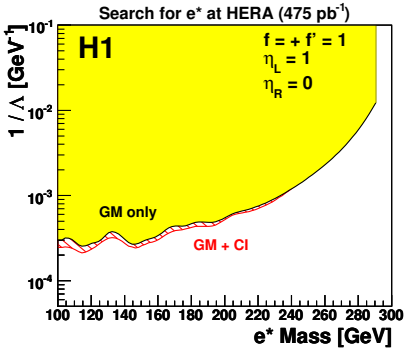

Figure 4: Exclusion limits at 95% CL on the inverse of the compositeness scale $1/\Lambda$ as a function of the mass of the excited electron. The excluded domain obtained by considering e^* production via gauge mediated interactions only and under the assumption $f = +f' = 1$ is represented by the shaded area. The hatched area corresponds to the additional domain excluded if gauge mediated and contact interactions are considered together for e^* production. Areas above the curves are excluded.

Annexe G

Search for Excited Quarks in ep Collisions at HERA

F.D. Aaron *et al.* [H1 Collaboration],
Phys. Lett. B **678** (2009) 335,
arXiv:0904.3392

Abstract

A search for excited quarks is performed using the full $e^{\pm}p$ data sample collected by the H1 experiment at HERA, corresponding to a total integrated luminosity of 475 pb^{-1}. The electroweak decays of excited quarks $q^* \to q\gamma$, $q^* \to qZ$ and $q^* \to qW$ with subsequent hadronic or leptonic decays of the W and Z bosons are considered. No evidence for first generation excited quark production is found. Mass dependent exclusion limits on q^* production cross sections and on the ratio f/Λ of the coupling to the compositeness scale are derived within gauge mediated models. These limits extend the excluded region compared to previous excited quark searches.

1 Introduction

The three-family structure and mass hierarchy of the known fermions is one of the most puzzling characteristics of the Standard Model (SM) of particle physics. Attractive explanations are provided by models assuming a composite structure of quarks and leptons [1]. The existence of excited states of leptons and quarks is a natural consequence of these models and their discovery would be a convincing evidence of a new scale of matter. Electron[1]-proton interactions at high energies provide the opportunity to search for excited states of first generation fermions. For instance, excited quarks (q^*) could be singly produced through the exchange of a γ or a Z boson.

In this paper a search for excited quarks using the complete $e^{\pm}p$ HERA collider data of the H1 experiment is presented. Electroweak decays of the excited quark into a SM quark and a gauge boson (γ, W and Z) are considered and both hadronic and leptonic decays of the W and Z bosons are analysed.

The data were recorded at an electron beam energy of 27.6 GeV and proton beam energies of 820 GeV or 920 GeV, corresponding to centre-of-mass energies $\sqrt{s}$ of 301 GeV and 319 GeV, respectively. The total integrated luminosity of the data sample is 475 pb^{-1}. The data comprise 184 pb^{-1} recorded in e^-p collisions and 291 pb^{-1} in e^+p collisions, of which 35 pb^{-1} were recorded at $\sqrt{s} = 301$ GeV. With more than a twelve-fold increase in statistics and a higher centre-of-mass energy, this analysis supersedes the result of previous searches for excited quarks at HERA by the H1 [2] and ZEUS [3] Collaborations and is complementary to exclusion limits obtained at the LEP collider [4] and at the Tevatron [5–8]. The analysis also complements searches for first generation excited neutrinos [9] and electrons [10] at HERA.

2 Phenomenology

In the present study a model [11–13] is considered in which excited fermions are assumed to have spin $1/2$ and weak isospin $1/2$. The left-handed and right-handed components of the excited fermions form weak iso-doublets F^*_L and F^*_R. Interactions between excited and ordinary fermions may be mediated by gauge bosons, as described by the effective Lagrangian [12, 13]:

$$\mathcal{L}_{int.} = \frac{1}{2\Lambda}\bar{F^*_R}\,\sigma^{\mu\nu}\left[gf\frac{\tau^a}{2}W^a_{\mu\nu} + g'f'\frac{Y}{2}B_{\mu\nu} + g_s f_s\frac{\lambda^a}{2}G^a_{\mu\nu}\right]\,F_L + h.c.\,. \qquad (1)$$

Only the right-handed component of the excited fermions F^*_R is allowed to couple to light fermions F_L, in order to protect the light leptons from radiatively acquiring a large anomalous magnetic moment [14, 15]. The matrix $\sigma^{\mu\nu}$ is the covariant bilinear tensor, $W^a_{\mu\nu}$, $B_{\mu\nu}$ and $G^a_{\mu\nu}$ are the field-strength tensors of the SU(2), U(1) and SU(3)$_C$ gauge fields, τ^a, Y and λ^a are the Pauli matrices, the weak hypercharge operator and the Gell-Mann matrices. The standard electroweak and strong gauge couplings are denoted by g, g' and g_s, respectively. The parameter Λ has units of energy and can be regarded as the compositeness scale which reflects the range

[1] In this paper the term "electron" is used generically to refer to both electrons and positrons, unless otherwise stated.

of the new confinement force. The constants f, f' and f_s are coupling parameters associated with the three gauge groups and are determined by the yet unknown composite dynamics.

Following this model of gauge mediated interactions, excited quarks may be resonantly produced in ep collisions through a gauge boson exchange between the incoming electron and a quark of the proton (see figure 1(a)). The exchange of excited quarks in the u-channel (figure 1(b)) is also possible for the high q^* masses and low values of Λ probed in this analysis. For example, for $\Lambda = 50$ GeV, $f = f' = 1$ and an excited quark of mass $M_{q^*} = 300$ GeV, the u-channel production cross section is 0.016 pb while the resonant production cross section is 0.27 pb.

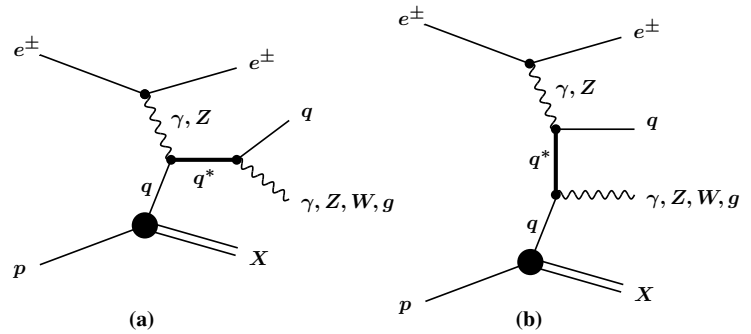

Figure 1: Diagrams for the production and decay of excited quarks in ep collisions.

The excited quark may decay into a quark and a gauge boson via $q^*\to q\gamma$, $q^*\to qW$, $q^*\to qZ$ and $q^*\to qg$. For a given q^* mass value and assuming a numerical relation between f, f' and f_s, the q^* branching ratios are fixed and the production cross section depends only on f/Λ. Only γ, W and Z decays of the q^* are considered in the present study. In this analysis, the assumptions are made that the coupling parameters f and f' are of comparable strength, with the relationship $f = f'$, and that $f_s = 0$. These assumptions lead to results which are complementary to the q^* searches performed at the Tevatron [5–8], since at a $p\bar{p}$ collider excited quarks are dominantly produced in a quark-gluon fusion mechanism, which requires $f_s \neq 0$. The effect of non-zero values of f_s is also studied in the present analysis.

3 Simulation of Signal and Background Processes

A Monte Carlo (MC) program developed for this analysis is used for the calculation of the q^* production cross section and the simulation of signal events. The events are simulated using the cross section calculated from the Lagrangian described in equation (1) using the CompHEP program [16]. Both resonant q^* production and u-channel exchange processes, as well as their interference are included. Initial state radiation of a photon from the incident electron is included using the Weizsäcker-Williams approximation [17]. The proton parton densities are

taken from the CTEQ5L [18] parametrisation and are evaluated at the scale $\sqrt{\hat{s}} = \sqrt{sx}$, where x is the momentum fraction of the proton carried by the interacting quark. The parton shower approach [19] is applied in order to simulate Quantum Chromodynamics (QCD) corrections in the initial and final states. Hadronisation is performed using Lund string fragmentation as implemented in PYTHIA [19].

In the MC generator the full transition matrix including both q^* production and decay is implemented. This is important if the natural width of the q^* is large, which is typically the case at high mass. In order to incorporate the width effects in the signal efficiency determination, events are generated with the coupling f/Λ corresponding, for each q^* mass, to the expected boundary of the probed domain in the plane defined by M_{q^*} and f/Λ.

Excited quarks will be searched for in the $q\gamma$, $qq\bar{q}$, $qe\nu$, $q\mu\nu$, qee and $q\mu\mu$ final states. The SM background processes that may mimic the q^* signal are prompt photon production, neutral current (NC) deep inelastic scattering (DIS), photoproduction, single W boson production and lepton pair production.

The RAPGAP [20] event generator, which implements the Born, QCD Compton and Boson Gluon Fusion matrix elements, is used to model NC DIS events. The QED radiative effects arising from real photon emission from both the incoming and outgoing electrons are simulated using the HERACLES [21] program. Direct and resolved photoproduction of jets and prompt photon production are simulated using the PYTHIA event generator. The simulation is based on Born level scattering matrix elements with radiative QED corrections. In RAPGAP and PYTHIA, jet production from higher order QCD radiation is simulated using leading logarithmic parton showers and hadronisation is modelled with Lund string fragmentation. The leading order MC prediction of NC DIS and photoproduction processes with two or more high transverse momentum jets is scaled by a factor of 1.2 to account for the incomplete description of higher orders in the MC generators [22,23]. Charged current DIS events are simulated using the DJANGO [24] program, which includes first order leptonic QED radiative corrections based on HERACLES. The production of two or more jets in DJANGO is accounted for using the colour dipole model [25]. Contributions from elastic and quasi-elastic QED Compton scattering are simulated with the WABGEN [26] generator. Contributions arising from the production of single W bosons and multi-lepton events are modelled using the EPVEC [27] and GRAPE [28] event generators, respectively.

Generated events are passed through a GEANT [29] based simulation of the H1 apparatus, which takes into account the actual running conditions of the data taking, and are reconstructed and analysed using the same program chain as is used for the data.

4 Experimental Conditions

A detailed description of the H1 detector can be found in [30]. Only the detector components relevant to the present analysis are briefly described here. The origin of the H1 coordinate system is the nominal ep interaction point, with the direction of the proton beam defining the positive z-axis (forward region). Transverse momentum (P_T) is measured in the x–y plane. The pseudorapidity η is related to the polar angle θ by $\eta = -\ln\tan(\theta/2)$. The Liquid Argon (LAr) calorimeter [31] is used to measure energy and direction of electrons, photons and hadrons. It covers the polar angle range $4^\circ < \theta < 154^\circ$ with full azimuthal acceptance. Electromagnetic shower energies are measured with a precision of $\sigma(E)/E = 12\%/\sqrt{E/\text{GeV}} \oplus 1\%$ and hadronic energies with $\sigma(E)/E = 50\%/\sqrt{E/\text{GeV}} \oplus 2\%$, as measured in test beams [32,33]. In the backward region, energy measurements are provided by a lead/scintillating-fibre (SpaCal) calorimeter[2] [34] covering the angular range $155^\circ < \theta < 178^\circ$. The central ($20^\circ < \theta < 160^\circ$) and forward ($7^\circ < \theta < 25^\circ$) tracking detectors are used to measure charged particle trajectories, to reconstruct the interaction vertex and to complement the measurement of hadronic energy. The innermost proportional chamber CIP ($9^\circ < \theta < 171^\circ$) is used to veto charged particles for the identification of photons. The LAr calorimeter and inner tracking detectors are enclosed in a superconducting magnetic coil with a field strength of 1.16 T. From the curvature of charged particle trajectories in the magnetic field, the central tracking system provides transverse momentum measurements with a resolution of $\sigma_{P_T}/P_T = 0.5\%\ P_T/\text{GeV} \oplus 1.5\%$ [35]. The return yoke of the coil is the outermost part of the central detector and is equipped with streamer tubes forming the central muon detector ($4^\circ < \theta < 171^\circ$). In the forward region of the detector ($3^\circ < \theta < 17^\circ$) a set of drift chambers detects muons and measures their momenta using an iron toroidal magnet. The luminosity is determined from the rate of the Bethe-Heitler process $ep \to ep\gamma$, measured using a photon detector located close to the beam pipe at $z = -103$ m, in the backward direction.

5 Data Analysis

The triggers employed for collecting the data used in this analysis are based on the detection of electromagnetic and hadronic energy deposits or missing transverse energy in the LAr calorimeter [36]. For events with missing transverse energy of 20 GeV, the trigger efficiency is $\sim 90\%$ and increases to above 95% for missing transverse energy above 30 GeV. Events containing an electromagnetic deposit (electron or photon) with an energy greater than 10 GeV are triggered with an efficiency close to 100% [37]. Events with two or three jets of transverse momentum larger than 20 GeV are triggered with an efficiency of nearly 100%.

In order to remove background events induced by cosmic showers and other non-ep sources, the event vertex is required to be reconstructed within 35 cm in z of the nominal interaction point. In addition, topological filters and timing vetoes are applied [38].

In a first analysis step, calorimetric energy deposits and tracks of the event are used to look for electron, photon and muon candidates. Electron and photon candidates are characterised by compact and isolated electromagnetic showers in the LAr calorimeter. The identification of muon candidates is based on a track measured in the inner tracking systems associated with signals in the muon detectors [39,40]. Calorimeter energy deposits and tracks not previously identified as electron, photon or muon candidates are used to form combined cluster-track objects, from which the hadronic energy is reconstructed [41,42]. Jet candidates are reconstructed, with a minimum transverse momentum of 2.5 GeV, from these combined cluster-track objects using an inclusive k_T algorithm [43,44] with a P_T weighted recombination scheme in which the jets are treated as massless. The missing transverse momentum P_T^{miss} of the event is derived from all

[2] This device was installed in 1995, replacing a lead-scintillator "sandwich" calorimeter [30].

detected particles and energy deposits in the event. In events with large $P_T^{\rm miss}$, a neutrino candidate is reconstructed. The four-vector of this neutrino candidate is calculated assuming transverse momentum conservation and the relation $\sum_i (E^i - P_z^i) + (E^\nu - P_z^\nu) = 2E_e^0 = 55.2$ GeV, where the sum runs over all detected particles; P_z is the momentum along the proton beam axis and E_e^0 is the electron beam energy. The later relation assumes that no significant losses are present in the electron beam direction.

In a second step, additional requirements are applied to ensure a clear identification of particles. For electrons and photons, the hadronic energy within a distance in the pseudorapidity-azimuth $(\eta - \phi)$ plane $R = \sqrt{\Delta\eta^2 + \Delta\phi^2} < 0.5$ around the electron (photon) is required to be below 3% of the electron (photon) energy. Furthermore, each electron (photon) must be isolated from jets by a minimum distance in pseudorapidity-azimuth of $R > 0.5$ to any jet axis. In the polar angle region $\theta^e > 35^\circ$ electrons must be associated to a charged track and be isolated from any other track by a minimum distance of $R > 0.5$. In the central region ($\theta^\gamma > 20^\circ$), photons are selected only if no track points to the electromagnetic cluster neither within a distance of closest approach (DCA) of 30 cm nor within $R < 0.5$. In the forward region ($\theta^\gamma < 20^\circ$) only photon candidates with no good quality track with a DCA to the cluster below 12 cm are accepted. In this region, the calorimetric isolation of the photon candidate is tightened by requiring that the hadronic energy within $R < 1$, instead of $R < 0.5$, around the photon be below 3% of the photon energy. In addition, it is required that no hit in the CIP be associated to the photon candidate. A muon should have no more than 5 GeV deposited in a cylinder, centred on the muon track direction, of radius 25 cm and 50 cm in the electromagnetic and hadronic sections of the LAr calorimeter, respectively. Additionally, the muon is required to be separated from the closest jet and from any track by $R > 1$ and $R > 0.5$, respectively.

Specific selection criteria applied in each decay channel are presented in the following subsections.

5.1 $q\gamma$ Resonance Search

The signature of the $q^* \to q\gamma$ decay channel consists of one high P_T isolated electromagnetic cluster and one high P_T jet. SM background arises from radiative NC DIS and prompt photon events. As decay products of a massive particle have large transverse momenta and are boosted in the forward region, events are selected with a photon with transverse momentum $P_T^\gamma > 35$ GeV in a polar angle range $5^\circ < \theta^\gamma < 90^\circ$. The events are required to have at least one jet in the polar angle range $5^\circ < \theta^{\rm jet} < 80^\circ$ with a transverse momentum larger than 20 GeV. Photoproduction background events typically have low values of the Bjorken scaling variable, x_h, calculated from the hadronic system using the Jacquet-Blondel method [45, 46]. Their contribution is reduced by a factor of two by requiring $x_h > 0.1$. Finally, to further reduce the background from NC DIS, it is required that no electromagnetic deposit with an energy larger than 10 GeV with an associated track is present in the LAr.

After this selection, 44 events are found in the data compared to a SM expectation of 46 ± 8 events. The errors on the SM prediction include model and experimental systematic errors added in quadrature (see section 5.5). The remaining dominant SM background contributions are prompt photon (66%) and radiative NC DIS (26%) events. The invariant mass of the q^* candidate is calculated from the four-vectors of the photon and the jet candidate of highest P_T. The invariant mass distribution of the q^* candidates and the SM background expectation is presented in figure 2(a). From Monte Carlo studies, the selection efficiency is 35% for $M_{q^*} = 120$ GeV, increasing to 45% for $M_{q^*} = 260$ GeV. The total width of the reconstructed q^* mass distribution is 6 GeV for a generated q^* mass of 120 GeV, increasing to 12 GeV for a q^* mass of 260 GeV.

5.2 $qq\bar{q}$ Resonance Search

The signatures of the $q^* \to qW \to qq\bar{q}$ and $q^* \to qZ \to qq\bar{q}$ decay channels are similar to each other and consist of three high transverse momentum jets. The SM background is dominated by multi-jet photoproduction and NC DIS events. Events are selected with at least three jets in the polar angle range $5^\circ < \theta^{\rm jet} < 120^\circ$ with transverse momenta larger than 50, 30 and 15 GeV, respectively. In each event, a W or Z boson candidate is reconstructed from the combination of the two jets with an invariant mass closest to the nominal W or Z boson mass. The reconstructed mass of the W or Z candidate is required to be larger than 70 GeV and smaller than 100 GeV. From MC studies, in decays of q^* of large mass, the highest P_T jet often does not originate from the boson decay. Therefore, only events in which the highest P_T jet is not associated to the W or Z boson candidate are selected. This requirement is particularly effective in suppressing the photoproduction background at high q^* masses. However, it reduces the q^* selection efficiency at low masses.

After this selection, 341 events are observed while 326 ± 78 are expected from the SM. The remaining dominant SM background contributions are photoproduction (52%) and NC DIS (39%) events. The invariant mass of the q^* candidate is calculated from the highest P_T jet and W or Z candidate four-vectors. The invariant mass distributions of the q^* candidates and of the SM background are presented in figure 2(b). The selection efficiency in this channel is 5% for $M_{q^*} = 120$ GeV, increasing to 35% for $M_{q^*} = 160$ GeV and to 55% for $M_{q^*} = 260$ GeV. The total width of the reconstructed q^* mass distribution is 11 GeV for a generated q^* mass of 120 GeV, increasing to 25 GeV for a q^* mass of 260 GeV.

5.3 $qe\nu$ and $q\mu\nu$ Resonance Searches

The signature of the $q^* \to qW \to qe\nu$ and $q^* \to qW \to q\mu\nu$ decay channels consists of one energetic lepton, a prominent jet and missing transverse momentum. Events with this topology correspond in the SM to single W production [47]. Other SM background processes that may mimic the signature through misidentification or mismeasurement are NC and CC DIS, photoproduction and lepton pair production.

In the search for $q^* \to qW \to qe\nu$, events with $P_T^{\rm miss} > 25$ GeV, one electron with $P_T^e > 10$ GeV and one jet with $P_T^{\rm jet} > 20$ GeV are selected. The electron and the jet must be detected in the polar angle range $5^\circ < \theta^{e,{\rm jet}} < 100^\circ$. Furthermore, the electron must be isolated from jets by a minimum distance of $R > 1$. The ratio V_{ap}/V_p of transverse energy flow anti-parallel and parallel to the hadronic final state [45] is used to suppress photoproduction and NC DIS events. Events with $V_{ap}/V_p > 0.25$ are rejected. The invariant mass of the W boson candidate,

reconstructed from the four-vectors of the electron and neutrino candidates, is required to be between 55 and 100 GeV. After this selection six data events remain, while 6.0 ± 0.8 SM events are expected, of which 82% are from single W production. The invariant mass of the q^* candidate is calculated from the jet and W candidate four-vectors. For this calculation, the W candidate four-vector is scaled such that its mass is set to the nominal W boson mass. The invariant mass distribution of the q^* candidates and the SM background is presented in figure 2(c). The selection efficiency in this channel is $\sim 20\%$ for $M_{q^*} = 120$ GeV, increasing to 30% for $M_{q^*} = 260$ GeV. The total width of the reconstructed q^* mass distribution is 10 GeV for a generated q^* mass of 120 GeV, increasing to 20 GeV for a q^* mass of 260 GeV.

In the search for $q^* \to qW \to q\mu\nu$, events with $P_T^{\rm miss} > 25$ GeV, one muon with $P_T^{\mu} > 10$ GeV and one jet with $P_T^{\rm jet} > 15$ GeV are selected. The muon and the jet must be detected in the polar angle ranges $5^\circ < \theta^{\mu} < 100^\circ$ and $5^\circ < \theta^{\rm jet} < 160^\circ$, respectively. To reduce the background contribution from SM W production, the P_T of the jet is required to be larger than 25 GeV in the polar angle range $\theta^{\rm jet} < 60^\circ$. A W candidate is reconstructed from the combination of the four-vectors of the muon and neutrino candidates and its mass is required to be larger than 40 GeV. After this selection five data events remain, while 4.4 ± 0.7 SM events are expected, of which 90% are from single W production. The invariant mass of the q^* candidate is calculated from the jet and W candidate four-vectors. For this calculation, the W candidate four-vector is scaled such that its mass is set to the nominal W boson mass. The invariant mass distribution of the q^* candidates and the SM background is presented in figure 2(d). The selection efficiency in this channel is $\sim 20\%$ for $M_{q^*} = 120$ GeV, increasing to 40% for $M_{q^*} = 260$ GeV. The total width of the reconstructed q^* mass distribution is 14 GeV for a generated q^* mass of 120 GeV, increasing to 30 GeV for a q^* mass of 260 GeV.

5.4 qee and $q\mu\mu$ Resonance Searches

The signature of the $q^* \to qZ \to qee$ and $q^* \to qZ \to q\mu\mu$ decay channels consists of two high P_T leptons and an energetic jet. The production of lepton pairs constitutes the main background contribution from SM processes [40].

In the search for $q^* \to qZ \to qee$, events with two electrons and one jet of high transverse momenta are selected. Events are selected with two electrons in the polar angle range $5^\circ < \theta^e < 100^\circ$ and transverse momenta larger than 20 and 10 GeV. A jet with a transverse momentum larger than 20 GeV must be detected in the polar angle range $5^\circ < \theta^{\rm jet} < 100^\circ$. To reduce the background from QED Compton and NC DIS processes, each electron must be associated to a good quality track also in the forward region ($5^\circ < \theta^e < 35^\circ$). A Z candidate is reconstructed from the combination of the two electrons and its reconstructed mass is required to be compatible with the nominal Z boson mass within 7 GeV. After this selection no data event remains, while 0.44 ± 0.08 SM events are expected.

In the search for $q^* \to qZ \to q\mu\mu$, events with two muons and one jet of high transverse momenta are selected. Events are selected with two muons in the polar angle range $5^\circ < \theta^{\mu} < 160^\circ$ and transverse momenta larger than 15 and 10 GeV, respectively. A jet with a transverse momentum larger than 20 GeV must be detected in the polar angle range $5^\circ < \theta^{\rm jet} < 100^\circ$. A Z candidate is reconstructed from the combination of the two muons and its reconstructed mass is

required to be larger than 50 GeV. After this selection no data event remains, while 0.87 ± 0.11 SM events are expected.

In both channels, the selection efficiency is $\sim 30\%$ for events with $m_{q^*} > 120$ GeV. The total width of the reconstructed q^* mass distribution in the qee ($q\mu\mu$) channel is 5 GeV (25 GeV) for a generated q^* mass of 120 GeV, increasing to 20 GeV (30 GeV) for a q^* mass of 260 GeV.

5.5 Systematic Uncertainties

The following experimental systematic uncertainties are considered:

- The uncertainty on the electromagnetic energy scale varies between 0.7% and 2% depending on the polar angle [48]. The polar angle measurement uncertainty is 3 mrad for electromagnetic clusters. The identification efficiency of electrons is known with an uncertainty of 3%.
- The efficiency to identify photons is known with a precision of 10% for photons with $P_T > 10$ GeV [48].
- The scale uncertainty on the transverse momentum of high P_T muons amounts to 2.5%. The uncertainty on the reconstruction of the muon polar angle is 3 mrad. The identification efficiency of muons is known with an uncertainty of 3%.
- The hadronic energy scale is known within 2% [48]. The uncertainty on the jet polar angle determination is 10 mrad.
- The uncertainty on the trigger efficiency is 3%.
- The luminosity measurement has an uncertainty of 3%.

The effect of the above systematic uncertainties on the SM expectation and the signal efficiency is determined by varying the experimental quantities by ± 1 standard deviation in the MC samples and propagating these variations through the whole analysis chain.

Additional model systematic uncertainties are attributed to the SM background MC generators described in section 3. An error of 20% is attributed to NC DIS, CC DIS and photoproduction processes with at least two high P_T jets. It includes uncertainties from the proton distribution functions, from missing higher order QCD corrections and from hadronisation. The error on the elastic and quasi-elastic QED Compton cross sections is conservatively estimated to be 5%; the error on the inelastic QED Compton cross section is 10%. The errors attributed to lepton pair and W production are 3% and 15%, respectively. The total error on the SM background prediction is determined by adding the effects of all model and experimental systematic uncertainties in quadrature.

The theoretical uncertainty on the q^* production cross section is dominated by the uncertainty on the scale at which the proton parton densities are evaluated. It is estimated by varying this scale from $\sqrt{\hat{s}}/2$ to $2\sqrt{\hat{s}}$. The resulting uncertainty depends on the q^* mass and is 5% at $M_{q^*} = 100$ GeV, increasing to 12% at $M_{q^*} = 300$ GeV.

6 Interpretation and Limits

The event yields observed in all decay channels are in agreement with the corresponding SM expectations and are summarised in table 1. The SM predictions are dominated by photoproduction and NC DIS for searches in the $q\gamma$ and $qq\bar{q}$ channels and by SM W production in the $qe\nu$ and $q\mu\nu$ channels. The observed invariant mass distributions are in agreement with those of the SM background as shown in figure 2. No data events are observed in channels corresponding to leptonic decays of the Z boson, in agreement with the low SM expectations.

Since no evidence for the production of excited quarks is observed, upper limits on the q^* production cross section and on the model parameters are derived as a function of the mass of the excited quark. Limits are presented at the 95% confidence level (CL) and are obtained from the mass spectra using a modified frequentist approach which takes statistical and systematic uncertainties into account [49].

Upper limits on the product of the q^* production cross section and of the q^* final state branching ratio are shown in figure 3. The analysed q^* decays into W and Z gauge bosons are combined. The resulting limit on f/Λ after combination of all decay channels is displayed as a function of the q^* mass in figure 4, for $f_s = 0$ and the conventional assumption $f = f'$. Under the assumption $f/\Lambda = 1/M_{q^*}$ excited quarks with masses below 252 GeV are excluded. The individual limits from different q^* decay channels are also shown in figure 4(a). At low mass, the combined limit on f/Λ is dominated by the $q^*{\to}q\gamma$ channel, while the $q^* \to qW$ and $q^* \to qZ$ channels start to contribute for masses above 150 GeV and dominate for masses above 200 GeV. These new results extend the previously published limits by H1 [2] and ZEUS [3] by a factor of two to five in f/Λ. Constraints on q^* masses beyond the HERA kinematic limit are set. Excited quarks with masses below 380 GeV are excluded for coupling values $f/\Lambda > 0.03$ GeV^{-1} (see figure 4(b)). The exclusion limit obtained at LEP by the DELPHI Collaboration [4] assuming that the branching ratio of the $q^* \to q\gamma$ is equal to 1 is also shown in figure 4(b) and is considerably weaker than the present result.

The sensitivity of this analysis to non-zero values of f_s and its complementarity to results obtained at the Tevatron is also studied. The limit on f obtained for two example values of f_s and under the assumptions $f = f'$ and $\Lambda = M_{q^*}$ is presented in figure 5. This limit is derived using the γ, W and Z decay channels of excited quarks. The $q^* \to qg$ decay channel gives rise to a dijet resonance. It was verified in a complementary analysis [50] that no resonance from two high P_T jets is observed in the present data. Due to the overwhelming dijet SM background, the total limit on q^* production is not improved if the $q^* \to qg$ decay channel is included. The present limit is compared to the limit obtained by the CDF Collaboration for $f_s = 0.1$ and the same assumptions [5]. For $f_s < 0.1$ and for $M_{q^*} < 190$ GeV, the present analysis probes a domain not excluded by Tevatron experiments. In the case $f = f' = f_s = 1$ and $\Lambda = M_{q^*}$, Tevatron experiments are able to exclude excited quark masses up to 870 GeV [7, 8].

7 Conclusion

A search for the production of excited quarks is performed using the full $e^{\pm}p$ data sample collected by the H1 experiment at HERA with an integrated luminosity of 475 pb^{-1}. The excited quark decay channels $q^*{\to}q\gamma$, $q^*{\to}qZ$ and $q^*{\to}qW$ with subsequent hadronic or leptonic decays of the W and Z bosons are considered and no indication of a signal is found. Improved limits on the production cross section of excited quarks are obtained. Within gauge mediated models, an upper limit on the coupling f/Λ as a function of the excited quark mass is established for the specific relations $f = f'$ and $f_s = 0$. For $f/\Lambda = 1/M_{q^*}$ excited quarks with a mass below 252 GeV are excluded at 95% confidence level. The results presented in this paper extend previously excluded domains at HERA and LEP and are complementary to q^* searches performed at the Tevatron.

Acknowledgements

We are grateful to the HERA machine group whose outstanding efforts have made this experiment possible. We thank the engineers and technicians for their work in constructing and maintaining the H1 detector, our funding agencies for financial support, the DESY technical staff for continual assistance and the DESY directorate for the hospitality which they extend to the non-DESY members of the collaboration.

References

[1] H. Harari, Phys. Rept. **104** (1984) 159.

[2] C. Adloff *et al.* [H1 Collaboration], Eur. Phys. J. C **17** (2000) 567 [hep-ex/0007035].

[3] S. Chekanov *et al.* [ZEUS Collaboration], Phys. Lett. B **549** (2002) 32 [hep-ex/0109018].

[4] P. Abreu *et al.* [DELPHI Collaboration], Eur. Phys. J. C **8** (1999) 41 [hep-ex/9811005].

[5] F. Abe *et al.* [CDF Collaboration], Phys. Rev. Lett. **72** (1994) 3004.

[6] F. Abe *et al.* [CDF Collaboration], Phys. Rev. D **55** (1997) 5263 [hep-ex/9702004].

[7] V. M. Abazov *et al.* [D0 Collaboration], Phys. Rev. D **69** (2004) 111101 [hep-ex/0308033].

[8] T. Aaltonen *et al.* [CDF Collaboration], arXiv:0812.4036 [hep-ex].

[9] F. D. Aaron *et al.* [H1 Collaboration], Phys. Lett. B **663** (2008) 382 [arXiv:0802.1858 [hep-ex]].

[10] F. D. Aaron *et al.* [H1 Collaboration], Phys. Lett. B **666** (2008) 131 [arXiv:0805.4530 [hep-ex]].

[11] K. Hagiwara, S. Komamiya and D. Zeppenfeld, Z. Phys. C **29** (1985) 115.

[12] U. Baur, M. Spira and P. M. Zerwas, Phys. Rev. D **42** (1990) 815.

[13] F. Boudjema, A. Djouadi and J. L. Kneur, Z. Phys. C **57** (1993) 425.

[14] S. J. Brodsky and S. D. Drell, Phys. Rev. D **22** (1980) 2236.

[15] F. M. Renard, Phys. Lett. B **116** (1982) 264.

[16] E. Boos *et al.* [CompHEP Collaboration], Nucl. Instrum. Meth. A **534** (2004) 250 [hep-ph/0403113];
A. Pukhov *et al.*, "CompHEP - a package for evaluation of Feynman diagrams and integration over multi-particle phase space. User's manual for version 3.3", INP MSU report 98-41/542, hep-ph/9908288, available at `http://comphep.sinp.msu.ru`.

[17] C. F. von Weizsäcker, Z. Phys. **88** (1934) 612;
E. J. Williams, Phys. Rev. **45** (1934) 729;
C. Berger and W. Wagner, Phys. Rept. **146** (1987) 1.

[18] J. Pumplin *et al.*, JHEP **0207** (2002) 012 [hep-ph/0201195].

[19] T. Sjöstrand *et al.*, PYTHIA version 6.1, Comput. Phys. Commun. **135** (2001) 238 [hep-ph/0010017], available at `http://home.thep.lu.se/~torbjorn/Pythia.html`.

[20] H. Jung, RAPGAP version 3.1, Comput. Phys. Commun. **86** (1995) 147, available at `http://www.desy.de/~jung/rapgap/`.

[21] A. Kwiatkowski, H. Spiesberger and H. J. Möhring, Comput. Phys. Commun. **69** (1992) 155.

[22] C. Adloff *et al.* [H1 Collaboration], Eur. Phys. J. C **25** (2002) 13 [hep-ex/0201006].

[23] A. Aktas *et al.* [H1 Collaboration], Phys. Lett. B **602** (2004) 14 [hep-ex/0408044].

[24] G. A. Schuler and H. Spiesberger, DJANGOH version 1.4, "Django: The Interface for The Event Generators Heracles and Lepto", Proceedings of the Workshop "Physics at HERA", eds. W. Buchmüller and G. Ingelman, DESY (1991), vol. 3, p. 1419.

[25] L. Lönnblad, Comput. Phys. Commun. **71** (1992) 15.

[26] C. Berger and P. Kandel, "A New Generator For Wide Angle Bremsstrahlung," Proceedings of the Workshop "Monte Carlo Generators for HERA Physics", eds. A. T. Doyle, G. Grindhammer *et al.*, DESY (1998).

[27] U. Baur, J. A. Vermaseren and D. Zeppenfeld, Nucl. Phys. B **375** (1992) 3.

[28] T. Abe, GRAPE-Dilepton version 1.1, Comput. Phys. Commun. **136** (2001) 126 [hep-ph/0012029].

[29] R. Brun *et al.*, "Geant3," CERN-DD/EE/84-1.

[30] I. Abt *et al.* [H1 Collaboration], Nucl. Instrum. Meth. A **386** (1997) 310;
I. Abt *et al.* [H1 Collaboration], Nucl. Instrum. Meth. A **386** (1997) 348.

[31] B. Andrieu *et al.* [H1 Calorimeter Group Collaboration], Nucl. Instrum. Meth. A **336** (1993) 460.

[32] B. Andrieu *et al.* [H1 Calorimeter Group Collaboration], Nucl. Instrum. Meth. A **350** (1994) 57.

[33] B. Andrieu *et al.* [H1 Calorimeter Group Collaboration], Nucl. Instrum. Meth. A **336** (1993) 499.

[34] R. D. Appuhn *et al.* [H1 SPACAL Group Collaboration], Nucl. Instrum. Meth. A **386** (1997) 397.

[35] C. Kleinwort [H1 Collaboration], "H1 Alignment Experience", Proceedings of the "First LHC Detector Alignment Workshop", eds. S. Blusk *et al.*, CERN (2006), CERN-2007-04.

[36] C. Adloff *et al.* [H1 Collaboration], Eur. Phys. J. C **30** (2003) 1 [hep-ex/0304003].

[37] A. Nikiforov, "Measurements of the neutral current $e^{\pm}p$ cross sections using longitudinally polarised lepton beams at HERA II", Ph.D. thesis, Ludwig-Maximilians University (2007), available at `http://www-h1.desy.de/publications/theses_list.html`.

[38] I. Negri, "Recherche de fermions excités dans l'expérience H1 auprès du collisionneur positron-proton HERA", Ph.D. thesis, Université de la Méditerranée Aix-Marseille II (1998), CPPM-T-1998-02, DESY-THESIS-1998-022, available at `http://www-h1.desy.de/publications/theses_list.html`.

[39] V. Andreev *et al.* [H1 Collaboration], Phys. Lett. B **561** (2003) 241 [hep-ex/0301030].

[40] F. D. Aaron *et al.* [H1 Collaboration], Phys. Lett. B **668** (2008) 268, [arXiv:0806.3987 [hep-ex]].

[41] M. Peez, "Recherche de déviations au Modèle Standard dans les processus de grande énergie transverse sur le collisionneur électron - proton HERA", Ph.D. thesis, Université de Lyon (2003), DESY-THESIS-2003-023, available at `http://www-h1.desy.de/publications/theses_list.html`.

[42] B. Portheault, "Première mesure des sections efficaces de courant chargé et neutre avec le faisceau de positrons polarisé à HERA II et analyses QCD-électrofaibles", Ph.D. thesis, Université Paris XI (2005), LAL-05-05, available at `http://www-h1.desy.de/publications/theses_list.html`.

[43] S. D. Ellis and D. E. Soper, Phys. Rev. D **48** (1993) 3160 [hep-ph/9305266].

[44] S. Catani *et al.*, Nucl. Phys. B **406** (1993) 187.

[45] C. Adloff *et al.* [H1 Collaboration], Eur. Phys. J. C **13** (2000) 609 [hep-ex/9908059].

[46] A. Blondel and F. Jacquet, Proceedings of the Study of an ep Facility for Europe, ed. U. Amaldi, DESY 79/48 (1979) 391.

[47] F. D. Aaron *et al.* [H1 Collaboration], Submitted to Eur. Phys. J. C, arXiv:0901.0488 [hep-ex].

[48] T. N. Trinh, "Recherche de leptons excités sur le collisionneur HERA avec le détecteur H1", Ph.D. thesis, Université de la Méditerranée Aix-Marseille II (2008), available at http://www-h1.desy.de/publications/theses_list.html.

[49] T. Junk, Nucl. Instrum. Meth. A **434** (1999) 435 [hep-ex/9902006].

[50] F. D. Aaron *et al.* [H1 Collaboration], Accepted for publication in Phys. Lett. B, arXiv:0901.0507 [hep-ex].

H1 Search for q^* at HERA ($475\ \mathrm{pb}^{-1}$)

Channel	Data	SM	Signal Efficiency [%]
$q^*\to q\gamma$	44	$46 \pm 4 \pm 7$	35 – 45
$q^*\to qW/Z\to qq\bar{q}$	341	$326 \pm 48 \pm 62$	5 – 55
$q^*\to qW\to qe\nu$	6	$6.0 \pm 0.2 \pm 0.8$	20 – 30
$q^*\to qW\to q\mu\nu$	5	$4.4 \pm 0.2 \pm 0.7$	20 – 40
$q^*\to qZ\to qee$	0	$0.44 \pm 0.06 \pm 0.04$	15 – 30
$q^*\to qZ\to q\mu\mu$	0	$0.87 \pm 0.10 \pm 0.04$	15 – 30

Table 1: Observed and predicted event yields for the studied q^* decay channels. The first and second errors on the SM predictions correspond to experimental and model systematic errors, respectively. Typical selection efficiencies obtained from MC studies for q^* masses ranging from 120 to 260 GeV are also indicated.

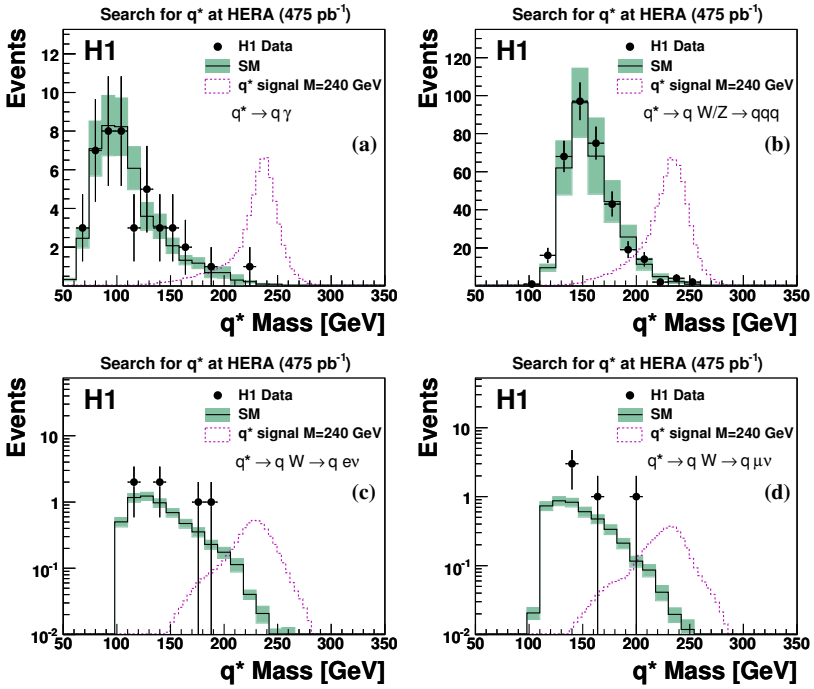

Figure 2: Invariant mass distribution of the q^* candidates in the $q^*{\to}q\gamma$ (a), $q^*{\to}qW/Z{\to}qq\bar{q}$ (b), $q^*{\to}qW{\to}qe\nu$ (c), and $q^*{\to}qW{\to}q\mu\nu$ (d) search channels. The points correspond to the data and the histograms to the SM expectation after the final selections. The error bands on the SM prediction include model uncertainties and experimental systematic errors added in quadrature. The dashed line represents the reconstructed mass distribution of MC q^* signal events with $M_{q^*} = 240$ GeV, with an arbitrary normalisation.

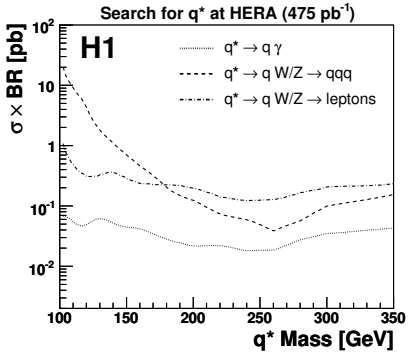

Figure 3: Upper limits at 95% CL on the product of the q^* cross section and decay branching ratio, $\sigma\times$ BR, in the three types of final states for q^* events as a function of the excited quark mass. The q^* decay channels into the W and Z bosons are combined. Values above the curves are excluded.

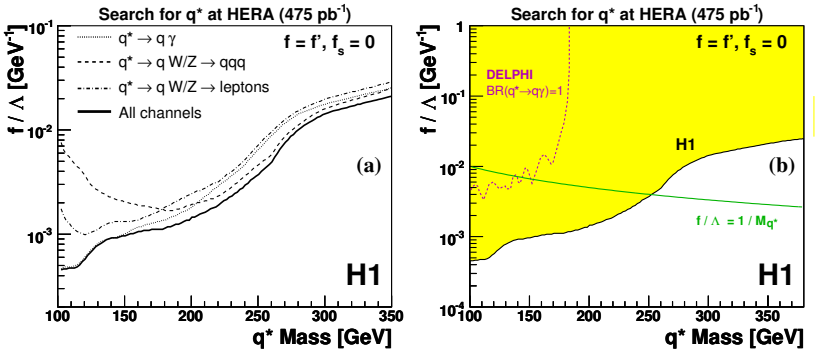

Figure 4: Exclusion limits at 95% CL on f/Λ as a function of the mass of the excited quark with the assumptions $f = f'$ and $f_s = 0$. The individual contributions of the q^* decay channels are presented in (a). Values of the couplings above the curves are excluded. The excluded domain based on all H1 $e^{\pm}p$ data is represented in (b) by the shaded area. It is compared to the exclusion limit obtained at LEP by the DELPHI Collaboration [4] (dashed line), assuming that the branching ratio of the $q^* \to q\gamma$ is equal to 1. The curve $f/\Lambda = 1/M_{q^*}$ is indicated in (b).

Annexe H

Multi-Electron Production at High Transverse Momenta in ep Collisions at HERA

A. Aktas *et al.* [H1 Collaboration],
Eur. Phys. J C **31** (2003) 17,
arXiv:hep-ex/0307015

Abstract

Multi-electron production is studied at high electron transverse momentum in positron- and electron-proton collisions using the H1 detector at HERA. The data correspond to an integrated luminosity of 115 pb^{-1}. Di-electron and tri-electron event yields are measured. Cross sections are derived in a restricted phase space region dominated by photon-photon collisions. In general good agreement is found with the Standard Model predictions. However, for electron pair invariant masses above 100 GeV, three di-electron events and three tri-electron events are observed, compared to Standard Model expectations of 0.30 ± 0.04 and 0.23 ± 0.04, respectively.

1 Introduction

In this paper we describe the first measurement of multi–electron production at high transverse momentum (P_T) in electron[1]–proton interactions at HERA. Within the Standard Model (SM), the production of multi–lepton events in ep collisions proceeds mainly through photon–photon interactions; photons radiated from the incident electron and proton interact to produce a pair of leptons, $\gamma\gamma \to \ell^+\ell^-$ [1]. At large invariant masses, multi–lepton production may be sensitive to new phenomena, for instance the production of a doubly charged Higgs boson [2] or processes involving bileptons, generic bosons carrying two units of lepton number [3].

The analysis presented here is based on data recorded in 1994–2000 by the H1 experiment. Electrons of 27.6 GeV collided with protons of 820 or 920 GeV, corresponding to centre–of–mass energies $\sqrt{s}$ of 301 GeV or 319 GeV, respectively. The total integrated luminosity of 115.2 pb^{-1} consists of 36.5 pb^{-1} of e^+p collisions recorded at $\sqrt{s}$ = 301 GeV and 65.1 pb^{-1} recorded at 319 GeV, as well as 13.6 pb^{-1} of e^-p collisions recorded at $\sqrt{s}$ = 319 GeV. A related study of muon pair production is presented in [4].

2 Standard Model Processes and their Simulation

The main SM processes contributing to multi–electron production at HERA are summarised in figure 1. The dominant contribution, shown in diagram 1a, is due to electron pair production through the interaction of two photons radiated from the incident electron and proton. Electron pairs can also originate from internal conversion of a photon (γ) or a Z^0 boson, radiated either from the electron line (diagram 1b) or from the quark line (diagram 1c). The pole due to the electron propagator in diagrams 1a and 1b corresponds to an e^+e^- interaction in which one of the electrons is emitted from a photon radiated from the proton. This mechanism is called the Cabibbo–Parisi process. Its contribution is one order of magnitude lower than the photon-photon contribution, except at high transverse momentum, where it is more significant due to s-channel Z^0 boson production (diagram 1b). In diagram 1c, the pole due to the quark propagator corresponds to the Drell–Yan process, $q\bar{q} \to e^+e^-$. Its contribution is small compared with the photon–photon and Cabibbo–Parisi processes [5].

If the photon coupled to the incoming electron has a high virtuality, the incident electron can scatter through a large angle and with high transverse momentum. If the scattered electron is observed in the detector, it is indistinguishable from the pair–produced electron of the same charge.

The Monte Carlo generator GRAPE [6] simulates lepton pair production in ep collisions using the full set of electroweak matrix elements at the tree level, with the exception of the Drell-Yan pole contribution. GRAPE is based on the automatic Feynman graphs calculation program GRACE [7]. Initial and final state radiation processes (QED and QCD parton showers) are simulated in the leading log approximation. The production of τ lepton pairs and their subsequent electronic decay is also simulated with GRAPE and composes about 2% of the multi–electron event sample. The Drell–Yan contribution is simulated using the PYTHIA [8] event generator. Its contribution is found to be very small in the phase space relevant here and is neglected in the following.

In GRAPE the proton interaction is divided into in three phase space regions: elastic, quasi–elastic and inelastic. In the case of elastic scattering, $ep \to ee^+e^-p$, the proton vertex is described in terms of dipole form factors. The quasi–elastic domain is defined by requiring that the mass of the hadronic final state $M_X < 5$ GeV or that the virtuality of the photon coupled to the proton $Q_p^2 < 1$ GeV^2. In the region $M_X < 2$ GeV a resonance parameterisation [9] is used for the proton vertex. In the remaining quasi–elastic phase space, a fit to photoproduction and deep inelastic scattering data is used [10]. The inelastic regime corresponds to electron–quark interactions with $M_X > 5$ GeV and $Q_p^2 > 1$ GeV^2. In this case, the proton structure is parameterised using the CTEQ5L parton distributions [11]. The fragmentation and hadronisation processes are simulated using the SOPHIA program [12] in the quasi-elastic and PYTHIA [8] in the inelastic regime.

The uncertainty attributed to the GRAPE calculation in this analysis is 3%. This value results mainly from the uncertainties in the QED matrix element calculation (1%), the parameterisation of the structure functions and the phase space separation between quasi-elastic and inelastic processes.

The GRAPE prediction is cross–checked using the LPAIR generator [13], which contains only the photon–photon process. When restricted to this process, the total and differential cross sections produced with LPAIR and GRAPE agree at the percent level. The additional diagrams in GRAPE increase the predicted cross section by 10 % on average in the phase space considered here. The increase is more pronounced (up to 30 %) for di–lepton masses which are either very low (photon internal conversions) or around 90 GeV (Z^0 resonance production).

The main experimental backgrounds to multi–electron production are processes in which, in addition to a true electron, one or more fake electrons are reconstructed in the final state. The dominant contribution arises from neutral current Deep Inelastic Scattering (DIS) events ($ep \to eX$) in which, in addition to the scattered electron, hadrons or radiated photons are incorrectly identified as electrons. QED Compton scattering ($ep \to e\gamma X$) can also contribute if the photon is misidentified as an electron. The DIS and elastic Compton processes are simulated using the DJANGO [14] and WABGEN [15] generators, respectively.

All generated events are passed through the full GEANT [16] based simulation of the H1 apparatus and are reconstructed using the same program chain as for the data.

3 Experimental Conditions

A detailed description of the H1 detector can be found in [17]. The components essential for this analysis are described briefly here.

A tracking system consisting of central and forward[2] drift chambers is used to measure charged particle trajectories and to determine the interaction vertex. The central tracker is composed of two concentric cylindrical drift chambers with an active detection region starting at a

[1] In this paper the term "electron" is used generically to refer to both electrons and positrons.

[2] The origin of the H1 coordinate system is the nominal ep interaction point. The direction of the proton beam defines the positive z–axis (forward direction). Transverse momenta are measured in the x–y plane. Polar (θ) and azimuthal (ϕ) angles are measured with respect to this reference system. The pseudorapidity is defined as $\eta = -\log\tan(\theta/2)$.

radius of 22 cm. The angular range $37^\circ < \theta < 144^\circ$ is covered by both chambers. The inner drift chamber provides full acceptance for particles in the range $22^\circ < \theta < 159^\circ$. Particles at $\theta = 20^\circ$ cross 83% of its acceptance region. Transverse momenta (P_T) are determined from the curvature of the particle trajectories in a magnetic field of 1.15 Tesla. The central tracking system provides transverse momentum measurements with a resolution of $\sigma_{P_T}/P_T^2 = 5 \times 10^{-3}$ GeV^{-1}. The tracking is complemented in the region $7^\circ < \theta < 25^\circ$ by a system of drift chambers perpendicular to the beam axis.

Hadronic and electromagnetic final state particles are absorbed in a highly segmented liquid argon calorimeter [18] covering the range $4^\circ < \theta < 153^\circ$. The calorimeter is 5 to 8 hadronic interaction lengths deep, depending on the polar angle and has an electromagnetic section which is 20 to 30 radiation lengths deep. Electromagnetic shower energies are measured with a precision of $\sigma(E)/E = 12\%/\sqrt{E/\mathrm{GeV}} \oplus 1\%$ and hadronic shower energies with a precision of $\sigma(E)/E = 50\%/\sqrt{E/\mathrm{GeV}} \oplus 2\%$, as measured in test beams [19]. The electromagnetic energy scale is known to 0.7% in the central region and to 3% in the forward region. The hadronic energy scale is known to 2%.

In the backward region, energy measurements are provided by a lead/scintillating–fibre calorimeter[3] [20] covering the range $155^\circ < \theta < 178^\circ$. The calorimeter system is surrounded by a superconducting coil with an iron yoke which is instrumented with streamer tubes. The electron and photon taggers located downstream of the interaction point in the electron beam direction are used to determine the luminosity through the measurement of the Bethe-Heitler $ep \to e\gamma p$ process.

The trigger used relies on the liquid argon calorimeter signals and has an efficiency which is greater than 95% for events in which an electron of energy above 10 GeV is detected.

4 Data Analysis

4.1 Multi–electron event selection

The multi–electron event selection is based on a procedure which is designed to minimise the contribution of fake electrons, while keeping a high efficiency for identifying true electrons and allowing reliable monitoring of the overall selection efficiency.

As a first step, electron candidates with energies above 5 GeV are identified in the liquid argon and backward calorimeters, in the range $5^\circ < \theta < 175^\circ$. Electromagnetic showers are identified with an efficiency of better than 98% using pattern recognition algorithms based on the geometric profiles expected for electrons. The remaining calorimeter clusters are attributed to hadronic activity and are combined into jets using an inclusive k_T algorithm [21], with a minimum jet transverse momentum of 4 GeV. Electron candidates are required to be isolated by demanding that they are separated from other electrons or jets by at least 0.5 units in the $\eta - \phi$ plane. In addition, the total hadronic energy within 0.75 units in $\eta - \phi$ of the electron direction is required to be below 2.5% of the electron energy.

[3]This device was installed in 1995, replacing a lead–scintillator "sandwich" calorimeter [17].

In the region of angular overlap between the liquid argon calorimeter and the central drift chambers ($20^\circ < \theta < 150^\circ$), the calorimetric electron identification is complemented by tracking conditions. In this region it is required that a high quality track be geometrically matched to the electromagnetic cluster with a distance of closest approach to the cluster centre of gravity of less than 12 cm. The starting radius of the measured track, defined as the distance between the first measured point in the central drift chambers and the beam axis, is required to be below 30 cm in order to reject photons that convert in the central tracker material beyond this radius. The transverse momentum of the associated track P_T^{etk} and the calorimetric transverse momentum P_T^e are required to satisfy the condition $1/P_T^{etk} - 1/P_T^e < 0.02$ GeV^{-1}. No other high quality track is allowed within 0.5 units in $\eta - \phi$ of the electron direction. These additional constraints strongly reduce the contribution of fake electrons from misidentified photons and hadrons. The resulting electron finding efficiency is 88%. Electrons selected in this polar angular range are called "central electrons" hereinafter.

Due to the higher material density in the forward region ($5^\circ < \theta < 20^\circ$) the electrons are more likely to shower and therefore no track conditions are required. The same applies in the backward region ($150^\circ < \theta < 175^\circ$). The forward electron energy threshold is raised to 10 GeV in order to reduce the number of fake electrons arising from hadrons in DIS events.

The final multi–electron event selection requires that there be two central electron candidates, of which one must have $P_T^e > 10$ GeV and the other $P_T^e > 5$ GeV. Additional electron candidates are identified in the central and backward regions with $E^e > 5$ GeV and in the forward region with $E^e > 10$ GeV. The electron candidates are ordered according to decreasing P_T, $P_T^{e_i} > P_T^{e_{i+1}}$.

The selected events are classified as "2e" if only the two central electron candidates are identified and "3e" if exactly one additional electron candidate is identified. A subsample of the "2e" sample, labelled "$\gamma\gamma$", is selected in order to measure the pair production cross section in a well defined phase space region dominated by photon–photon collisions with low background. In this subsample, the two electrons must be of opposite charge and a significant deficit compared to the initial state must be observed in the difference $E - P_z$ of the energy and longitudinal momentum of all visible particles ($E - P_z < 45$ GeV) [4]. These two conditions ensure that the incident electron is lost in the beam pipe after radiating a quasi–real photon of squared four–momentum Q^2 lower than 1 GeV^2.

4.2 Background studies

DIS and Compton processes can contribute to the selected multi–electron sample if a photon or a particle from the hadronic final state is misidentified as an electron. In order to quantify the uncertainty on the background prediction and test the performance and reliability of the electron identification procedure, several samples in which these background processes are enhanced are studied.

[4]For fully contained events or events where only longitudinal momentum along the proton direction ($+z$) is undetected, one expects $E - P_z = 2E_e^0 = 55.2$ GeV, where E_e^0 is the energy of the incident electron. If the scattered electron is undetected, the threshold $E - P_z < 45$ GeV corresponds to a cut on the fractional energy loss $y = (E - P_z)/2E_e^0 < 0.82$.

- Electron misidentification in the central region is investigated by measuring the probability of selecting a second electron in addition to the scattered electron in DIS candidate events when the track quality criteria are relaxed. From a sample of 244980 DIS candidates, 1563 events with a second electromagnetic central cluster are selected if no tracking conditions are applied to this cluster. The fake electrons are predominantly photons from DIS or Compton events (figure 2a). This contribution is greatly reduced by requiring a geometrical track–cluster match (figure 2b). The remaining sample consists of 250 events. The fake electron background is described by the simulation at the 20% level.

- Electron misidentification in the forward region affects only the "3e" selection. The dominant contribution to this background is the misidentification of a hadron as an electron. The fake electron background in this region is studied with the DIS event sample in an analysis similar to that described above. Fake electrons in the forward region are also searched for in an inelastic Compton event sample with one electron and one photon in the central region. The fake electron background in the forward region is described by the simulation at the 20% level.

- Detailed studies of photon conversions are performed using a sample enriched with elastic Compton events, selected by requiring one central electron plus a second central electromagnetic cluster (photon candidate) and no significant additional energy in the calorimeters. Distributions of the charged tracks associated with the photon candidate are shown in figures 2c and 2d. The number of tracks (figure 2c) and their starting radius (figure 2d) are well reproduced by the simulation. In figure 2d, the central tracker structure is visible as peaks in the distribution, corresponding to photon conversions in the tracker walls. The first peak is populated by tracks associated with true electrons and by tracks from conversions which occur before the active tracker volume. The second peak is due to photon conversions in the dead material between the inner and outer central trackers. These conversions are described by the simulation to better than 20%.

Based on those studies, the uncertainty on the background simulation is estimated to be 20%.

4.3 Systematic uncertainties

The systematic uncertainties are related to the measurement of the electron pair production process, to the theoretical description of this process and to the background simulation.

The main measurement uncertainty is due to the tracking conditions in the electron identification procedure. The electron track association efficiency is measured with a DIS sample selected with $E - P_z > 45$ GeV and a single electromagnetic cluster in the calorimeter with a transverse momentum above 10 GeV in the polar angle interval $20^\circ < \theta < 150^\circ$. The measured average track association efficiency is 90% and varies only slightly with the track momentum and polar angle. This efficiency, measured to a precision ranging from 3% for polar angles around 90° to 15% at the forward edge of the angular acceptance of the central tracker ($\theta = 20^\circ$), is well described by the simulation. Uncertainties on the energy scales of the calorimeters, on the trigger efficiency and on the luminosity measurement are also taken into account. The total measurement uncertainty is typically 7% for the "2e" selection and 10% for the "3e" selection.

The theoretical uncertainty on the pair production process cross section, calculated with GRAPE, is 3%, as explained in section 2. The uncertainty on the Compton and DIS background contributions is 20%, deduced from the studies presented in section 4.2.

The error on the event yields predicted by GRAPE (section 5.1) contains all measurement and theoretical errors added in quadrature. The uncertainty on the total SM prediction also includes the errors on the Compton and DIS backgrounds.

The error on the extracted cross sections (section 5.2) includes all measurement and background errors as described above. Theoretical errors are applied to the GRAPE prediction of the cross sections.

5 Results

5.1 Multi–electron event samples

The multi–electron event yields are summarised in table 1. The observed numbers of "2e" and "3e" events are in agreement with the expectations, as is the number of events in the "$\gamma\gamma$" sample. No event is found with four or more identified electrons.

The distributions of longitudinal momentum balance $E - P_z$, missing transverse momentum P_T^{miss} and hadronic transverse momentum $P_T^{hadrons}$ are presented in figure 3. The "3e" events accumulate at $E - P_z$ values around 55 GeV, as expected if the scattered electron is visible in the detector. The "2e" events show a tail at lower $E - P_z$, due to the scattered electron being lost in the beam pipe, corresponding to the dominant $\gamma\gamma$ topology. The missing transverse momentum P_T^{miss} is taken to be the modulus of the vector sum of the transverse momenta of all visible particles. The P_T^{miss} distributions are consistent with the expectation for no emission of undetected particles with substantial transverse momentum. The spectrum of the transverse momentum $P_T^{hadrons}$ of all visible particles except identified electrons is also well described by the SM prediction.

The distributions of the individual electron transverse momenta $P_T^{e_i}$ are steeply falling as shown in figure 4. The "2e" and "3e" samples are in good overall agreement with the SM, except for three "2e" events with $P_T^{e_1}$ above 50 GeV, where the SM expectation is small.

The distribution of the invariant mass of the two highest P_T electrons in the event (M_{12}) and the correlation with the scalar sum $P_T^{e_1} + P_T^{e_2}$ are shown in figure 5. The agreement with the SM prediction is good at low M_{12}. However, three "2e" and three "3e" events are seen with invariant masses M_{12} above 100 GeV, where the SM expectation is small. The three "2e" events are the same as those observed at high $P_T^{e_1}$. The invariant masses M_{13}, M_{23} and M_{123} of the other possible electron combinations in the "3e" sample are shown in figure 6. No event is seen with an unexpectedly high M_{13} or M_{23}. The three high M_{12} events also give rise to the largest tri–electron masses M_{123}. The comparison of the observed events with masses M_{12} above 100 GeV with the SM expectations is presented in table 2. These events are discussed in detail in section 5.3.

5.2 Cross section measurement

Using the selected "$\gamma\gamma$" sample, electron pair production cross sections are measured in the kinematic region defined by

$$20^\circ < \theta^{e_{1,2}} < 150^\circ, \quad P_T^{e_1} > 10 \text{ GeV}, \quad P_T^{e_2} > 5 \text{ GeV}, \quad y < 0.82, \quad Q^2 < 1 \text{ GeV}^2 .$$

For this measurement, the data samples collected at $\sqrt{s}$=301 GeV and 319 GeV are combined taking into account their respective luminosities. Assuming a linear dependence of the cross section on the proton beam energy, as predicted by the SM, the resulting cross section corresponds to an effective $\sqrt{s}$ = 313 GeV.

After background subtraction, the observed number of events is corrected for acceptance and detector effects to obtain the cross section. The generator GRAPE is used to calculate the detector acceptance A for this region of phase space. The acceptance accounts for detection efficiencies and migrations. The cross section is thus

$$\sigma = \frac{\mathrm{N_{data}} - \mathrm{N_{bgd}}}{\mathcal{L}A},$$

where $\mathrm{N_{data}}$ is the number of events observed, $\mathrm{N_{bgd}}$ is the number of events expected from background processes (DIS and Compton) and $\mathcal{L}$ is the integrated luminosity of the data sample.

The $ep \to ee^+e^-X$ cross section, integrated over the phase space defined above, is

$$\sigma = (0.59 \pm 0.08 \pm 0.05) \text{ pb},$$

where the first error is statistical and the second systematic, obtained as described in section 4.2. This result agrees well with the SM expectation of (0.62 ± 0.02) pb, calculated with GRAPE. The differential cross sections as a function of $P_T^{e_1}$, M_{12} and $P_T^{hadrons}$ are shown in figure 7 and table 3. The measurements are in good agreement with the expected cross sections.

5.3 Discussion of high mass events

All six events with $M_{12} > 100$ GeV were recorded during positron–proton collisions. For these events, displayed in figure 8, all available detector information supports the interpretation of the electron candidates as being true electrons. The electromagnetic shower shapes are checked individually and found to be similar to those expected from the calorimeter response to electrons. All central tracks yield a specific ionisation in the central drift chamber as expected for single electrons. The measurements of the central electron momenta by the tracker and the calorimeter are compatible within errors. The forward electron candidates in the "3e" events 4, 5 and 6 all have at least one track pointing to the calorimetric energy cluster, although no such requirement is made in the identification procedure.

Although classified as "2e", event 1 also contains a third electron candidate with energy below the identification threshold. Similarly, event 3 has a compact electromagnetic energy deposit located at the forward boundary of the liquid argon calorimeter, outside the electron identification fiducial volume. This event also contains a low energy converted photon radiated

close to electron e_2. With the exception of event 6, which has a high energy forward hadronic jet, the events show no hadronic activity in the detector. It should be noted that the high mass di–electron topology differs for the observed events classified as "2e" and "3e". In the former case, the high–mass is formed from two central high–P_T electrons, whereas in the latter it is formed from one forward and one central electron, both of intermediate P_T (figure 5).

The event kinematics of the six high mass events are presented in table 4. The electron energy, electron polar angle and forward and backward electron azimuthal angles are measured from the calorimetric deposits. For the central electrons, the azimuthal angle is measured from the associated track, which yields a better precision. The electric charge of the electrons, measured in the central region from the associated track curvature, is given in table 4 if the significance of its determination exceeds two standard deviations. All events are compatible with the presence of one e^- and two e^+ in the final state, as expected from pair production process.

Imposing longitudinal and transverse momentum conservation, a constrained fit can be performed to improve the kinematic measurement. This corresponds to an adjustment of particle observables (energy, polar and azimuthal angles) within experimental errors in order to achieve $E - P_z = 55.2$ GeV and $P_T^{miss} = 0$ GeV. In event 2 only two electrons are visible and the measured $E - P_z$ value is significantly lower than 55 GeV. For this event it is supposed that the scattered electron has escaped down the beampipe and therefore the $E - P_z$ constraint is removed in the kinematic fit. The M_{12} values obtained from the kinematic fit are indicated in table 4. They are consistent with the direct measurements. The errors are reduced by more than a factor of two with the exception of event 2. The χ^2 per degree of freedom of the kinematic fit is in the range 0.7 to 1.7 for the six events, showing that the kinematics of the six high mass events are well understood within the measurement errors. The M_{12} values are incompatible with the interpretation of the six high mass electron pairs as the decay of a single narrow resonance. The same is true for the M_{123} values in the "3e" high mass events.

6 Summary

High–P_T multi–electron production is measured for the first time in ep scattering at HERA. The di–electron and tri–electron event yields are in good overall agreement with the SM predictions. No events are observed with more than three identified electrons, again in agreement with the SM expectation. Differential cross sections for electron pair production are extracted in a restricted phase space region dominated by photon–photon interactions and are found to agree with the predictions.

Within the di– and tri–electron samples, the invariant mass of the two electrons with the highest transverse momenta is studied. For masses above 100 GeV, three events classified as di–electrons and three events classified as tri–electrons are observed, compared to SM expectations of 0.30 ± 0.04 and 0.23 ± 0.04, respectively.

Acknowledgements

We are grateful to the HERA machine group whose outstanding efforts have made and continue to make this experiment possible. We thank the engineers and technicians for their work in

constructing and maintaining the H1 detector, our funding agencies for financial support, the DESY technical staff for continual assistance, and the DESY directorate for support and the hospitality which they extend to the non–DESY members of the collaboration. The authors wish to thank J. A. M. Vermaseren and T. Abe for many useful discussions.

References

[1] J. A. M. Vermaseren, Nucl. Phys. B **229** (1983) 347.

[2] E. Accomando and S. Petrarca, Phys. Lett. B **323** (1994) 212 [hep-ph/9401242].

[3] F. Cuypers and S. Davidson, Eur. Phys. J. C **2** (1998) 503 [hep-ph/9609487].

[4] A. Aktas *et al.* [H1 Collaboration], in preparation.

[5] N. Arteaga-Romero, C. Carimalo and P. Kessler, Z. Phys. C **52** (1991) 289.

[6] T. Abe, Comput. Phys. Commun. **136** (2001) 126 [hep-ph/0012029].

[7] T. Ishikawa *et al.* [MINAMI-TATEYA group Collaboration], KEK-92-19.

[8] PYTHIA 5.7; T. Sjöstrand, CERN-TH-6488 (1992), Comp. Phys. Comm. **82** (1994) 74.

[9] F. W. Brasse *et al.*, Nucl. Phys. B **110** (1976) 413.

[10] H. Abramowicz and A. Levy, [hep-ph/9712415].

[11] H. L. Lai *et al.* [CTEQ Collaboration], Eur. Phys. J. C **12** (2000) 375 [hep-ph/9903282].

[12] A. Mucke *et al.*, Comp. Phys. Comm. **124** (2000) 290 [astro-ph/9903478].

[13] LPAIR; S. P. Baranov, O. Dünger, H. Shooshtari and J. A. Vermaseren, Proc. of the Workshop "Physics at HERA" (1991), Eds. W. Buchmüller and G. Ingelman, Vol. 3, p. 1478.

[14] DJANGO 2.1; G.A. Schuler and H. Spiesberger, Proc. of the Workshop "Physics at HERA" (1991), Eds. W. Buchmüller and G. Ingelman, Vol. 3, p. 1419.

[15] WABGEN; C. Berger and P. Kandel, Proc. of the Workshop "Monte Carlo Generators for HERA Physics" (1998/1999), DESY-PROC-1999-02, p. 596.

[16] GEANT3; R. Brun *et al.*, CERN-DD/EE/84-1.

[17] I. Abt *et al.* [H1 Collaboration], Nucl. Instrum. Meth. A **386** (1997) 310;
I. Abt *et al.* [H1 Collaboration], Nucl. Instrum. Meth. A **386** (1997) 348.

[18] B. Andrieu *et al.* [H1 Calorimeter Group], Nucl. Instrum. Meth. A **336** (1993) 460.

[19] B. Andrieu *et al.* [H1 Calorimeter Group], Nucl. Instrum. Meth. A **344** (1994) 492; *idem*, Nucl. Instrum. Meth. A **350** (1994) 57; *idem*, Nucl. Instrum. Meth. A **336** (1993) 499.

[20] R. D. Appuhn *et al.* [H1 SPACAL Group], Nucl. Instrum. Meth. A **386** (1997) 397.

[21] S. D. Ellis and D. E. Soper, Phys. Rev. D **48** (1993) 3160 [hep-ph/9305266];
C. Adloff *et al.* [H1 Collaboration], Nucl. Phys. B **545** (1999) 3 [hep-ex/9901010].

Selection	Data	SM	Pair Production (GRAPE)	DIS + Compton
"2e"	108	117.1 ± 8.6	91.4 ± 6.9	25.7 ± 5.2
"3e"	17	20.3 ± 2.1	20.2 ± 2.1	0.1 ± 0.1
"4e" or more	0	0.12 ± 0.04	0.12 ± 0.04	< 0.02 (95% C.L.)
"$\gamma\gamma$" subsample	42	44.9 ± 4.2	43.7 ± 4.2	1.2 ± 0.4

Table 1: Observed and predicted multi–electron event yields for the samples described in the text. The analysed data sample corresponds to an integrated luminosity of 115.2 pb^{-1}. The errors on the predictions include model uncertainties and experimental systematic errors added in quadrature.

Selection	Data	SM	Pair Production (GRAPE)	DIS + Compton
"2e" $M_{12} > 100$ GeV	3	0.30 ± 0.04	0.21 ± 0.03	0.09 ± 0.02
"3e" $M_{12} > 100$ GeV	3	0.23 ± 0.04	0.23 ± 0.03	< 0.02 (95% C.L.)

Table 2: Observed and predicted multi–electron event yields for masses $M_{12} > 100$ GeV for the samples described in the text. The analysed data sample corresponds to an integrated luminosity of 115.2 pb^{-1}. The errors on the predictions include model uncertainties and experimental systematic errors added in quadrature.

Variable range [GeV]	Measured cross section [pb/GeV]	Pair Production (GRAPE) cross section [pb/GeV]
$d\sigma/dP_T^{e_1}$		
$10 < P_T^{e_1} < 15$	$0.092 \pm 0.016 \pm 0.009$	0.090 ± 0.003
$15 < P_T^{e_1} < 20$	$0.021 \pm 0.008 \pm 0.002$	0.023 ± 0.001
$20 < P_T^{e_1} < 25$	$0.0053 \pm 0.0037 \pm 0.0007$	0.0065 ± 0.0002
$d\sigma/dM_{12}$		
$15 < M_{12} < 25$	$0.030 \pm 0.007 \pm 0.003$	0.027 ± 0.001
$25 < M_{12} < 40$	$0.015 \pm 0.004 \pm 0.001$	0.017 ± 0.001
$40 < M_{12} < 60$	$0.0020 \pm 0.0012 \pm 0.0002$	0.0026 ± 0.0001
$d\sigma/dP_T^{hadrons}$		
$0 < P_T^{hadrons} < 5$	$0.079 \pm 0.014 \pm 0.009$	0.087 ± 0.003
$5 < P_T^{hadrons} < 12$	$0.028 \pm 0.011 \pm 0.002$	0.018 ± 0.001
$12 < P_T^{hadrons} < 25$	$0.0032 \pm 0.0023 \pm 0.0005$	0.0041 ± 0.0001

Table 3: Differential cross sections $d\sigma/dP_T^{e_1}$, $d\sigma/dM_{12}$ and $d\sigma/dP_T^{hadrons}$ for the process $ep \to ee^+e^-X$ in a restricted phase space (see text). The differential cross sections are averaged over the quoted intervals. The first error is statistical and the second is systematic. Theoretical predictions with GRAPE are also shown.

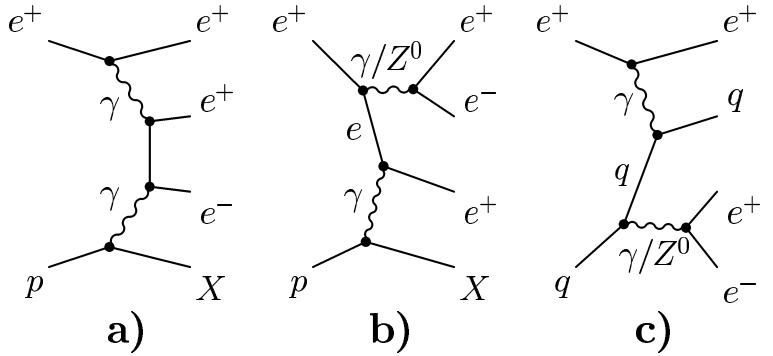

Figure 1: The main processes involved in lepton pair production. Examples of Feynman diagrams are shown for: a) photon–photon interaction; b) and c) γ/Z^0 boson conversion. The hadronic final state (X) can be a proton (elastic process) or a higher mass system (quasi-elastic and inelastic processes).

Particle	E [GeV]	θ [degrees]	ϕ [degrees]	Charge (signifi cance)
Multi–electron Event 1 (2e)				
Run 83507	$E-P_z$ = 54.0 ± 1.1 GeV		P_T^{miss}=3.1 ± 1.8 GeV	
Event 16817	M_{12} = 111.2 ± 2.4 GeV		M_{12}^{fit} = 111.3 ± 0.4 GeV	
e_1	90.3 ± 3.1	36.6 ± 0.2	98.48 ± 0.05	- (4σ)
e_2	53.6 ± 1.4	69.6 ± 0.3	-77.05 ± 0.05	undetermined
low energy e	4.4 ± 0.3	44.3 ± 0.3	-155.46 ± 0.03	+ (70σ)
Multi–electron Event 2 (2e)				
Run 89256	$E-P_z$ = 43.9 ± 0.8 GeV		P_T^{miss}=1.9 ± 1.8 GeV	
Event 224212	M_{12} = 130.0 ± 2.6 GeV		M_{12}^{fit} = 129.3 ± 2.4 GeV	
e_1	132.4 ± 4.3	28.6 ± 0.1	8.73 ± 0.06	undetermined
e_2	82.4 ± 1.8	48.4 ± 0.2	-171.50 ± 0.03	- (6σ)
Multi–electron Event 3 (2e)				
Run 254959	$E-P_z$ = 57.3 ± 1.4 GeV		P_T^{miss}=3.5 ± 2.0 GeV	
Event 17892	M_{12} = 112.5 ± 2.4 GeV		M_{12}^{fit} = 109.5 ± 1.0 GeV	
e_1	96.9 ± 3.3	34.6 ± 0.3	52.66 ± 0.02	+ (10σ)
e_2	46.1 ± 1.1	80.1 ± 0.9	-125.62 ± 0.01	+ (15σ)
fwd em cluster	70^{+100}_{-2} [a]	4.5 ± 0.1	-132.7 ± 1.0	undetermined
photon	1.1 ± 0.1	132.0 ± 5.5	39.8 ± 7.3	0
[a] this error includes the uncertainty due to energy loss in the beampipe				
Multi–electron Event 4 (3e)				
Run 168058	$E-P_z$ = 55.7 ± 1.4 GeV		P_T^{miss}=1.1 ± 0.8 GeV	
Event 42123	M_{12} = 137.4 ± 2.9 GeV		M_{12}^{fit} = 138.8 ± 1.2 GeV	
e_1	35.8 ± 0.9	115.6 ± 0.9	-5.98 ± 0.02	+ (18σ)
e_2	173.0 ± 5.5	6.6 ± 0.1	-159.1 ± 0.5	undetermined
e_3	44.8 ± 1.7	21.8 ± 0.2	139.10 ± 0.03	- (12σ)
Multi–electron Event 5 (3e)				
Run 192864	$E-P_z$ = 53.8 ± 1.4 GeV		P_T^{miss}=0.7 ± 0.6 GeV	
Event 123614	M_{12} = 118.1 ± 2.6 GeV		M_{12}^{fit} = 121.9 ± 0.6 GeV	
e_1	138.9 ± 4.5	10.2 ± 0.1	44.1 ± 0.6	undetermined
e_2	28.1 ± 0.8	134.7 ± 0.3	-95.85 ± 0.01	+ (25σ)
e_3	35.3 ± 1.5	26.6 ± 0.1	172.71 ± 0.05	+ (5σ)
Multi–electron Event 6 (3e)				
Run 267312	$E-P_z$ = 57.4 ± 1.6 GeV		P_T^{miss}=2.4 ± 0.8 GeV	
Event 203075	M_{12} = 134.7 ± 3.1 GeV		M_{12}^{fit} = 132.3 ± 1.4 GeV	
e_1	186.0 ± 5.9	7.11 ± 0.05	-71.3 ± 0.4	undetermined
e_2	25.5 ± 0.8	148.8 ± 0.2	120.25 ± 0.02	+ (32σ)
e_3	8.5 ± 0.5	69.7 ± 0.3	164.90 ± 0.01	+ (57σ)
hadrons[b]	123.2 ± 6.7	6.1 ± 1.1	53.5 ± 1.1	
[b] mass of the visible hadronic system: 24.0 ± 2.5 GeV				

Table 4: Reconstructed kinematics of the six multi-electron events with $M_{12} > 100$ GeV (see text). E is the particle's energy and θ and ϕ its polar and azimuthal angles, respectively . The charges of the electron candidates are also given, if they are measured with a significance of better than two standard deviations. The six events were recorded in e^+p collisions.

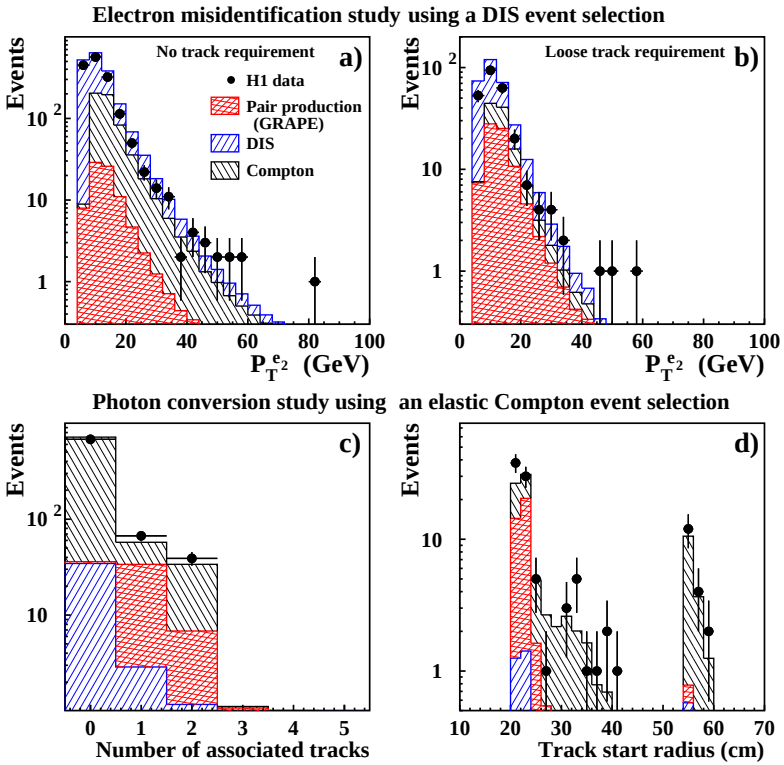

Figure 2: (a and b) Distributions associated with misidentified electrons for a DIS event selection. Transverse momentum spectrum of second electrons identified with either no track requirement (a) or a loose track requirement (b) compared with expectations. (c and d) Study of photon conversions using an elastic Compton event selection: number (c) and starting radius (d) of the tracks associated with the photon candidates compared with expectations.

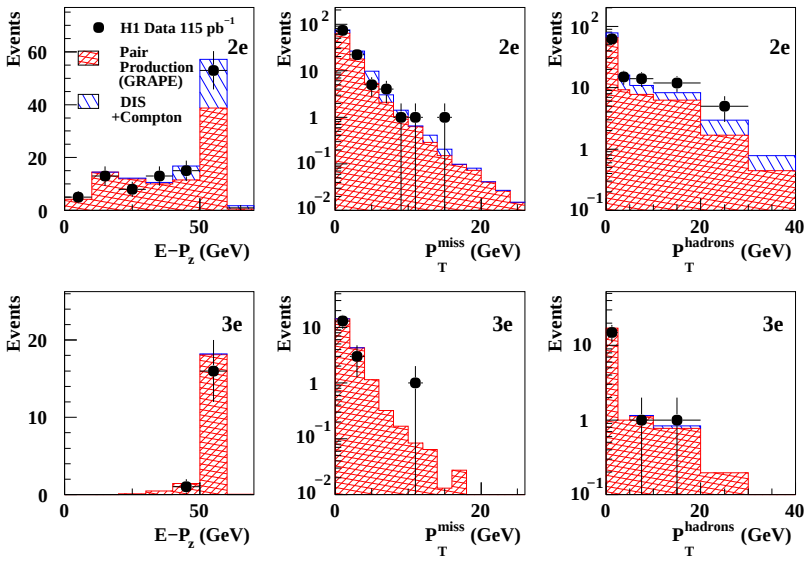

Figure 3: Distributions of $E - P_z$, P_T^{miss} and $P_T^{hadrons}$ for events classified as "2e" (top) and "3e" (bottom), compared with expectations.

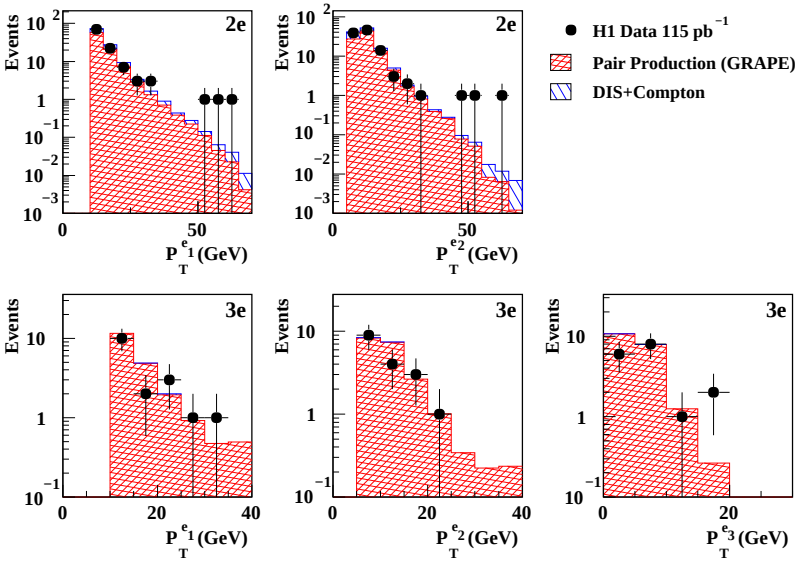

Figure 4: Electron transverse momentum distributions for events classified as "2e" (top) and "3e" (bottom) compared with expectations. Electrons are ordered according to decreasing transverse momentum, $P_T^{e_i} > P_T^{e_{i+1}}$.

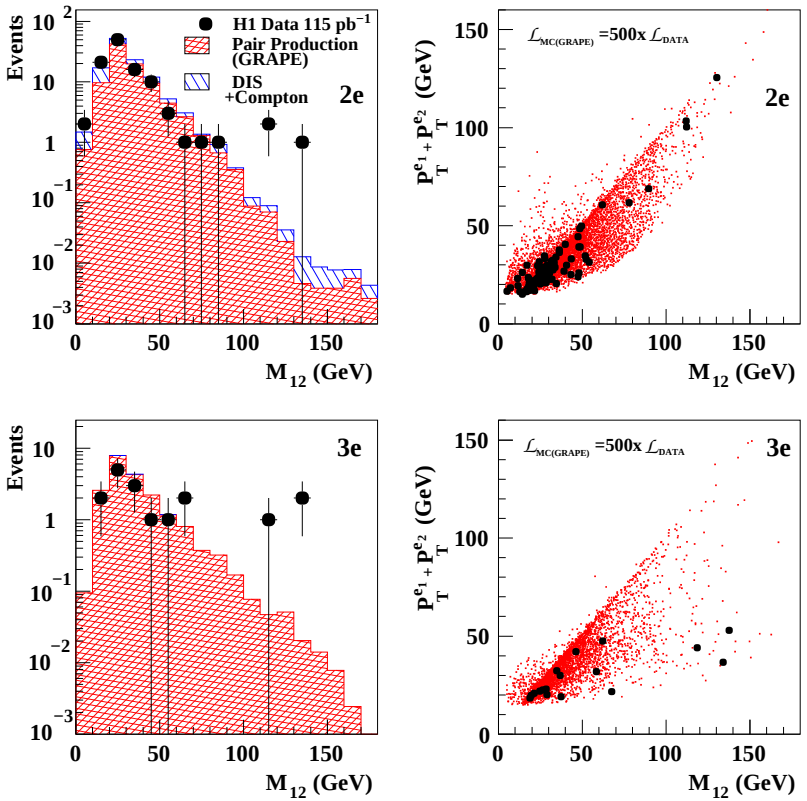

Figure 5: Distribution of the invariant mass M_{12} of the two highest P_T electrons compared with expectations (left) and the correlation of M_{12} with the scalar sum of the P_T's of the electrons (right) for events classified as "2e" (top) and "3e" (bottom). The bold dots on the right plots represent the data while the small points represent the pair production (GRAPE) prediction for a luminosity 500 times higher than that of the data.

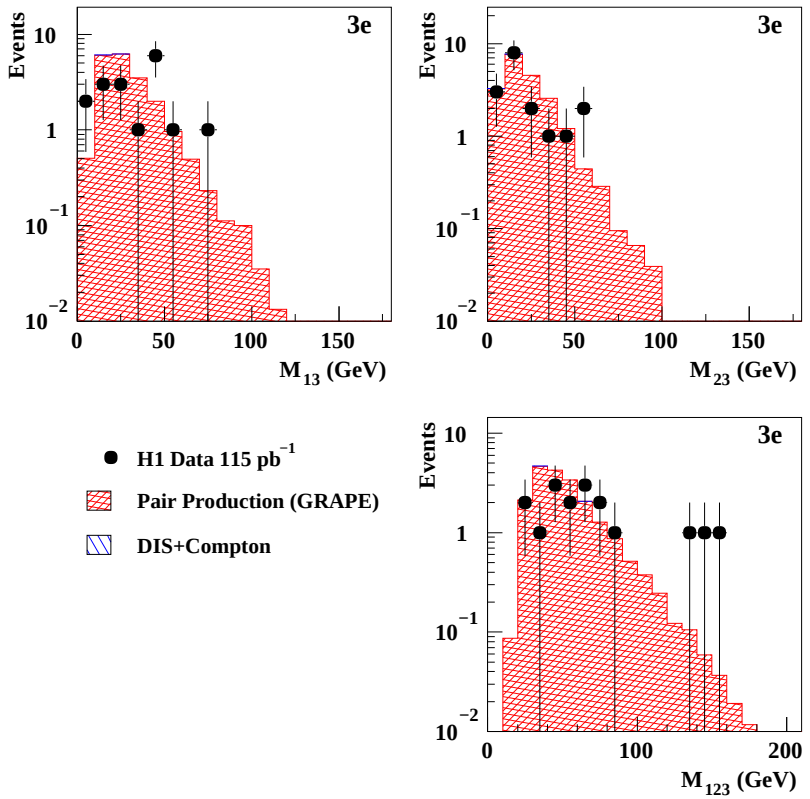

Figure 6: Invariant mass distributions of electron pairs 1-3 and 2-3 (top left and right) and of the tri–electron system (bottom right) for events classified as "3e".

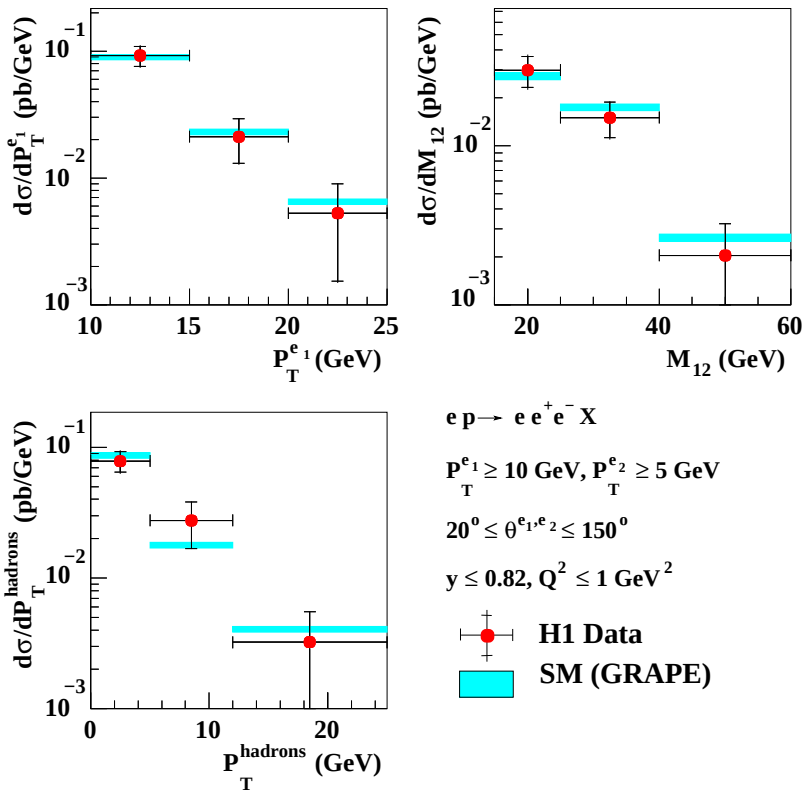

Figure 7: Cross section measurements in a restricted phase space dominated by the photon–photon process as a function of the leading electron transverse momentum (P_T^{e1}), the invariant mass of the electron–positron pair (M_{12}) and the hadronic transverse momentum ($P_T^{hadrons}$). The differential cross sections are averaged over the intervals shown. The inner error bars on the data points represent the statistical error, which dominates the measurement uncertainty. The outer error bars show the statistical and systematic uncertainties added in quadrature. The bands represent the one standard deviation uncertainty in the SM prediction.

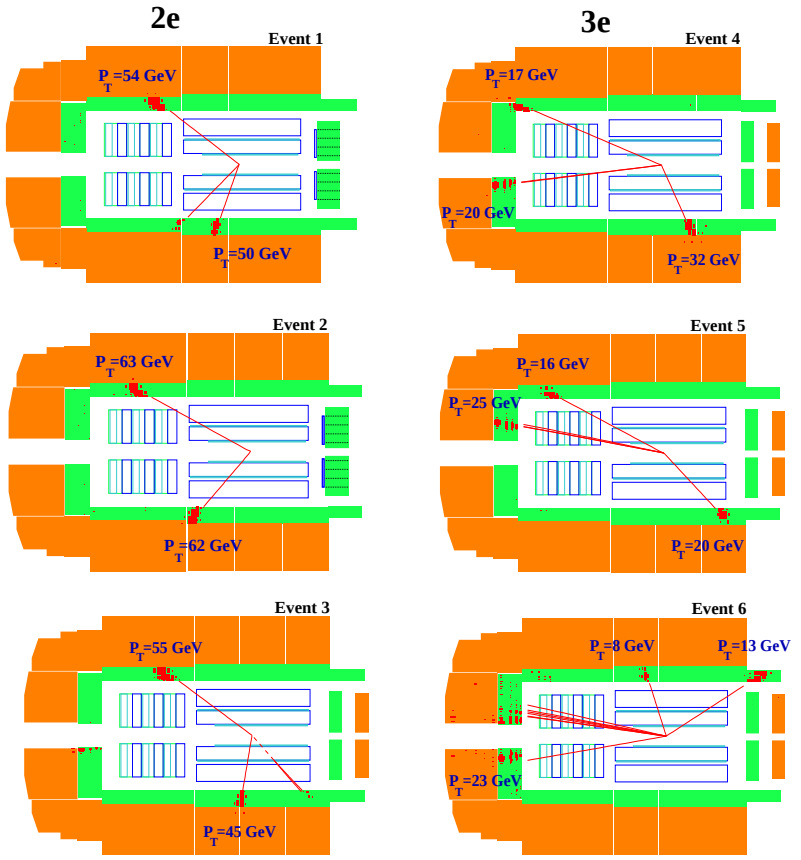

Figure 8: Displays of the three "2e" events (left) and the three "3e" events (right) with $M_{12} > 100$ GeV in the $R - z$ view. The reconstructed tracks and the energy deposits in the calorimeters are indicated (see text and table 4). The beam positrons enter the detector from the left and the protons from the right.

Annexe I

Multi-Lepton Production at High Transverse Momenta in ep Collisions at HERA

F.D. Aaron *et al.* [H1 Collaboration],
Phys. Lett. B **668** (2008) 268,
arXiv:0806.3987

Abstract

Processes leading to a final state with at least two high transverse momentum leptons (electrons or muons) are studied using the full $e^{\pm}p$ data sample collected by the H1 experiment at HERA. The data correspond to an integrated luminosity of 463 pb^{-1}. Di-lepton and tri-lepton event classes are investigated. Cross sections of the production of e^+e^- and $\mu^+\mu^-$ pairs are derived in a restricted phase space dominated by photon-photon collisions. In general, good agreement is found with Standard Model predictions. Events are observed with a total scalar sum of lepton transverse momenta above 100 GeV where the Standard Model expectation is low. In this region, combining di-lepton and tri-lepton classes, five events are observed in e^+p collisions, compared to a Standard Model expectation of 0.96 ± 0.12, while no such event is observed in e^-p data for 0.64 ± 0.09 expected.

1 Introduction

Within the Standard Model (SM) the production of multi-lepton events in electron[1]–proton collisions proceeds mainly via photon–photon interactions, $\gamma\gamma \to \ell^+\ell^-$, where photons are radiated from the incident beam particles [1]. The clean experimental signature and the precise SM prediction of this process provide a high sensitivity to searches for new phenomena producing multi-lepton final states. For example, the production of a doubly charged Higgs boson [2, 3] or processes involving generic bosons carrying two units of lepton number (bileptons) [4], could lead to multi-lepton events of large invariant mass. Measurements of both multi-electron [5] and muon pair [6] production at high transverse momentum (P_T) have already been performed by the H1 Collaboration using a data sample corresponding to an integrated luminosity of 115 pb^{-1}. Events with high invariant mass M_{12} of the two highest P_T electrons were measured. Three events with two electrons and three events with three electrons were observed in the region $M_{12} > 100$ GeV, where the SM prediction is low [5].

In the present paper a measurement of multi-lepton production at high P_T using the complete $e^{\pm}p$ HERA collider data of the H1 experiment is presented. The data are recorded at electron and proton beam energies of 27.6 GeV and 820 GeV or 920 GeV, corresponding to centre-of-mass energies $\sqrt{s}$ of 301 GeV or 319 GeV, respectively. The total integrated luminosity of the data is 463 pb^{-1}, which represents a factor of four increase with respect to the previous published results. The data comprise 178 pb^{-1} recorded in e^-p collisions and 285 pb^{-1} in e^+p collisions, of which 35 pb^{-1} were recorded at $\sqrt{s} = 301$ GeV. While previous measurements were performed mainly using e^+p data, an e^-p data set with more than a ten-fold increase in integrated luminosity is now analysed. The current analysis is extended with respect to those presented in [5, 6], such that all event final states with at least two high P_T leptons, electrons (e) or muons (μ), are now investigated. In addition, differential cross sections of the production of e^+e^- and $\mu^+\mu^-$ pairs are measured in a restricted phase space dominated by photon-photon collisions.

2 Standard Model Processes and their Simulation

Multi-lepton events are simulated with the GRAPE [7] generator, which includes all electroweak matrix elements at tree level. The production mechanisms include $\gamma\gamma$, γZ, ZZ interactions, internal photon conversion and the decay of virtual or real Z bosons. Different approaches for the cross section calculation are followed depending on the virtuality Q^2 of the photon coupled to the proton and on the mass W of the hadronic final state. In the elastic region, $ep \to e\,\ell^+\ell^-p$, the proton vertex is described in terms of dipole form factors. The quasi-elastic domain is defined by $W < 5$ GeV or $Q^2 < 1$ GeV^2. In the region $W < 2$ GeV, a resonance parametrisation [8] is used for the proton vertex. In the remaining quasi-elastic phase space, a fit to photoproduction and deep inelastic scattering data is used [9]. In the inelastic regime, corresponding to electron-quark interactions with $W > 5$ GeV and $Q^2 > 1$ GeV^2, proton parton densities taken from the CTEQ5L [10] parametrisation are used. Initial and final state QED radiation is included. The hadronic final state is simulated via interfaces to PYTHIA [11] and SOPHIA [12] for the inelastic and quasi-elastic regimes, respectively. GRAPE predicts cross sections for $ep \to e\,\mu^+\mu^-X$ and $ep \to e\,e^+e^-X$ processes, leading to $e\mu\mu$ and eee final states. Events with only two leptons ($\mu\mu$, $e\mu$ or ee) are observed if the scattered electron or one lepton of the pair is not detected. The $ep \to e\,\tau^+\tau^-X$ process with subsequent leptonic tau decays is also simulated with GRAPE and its contribution to the studied final states is found to be at most 4%.

Experimental backgrounds to ee and eee final states arise from events in which, in addition to a genuine electron, one or two fake electrons are reconstructed. Neutral current (NC) deep-inelastic scattering (DIS) events ($ep \to eX$) in which hadrons or radiated photons are wrongly identified as electrons constitute the dominant background contribution. QED Compton scattering $ep \to e\gamma X$ may also contribute if the photon is misidentified as an electron. Background to the $e\mu$ final state may arise from NC DIS events if hadrons are misidentified as muons. The NC DIS and Compton processes are simulated using the RAPGAP [13] and WABGEN [14] Monte Carlo (MC) generators, respectively.

Generated events are passed through the full GEANT [15] based simulation of the H1 apparatus, which takes into account the running conditions of the different data taking periods, and are reconstructed and analysed with the same program chain as is used for the data.

3 Experimental Conditions

A detailed description of the H1 experiment can be found in [16]. Only the detector components relevant to the present analysis are briefly described here. The origin of the H1 coordinate system is the nominal ep interaction point, with the direction of the proton beam defining the positive z-axis (forward region). Transverse momentum is measured in the xy plane. The pseudorapidity η is related to the polar angle θ by $\eta = -\ln\tan(\theta/2)$. The Liquid Argon (LAr) calorimeter [17] covers the polar angle range $4^\circ < \theta < 154^\circ$ with full azimuthal acceptance. Electromagnetic shower energies are measured with a precision of $\sigma(E)/E = 12\%/\sqrt{E/\text{GeV}} \oplus 1\%$ and hadronic energies with $\sigma(E)/E = 50\%/\sqrt{E/\text{GeV}} \oplus 2\%$, as measured in test beams [18, 19]. In the backward region, energy measurements are provided by a lead/scintillating-fiber (SpaCal) calorimeter [20] covering the range $155^\circ < \theta < 178^\circ$. The central ($20^\circ < \theta < 160^\circ$) and forward ($7^\circ < \theta < 25^\circ$) inner tracking detectors are used to measure charged particle trajectories, to reconstruct the interaction vertex and to complement the measurement of hadronic energies. The LAr calorimeter and inner tracking detectors are enclosed in a super-conducting magnetic coil with a field strength of 1.16 T. From the curvature of charged particle trajectories in the magnetic field, the central tracking system provides transverse momentum measurements with a resolution of $\sigma_{P_T}/P_T = 0.005P_T/\text{GeV} \oplus 0.015$ [21]. The return yoke of the magnetic coil is the outermost part of the detector and is equipped with streamer tubes forming the central muon detector ($4^\circ < \theta < 171^\circ$).

The luminosity is determined from the rate of the Bethe-Heitler process $ep \to ep\gamma$, measured using a photon detector located close to the beam pipe at $z = -103$ m, in the backward direction.

[1] In this paper the term "electron" is used generically to refer to both electrons and positrons, if not otherwise stated.

Events having an electromagnetic deposit in the LAr with an energy greater than 10 GeV are detected by the LAr trigger with an efficiency close to 100% [22]. The muon trigger is based on single muon signatures from the central muon detector, combined with signals from the central tracking detector. The trigger efficiency is about 90% for di-muon events with muon transverse momenta larger than 10 and 5 GeV. A combination of the LAr and muon triggers is used if an electron and a muon are both present in the final state, resulting in an efficiency close to 100% for electron and muon transverse momenta above 5 GeV.

4 Data Analysis

4.1 Particle Identification

Electron candidates are identified in the polar angle range $5^\circ < \theta < 175^\circ$ as a compact and isolated electromagnetic shower in either the LAr or SpaCal calorimeter. The electron energy and angular direction are measured by the calorimeters. The electron energy threshold is 5 GeV in the polar angle range $20^\circ < \theta < 175^\circ$ and is raised to 10 GeV in the forward region ($5^\circ < \theta < 20^\circ$). The calorimetric energy measured within a distance in the pseudorapidity-azimuth $(\eta - \phi)$ plane $R = \sqrt{\Delta\eta^2 + \Delta\phi^2} < 0.75$ around the electron is required to be below 2.5% of the electron energy. In the region of angular overlap between the LAr and the central tracking detectors ($20^\circ < \theta < 150^\circ$), hereafter referred to as the central region, the calorimetric electron identification is complemented by tracking information. In this region it is required that a well measured track geometrically matches the centre-of-gravity of the electromagnetic cluster within a distance of closest approach of 12 cm. The electron is required to be isolated from any other well measured track by a distance $R > 0.5$ to the electron direction. Furthermore, the distance from the first measured track point in the central drift chambers to the beam axis is required to be below 30 cm in order to reject photons that convert late in the central tracker material. In addition, in the central region the transverse momentum of the associated electron track P_T^{etk} is required to match the calorimetric measurement P_T^e such that $1/P_T^{etk} - 1/P_T^e < 0.02$ GeV^{-1} in order to reject hadronic showers. Due to a lower track reconstruction efficiency and higher showering probability, no track conditions are required for electron candidates in the forward ($5^\circ < \theta < 20^\circ$) and backward ($150^\circ < \theta < 175^\circ$) regions. In these regions, no distinction between electrons and photons is made. The resulting electron identification efficiency is 80% in the central region and larger than 95% in the forward and backward regions.

Muon candidates are identified in the polar angle range $20^\circ < \theta < 160^\circ$ with a minimum transverse momentum of 2 GeV. Muon identification is based on the measurement of a track in the inner tracking systems associated with a track segment or an energy deposit in the central muon detector [6, 23]. The muon momentum is measured from the inner track curvature in the solenoidal magnetic field. A muon candidate should have no more than 3.5 GeV deposited in a cylinder, centred on the muon track direction, of radius 25 cm and 50 cm in the electromagnetic and hadronic sections of the LAr calorimeter, respectively. Misidentified hadrons are strongly suppressed by requiring that the muon candidate be separated from any jet and from any track by $R > 1$. The efficiency to identify muons is $\sim 90\%$.

Calorimeter energy deposits and tracks not previously identified as electron or muon candidates are used to form combined cluster-track objects, from which the hadronic energy is

reconstructed [24, 25]. Jets are reconstructed from these combined cluster-track objects using an inclusive k_T algorithm [26, 27] with a minimum transverse momentum of 2.5 GeV.

4.2 Event Selection

In order to remove background events induced by cosmic rays and other non-ep sources, the event vertex is required to be reconstructed within 35 cm in z of the nominal interaction point. In addition, to remove non-ep background topological filters and timing vetoes are applied.

Multi-lepton events are selected by requiring at least two central ($20^\circ < \theta < 150^\circ$) electron or muon candidates, of which one must have $P_T^\ell > 10$ GeV and the other $P_T^\ell > 5$ GeV. Additional lepton candidates are identified in the detector according to the criteria defined in section 4.1. All lepton candidates are required to be isolated with respect to each other by a minimum distance in pseudorapidity-azimuth of $R > 0.5$. Lepton candidates are ordered according to decreasing transverse momentum, $P_T^{\ell_i} > P_T^{\ell_{i+1}}$. Final states with all possible combinations of lepton candidates are investigated. Selected events are classified into independent samples according to the flavour and the number of lepton candidates (e.g. ee, $e\mu$, $e\mu\mu$).

In order to measure the lepton pair production cross section in a well defined region of phase space, sub-samples of ee and $\mu\mu$ events dominated by photon-photon collisions are selected, labelled $(\gamma\gamma)_e$ and $(\gamma\gamma)_\mu$, respectively. In these subsamples the two leptons are required to be of opposite charge and a significant deficit compared to the initial state must be observed in the difference[2] $E - P_z$ of the energy and the longitudinal momentum of all visible particles, $E - P_z < 45$ GeV. These two conditions ensure that the incident electron is lost in the beam pipe after radiating a quasi-real photon of squared four-momentum Q^2 lower than 1 GeV^2.

4.3 Systematic Uncertainties

The following experimental systematic uncertainties are considered:

- The uncertainty on the electromagnetic energy scale varies depending on the polar angle from 0.7% in the backward and central region to 2% in the forward region. The polar angle measurement uncertainty of electromagnetic clusters is 3 mrad. The identification efficiency of electrons is known with an uncertainty of 3 to 5%, depending on the polar angle.
- The scale uncertainty on the transverse momentum of high P_T muons is 2.5%. The uncertainty on the reconstruction of the muon polar angle is 3 mrad. The identification efficiency of muons is known with an uncertainty of 5%.
- The hadronic energy scale is known within 2% at high transverse momentum and 5% for events with a total hadronic transverse momentum below 8 GeV.

[2] For fully contained events or events where only longitudinal momentum along the proton direction ($+z$) is undetected, one expects $E - P_z = 2E_e^0 = 55.2$ GeV, where E_e^0 is the energy of the incident electron. If the scattered electron is undetected, the threshold $E - P_z < 45$ GeV corresponds to a cut on the fractional energy loss $y = (E - P_z)/2E_e^0 < 0.82$.

- The uncertainty on the trigger efficiency is estimated to be 3% if at least one electron candidate is detected, and 6% if only muons are present in the final state.
- The luminosity measurement has an uncertainty of 3%.

The effect of the above systematic uncertainties on the SM expectation is determined by varying the experimental quantities by ± 1 standard deviation in the MC samples and propagating these variations through the whole analysis chain.

Additional model systematic uncertainties are attributed to the SM Monte Carlo generators described in section 2. The theoretical uncertainty on the lepton pair production cross section calculated with GRAPE is 3%. The uncertainty on the QED Compton and NC DIS background is 20%, as deduced from dedicated studies [5]. The total error on the SM prediction is determined by adding the effects of all model and experimental systematic uncertainties in quadrature.

5 Results

5.1 Multi–Lepton Event Samples

The observed event yields are summarised in table 1. Only classes for which at least one data event is selected are shown. In all other classes, no event is observed and the SM prediction is also negligible. The observed numbers of events are in good agreement with the SM expectations. The eee and ee channels are dominated by electron pair production. The $e\mu\mu$, $\mu\mu$ and $e\mu$ channels contain mainly events from muon pair production. The $e\mu$ channel is populated if the scattered electron and only one muon of the pair is selected. Four data events are classified as $ee\mu$ compared to a SM expectation of 1.43 ± 0.26, dominated by the production of muon pair events where one muon is lost and the second electron candidate is due to a radiated photon. One event with four electron candidates is observed compared to a prediction of 0.33 ± 0.07. According to MC simulations, this signature is due to tri-electron events with a radiated photon.

The distributions of the invariant mass M_{12} of the two highest P_T leptons for the eee and $e\mu\mu$ samples are shown in figures 1(a) and (b), respectively. The distributions of the invariant mass M_{12} of the two leptons in the di-lepton event classes are presented in figures 1(c), (d) and (e). An overall agreement with the SM prediction is observed in all cases.

High invariant mass events ($M_{12} > 100$ GeV) are observed in the data. The corresponding observed and predicted event yields are summarised for all channels in table 2. The three ee, three eee and one $\mu\mu$ high mass events have already been discussed extensively in previous H1 publications [5, 6]. No additional events in these classes are observed in the new data. One $e\mu$ and two $e\mu\mu$ high mass events are observed in the new data. The $e\mu\mu$ event with the largest invariant mass $M_{12} = 127 \pm 10$ GeV is presented in figure 2. In this event, M_{12} is formed by the electron and the highest P_T muon. In the other $e\mu\mu$ event, M_{12} is formed by the two muons. No $eeee$ or $ee\mu$ event is observed with a di-lepton invariant mass above 100 GeV, in agreement with the corresponding SM expectations below 0.01.

The results for e^+p and e^-p data are shown separately in table 2. The di-lepton (ee, $e\mu$ and $\mu\mu$) and tri-lepton (eee and $e\mu\mu$) events at high mass $M_{12} > 100$ GeV are all observed in e^+p collisions whereas no such event is observed in the e^-p data.

The topology of the multi-lepton events can be further investigated using the scalar sum of the lepton transverse momenta $\sum P_T$. This variable indicates the "hardness" of the event and also offers a good sensitivity for new physics searches [28]. Figure 3 presents the correlation between $\sum P_T$ and the invariant mass M_{12}, separately for di-lepton and tri-lepton events. It can be seen that tri-lepton events may have a large M_{12} but only intermediate $\sum P_T$. In such cases, the high mass is formed by one forward and one backward lepton. However, for di-lepton event classes high M_{12} values also imply a large $\sum P_T$.

The quantity $\sum P_T$ can be used to select the most energetic events and allows the combination of different topologies of di-lepton and tri-lepton events with electrons and muons. Figure 4 presents the distributions of $\sum P_T$ of the observed multi-lepton events compared to the SM expectation. A good overall agreement between the data and the SM prediction is observed. For $\sum P_T > 100$ GeV, five events are observed in total, compared to 1.60 ± 0.20 expected from the SM (see table 3). These five events were all recorded in the e^+p data, for which the SM expectation is 0.96 ± 0.12. Furthermore, the events correspond to the three ee and the two $e\mu\mu$ events observed with $M_{12} > 100$ GeV.

5.2 Cross Section Measurements

Cross sections of the production of electron and muon pairs from photon-photon collisions are measured using the selected $(\gamma\gamma)_e$ and $(\gamma\gamma)_\mu$ samples. The kinematic domain of the measurement is defined by $20^\circ < \theta^{\ell_{1,2}} < 150^\circ$, $P_T^{\ell_1} > 10$ GeV, $P_T^{\ell_2} > 5$ GeV, $Q^2 < 1$ GeV^2 and $y < 0.82$. The data samples collected at $\sqrt{s} = 301$ GeV and 319 GeV are combined taking into account their respective luminosities. Assuming a linear dependence of the cross section on the proton beam energy, as predicted by the SM, the resulting cross section corresponds to an effective $\sqrt{s} = 318$ GeV. The total numbers of observed $(\gamma\gamma)_e$ and $(\gamma\gamma)_\mu$ events are in agreement with the SM expectations, as summarised in table 1. In the $(\gamma\gamma)_e$ sample, the contamination from NC DIS and QED Compton background events is 2%. No significant background is present in the $(\gamma\gamma)_\mu$ sample.

The cross section is evaluated in each bin i using the formula

$$\sigma_i = \frac{N_i^{\mathrm{data}} - N_i^{\mathrm{bgr}}}{\mathcal{L} \cdot A_i}, \tag{1}$$

where N_i^{data} is the number of observed events in bin i, N_i^{bgr} the expected contribution from background processes in bin i, $\mathcal{L}$ the integrated luminosity of the data and A_i the signal acceptance in bin i. The signal acceptance is calculated using GRAPE MC events, as the ratio of the number of events reconstructed in bin i divided by the number of events generated in the same bin. It accounts for detection efficiencies and migrations between bins. The mean signal acceptance is 45% for $ep \to e\, e^+e^-X$ events and 60% for $ep \to e\, \mu^+\mu^-X$ events. The systematic

error of the measured cross section is determined by repeating the analysis after applying the appropriate variations to the MC for each systematic source, as described in section 4.3.

The measured $ep \to e\, e^+e^- X$ cross section integrated over the phase space defined above is $\sigma = 0.67 \pm 0.06 \pm 0.05$ pb, where the first error is statistical and the second systematic. The measured cross section for muon pair production, $ep \to e\, \mu^+\mu^- X$, in the same phase space is $\sigma = 0.63 \pm 0.05 \pm 0.09$ pb. The results are in agreement with the SM expectation of 0.63 ± 0.02 pb calculated using the GRAPE generator. Combining the di-electron and di-muon samples, an average lepton pair production cross section of $\sigma = 0.65 \pm 0.04 \pm 0.06$ pb is measured.

The differential cross sections of lepton pair production as a function of the transverse momentum of the leading lepton $P_T^{\ell_1}$, the invariant mass of the lepton pair $M_{\ell\ell}$ and the hadronic transverse momentum P_T^X are listed for each sample in table 4 and shown in figure 5 for the combined electron and muon samples. The measurements are in good agreement with the SM cross sections.

6 Conclusion

The production of multi-lepton (electron or muon) events at high transverse momenta is studied in e^+p and e^-p scattering. The full $e^\pm p$ data sample collected by the H1 experiment at HERA with an integrated luminosity of 463 pb^{-1} is analysed. The yields of di-lepton and tri-lepton events are in good agreement with the SM predictions. In each sample distributions of the invariant mass M_{12} of the two highest P_T leptons and of the scalar sum of the lepton transverse momenta $\sum P_T$ are studied and found to be in good overall agreement with the SM expectation.

Events are observed in the di-lepton and tri-lepton channels with high invariant masses M_{12} above 100 GeV. All such events are observed in e^+p collisions. Five of them have a $\sum P_T > 100$ GeV, whereas the corresponding SM expectation for e^+p collisions is 0.96 ± 0.12.

Differential cross sections for electron and muon pair production are measured in a restricted phase space dominated by photon-photon interactions. The measured cross sections are in agreement with the SM expectations.

Acknowledgements

We are grateful to the HERA machine group whose outstanding efforts have made this experiment possible. We thank the engineers and technicians for their work in constructing and maintaining the H1 detector, our funding agencies for financial support, the DESY technical staff for continual assistance and the DESY directorate for the hospitality which they extend to the non DESY members of the collaboration.

References

[1] J. A. M. Vermaseren, Nucl. Phys. B **229** (1983) 347.

[2] E. Accomando and S. Petrarca, Phys. Lett. B **323** (1994) 212 [hep-ph/9401242].

[3] A. Aktas *et al.* [H1 Collaboration], Phys. Lett. B **638** (2006) 432 [hep-ex/0604027].

[4] F. Cuypers and S. Davidson, Eur. Phys. J. C **2** (1998) 503 [hep-ph/9609487].

[5] A. Aktas *et al.* [H1 Collaboration], Eur. Phys. J. C **31** (2003) 17 [hep-ex/0307015].

[6] A. Aktas *et al.* [H1 Collaboration], Phys. Lett. B **583** (2004) 28 [hep-ex/0311015].

[7] T. Abe, GRAPE-Dilepton version 1.1, Comput. Phys. Commun. **136** (2001) 126 [hep-ph/0012029].

[8] F. W. Brasse *et al.*, Nucl. Phys. B **110** (1976) 413.

[9] H. Abramowicz and A. Levy, hep-ph/9712415.

[10] J. Pumplin *et al.*, JHEP **0207** (2002) 012 [hep-ph/0201195].

[11] T. Sjöstrand *et al.*, PYTHIA version 6.1, Comput. Phys. Commun. **135** (2001) 238 [hep-ph/0010017].

[12] A. Mucke *et al.*, Comput. Phys. Commun. **124** (2000) 290 [astro-ph/9903478].

[13] H. Jung, RAPGAP version 3.1, Comput. Phys. Commun. **86** (1995) 147.

[14] C. Berger and P. Kandel, "A New Generator For Wide Angle Bremsstrahlung," Proceedings of the Workshop "Monte Carlo Generators for HERA Physics", eds. A. T. Doyle *et al.*, DESY (1998).

[15] R. Brun *et al.*, "GEANT3," CERN-DD/EE/84-1.

[16] I. Abt *et al.* [H1 Collaboration], Nucl. Instrum. Meth. A **386** (1997) 310;
I. Abt *et al.* [H1 Collaboration], Nucl. Instrum. Meth. A **386** (1997) 348.

[17] B. Andrieu *et al.* [H1 Calorimeter Group Collaboration], Nucl. Instrum. Meth. A **336** (1993) 460.

[18] B. Andrieu *et al.* [H1 Calorimeter Group Collaboration], Nucl. Instrum. Meth. A **336** (1993) 499.

[19] B. Andrieu *et al.* [H1 Calorimeter Group Collaboration], Nucl. Instrum. Meth. A **350** (1994) 57.

[20] R. D. Appuhn *et al.* [H1 SPACAL Group Collaboration], Nucl. Instrum. Meth. A **386** (1997) 397.

[21] C. Kleinwort [H1 Collaboration], "H1 Alignment Experience," Proceedings of the Workshop "First LHC Detector Alignment Workshop", eds. S. Blusk *et al.*, CERN (2006), CERN-2007-04.

[22] C. Adloff *et al.* [H1 Collaboration], Eur. Phys. J. C **30** (2003) 1 [hep-ex/0304003].

[23] V. Andreev *et al.* [H1 Collaboration], Phys. Lett. B **561** (2003) 241 [hep-ex/0301030].

[24] M. Peez, "Recherche de déviations au Modèle Standard dans les processus de grande énergie transverse sur le collisionneur électron - proton HERA", Ph.D. thesis, Université de Lyon (2003), DESY-THESIS-2003-023. (available at http://www-h1.desy.de/psfiles/theses/).

[25] B. Portheault, "Première mesure des sections efficaces de courant chargé et neutre avec le faisceau de positrons polarisé à HERA II et analyses QCD-électrofaibles", Ph.D. thesis, Université Paris XI (2005), LAL-05-05. (available at http://www-h1.desy.de/psfiles/theses/).

[26] S. D. Ellis and D. E. Soper, Phys. Rev. D **48** (1993) 3160 [hep-ph/9305266].

[27] S. Catani *et al.*, Nucl. Phys. B **406** (1993) 187.

[28] A. Aktas *et al.* [H1 Collaboration], Phys. Lett. B **602** (2004) 14 [hep-ex/0408044].

Multi-Leptons at HERA (463 pb^{-1})

Selection	Data	SM	Pair Production (GRAPE)	NC DIS + Compton
ee	368	390 ± 46	332 ± 26	58 ± 30
$\mu\mu$	201	211 ± 32	211 ± 32	< 0.005
$e\mu$	132	128 ± 9	118 ± 8	10.0 ± 2.5
eee	73	70 ± 7	69.8 ± 7.0	0.2 ± 0.1
$e\mu\mu$	97	102 ± 14	102 ± 14	< 0.005
$ee\mu$	4	1.43 ± 0.26	1.18 ± 0.20	0.25 ± 0.14
$eeee$	1	0.33 ± 0.07	0.33 ± 0.07	< 0.005
$(\gamma\gamma)_e$	146	138 ± 12	135 ± 11	3.0 ± 1.0
$(\gamma\gamma)_\mu$	163	162 ± 24	162 ± 24	< 0.005

Table 1: Observed and predicted event yields for the different event classes. The errors on the predictions include model uncertainties and experimental systematic errors added in quadrature. The limits on the background estimations correspond to the selection of no event in the simulated sample and are quoted at 95% confidence level.

Multi-Leptons at HERA (463 pb^{-1})

M_{12} >100 GeV

Selection	Data	SM	Pair Production (GRAPE)	NC DIS + Compton
All data (463 pb^{-1})				
ee	3	1.34 ± 0.20	0.83 ± 0.11	0.51 ± 0.13
$\mu\mu$	1	0.17 ± 0.07	0.17 ± 0.07	< 0.005
$e\mu$	1	0.59 ± 0.06	0.59 ± 0.06	< 0.005
eee	3	0.66 ± 0.09	0.66 ± 0.09	< 0.005
$e\mu\mu$	2	0.16 ± 0.05	0.16 ± 0.05	< 0.005
e^+p collisions (285 pb^{-1})				
ee	3	0.76 ± 0.11	0.49 ± 0.07	0.27 ± 0.07
$\mu\mu$	1	0.10 ± 0.04	0.10 ± 0.04	< 0.005
$e\mu$	1	0.35 ± 0.04	0.35 ± 0.04	< 0.005
eee	3	0.39 ± 0.05	0.39 ± 0.05	< 0.005
$e\mu\mu$	2	0.09 ± 0.03	0.09 ± 0.03	< 0.005
e^-p collisions (178 pb^{-1})				
ee	0	0.58 ± 0.09	0.34 ± 0.04	0.24 ± 0.07
$\mu\mu$	0	0.07 ± 0.03	0.07 ± 0.03	< 0.005
$e\mu$	0	0.24 ± 0.03	0.24 ± 0.03	< 0.005
eee	0	0.27 ± 0.04	0.27 ± 0.04	< 0.005
$e\mu\mu$	0	0.07 ± 0.03	0.07 ± 0.03	< 0.005

Table 2: Observed and predicted multi-lepton event yields for masses $M_{12} > 100$ GeV for the different event classes in all analysed samples. The errors on the predictions include model uncertainties and experimental systematic errors added in quadrature. The limits on the background estimations correspond to the selection of no event in the simulated sample and are quoted at 95% confidence level.

Multi-Leptons at HERA (463 pb^{-1})

$\sum P_T$ >100 GeV				
Data sample	Data	SM	Pair Production (GRAPE)	NC DIS + Compton
e^+p (285 pb^{-1})	5	0.96 ± 0.12	0.78 ± 0.09	0.18 ± 0.05
e^-p (178 pb^{-1})	0	0.64 ± 0.09	0.51 ± 0.07	0.13 ± 0.04
All (463 pb^{-1})	5	1.60 ± 0.20	1.29 ± 0.15	0.31 ± 0.09

Table 3: Observed and predicted multi-lepton event yields for $\sum P_T > 100$ GeV. Di-lepton and tri-lepton events are combined. The errors on the predictions include model uncertainties and experimental systematic errors added in quadrature.

Multi-Leptons at HERA (463 pb^{-1})

Variable range [GeV]	Measured (e^+e^-) [fb/GeV]	Measured ($\mu^+\mu^-$) [fb/GeV]	Measured (average) [fb/GeV]	Pair Production (GRAPE) [fb/GeV]
$P_T^{\ell_1}$		$d\sigma/dP_T^{\ell_1}$		
[10, 15]	$108 \pm 10 \pm 8$	$95 \pm 9 \pm 14$	$101 \pm 7 \pm 9$	92 ± 3
[15, 20]	$16 \pm 4 \pm 2$	$23 \pm 4 \pm 4$	$20 \pm 3 \pm 2$	22 ± 1
[20, 25]	$7.4 \pm 2.5 \pm 0.6$	$3.7 \pm 1.7 \pm 0.5$	$5.5 \pm 1.5 \pm 0.5$	6.6 ± 0.2
[25, 50]	$0.60 \pm 0.30 \pm 0.06$	$0.70 \pm 0.30 \pm 0.10$	$0.70 \pm 0.20 \pm 0.07$	0.86 ± 0.03
$M_{\ell\ell}$		$d\sigma/dM_{\ell\ell}$		
[15, 25]	$34 \pm 4 \pm 3$	$29 \pm 3 \pm 4$	$32 \pm 3 \pm 3$	28 ± 1
[25, 40]	$16 \pm 2 \pm 2$	$17 \pm 2 \pm 3$	$17 \pm 2 \pm 2$	18.0 ± 0.5
[40, 60]	$2.7 \pm 0.8 \pm 0.2$	$1.7 \pm 0.6 \pm 0.3$	$2.2 \pm 0.5 \pm 0.2$	2.9 ± 0.1
[60, 100]	$0.20 \pm 0.15 \pm 0.02$	$0.40 \pm 0.20 \pm 0.07$	$0.30 \pm 0.13 \pm 0.04$	0.24 ± 0.01
P_T^X		$d\sigma/dP_T^X$		
[0, 5]	$95 \pm 9 \pm 8$	$94 \pm 8 \pm 14$	$94 \pm 6 \pm 9$	93 ± 3
[5, 12]	$25 \pm 6 \pm 2$	$13 \pm 4 \pm 2$	$18 \pm 3 \pm 2$	15.4 ± 0.5
[12, 25]	$2.8 \pm 1.3 \pm 0.3$	$4.2 \pm 1.2 \pm 0.6$	$3.8 \pm 0.9 \pm 0.4$	3.8 ± 0.1
[25, 50]	$0.20 \pm 0.30 \pm 0.03$	$0.50 \pm 0.30 \pm 0.09$	$0.40 \pm 0.20 \pm 0.06$	0.20 ± 0.01

Table 4: Differential cross sections $d\sigma/dP_T^{\ell_1}$, $d\sigma/dM_{\ell\ell}$ and $d\sigma/dP_T^X$ averaged for each quoted interval for the process $ep \to e\ell^+\ell^-X$ in a restricted phase space dominated by the photon-photon process (see text for details). Cross sections are measured for e^+e^- or $\mu^+\mu^-$ pairs. The cross section obtained from the combination of e^+e^- and $\mu^+\mu^-$ channels is also presented. The first error is statistical and the second is systematic. Theoretical predictions, calculated with GRAPE, are shown in the last column.

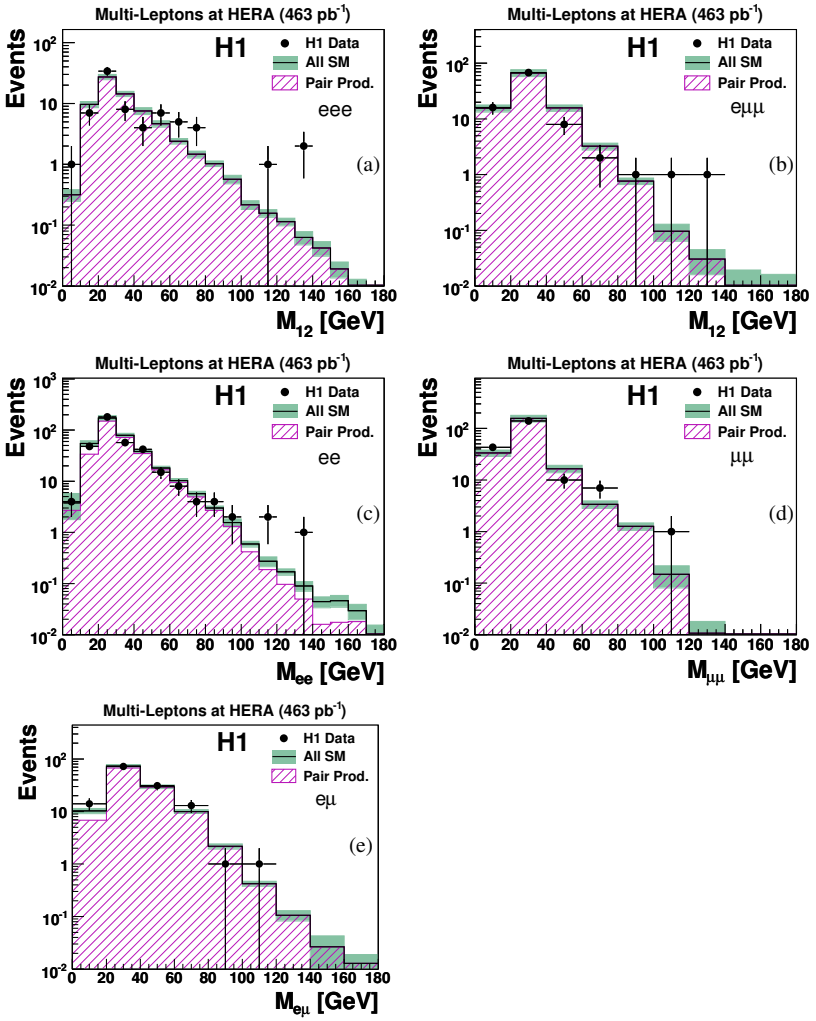

Figure 1: The distribution of the invariant mass of the two highest P_T leptons for events classified as eee (a), $e\mu\mu$ (b) and ee (c), $\mu\mu$ (d) and $e\mu$ (e). The points correspond to the observed data events and the open histogram to the SM expectation. The total error on the SM expectation is given by the shaded band. The component of the SM expectation arising from lepton pair production is given by the hatched histogram.

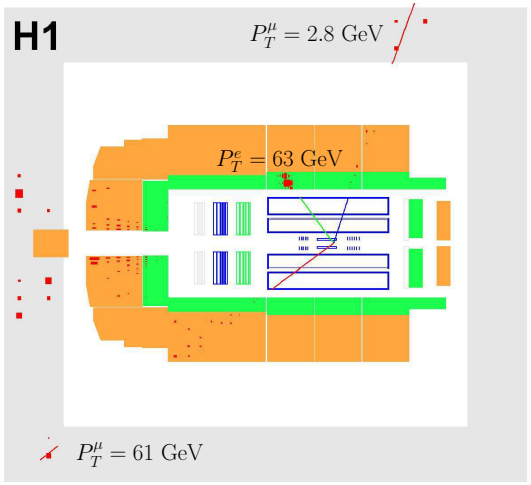

Figure 2: Display (side view) of the $e\mu\mu$ event observed with the highest M_{12} invariant mass. Indicated are the reconstructed tracks and the energy depositions in the calorimeters. The beam positrons enter the detector from the left and the protons from the right.

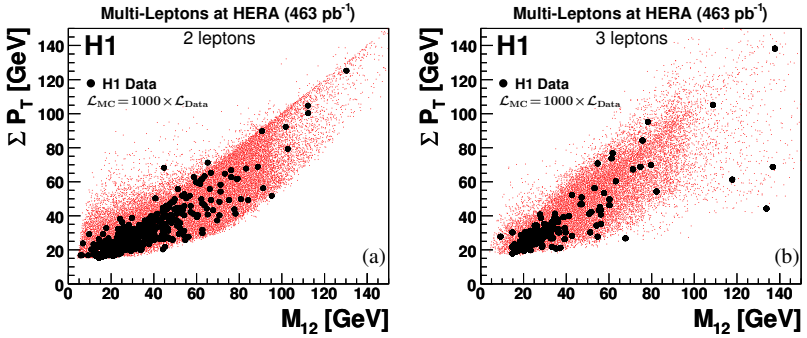

Figure 3: Correlation of the invariant mass M_{12} with the scalar sum of the transverse momenta $\sum P_T$ for di-lepton (a) and tri-lepton (b) events. The bold dots represent the data while the small points represent the pair production (GRAPE) prediction for a luminosity ~ 1000 times higher than that of data.

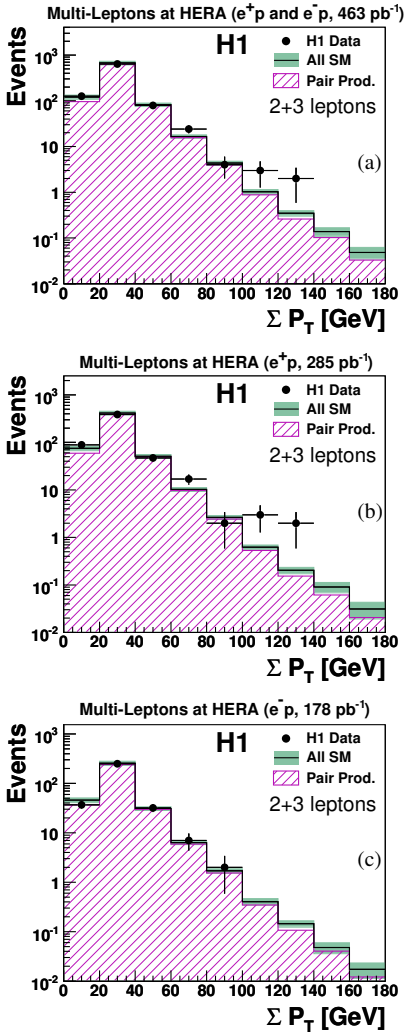

Figure 4: The distribution of the scalar sum of the transverse momenta $\sum P_T$ for combined di-lepton and tri-lepton event samples for all data (a) as well as for e^+p (b) and e^-p (c). The points correspond to the observed data events and the open histogram to the SM expectation. The total error on the SM expectation is given by the shaded band. The component of the SM expectation arising from lepton pair production is given by the hatched histogram.

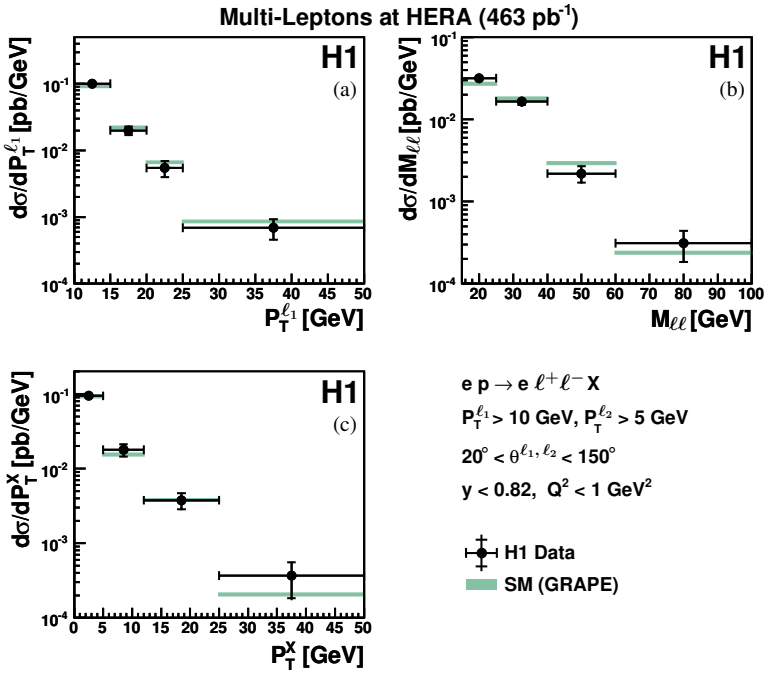

Figure 5: The measured cross section for lepton pair production in a restricted phase space dominated by the photon-photon process as a function of the leading lepton transverse momentum $P_T^{\ell_1}$ (a), the invariant mass of the lepton pair $M_{\ell\ell}$ (b) and the hadronic transverse momentum P_T^X (c). The differential cross section is averaged over the intervals shown. The inner error bars represent the statistical errors, the outer error bars the statistical and systematic errors added in quadrature. The bands represent the SM prediction with its one standard deviation uncertainty.

Annexe J

Multi-Leptons with High Transverse Momentum at HERA

F.D. Aaron *et al.* [H1 and ZEUS Collaborations],
JHEP 10 (2009) 013,
arXiv:0907.362

Abstract

Events with at least two high transverse momentum leptons (electrons or muons) are studied using the H1 and ZEUS detectors at HERA with an integrated luminosity of 0.94 fb^{-1}. The observed numbers of events are in general agreement with the Standard Model predictions. Seven di- and tri-lepton events are observed in e^+p collision data with a scalar sum of the lepton transverse momenta above 100 GeV while 1.94 ± 0.17 such events are expected. Such events are not observed in e^-p collisions for which 1.19 ± 0.12 are predicted. Total visible and differential di-electron and di-muon photoproduction cross sections are extracted in a restricted phase space dominated by photon-photon collisions.

1 Introduction

According to predictions of the Standard Model (SM) the production of multi-lepton final states in electron[1]-proton collisions proceeds mainly via photon-photon interactions [1]. The clean experimental signature of leptons with high transverse momenta, P_T, together with the precisely calculable small SM cross section provides high sensitivity to possible contributions of physics beyond the SM. Measurements of multi-lepton production at the HERA collider have already been performed by the H1 [2–5] and ZEUS [6] collaborations using data samples corresponding to an integrated luminosity of ~ 0.5 fb^{-1} per experiment. Events with high invariant mass M_{12} of the two highest P_T leptons or high scalar sum of transverse momenta of all leptons $\sum P_T$ were measured by both experiments in a region where the SM expectation is low. The yields of multi-lepton events were found to be in general agreement with the SM predictions in both H1 and ZEUS analyses.

A combination of the H1 and ZEUS results which exploits the complete $e^{\pm}p$ data samples of both experiments is presented in this paper. Total yields and kinematic distributions of multi-lepton final states with electrons or muons are measured and compared to the SM. The two-fold increase in the available data statistics allows a more stringent test of the SM in the high mass and high $\sum P_T$ regions. In addition, total visible and differential photoproduction cross sections of e^+e^- and $\mu^+\mu^-$ pairs are measured in a restricted phase-space region dominated by photon-photon collisions.

The analysed data were collected between 1994 and 2007 at the HERA electron-proton collider using the H1 and ZEUS detectors. The electron and proton beam energies were respectively 27.6 GeV and 820 GeV or 920 GeV, corresponding to centre-of-mass energies $\sqrt{s}$ of 301 GeV or 319 GeV. The data correspond to an integrated luminosity of 0.94 fb^{-1}, comprising 0.38 fb^{-1} of e^-p collisions and 0.56 fb^{-1} of e^+p collisions, with 8% of the total collected at $\sqrt{s} = 301$ GeV.

The H1 and ZEUS detectors are general purpose instruments which consist of tracking systems surrounded by electromagnetic and hadronic calorimeters and muon detectors, ensuring close to 4π coverage of the ep interaction point. The origin of the coordinate system is the nominal ep interaction point, with the direction of the proton beam defining the positive z-axis (forward region). The $x-y$ plane is called the transverse plane and ϕ is the azimuthal angle. The pseudorapidity η is defined as $\eta = -\ln\tan(\theta/2)$, where θ is the polar angle. Detailed descriptions of the H1 and ZEUS detectors can be found elsewhere [7, 8].

2 Experimental Method

For this analysis, a common phase-space region is chosen according to the individual performances of the H1 and ZEUS detectors, such that both detectors have high and well understood acceptance. The common phase-space region is somewhat smaller than those used by the respective collaborations [5, 6] and is described in the following.

[1]Here and in the following, the term "electron" denotes generically both the electron and the positron.

The event selection proceeds in two steps. Electron or muon candidates are first identified using a wider angular range and lower energy thresholds allowed by the detectors. In a second step, in order to minimise the background present in some of the event topologies, at least two central ($20^\circ < \theta < 150^\circ$) lepton candidates are required.

Electron candidates are identified in the polar-angle range $5^\circ < \theta < 175^\circ$ as compact and isolated energy deposits in the electromagnetic calorimeters. The electron energy threshold is 10 GeV in the range $5^\circ < \theta < 150^\circ$ and 5 GeV in the backward region $150^\circ < \theta < 175^\circ$. Compared to the published H1 analysis [5], the electron energy threshold is here raised in the central region $20^\circ < \theta < 150^\circ$ from 5 to 10 GeV. Muon candidates are identified in the range $20^\circ < \theta < 160^\circ$ with a minimum transverse momentum of 2 GeV. Muon identification is based on the measurement of a track in the inner tracking system associated to a track segment reconstructed in the muon chambers or an energy deposit in the calorimeter compatible with a minimum ionising particle. Only tracks associated with the primary event vertex are used in the analysis. Detailed descriptions of electron and muon identification criteria used by the H1 and ZEUS experiments are given in the individual publications [5, 6]. For the H1 experiment, the resulting electron identification efficiency is 80% in the central region and larger than 95% in the forward and backward regions, while for the ZEUS detector the electron identification efficiency is 90%. The lower electron identification efficiency in the H1 analysis is mainly due to a tight matching requirement between the transverse momenta measured by the tracker and the calorimeter [3, 5]. The efficiency to identify muons in the H1 and ZEUS analyses is 90% and 55%, respectively. The lower muon identification efficiency for ZEUS is due to a lower performance and a smaller fiducial volume of the muon system and a low efficiency of the track trigger for low multiplicity events [6].

Multi-lepton events are selected by requiring at least two central lepton candidates, of which one must have $P_T^\ell > 10$ GeV and the other $P_T^\ell > 5$ GeV. Additional leptons identified in the detector according to the criteria defined above may be present in the event. All lepton candidates are required to be isolated with respect to each other by a minimum distance of at least 0.5 units in the $\eta - \phi$ plane. No explicit requirement on the charge of the lepton candidates is imposed. Lepton candidates are ordered according to decreasing transverse momentum, $P_T^{\ell_i} > P_T^{\ell_{i+1}}$. According to the number and the flavour of the lepton candidates, the events are classified into mutually exclusive topologies.

The production cross section of e^+e^- and $\mu^+\mu^-$ pairs is measured in the photoproduction regime, in which the virtuality Q^2 of the photon emitted by the beam electron is low. Subsamples of ee and $\mu\mu$ events, dominated by photon-photon collisions, labelled $(\gamma\gamma)_e$ and $(\gamma\gamma)_\mu$, are selected by requiring the difference $E - P_z$ between the energy and the longitudinal momentum of all visible particles to be lower than 45 GeV. This requirement selects events in which the scattered electron is lost in the beampipe and corresponds to cuts on $Q^2 < 1$ GeV^2 and on the event inelasticity, $y = (E - P_z)/2E_e < 0.82$, where E_e is the electron beam energy.

The GRAPE [9] Monte Carlo (MC) event generator is used to calculate SM production cross sections, dominated by photon-photon interactions, $\gamma\gamma \to \ell^+\ell^-$, and to simulate multi-lepton events. GRAPE predicts cross sections for $ep \to e\,\mu^+\mu^- X$ and $ep \to e\,e^+e^- X$ processes, leading to $e\mu\mu$ and eee final states. Events with only two leptons ($\mu\mu$, $e\mu$ or ee) are observed if the scattered electron or one lepton of the pair is not detected. The $ep \to e\,\tau^+\tau^- X$ process with subsequent leptonic tau decays is also simulated with GRAPE.

Experimental background contributions from various SM processes to the selected multi-lepton topologies were studied [5,6]. Backgrounds to the ee final state arise from neutral current (NC) deep inelastic scattering (DIS) events ($ep \to eX$) in which, in addition to the scattered electron, hadrons or radiated photons are wrongly identified as electrons, and from QED Compton (QEDC) events ($ep \to e\gamma X$) if the photon is misidentified as an electron. Background to the $e\mu$ final state arises from NC DIS events if hadrons are misidentified as muons. The background contributions to eee, $e\mu\mu$ and $\mu\mu$ final states are negligible.

The combination of the results of the H1 and ZEUS experiments is performed both on the number of observed events and at the cross section level. Distributions of data events and of MC expectations are added bin by bin. Experimental systematic uncertainties are treated as uncorrelated between the experiments. A detailed list of all experimental systematic uncertainties of both experiments can be found in the individual publications [5, 6]. The theoretical uncertainty of 3% on the total lepton pair contribution calculated from the GRAPE MC is considered to be correlated between the experiments. Cross sections measured by H1 and ZEUS are combined using a weighted average [10].

3 Results

The total number of selected events in the data are compared to SM predictions in Table 1 for the ee, $\mu\mu$, $e\mu$, eee and $e\mu\mu$ topologies and for the $\gamma\gamma$ subsamples. The observed numbers of events are in good agreement with the SM expectations. The $e\mu\mu$, $\mu\mu$ and $e\mu$ topologies are dominated by muon pair production while the eee and ee topologies contain mainly events from electron pair production. The contribution from tau pair production is $\sim 4\%$ in the $e\mu$ topology, negligible in the others, and is considered as signal. The NC DIS and QEDC processes give rise to a sizeable background contribution in the ee topology where the H1 and ZEUS analyses have slightly different background rejection capabilities. The contribution from NC DIS and QEDC processes to the total SM expectation amounts to 24% for ZEUS and 11% for H1 due to the tighter electron identification criteria. Most of the events in the $e\mu$ topology arise from muon pair production at high Q^2, in which the beam electron is scattered at a large angle in the detector, while one of the muons is outside the acceptance region. In this topology, the NC DIS background contributes $\sim 10\%$ in both the H1 and ZEUS experiments.

The distributions of the invariant mass M_{12} of the two highest P_T leptons for the different topologies are shown in Fig. 1. An overall agreement with the SM prediction is observed in all cases. Events with high invariant mass ($M_{12} > 100$ GeV) are observed in the data. The corresponding observed and predicted event yields are summarised for all topologies in Table 2. One ee and two eee high mass events are observed by ZEUS [6]. Nine high mass events are observed by H1. Compared to the H1 results [5], one eee high mass event is not selected in this combined analysis due to the increased electron energy threshold of 10 GeV in the central region. The results for e^+p and e^-p data are also shown separately in Table 2. All high mass events observed by both experiments originate from e^+p collisions. Several of these events also have high $\sum P_T$ values.

Figure 2 presents the distributions of $\sum P_T$ of the observed multi-lepton events compared to the SM expectation. Good overall agreement between the data and the SM prediction is

observed. For $\sum P_T > 100$ GeV, seven events are observed in total, compared to 3.13 ± 0.26 expected from the SM (see Table 3). These seven events were all recorded in the e^+p data, for which the SM expectation is 1.94 ± 0.17. The events correspond to the four ee and the two $e\mu\mu$ events observed with $M_{12} > 100$ GeV, together with one eee event observed with $M_{12} = 93$ GeV.

Total visible and differential cross sections for di-electron and di-muon production are measured using the selected $(\gamma\gamma)_e$ and $(\gamma\gamma)_\mu$ subsamples. The kinematic domain of the measurement is defined by $20^\circ < \theta^{\ell_{1,2}} < 150^\circ$, $P_T^{\ell_1} > 10$ GeV, $P_T^{\ell_2} > 5$ GeV, $Q^2 < 1$ GeV^2, $y < 0.82$ and $D_{\eta-\phi}^{\ell_1,\ell_2} > 0.5$, where $D_{\eta-\phi}^{\ell_1,\ell_2}$ is the distance in the $\eta - \phi$ plane between the two leptons. The effect of the $D_{\eta-\phi}^{\ell_1,\ell_2}$ requirement is small ($< 1\%$). The data samples at $\sqrt{s} = 301$ GeV and 319 GeV are combined. Assuming a linear dependence of the cross section on the proton beam energy, as predicted by the SM, the resulting cross section corresponds to an effective $\sqrt{s} = 318$ GeV. The effect of final-state radiation on the cross sections was found to be negligible.

The total numbers of observed $(\gamma\gamma)_e$ and $(\gamma\gamma)_\mu$ events are in agreement with the SM expectations, as summarised in Table 1. In the $(\gamma\gamma)_e$ sample, the contamination from NC DIS and QEDC background events is 2%. No significant background is present in the $(\gamma\gamma)_\mu$ sample. The contribution from τ pair production is negligible in both the $(\gamma\gamma)_e$ and $(\gamma\gamma)_\mu$ subsamples.

The total visible and differential cross sections for electron and muon pair production are evaluated bin by bin as the weighted mean of the values measured by the two collaborations. The same binning is used by both experiments. The signal acceptance is defined as the number of events reconstructed in a bin divided by the number of events generated in the same bin and is calculated using GRAPE MC events. For $ep \to e\, e^+e^-X$ events, the mean signal acceptances in the H1 and ZEUS experiments are 45% and 60%, respectively. In case of $ep \to e\, \mu^+\mu^-X$ events, it is 60% for H1 and 30% for ZEUS.

The total visible $ep \to ee^+e^-X$ cross section is $\sigma = 0.68 \pm 0.04 \pm 0.03$ pb, where the first uncertainty is statistical and the second systematic. The total visible $ep \to e\mu^+\mu^-X$ cross section is $\sigma = 0.63 \pm 0.05 \pm 0.06$ pb. The results are in agreement with the SM expectation, dominated by photon-photon collisions, of 0.69 ± 0.02 pb calculated using the GRAPE generator. Since the muon and electron cross sections are compatible, as expected, they are combined into a single measurement, leading to a measured lepton pair production cross section of $\sigma = 0.66 \pm 0.03 \pm 0.03$ pb. This result is in agreement with the individual H1 and ZEUS measurements [5, 6].

Differential cross sections of lepton pair production as a function of the transverse momentum of the leading lepton $P_T^{\ell_1}$ and of the invariant mass of the lepton pair $M_{\ell\ell}$ are listed for each sample in Table 4 and shown in Fig. 3 for the combined electron and muon samples. The measurements are in good agreement with the SM predictions.

4 Conclusion

The production of multi-lepton (electron or muon) events at high transverse momenta was studied using the full $e^\pm p$ data sample collected by the H1 and ZEUS experiments at HERA, corresponding to a total integrated luminosity of 0.94 fb^{-1}. The yields of di-lepton and tri-lepton

events are in good agreement with the SM predictions. Distributions of the invariant mass M_{12} of the two highest P_T leptons and of the scalar sum of the lepton transverse momenta $\sum P_T$ are in good overall agreement with the SM expectation.

Events are observed in ee, $\mu\mu$, $e\mu$, eee and $e\mu\mu$ topologies with invariant masses M_{12} above 100 GeV, where the SM expectation is low. Both experiments observe high mass and high $\sum P_T$ events in e^+p collisions only, while, for comparable SM expectations, none are observed in e^-p collisions. Seven events have a $\sum P_T > 100$ GeV, whereas the corresponding SM expectation for e^+p collisions is 1.94 ± 0.17.

The total and differential cross sections for electron and muon pair photoproduction are measured in a restricted phase space dominated by photon-photon interactions. The measured cross sections are in agreement with the SM predictions.

Acknowledgements

We are grateful to the HERA machine group whose outstanding efforts have made these experiments possible. We appreciate the contributions to the construction and maintenance of the H1 and ZEUS detectors of many people who are not listed as authors. We thank our funding agencies for financial support, the DESY technical staff for continuous assistance and the DESY directorate for their support and for the hospitality they extended to the non-DESY members of the collaborations.

References

[1] J. A. M. Vermaseren, Nucl. Phys. B **229** (1983) 347.

[2] A. Aktas *et al.* [H1 Collaboration], Phys. Lett. B **638** (2006) 432 [hep-ex/0604027].

[3] A. Aktas *et al.* [H1 Collaboration], Eur. Phys. J. C **31** (2003) 17 [hep-ex/0307015].

[4] A. Aktas *et al.* [H1 Collaboration], Phys. Lett. B **583** (2004) 28 [hep-ex/0311015].

[5] F. D. Aaron *et al.* [H1 Collaboration], Phys. Lett. B **668** (2008) 268 [arXiv:0806.3987].

[6] S. Chekanov *et al.* [ZEUS Collaboration], Submitted to Phys. Lett. B. [arXiv:0906.1504].

[7] I. Abt *et al.* [H1 Collaboration], Nucl. Instrum. Meth. A **386** (1997) 310;
I. Abt *et al.* [H1 Collaboration], Nucl. Instrum. Meth. A **386** (1997) 348;
R. D. Appuhn *et al.* [H1 SPACAL Group], Nucl. Instrum. Meth. A **386** (1997) 397.

[8] ZEUS Collaboration, U. Holm (ed.), *the ZEUS Detector*. Status Report (unpublished), DESY (1993), available on http://www-zeus.desy.de/bluebook/bluebook.html.

[9] T. Abe, GRAPE-Dilepton version 1.1, Comput. Phys. Commun. **136** (2001) 126 [hep-ph/0012029].

[10] C. Amsler *et al.* [Particle Data Group], Phys. Lett. B **667** (2008) 1.

Multi-Leptons at HERA (0.94 fb^{-1})

Sample	Data	SM	Pair Production (GRAPE)	NC DIS + QEDC
ee	873	895 ± 57	724 ± 41	171 ± 28
$\mu\mu$	298	320 ± 36	320 ± 36	< 0.5
$e\mu$	173	167 ± 10	152 ± 9	15 ± 3
eee	116	119 ± 7	117 ± 6	< 4
$e\mu\mu$	140	147 ± 15	147 ± 15	< 0.5
$(\gamma\gamma)_e$	284	293 ± 18	289 ± 18	4 ± 1
$(\gamma\gamma)_\mu$	235	247 ± 26	247 ± 26	< 0.5

Table 1: Observed and predicted event yields for the different event topologies and for the $\gamma\gamma$ subsamples. The uncertainties on the predictions include model uncertainties and experimental systematic uncertainties added in quadrature. The limits on the background estimations are quoted at 95% confidence level.

Multi-Leptons at HERA (0.94 fb^{-1})

M_{12} >100 GeV

Sample	Data	SM	Pair Production (GRAPE)	NC DIS + QEDC
e^+p collisions (0.56 fb^{-1})				
ee	4	1.68 ± 0.18	0.94 ± 0.11	0.74 ± 0.12
$\mu\mu$	1	0.32 ± 0.08	0.32 ± 0.08	< 0.01
$e\mu$	1	0.40 ± 0.05	0.39 ± 0.05	< 0.02
eee	4	0.79 ± 0.09	0.79 ± 0.09	< 0.03
$e\mu\mu$	2	0.16 ± 0.04	0.16 ± 0.04	< 0.01
e^-p collisions (0.38 fb^{-1})				
ee	0	1.25 ± 0.13	0.71 ± 0.11	0.54 ± 0.08
$\mu\mu$	0	0.23 ± 0.10	0.23 ± 0.10	< 0.01
$e\mu$	0	0.26 ± 0.03	0.25 ± 0.03	< 0.02
eee	0	0.49 ± 0.07	0.49 ± 0.07	< 0.03
$e\mu\mu$	0	0.14 ± 0.05	0.14 ± 0.05	< 0.01
All data (0.94 fb^{-1})				
ee	4	2.93 ± 0.28	1.65 ± 0.16	1.28 ± 0.18
$\mu\mu$	1	0.55 ± 0.12	0.55 ± 0.12	< 0.01
$e\mu$	1	0.65 ± 0.07	0.64 ± 0.06	< 0.02
eee	4	1.27 ± 0.12	1.27 ± 0.12	< 0.03
$e\mu\mu$	2	0.31 ± 0.06	0.31 ± 0.06	< 0.01

Table 2: Observed and predicted multi-lepton event yields for masses $M_{12} > 100$ GeV for the different event topologies, for all data and divided into e^+p and e^-p collisions. The uncertainties on the predictions include model uncertainties and experimental systematic uncertainties added in quadrature. The limits on the background estimations correspond to the selection of no event in the simulated topology and are quoted at 95% confidence level.

Multi-Leptons at HERA (0.94 fb^{-1})

$\sum P_T$ >100 GeV				
Data sample	Data	SM	Pair Production (GRAPE)	NC DIS + QEDC
e$^+$p (0.56 fb^{-1})	7	1.94 ± 0.17	1.52 ± 0.14	0.42 ± 0.07
e$^-$p (0.38 fb^{-1})	0	1.19 ± 0.12	0.90 ± 0.10	0.29 ± 0.05
All (0.94 fb^{-1})	7	3.13 ± 0.26	2.42 ± 0.21	0.71 ± 0.10

Table 3: Observed and predicted multi-lepton event yields for $\sum P_T > 100$ GeV. Di-lepton and tri-lepton events are combined. The uncertainties on the predictions include model uncertainties and experimental systematic uncertainties added in quadrature.

Multi-Leptons at HERA (0.94 fb^{-1})

Variable range [GeV]	Measured (e^+e^-) [fb/GeV]	Measured $(\mu^+\mu^-)$ [fb/GeV]	Measured (average) [fb/GeV]	Pair Production (GRAPE) [fb/GeV]
$P_T^{\ell_1}$		$d\sigma/dP_T^{\ell_1}$		
$[10, 15]$	$101.1 \pm 7.1 \pm 5.5$	$97.7 \pm 7.7 \pm 9.2$	$99.9 \pm 5.3 \pm 4.9$	101.3 ± 3.1
$[15, 20]$	$22.4 \pm 3.1 \pm 1.3$	$15.9 \pm 3.2 \pm 1.7$	$19.4 \pm 2.3 \pm 1.0$	23.9 ± 0.7
$[20, 25]$	$5.0 \pm 1.5 \pm 0.6$	$4.9 \pm 1.6 \pm 0.6$	$5.0 \pm 1.1 \pm 0.4$	7.3 ± 0.2
$[25, 50]$	$0.56 \pm 0.22 \pm 0.05$	$0.75 \pm 0.29 \pm 0.09$	$0.63 \pm 0.18 \pm 0.04$	0.93 ± 0.03
$M_{\ell\ell}$		$d\sigma/dM_{\ell\ell}$		
$[15, 25]$	$27.3 \pm 2.8 \pm 1.5$	$31.9 \pm 2.9 \pm 3.0$	$29.0 \pm 2.1 \pm 1.5$	30.0 ± 0.9
$[25, 40]$	$18.4 \pm 1.6 \pm 1.1$	$14.9 \pm 1.8 \pm 1.4$	$16.9 \pm 1.2 \pm 0.9$	19.5 ± 0.6
$[40, 60]$	$3.4 \pm 0.6 \pm 0.2$	$2.0 \pm 0.5 \pm 0.2$	$2.6 \pm 0.4 \pm 0.2$	3.1 ± 0.1
$[60, 100]$	$0.17 \pm 0.09 \pm 0.03$	$0.32 \pm 0.15 \pm 0.04$	$0.21 \pm 0.08 \pm 0.02$	0.26 ± 0.01

Table 4: Differential photoproduction cross sections $d\sigma/dP_T^{\ell_1}$ and $d\sigma/dM_{\ell\ell}$ averaged for each quoted interval for the process $ep \to e\ell^+\ell^- X$ in a restricted phase space (see text for details). Cross sections are measured for e^+e^- or $\mu^+\mu^-$ pairs. The average is also shown. The first uncertainty is statistical and the second is systematic. Theoretical predictions, calculated with GRAPE, dominated by the photon-photon process, are shown in the last column.

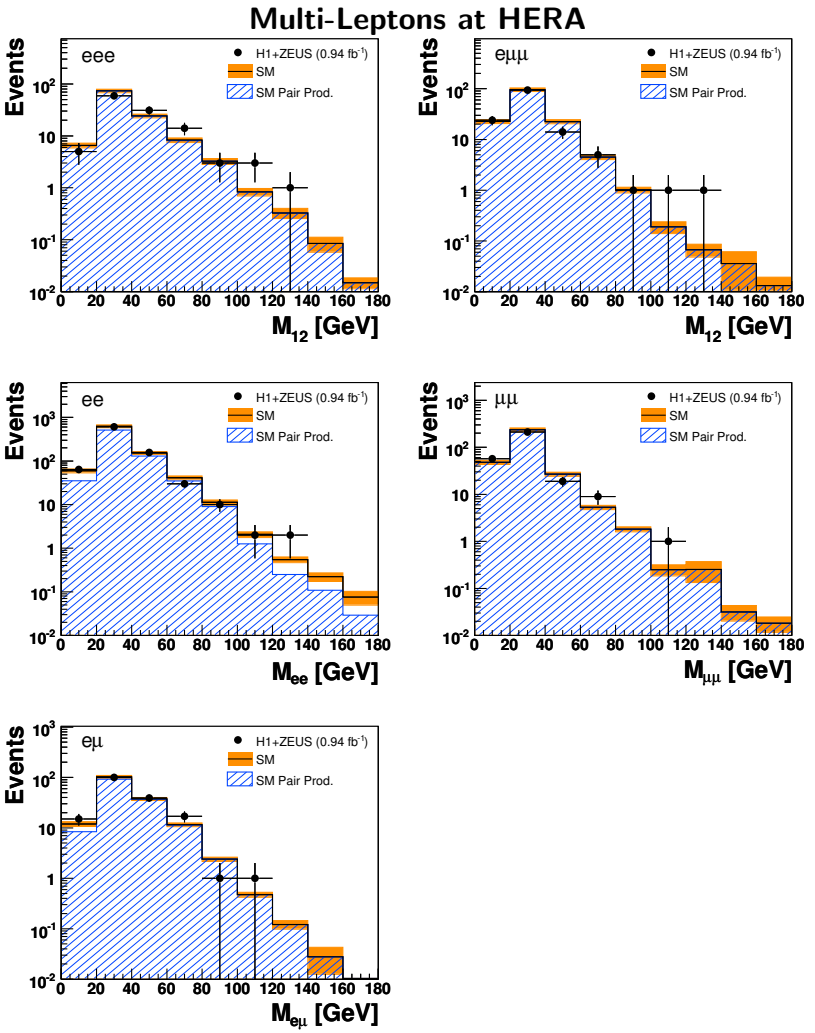

Fig. 1: The distribution of the invariant mass of the two highest P_T leptons for events classified as eee, $e\mu\mu$, ee, $\mu\mu$ and $e\mu$. The points correspond to the observed data events and the histogram to the SM expectation. The total uncertainty on the SM expectation is given by the shaded band. The component of the SM expectation arising from lepton pair production is given by the hatched histogram.

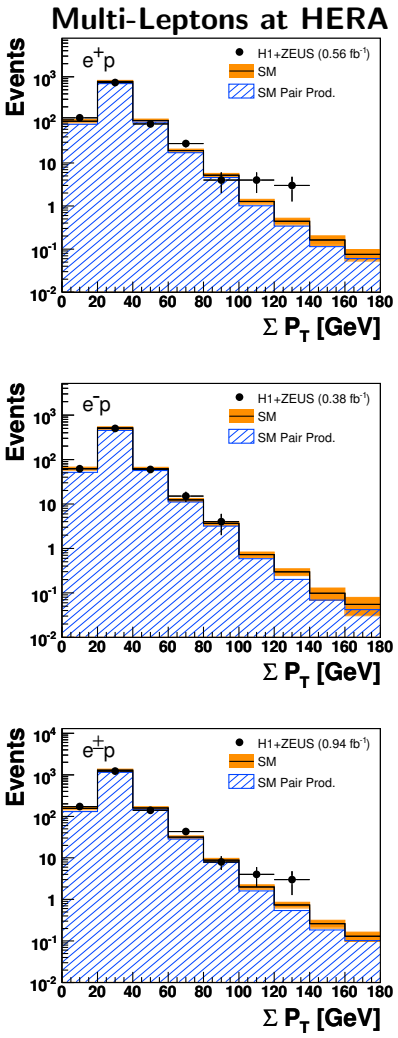

Fig. 2: The distribution of the scalar sum of the transverse momenta $\sum P_T$ for combined di-lepton and tri-lepton event topologies for all data as well as for e^+p and e^-p. The points correspond to the observed data events and the histogram to the SM expectation. The total uncertainty on the SM expectation is given by the shaded band. The component of the SM expectation arising from lepton pair production is given by the hatched histogram.

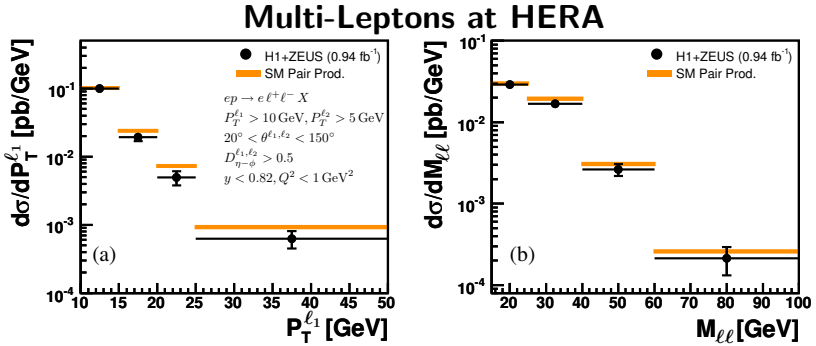

Fig. 3: The cross section for lepton pair photoproduction in a restricted phase space as a function of the leading lepton transverse momentum $P_T^{\ell_1}$ (a) and the invariant mass of the lepton pair $M_{\ell\ell}$ (b). The total error bar is shown, representing the statistical and systematic uncertainties added in quadrature, which is dominated by the statistical. The bands represent the one standard deviation uncertainty in the SM prediction, dominated by the photon-photon process.

Annexe K

Search for Doubly-Charged Higgs Boson Production at HERA

A. Aktas *et al.* [H1 Collaboration],
Phys. Lett. B **638** (2008) 432,
arXiv:hep-ex/0604027

Abstract

A search for the single production of doubly-charged Higgs bosons $H^{\pm\pm}$ in ep collisions is presented. The signal is searched for via the Higgs decays into a high mass pair of same charge leptons, one of them being an electron. The analysis uses up to 118 pb^{-1} of ep data collected by the H1 experiment at HERA. No evidence for doubly-charged Higgs production is observed and mass dependent upper limits are derived on the Yukawa couplings h_{el} of the Higgs boson to an electron-lepton pair. Assuming that the doubly-charged Higgs only decays into an electron and a muon via a coupling of electromagnetic strength $h_{e\mu} = \sqrt{4\pi\alpha_{em}} = 0.3$, a lower limit of 141 GeV on the $H^{\pm\pm}$ mass is obtained at the 95% confidence level. For a doubly-charged Higgs decaying only into an electron and a tau and a coupling $h_{e\tau} = 0.3$, masses below 112 GeV are ruled out.

1 Introduction

Doubly-charged Higgs bosons ($H^{\pm\pm}$) appear when the Higgs sector of the Standard Model (SM) is extended by one or more triplet(s) with non-zero hypercharge [1–3]. Examples are provided by some Left-Right Symmetric models [4], or their supersymmetric extensions, which are of particular interest since they provide a mechanism to generate small non-zero neutrino masses. Such models can lead to a doubly-charged Higgs boson light enough [5] to be produced at the existing colliders. The Higgs triplet(s) may be coupled to matter fields via Yukawa couplings which are generally not related to the fermion masses. A non-vanishing coupling of a doubly-charged Higgs to an electron would allow its single production in ep collisions at HERA. This possibility is investigated in this paper with a search for doubly-charged Higgs bosons decaying into a high mass pair of same charge leptons, one of them being an electron.

An analysis of multi-electron events was already presented by the H1 collaboration [6]. Six events were observed with a di-electron mass above 100 GeV, a domain in which the Standard Model prediction is low. In the present paper the compatibility of these events with the hypothesis of a doubly-charged Higgs coupling to ee is addressed and a further search for a $H^{\pm\pm}$ boson coupling to $e\mu$ and $e\tau$ is performed. The analysis is based on ep data collected by the H1 experiment between 1994 and 2000, which amount to a luminosity of up to 118 pb^{-1}.

2 Phenomenology

At tree level, doubly-charged Higgs bosons couple only to charged leptons and to other Higgs and gauge bosons. Couplings to quark pairs are forbidden by charge conservation. The couplings of a doubly-charged Higgs to charged leptons can be generically described by the Lagrangian:

$$\mathcal{L} = \sum_{i,j} h^{L,R}_{l_i l_j} \, H^{++}_{L,R} \, \bar{l}^{\,c}_i \, P_{L,R} \, l_j \qquad + \text{ h.c. } , \tag{1}$$

where l are the charged lepton fields, l^c denote the charge conjugate fields, i, j are generation indices, and $P_{L,R} = (1 \mp \gamma_5)/2$. The Higgs fields $H^{++}_{L,R}$ coupling to left-handed or right-handed leptons correspond to different particles and not all models predict their simultaneous existence. The Yukawa couplings $h^{L,R}_{l_i l_j} = h^{L,R}_{l_j l_i}$ are free parameters of the model.

The phenomenology of doubly-charged Higgs production at HERA was first discussed in [7]. For a non-vanishing coupling $h^{L,R}_{el}$ the single production of a doubly-charged Higgs boson is possible at HERA in $e\gamma^*$ interactions via the diagrams shown in Fig. 1, where a photon is radiated off the proton or one of its constituent quarks. The proton may remain intact or be broken during this interaction, leading to an elastic or inelastic reaction, respectively. With longitudinally unpolarised lepton beams, as were delivered by HERA until 2000, the $H^{\pm\pm}$ production cross section does not depend on whether the Higgs couples to left-handed or right-handed leptons. Hence a generic case is considered here of a doubly-charged Higgs boson which couples to either left-handed or right-handed leptons and the L, R indices are dropped in the following.

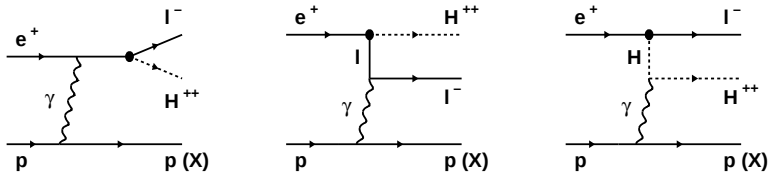

Figure 1: Diagrams for the single production of a doubly-charged Higgs boson in e^+p collisions at HERA via the h_{el} coupling. The hadronic final state is denoted by p (X) in the elastic (inelastic) case, where the initial proton remains intact (dissociates). The contribution of Z exchange can be safely neglected.

Within the mass range considered in this analysis, it is assumed that decays of the $H^{\pm\pm}$ into gauge bosons and other Higgs particles are not allowed kinematically such that the doubly-charged Higgs only decays via its Yukawa couplings into a lepton pair.

Indirect upper bounds on the Yukawa couplings of a doubly-charged Higgs to leptons are reviewed in [8]. The coupling h_{ee} of a doubly-charged Higgs to an electron pair is constrained by the contribution of virtual $H^{\pm\pm}$ exchange to Bhabha scattering in e^+e^- collisions. A recent OPAL analysis [9] sets the constraint $h_{ee} < 0.14$ for a doubly-charged Higgs mass $M_H = 100$ GeV. From low energy e^+e^- data, coupling values of $\mathcal{O}(0.1)$ are allowed for $h_{e\mu}$ and $h_{e\tau}$ for a Higgs mass of 100 GeV [10]. Taking these indirect constraints into account, the production of a doubly-charged Higgs mediated by h_{ee}, $h_{e\mu}$ or $h_{e\tau}$ might be observable at HERA. The Higgs signal would manifest itself as a peak in the invariant mass distribution of same charge ee, $e\mu$ or $e\tau$ leptons, respectively. For the range of masses and couplings probed in this analysis, the Higgs decay length is vanishingly small but its width remains negligible compared to the experimental resolution on the mass of the lepton pair.

3 Simulation of the Signal and Standard Model Backgrounds

The calculation of the cross section for doubly-charged Higgs production, as well as the simulation of signal events, relies on a dedicated Monte Carlo program developed for this analysis. The differential cross sections are integrated using the VEGAS package [11]. Different approaches are followed depending on the photon virtuality Q^2 and on the mass W of the hadronic final state:

- in the inelastic region ($W > m_p + m_\pi$, with the proton mass m_p and the pion mass m_π) and when the photon virtuality is large ($Q^2 > 4$ GeV^2), the interaction involves a quark inside the proton. The squared amplitude of the process $e^\pm q \to e^\mp H^{\pm\pm} q$ is evaluated using the CompHEP package [12, 13]. The parton densities in the proton are taken from the CTEQ4L [14] parameterisation and are evaluated at the scale $\sqrt{Q^2}$. The parton shower approach [15] based on the DGLAP [16] evolution equations is applied to

simulate QCD corrections in the initial and final states, and the hadronisation is performed using PYTHIA 6.1 [15].

- for the elastic region ($W = m_p$) and the inelastic region at low Q^2 ($W > m_p + m_\pi$, $Q^2 < 4$ GeV^2), the squared amplitude is calculated using the FORM program [17]. The hadronic tensor is parameterised in terms of the usual electromagnetic structure functions $F_1(x, Q^2)$ and $F_2(x, Q^2)$ of the proton, where $x = Q^2/(W^2 + Q^2 - m_p^2)$. For the elastic process these structure functions are expressed in terms of the electric and magnetic form factors of the proton. For the low Q^2 inelastic region they are taken from analytical parameterisations [18]. The simulation of the hadronic final state for low Q^2 inelastic events is performed via an interface to the SOPHIA program [19].

For a Yukawa coupling h_{ee} or $h_{e\mu}$ of electromagnetic strength ($h = \sqrt{4\pi\alpha_{em}} = 0.3$) the total cross section amounts to 0.39 pb (0.04 pb) for a Higgs mass of 100 GeV (150 GeV). The low Q^2 (high Q^2) inelastic contribution is found to be $\sim 30\%$ ($\sim 20\%$) of the total cross section in the mass range $80 - 150$ GeV. The cross section for producing a doubly-charged Higgs via a coupling $h_{e\tau}$ is lower by about 40% due to the non-negligible mass of the τ lepton produced in association with the Higgs.

The theoretical uncertainty on the cross sections obtained is taken to be 4% in the mass range considered. This is derived from an assessed uncertainty of 2% on the proton form factors [20] and from the uncertainty on the scale at which the parton densities for the inelastic contribution are evaluated. The latter uncertainty is estimated from the variation of the computed cross section as this scale is changed from $\sqrt{Q^2}/2$ to $2\sqrt{Q^2}$.

Separate signal event samples corresponding to the production and decay of a doubly-charged Higgs via a coupling h_{ee}, $h_{e\mu}$ and $h_{e\tau}$ have been produced for Higgs masses ranging between 80 and 150 GeV, in steps of 10 GeV.

Di-electron production, which proceeds mainly via two-photon interactions, constitutes an irreducible background for ee final states. The production of muon or tau pairs constitutes a background for the $e\mu$ and $e\tau$ analyses when the scattered electron is detected. The Cabibbo-Parisi process $ee \to \gamma, Z \to ll$, in which the incoming electron interacts with an electron emitted from a photon radiated from the proton, contributes at high transverse momentum only. The Drell-Yan process was calculated in [21] and found to be negligible. All these processes are simulated using the GRAPE Monte Carlo generator [22], which also takes into account contributions from Bremsstrahlung with subsequent photon conversion into a lepton pair and electroweak contributions.

Experimental backgrounds come dominantly from Neutral Current Deep Inelastic Scattering (NC DIS) where a jet is misidentified as an electron, a muon or a tau. Compton scattering is also a source of background for ee final states when the photon is misidentified as an electron. These processes are simulated with the DJANGO [23] and WABGEN [24] generators.

All generated events are passed through the full simulation of the H1 apparatus and are reconstructed using the same program chain as for the data.

4 The H1 Detector

A detailed description of the H1 experiment can be found in [25]. Only the H1 detector components relevant to the present analysis are briefly described here. Jets and electrons are measured with the Liquid Argon (LAr) calorimeter [26], which covers the polar angle[1] range $4^\circ < \theta < 154^\circ$. Electromagnetic shower energies are measured with a precision of $\sigma(E)/E = 12\%/\sqrt{E/\text{GeV}} \oplus 1\%$ and hadronic energies with $\sigma(E)/E = 50\%/\sqrt{E/\text{GeV}} \oplus 2\%$, as determined in test beams [27]. In the backward region a lead/scintillating-fibre[2] (SpaCal) calorimeter [28] covers the range $155^\circ < \theta < 178^\circ$. The central ($20^\circ < \theta < 160^\circ$) and forward ($7^\circ < \theta < 25^\circ$) tracking detectors are used to measure charged particle trajectories, to reconstruct the interaction vertex and to supplement the measurement of the hadronic energy. The LAr and inner tracking detectors are enclosed in a super-conducting magnetic coil with a strength of 1.15 T. The return yoke of the coil is the outermost part of the detector and is equipped with streamer tubes forming the central muon detector ($4^\circ < \theta < 171^\circ$). In the forward region of the detector ($3^\circ < \theta < 17^\circ$) a set of drift chamber layers (the forward muon system) detects muons and, together with an iron toroidal magnet, allows a momentum measurement. The luminosity measurement is based on the Bethe-Heitler process $ep \to ep\gamma$, where the photon is detected in a calorimeter located downstream of the interaction point.

5 Data Analysis

The analyses of ee and $e\mu$ final states use the full $e^\pm p$ data set recorded in the period 1994-2000, which corresponds to an integrated luminosity of $118\,\text{pb}^{-1}$. The analysis of $e\tau$ final states makes use of the e^+p data collected in the years 1996-1997 and 1999-2000, which amount to a luminosity of $88\,\text{pb}^{-1}$. The HERA collider was operated at a centre-of-mass energy $\sqrt{s}$ of 300 GeV in 1994-1997 and of 318 GeV in 1998-2000.

Events are first selected by requiring that the longitudinal position of the vertex be within 35 cm around the nominal interaction point. In addition topological filters and timing vetoes are applied to remove background events induced by cosmic showers and other non-ep sources. The main triggers for the events are provided by the LAr calorimeter and the muon system.

5.1 Lepton Identification

An electron[3] candidate is identified by the presence of a compact and isolated electromagnetic energy deposit above 5 GeV in the LAr or SpaCal calorimeter. The energy of the electron candidate is measured from the calorimetric information. In the angular range $20^\circ < \theta < 150^\circ$ the electron identification is complemented by tracking conditions, in which case the direction

[1] The origin of the H1 coordinate system is the nominal ep interaction point, with the direction of the proton beam defining the positive z-axis (forward region). The transverse momenta are measured in the xy plane. The pseudorapidity η is related to the polar angle θ by $\eta = -\ln\tan(\theta/2)$.

[2] Before 1995 a lead-scintillator calorimeter was used.

[3] Unless otherwise stated, the term "electron" is used in this paper to generically describe electrons or positrons.

of the electron candidate is given by that of the associated track. Electron candidates in the forward region, $5^\circ < \theta < 20^\circ$, are required to have an energy above 10 GeV.

A muon candidate is identified by associating an isolated track in the forward muon system or in the inner tracking system with a track segment or an energy deposit in the instrumented iron. The muon momentum is measured from the track curvature in the toroidal or solenoidal magnetic field, respectively.

Tau leptons are preselected as described in [29] by requiring a track with transverse momentum above 5 GeV measured in the inner tracking detector. The leptonic tau decays $\tau \to e\nu\nu$ and $\tau \to \mu\nu\nu$ are reconstructed by matching the selected track to an identified electron or muon. Tracks that are not identified as electrons or muons are attributed to hadronic tau decays if at least 40% of the track momentum is reconstructed in the LAr calorimeter as matched clustered energy. In that case it is moreover required that the track belong to a narrow jet: no other track should be reconstructed within $0.15 < R < 1.5$ around the track direction, where $R = \sqrt{\Delta\eta^2 + \Delta\varphi^2}$ with $\Delta\eta$ and $\Delta\varphi$ being the distances in pseudorapidity and azimuthal angle, respectively. The transverse momentum and the direction of the τ candidate are approximated by those of the associated track.

5.2 Analysis of the $H \to ee$ Decay

This analysis is based on the published H1 measurement of multi-electron production [6]. The event selection requires at least two central ($20^\circ < \theta^e < 150^\circ$) electron candidates, one of them with a transverse momentum $P_T^{e1} > 10$ GeV (ensuring a trigger efficiency close to 100% [30]) and the other one with $P_T^{e2} > 5$ GeV. After this preselection, 125 events are observed, in good agreement with the SM expectation of 137.4 ± 10.7. In each event, the two highest P_T electrons, one of those being possibly outside the central region, are assigned to the Higgs candidate. The distribution of their invariant mass M_{ee} is shown in Fig. 2a. At low mass a good agreement is observed between data and the SM expectation which is largely dominated by $\gamma\gamma$ contributions. Six events are observed at $M_{ee} > 100$ GeV, compared to the SM expectation of 0.53 ± 0.08.

Further selection criteria are then applied, which are designed to maximise the sensitivity of the analysis to a possible $H^{\pm\pm}$ signal. The charge measurement of the two leptons assigned to the Higgs candidate is exploited. In e^+p (e^-p) collisions, where H^{++} (H^{--}) bosons could be produced, events in which one of the two leptons is reliably assigned a negative (positive) charge are rejected. The charge assignment requires that the curvature κ of the track associated with the lepton be measured with an error $\delta\kappa$ satisfying $\mid \kappa/\delta\kappa \mid > 2$. The precise calorimetric measurement of the electron transverse momenta is further exploited by applying an additional M_{ee} dependent cut on the sum of the transverse momenta of the two electrons assigned to the Higgs candidate. The lower bound is optimised to keep 95% of the signal and varies between 45 GeV and 120 GeV. This cut suppresses events coming from $\gamma\gamma$ processes. The efficiency for selecting signal events varies from 50% for a $H^{\pm\pm}$ mass of 80 GeV to 35% for a $H^{\pm\pm}$ mass of 150 GeV. In this mass range the resolution on M_{ee} varies between 2.5 GeV and 5 GeV.

After these requirements, 3 events are observed at $M_{ee} > 65$ GeV, in agreement with the SM expectation of 2.45 ± 0.11 events. Amongst the six events[4] at $M_{ee} > 100$ GeV, only one satisfies the final selection criteria.

[4]Out of these, three do not fullfill the M_{ee} dependent P_T cut, and two do not satisfy the charge requirement.

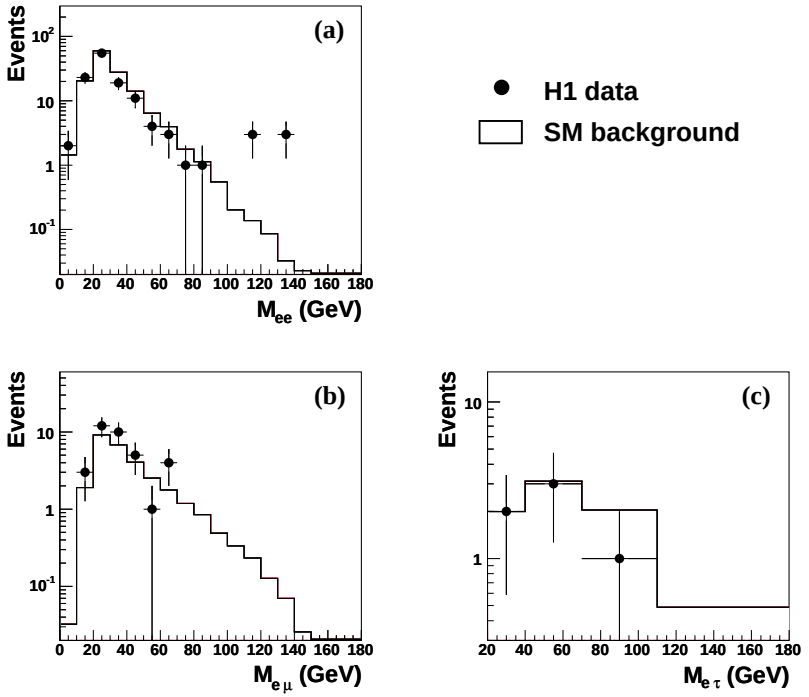

Figure 2: Distribution of (a) the invariant mass M_{ee} of the two highest P_T electrons for multi-electron events, (b) the electron-muon invariant mass $M_{e\mu}$, and (c) the electron-tau candidate invariant mass $M_{e\tau}$. The data (symbols) are compared with the Standard Model expectation (histogram). The distributions are shown at the preselection level (see text).

5.3 Analysis of the $H \to e\mu$ Decay

Events having one electron and one muon with minimal transverse momenta of $P_T^e > 10$ GeV and $P_T^\mu > 5$ GeV are selected. The polar angle of electron candidates is restricted to $20^\circ < \theta^e < 140^\circ$ to reduce the large background arising from NC DIS events. The θ range for muon candidates extends towards low angles, $10^\circ < \theta^\mu < 140^\circ$, which increases the efficiency for high $H^{\pm\pm}$ masses. The minimum transverse momentum required for electron candidates ensures a trigger efficiency close to 100% for these events. After this preselection, 35 data events are observed compared to a SM expectation of 29.6 ± 3.4. The distribution of the invariant mass of the electron and the muon $M_{e\mu}$ is shown in Fig. 2b. A good agreement is observed between the data and the SM expectation, which is dominated by $\gamma\gamma$ contributions.

For the final selection of $H \to e\mu$ candidates the charge of the e and μ is exploited using the same criteria as used in section 5.2. The efficiency for selecting signal events varies from 55%

to 40% for a $H^{\pm\pm}$ mass between 80 GeV and 150 GeV. The resolution on $M_{e\mu}$ varies between 3 GeV and 8 GeV. For $M_{e\mu} > 65$ GeV one event is observed while 4.17 ± 0.44 events are expected from the SM.

5.4 Analysis of the $H \rightarrow e\tau$ Decay

The search for a H^{++} boson decaying into $e\tau$ is performed in three final states, depending on whether the τ decays into an electron, a muon or hadronically (h). Details of this analysis can be found in [29]. Events are selected which contain either two electrons (ee), or an electron and a muon ($e\mu$), or an electron and a hadronic τ candidate (eh) as defined in section 5.1. The two leptons, or the electron and the hadronic-τ candidate, should have a transverse momentum above 5 GeV, be in the angular range $20^\circ < \theta < 140^\circ$, and be separated from each other by $R > 2.5$ in pseudorapidity-azimuth. One of them must have a transverse momentum above 10 GeV, which ensures a trigger efficiency above 95% in all three classes. For events in the $e\mu$ class the polar angle of the electron candidate is required to be below 120°.

A significant amount of missing transverse and longitudinal momentum is expected due to the neutrinos produced in the τ decays. Events in the ee class are required to have a missing transverse momentum $P_T^{miss} > 8$ GeV. For the eh class, which suffers from a large NC DIS background, it is required that $P_T^{miss} > 11$ GeV, that the energy deposited in the SpaCal calorimeter be below 5 GeV, and that the variable $\sum_i E^i - P_z^i$, where the sum runs over all visible particles, be smaller than 49 GeV. For fully contained events $\sum_i E^i - P_z^i$ is expected to peak at twice the lepton beam energy $E_0 = 27.5$ GeV, i.e. 55 GeV, while signal events are concentrated at lower values due to the non observed neutrinos. In total 6 events are preselected, in agreement with the SM prediction of 7.8 ± 1.5.

In each class, the $e\tau$ invariant mass $M_{e\tau}$ is reconstructed by imposing longitudinal momentum and energy conservation, and by minimising the total momentum imbalance in the transverse plane. Tau leptons are assumed to decay with a vanishing opening angle. This method yields a resolution of about 4 GeV on the mass $M_{e\tau}$. Figure 2c shows the $e\tau$ invariant mass distribution of the selected events together with the SM expectation.

For the final selection, events are rejected if the track associated with one of the Higgs decay product candidates is reliably assigned a negative charge, opposite to that of the incoming lepton beam. The signal efficiencies depend only weakly on M_H. The fractions of simulated $H \rightarrow e\tau$ events which are reconstructed in the various classes are given in table 1, for an example mass of $M_H = 100$ GeV. The total efficiency on the signal amounts to about 25%.

The final event yields are also shown in table 1. Only one event (in the eh class) satisfies the final criteria, while 2.1 ± 0.5 events are expected.

5.5 Systematic Uncertainties

The systematic uncertainties attributed to the Monte Carlo predictions for the ee analysis are detailed in [6]. The dominant systematic uncertainty is due to the electron-track association efficiency, which is 90% on average with an uncertainty increasing with decreasing polar angle

Event class	$H^{++} \rightarrow e^+\tau^+$ final selection		
	N_{obs}	N_{bckg}	Signal fraction
$e\mu$	0	0.27± 0.02	6 %
eh	1	1.66 ± 0.48	12 %
ee	0	0.14± 0.04	7 %
total	1	2.07± 0.54	25 %

Table 1: Number of observed (N_{obs}) and expected (N_{bckg}) events in each event class which satisfy all criteria to select $H^{++} \rightarrow e^+\tau^+$ candidates with a mass $M_{e\tau} > 65$ GeV. The last column shows the fractions of the $H \rightarrow e\tau$ Monte Carlo events which are reconstructed in the various classes, for a mass of 100 GeV.

from 3% to 15%. Systematic errors due to the uncertainty on the electromagnetic energy scale (known at the 0.7% to 3% level in the central and forward regions of the LAr calorimeter, respectively) and on the trigger efficiency (3%) are also taken into account.

For the $e\mu$ analysis, the dominant additional systematic uncertainty is due to the muon identification efficiency known within 6% [31]. The uncertainty due to the reconstruction efficiency of the central tracking detector for central muons contributes an additional 3%. The muon momentum scale is known within 5%, and the trigger efficiency for $e\mu$ final states is known within 3%.

The same systematic uncertainties affect the SM expectations in the ee and $e\mu$ classes of the $e\tau$ analysis. The uncertainty of the hadronic energy scale in the LAr calorimeter (4%) constitutes another source of uncertainty due to the cuts applied on the P_T^{miss} and $\sum_i E - P_z$ variables. For the eh event class the dominant uncertainties on the SM expectation, coming mainly from NC DIS processes, are due to the uncertainty of 3% of the track efficiency, to that of the hadronic energy scale, and to that of the hadronisation model.

The luminosity measurement leads to a normalisation uncertainty of 1.5%.

For both the expected signal and the predicted background, the systematic uncertainties resulting from the sources listed above are added in quadrature.

6 Interpretation

With the final Higgs selection no significant excess over the SM expectation is observed. Upper limits on the $H^{\pm\pm}$ production cross section times the branching ratio for the $H^{\pm\pm}$ to decay into one of the analysed final states are derived as a function of the $H^{\pm\pm}$ mass and are shown in Fig. 3a. The limits are presented at the 95% confidence level and are obtained using a modified frequentist approach [32]. Statistical uncertainties, as well as the influence of the various systematic uncertainties on both the shape and the normalisation of the mass distributions for signal and background events, are taken into account. The best sensitivity is obtained for a $H^{\pm\pm}$ produced and decaying via $h_{e\mu}$, with upper limits around 0.05 pb.

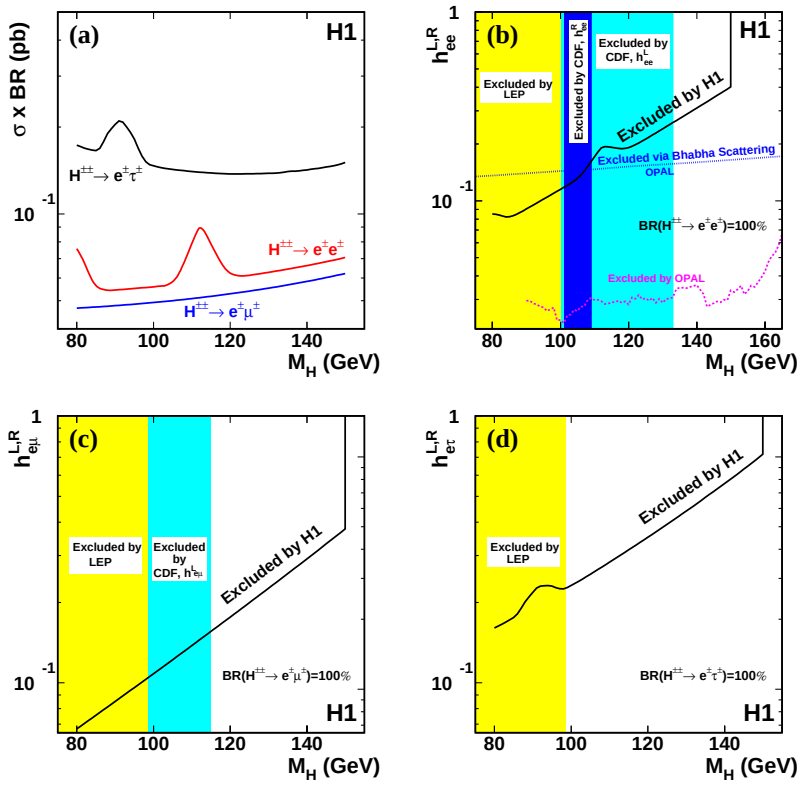

Figure 3: (a) Upper limits at the 95% confidence level on the $H^{\pm\pm}$ production cross section times the branching ratio for the $H^{\pm\pm}$ to decay into ee, $e\mu$ or $e\tau$, as a function of the Higgs mass. (b)-(d) Upper limits on the coupling h_{el} assuming that the $H^{\pm\pm}$ couples only (b) to ee, (c) to $e\mu$ or (d) to $e\tau$. Regions above the curves are excluded. The constraints obtained from pair production at LEP and at CDF and from single production at OPAL are also shown.

Assuming that only one Yukawa coupling h_{el} is non-vanishingly small, these constraints are translated into mass dependent upper limits on the coupling h_{el}, as shown in Fig. 3b-d.

If the doubly-charged Higgs boson couples only to an electron pair (Fig. 3b) the ee analysis rules out $H^{\pm\pm}$ masses below 138 GeV for a coupling h_{ee} of the electromagnetic strength, $h_{ee} = 0.3$. The result is compared to the bounds obtained from searches for $H^{\pm\pm}$ pair production at LEP [33] and by the CDF experiment [34], and to both the indirect and direct limits obtained by the OPAL experiment [9], the latter being the most stringent. The OPAL experiment has also set

similar stringent constraints on h_{ee} independently of the Higgs decay mode. These constraints also exclude a sizeable $H^{\pm\pm}$ production at HERA via h_{ee} followed by the $H^{\pm\pm}$ decay via $h_{\mu\mu}$ or $h_{\tau\tau}$, which is consistent with the non-observation of a resonance signal in the $\mu\mu$ [31] and $\tau\tau$ [29] final states in the present H1 data.

Assuming that the doubly-charged Higgs boson couples only to an electron-muon (electron-tau) pair, the $e\mu$ ($e\tau$) analysis allows masses below 141 GeV (112 GeV) to be ruled out for $h_{e\mu} = 0.3$ ($h_{e\tau} = 0.3$), as shown in Fig. 3c (Fig. 3d). The H1 limits extend the excluded region in the electron-muon and electron-tau channels to masses that are beyond those reached in previous searches for pair production at LEP [33] and the Tevatron [34].

7 Conclusion

A search for the single production of doubly-charged Higgs bosons coupling to ee, $e\mu$ or $e\tau$ is presented. In a previous model independent multi-electron analysis, H1 observed six events with a di-electron mass above 100 GeV, a region where the Standard Model expectation is small. Out of the six events, only one is compatible with the signature of a doubly-charged Higgs boson. No electron-muon or electron-tau event is found in this mass domain.

This analysis places new limits on the $H^{\pm\pm}$ mass and its Yukawa couplings h_{el} to an electron-lepton pair. Assuming that the doubly-charged Higgs boson only couples to electron-muon (electron-tau) pairs, a limit of 141 GeV (112 GeV) is obtained on the Higgs mass, for a coupling $h_{e\mu} = 0.3$ ($h_{e\tau} = 0.3$) corresponding to an interaction of electromagnetic strength.

Acknowledgements

We are grateful to the HERA machine group whose outstanding efforts have made this experiment possible. We thank the engineers and technicians for their work in constructing and maintaining the H1 detector, our funding agencies for financial support, the DESY technical staff for continual assistance and the DESY directorate for support and for the hospitality which they extend to the non-DESY members of the collaboration. We are especially grateful to J. Maalampi and N. Romanenko for providing the doubly-charged Higgs Lagrangian implementation in CompHEP which was used in this analysis. We would also like to thank K. Huitu and E. Boos for their help and valuable discussions.

References

[1] G. B. Gelmini and M. Roncadelli, Phys. Lett. B **99** (1981) 411.

[2] J. C. Pati and A. Salam, Phys. Rev. D **10** (1974) 275; R. E. Marshak and R. N. Mohapatra, Phys. Lett. B **91** (1980) 222.

[3] R. N. Mohapatra and G. Senjanovic, Phys. Rev. Lett. **44** (1980) 912.

[4] G. Senjanovic and R. N. Mohapatra, Phys. Rev. D **12** (1975) 1502; R. N. Mohapatra and R. E. Marshak, Phys. Rev. Lett. **44** (1980) 1316 [Erratum-ibid. **44** (1980) 1643].

[5] C. S. Aulakh, A. Melfo and G. Senjanovic, Phys. Rev. D **57** (1998) 4174 [hep-ph/9707256]; Z. Chacko and R. N. Mohapatra, Phys. Rev. D **58** (1998) 015003 [hep-ph/9712359]; B. Dutta and R. N. Mohapatra, Phys. Rev. D **59** (1999) 015018 [hep-ph/9804277].

[6] A. Aktas *et al.* [H1 Collaboration], Eur. Phys. J. C **31** (2003) 17 [hep-ex/0307015].

[7] E. Accomando and S. Petrarca, Phys. Lett. B **323** (1994) 212 [hep-ph/9401242].

[8] M. L. Swartz, Phys. Rev. D **40** (1989) 1521; J. F. Gunion *et al.*, Phys. Rev. D **40** (1989) 1546; M. Lusignoli and S. Petrarca, Phys. Lett. B **226** (1989) 397; G. Barenboim, K. Huitu, J. Maalampi and M. Raidal, Phys. Lett. B **394** (1997) 132 [hep-ph/9611362]; S. Godfrey, P. Kalyniak and N. Romanenko, Phys. Rev. D **65** (2002) 033009 [hep-ph/0108258].

[9] G. Abbiendi *et al.* [OPAL Collaboration], Phys. Lett. B **577** (2003) 93 [hep-ex/0308052].

[10] F. Cuypers and S. Davidson, Eur. Phys. J. C **2** (1998) 503.

[11] G.P. Lepage, CLNS-80/447 (1980).

[12] E. Boos *et al.* [CompHEP Collaboration], Nucl. Instrum. Meth. A **534** (2004) 250 [hep-ph/0403113]; A. Pukhov *et al.*, "CompHEP - a package for evaluation of Feynman diagrams and integration over multi-particle phase space", hep-ph/9908288; available at http://theory.sinp.msu.ru/comphep.

[13] S. Godfrey, P. Kalyniak and N. Romanenko, Phys. Rev. D **65** (2002) 033009 [hep-ph/0108258].

[14] H. L. Lai *et al.*, Phys. Rev. D **55** (1997) 1280 [hep-ph/9606399].

[15] T. Sjöstrand *et al.*, Comput. Phys. Commun. **135** (2001) 238 [hep-ph/0010017].

[16] V. N. Gribov and L. N. Lipatov, Yad. Fiz. **15** (1972) 781 [Sov. J. Nucl. Phys. **15** (1972) 438]; G. Altarelli and G. Parisi, Nucl. Phys. B **126** (1977) 298; Y. L. Dokshitzer, Sov. Phys. JETP **46** (1977) 641 [Zh. Eksp. Teor. Fiz. **73** (1977) 1216].

[17] J. A. M Vermaseren, "New features of FORM", math-ph/0010025.

[18] F.W. Brasse *et al.*, Nucl. Phys. B **39** (1972) 421.

[19] A. Mucke, R. Engel, J. P. Rachen, R. J. Protheroe and T. Stanev, Comput. Phys. Commun. **124** (2000) 290 [astro-ph/9903478].

[20] R. C. Walker *et al.*, Phys. Rev. D **49** (1994) 5671.

[21] N. Arteaga-Romero, C. Carimalo and P. Kessler, Z. Phys. C **52** (1991) 289.

[22] T. Abe, Comput. Phys. Commun. **136** (2001) 126 [hep-ph/0012029].

[23] DJANGO 6.2; G.A. Schuler and H. Spiesberger, Proc. of the Workshop Physics at HERA, W. Buchmüller and G. Ingelman (Editors), Vol. 3 p. 1419 (October 1991).

[24] Ch. Berger and P. Kandel, "A new Generator for Wide Angle Bremsstrahlung", Proc. of the Monte Carlo Generators for HERA Physics Workshop, A.T. Doyle, G. Grindhammer, G. Ingelman and H. Jung (Editors), DESY-PROC-1999-02, p. 596.

[25] I. Abt *et al.* [H1 Collaboration], Nucl. Instrum. Meth. A **386** (1997) 310 and 348.

[26] B. Andrieu *et al.* [H1 Calorimeter Group], Nucl. Instrum. Meth. A **336** (1993) 460.

[27] B. Andrieu *et al.* [H1 Calorimeter Group], Nucl. Instrum. Meth. A **344** (1994) 492; *idem*, Nucl. Instrum. Meth. A **350** (1994) 57; *idem*, Nucl. Instrum. Meth. A **336** (1993) 499.

[28] R. D. Appuhn *et al.* [H1 SPACAL Group], Nucl. Instrum. Meth. A **386** (1997) 397.

[29] S. Baumgartner, "Search for doubly-charged Higgs decaying into τ leptons at HERA", PhD thesis, ETH Zürich, ETH-16125 (2005), available at http://www-h1.desy.de/publications/theses_list.html.

[30] C. Adloff *et al.* [H1 Collaboration], Eur. Phys. J. C **30** (2003) 1 [hep-ex/0304003].

[31] A. Aktas *et al.* [H1 Collaboration], Phys. Lett. B **583** (2004) 28 [hep-ex/0311015].

[32] T. Junk, Nucl. Instr. Meth. A **434** (1999) 435 [hep-ex/9902006].

[33] J. Abdallah *et al.* [DELPHI Collaboration], Phys. Lett. B **552** (2003) 127 [hep-ex/0303026]; P. Achard *et al.* [L3 Collaboration], Phys. Lett. B **576** (2003) 18 [hep-ex/0309076]; G. Abbiendi *et al.* [OPAL Collaboration], Phys. Lett. B **526** (2002) 221 [hep-ex/0111059].

[34] D. Acosta *et al.* [CDF Collaboration], Phys. Rev. Lett. **93** (2004) 221802 [hep-ex/0406073].

Annexe L

A General Search for New Phenomena in ep Scattering at HERA

A. Aktas *et al.* [H1 Collaboration],
Phys. Lett. B **602** (2004) 14,
arXiv:hep-ex/0408044

Abstract

A model-independent search for deviations from the Standard Model prediction is performed in e^+p and e^-p collisions at HERA using H1 data corresponding to an integrated luminosity of 117 pb^{-1}. For the first time all event topologies involving isolated electrons, photons, muons, neutrinos and jets with high transverse momenta are investigated in a single analysis. Events are assigned to exclusive classes according to their final state. A statistical algorithm is developed to search for deviations from the Standard Model in the distributions of the scalar sum of transverse momenta or invariant mass of final state particles and to quantify their significance. A good agreement with the Standard Model prediction is observed in most of the event classes. The most significant deviation is found for a topology containing an isolated muon, missing transverse momentum and a jet, consistent with a previously reported observation.

1 Introduction

At HERA electrons[1] and protons collide at a centre-of-mass energy of up to 319 GeV. These high-energy electron-proton interactions provide a testing ground for the Standard Model (SM) complementary to e^+e^- and $p\overline{p}$ scattering. It is widely believed that the SM is incomplete and that new physics signals may appear below energies of 1 TeV. Many extensions to the SM have been constructed during the last decades predicting various phenomena which may be visible at high energies or large transverse momenta (P_T). HERA data have been used to test some of these models of new processes by analysing their anticipated experimental signatures and limits on their parameters have been derived [1].

The approach described in this paper consists of a comprehensive and generic search for deviations from the SM prediction at large transverse momenta. All high P_T final state configurations involving electrons (e), muons (μ), jets (j), photons (γ) or neutrinos (ν) are systematically investigated. The analysis covers phase space regions where the SM prediction is sufficiently precise to detect anomalies and does not rely on assumptions concerning the characteristics of any SM extension. Such a model-independent approach might discover unexpected manifestations of new physics. Therefore it addresses the important question of whether evidence for new physics might still be hidden in the data recorded at collider experiments. A similar strategy for a model-independent search was previously presented in [2].

All final states containing at least two objects (e, μ, j, γ, ν) with $P_T > 20$ GeV in the polar angle[2] range $10^\circ < \theta < 140^\circ$ are investigated. The complete HERA I data sample ($1994-2000$) is used, corresponding to an integrated luminosity of 117 pb^{-1}. All selected events are classified into exclusive event classes according to the number and types of objects detected in the final state (e.g. e-j, μ-j-ν, j-j-j-j-j). These exclusive event classes ensure a clear separation of final states and allow an unambiguous statistical interpretation of deviations. All experimentally accessible combinations of objects have been studied and data events are found in 22 of them.

In a first analysis step the global event yields of the event classes are compared with the SM expectation. The distributions of the invariant mass M_{all} and of the scalar sum of transverse momenta $\sum P_T$ of high P_T final state objects are presented. New physics may be visible as an excess or a deficit in one of these distributions. Therefore, in a second step these distributions are systematically investigated using a dedicated algorithm which locates the region with the largest deviation of the data from the SM prediction. The probability of occurrence of such a deviation is derived, both for each event class individually and globally for all classes combined.

This paper is organised as follows. Section 2 describes the Standard Model processes at HERA and their Monte Carlo simulation. The H1 detector, the event selection and measurement procedure are described in section 3. The event yields and distributions for each event class are presented in section 4. The search strategy and results are explained in section 5. Section 6 summarises the paper.

[1] In this paper "electrons" refers to both electrons and positrons, if not otherwise stated.

[2] The origin of the H1 coordinate system is the nominal ep interaction point, with the direction of the proton beam defining the positive z-axis (forward region). The transverse momenta are measured in the xy plane. The pseudorapidity η is related to the polar angle θ by $\eta = -\ln \tan(\theta/2)$.

2 Standard Model processes and Monte Carlo generation

Several Monte Carlo event generators are combined to simulate events for all SM processes which have large cross sections or are expected to be dominant for specific event classes, avoiding double-counting. All processes are generated with an integrated luminosity significantly higher than that of the data sample and events are passed through a full detector simulation [3]. At high transverse momenta the dominant SM processes are the photoproduction of two jets and neutral current (NC) deep-inelastic scattering (DIS). In the following the abbreviation X represents all reaction products other than the high P_T objects considered.

Photoproduction of jets and photons To simulate the direct and resolved photoproduction of jets $ep \to jjX$, prompt photon production $ep \to \gamma jX$ and the resolved photoproduction of photon pairs $ep \to \gamma\gamma X$, the PYTHIA 6.1 event generator [4] is used. Light and heavy flavoured jets are generated. The simulation contains the Born level hard scattering matrix elements and radiative QED corrections.

Neutral current deep-inelastic scattering The Born, QCD Compton and Boson Gluon Fusion matrix elements are used in the RAPGAP [5] event generator to model NC DIS events. The QED radiative effects arising from real photon emission from both the incoming and the outgoing electrons are simulated using the HERACLES [6] generator. Hence the NC DIS prediction contains the processes $ep \to ejX$, $ep \to ejjX$ and also models final states with an additional radiated photon.

Charged current deep-inelastic scattering Charged current (CC) DIS events are simulated using the DJANGO [7] program, which includes first order QED radiative corrections based on HERACLES. This prediction contributes to the final states $ep \to \nu jX$, $ep \to \nu jjX$ and to final states with an additional radiated photon.

QED Compton scattering Elastic and quasi-elastic Compton processes $ep \to e\gamma X$ are simulated with the WABGEN [9] generator. The inelastic contribution is already included in the NC DIS RAPGAP sample.

Electroweak production of lepton pairs Multi-lepton events (ee, $\mu\mu$, $\tau\tau$) are generated with the GRAPE [10] program, which includes all electroweak matrix elements at tree level. Multi-lepton production via $\gamma\gamma$, γZ, ZZ collisions, internal photon conversion and the decay of virtual or real Z bosons is considered. Initial and final state QED radiation is included. The complete hadronic final state is obtained via interfaces to PYTHIA and SOPHIA [11] for the inelastic and quasi-elastic regimes, respectively.

W production The production of W bosons $ep \to WX$ and $ep \to WjX$ is modelled using EPVEC [12]. Next-to-leading order QCD corrections [13] are taken into account by reweighting the events as a function of the transverse momentum and rapidity of the W boson [14].

Processes with the production of three or more jets, e.g. $ep \to jjjX$ or $ep \to jjjjX$, are accounted for using leading logarithmic parton showers as a representation of higher order QCD radiation, with the exception of CC DIS, where the colour-dipole model [8] is used. Hadronisation is modelled using Lund string fragmentation [4]. The prediction of processes with two or more high transverse momentum jets, e.g. $ep \to jjX$, $ep \to ejjX$, is scaled by a factor of 1.2 to normalise the leading order Monte Carlos to next-to-leading order QCD calculations [15].

3 Experimental technique

3.1 The H1 detector

The H1 detector [16] components relevant to the present analysis are briefly described here. Jets, photons and electrons are measured with the Liquid Argon (LAr) calorimeter [17], which covers the polar angle range $4^\circ < \theta < 154^\circ$ with full azimuthal acceptance. Electromagnetic shower energies are measured with a precision of $\sigma(E)/E = 12\%/\sqrt{E/\text{GeV}} \oplus 1\%$ and hadronic energies with $\sigma(E)/E = 50\%/\sqrt{E/\text{GeV}} \oplus 2\%$, as measured in test beams. The central and forward tracking detectors are used to measure charged particle trajectories, to reconstruct the interaction vertex and to supplement the measurement of the hadronic energy. The innermost proportional chamber CIP ($9^\circ < \theta < 171^\circ$) is used to veto charged particles for the identification of photons. The LAr and inner tracking detectors are enclosed in a superconducting magnetic coil with a strength of 1.15 T. The return yoke of the coil is the outermost part of the detector and is equipped with streamer tubes forming the central muon detector ($4^\circ < \theta < 171^\circ$). It is also used to supplement the measurement of hadrons. In the forward region of the detector ($3^\circ < \theta < 17^\circ$) a set of drift chamber layers (the forward muon system) detects muons and, together with an iron toroidal magnet, allows a momentum measurement. The luminosity measurement is based on the Bethe-Heitler process $ep \to ep\gamma$, where the photon is detected in a calorimeter located downstream of the interaction point.

The main trigger for events with high transverse momentum is provided by the LAr calorimeter. The trigger efficiency is close to 100% for events having an electromagnetic deposit in the LAr (electron or photon) with transverse momentum greater than 20 GeV [19]. Events triggered only by jets have a trigger efficiency above 90% for $P_T^{jet} > 20$ GeV and nearly 100% for $P_T^{jet} > 25$ GeV [20]. For events with missing transverse momentum above 20 GeV, determined from an imbalance in the transverse momentum measured in the calorimeter, the trigger efficiency is $\sim 90\%$. The muon trigger is based on single muon signatures from the central muon detector, which are combined with signals from the central tracking detector. The trigger efficiency for di-muon events is about 70% [21].

3.2 Event selection

At HERA electrons or positrons with an energy of 27.6 GeV collide with protons at an energy of 920 GeV resulting in a centre-of-mass energy of $\sqrt{s}$ = 319 GeV. Before 1998 the proton energy was 820 GeV resulting in a centre-of-mass energy of $\sqrt{s}$ = 301 GeV. The event sample studied

consists of the full 1994–2000 HERA I data set. It corresponds to an integrated luminosity of 36.4 pb^{-1} in e^+p scattering at $\sqrt{s} = 301$ GeV and 13.8 pb^{-1} in e^-p scattering and 66.4 pb^{-1} in e^+p scattering at $\sqrt{s} = 319$ GeV.

The data selection requires at least one isolated electromagnetic cluster, jet or muon to be found in the detector acceptance. Energy deposits in the calorimeters and tracks in the inner tracking system are used to form combined cluster-track objects, from which the hadronic energy is reconstructed. To reduce background it is demanded that the event vertex be reconstructed within 35 cm in z of the nominal position[3] and that $\sum_i (E_i - P_{z,i}) < 75$ GeV, where E_i is the particle energy and $P_{z,i}$ is the z component of the particle momentum. Here, the index i runs over all hadronic energy deposits, electromagnetic clusters and muons found in the event. Due to energy-momentum conservation events are expected to have a value of $\sum_i (E_i - P_{z,i}) = 55.2$ GeV, twice the electron beam energy, if only longitudinal momentum along the proton beam direction is unmeasured. Events with topologies typical of cosmic ray and beam-induced background are rejected [22]. Moreover, the timing of the event is required to coincide with that of the ep bunch crossing.

The identification criteria for each type of particle are based on those applied in previous analyses of specific final states [15, 19, 21, 23]. Additional requirements are chosen to ensure an unambiguous identification of particles, whilst retaining high efficiencies. The following paragraphs describe the identification criteria for the different objects and give the identification efficiencies for the kinematic region considered in the analysis.

Electron identification The electron identification is based on the measurement of a compact and isolated electromagnetic shower in the LAr calorimeter. The hadronic energy within a distance in the pseudorapidity-azimuth ($\eta - \phi$) plane $R = \sqrt{(\Delta\eta)^2 + (\Delta\phi)^2} < 0.75$ around the electron is required to be below 2.5% of the electron energy. This calorimetric electron identification is complemented by tracking conditions. A high quality track is required to geometrically match the electromagnetic cluster within a distance of closest approach to the cluster centre-of-gravity of 12 cm. No other good track is allowed within $R < 0.5$ around the electron direction. In the central region ($20^\circ < \theta < 140^\circ$) the distance between the first measured point in the central drift chambers and the beam axis is required to be below 30 cm in order to reject photons that convert late in the central tracker material. In addition, the transverse momentum measured from the associated track P_T^{etk} is required to match the calorimetric measurement P_T^e with $1/P_T^{etk} - 1/P_T^e < 0.02$ GeV^{-1}. In the region not fully covered by the central drift chambers ($10^\circ < \theta < 37^\circ$) a wider isolation cone of $R = 1$ is required to reduce the contribution of fake electrons from hadrons. In this forward region the identification is completed by the requirement of associated hits in the CIP, which reduces the contamination from neutral particles showering in the material of the forward region. The resulting electron finding efficiency is 85% in the central region and 70% in the forward region.

Photon identification The photon identification relies on the measurement of an electromagnetic shower and on the same calorimetric isolation criteria against hadrons as for the electron identification. In addition, photons are required to be separated from jets with $P_T^{jet} > 5$ GeV

[3] This is not required for the event classes containing only photons or photons and a neutrino.

by a distance of $R > 1$ to the jet axis. Vetoes are applied on any charged track pointing to the electromagnetic cluster. No track should be present with a distance of closest approach to the cluster below 24 cm or within $R < 0.5$. An additional veto on any hits in the CIP is applied. The resulting photon identification efficiency as derived using elastic QED Compton events is 90%.

Muon identification The muon identification is based on a track in the forward muon system or in the inner tracking systems associated with a track segment or an energy deposit in the central muon detector [23]. The muon momentum is measured from the track curvature in the toroidal or solenoidal magnetic fields. A muon candidate should have no more than 8 GeV deposited in the LAr calorimeter in a cylinder of radius 0.5 in ($\eta - \phi$) space, centred on the muon track direction. In di-muon events, the requirement of an opening angle between the two muons smaller than 165° discards cosmic ray background. Beam halo muons are rejected by requiring that the muons originate from the event vertex. Finally, misidentified hadrons are almost completely suppressed by requiring that the muon candidate is separated from the closest jet with $P_T^{jet} > 5$ GeV by $R > 1$. The efficiency to identify muons is greater than 90% [23].

Jet identification Jets are defined using the inclusive $k_\perp$ algorithm [24, 25]. The algorithm is applied in the laboratory frame with a separation parameter of 1 and using a P_T weighted recombination scheme [24] in which the jets are treated as massless. The jet algorithm is run on all combined cluster-track objects not previously identified as electron or photon candidates. The scattered electron may fake a jet. This effect is important for multi-jet events, especially at high transverse momenta. To reject these fake jets, the first radial moment of the jet transverse energy [26, 27] is required to be greater than 0.02 and the quantity M^{jet}/P_T^{jet} must be greater than 0.1 [15, 27]. The invariant mass M^{jet} is obtained using the four-vector of all objects belonging to the jet. If the fraction of the jet energy contained in the electromagnetic part of the LAr calorimeter is greater than 0.9, the above criteria are tightened to 0.04 and 0.15, respectively. The jet selection efficiency is 97%.

Neutrino identification A neutrino candidate is defined in events with missing transverse momentum above 20 GeV. The missing momentum is derived from all identified particles and energy deposits in the event. Fake missing transverse momentum may also arise from the mismeasurement of an identified object. This effect is reduced by requiring that the neutrino[4] be isolated from all identified objects with a transverse momentum above 20 GeV. Requiring $\sum_i (E_i - P_{z,i}) < 48$ GeV discards neutrino candidates from NC processes where the missing transverse momentum is caused by energy leakage in the forward region. If exactly one electron or muon object is found, a neutrino object is only assigned to an event if $\Delta\phi(l - X_{tot}) < 170^\circ$, where $\Delta\phi(l - X_{tot})$ is the separation in azimuthal angle between the lepton l and the direction of the system X_{tot} built of all hadronic energies.

[4] The four-vector of the neutrino is calculated under the assumption $\sum_i (E_i - P_{z,i}) + (E_\nu - P_{z,\nu}) = 55.2$ GeV.

Event classification The common phase space for electrons, photons, muons and jets is defined by $10^\circ < \theta < 140^\circ$ and $P_T > 20$ GeV. The neutrino phase space is defined by missing transverse momentum above 20 GeV and $\sum_i (E_i - P_{z,i}) < 48$ GeV. These values are chosen to retain a high selection and trigger efficiency. All particles with $P_T > 20$ GeV, including the neutrino defined by its reconstructed four-vector, are required to be isolated compared with each other by a minimum distance R of one unit in the $\eta - \phi$ plane. The events are classified, depending on the number and types of objects, into exclusive event classes. Events with an isolated calorimetric object in the considered phase space which is not identified as a photon, electron or jet are discarded from the analysis in order to minimise wrong classifications.

Based on these identification criteria, purities can be derived for each event class with a sizeable SM expectation. Purity is defined as the ratio of SM events reconstructed in the event class in which they are generated to the total number of reconstructed events in this class. Most purities are found to be above 60% and they are close to 100% for the j-j, e-j, j-ν and μ-μ event classes.

3.3 Systematic uncertainties

This section describes the sources of experimental and theoretical systematic uncertainties considered. Experimental systematic uncertainties arising from the measurement of the objects are listed in table 1 (for more details see [20, 27, 28]).

- The electromagnetic energy scale uncertainty varies between 0.7% and 3% depending on the particle's impact point on the LAr calorimeter surface [19]. The polar angular measurement uncertainty of electromagnetic clusters varies depending on θ between 1 and 3 mrad [19]. The identification of electron and photon candidates depends on the tracking efficiency, which is known with a precision ranging from 2% for polar angles above 37° to 7% in the forward region.
- The hadronic energy scale of the LAr calorimeter is known to 2%. The uncertainty on the jet polar angle determination is 5 mrad for $\theta < 30^\circ$ and 10 mrad for $\theta > 30^\circ$.
- The uncertainty on the transverse momentum measurement for muons amounts to 5%. The uncertainty on the polar angle is 3 mrad. The muon identification efficiency is known with a precision of 5%.
- The trigger uncertainties for each class are determined by the object with the highest trigger efficiency. The uncertainty on the trigger efficiency is estimated to be 3% if the event is triggered by a jet or missing transverse momentum and 5% if it is triggered by a muon. For electrons and photons the uncertainty on the trigger efficiency is negligible.
- The uncertainty in the integrated luminosity results in an overall normalisation error of 1.5%.
- The uncertainty in the reconstruction of $\sum_i (E_i - P_{z,i})$ and the missing P_T for the neutrino classification are obtained by propagation of the systematic errors for other objects.

Depending on the generator level production process, different theoretical uncertainties are used as listed in table 2. The errors attributed to the predictions for $ep \to jjX$, $ep \to j\gamma X$, $ep \to j\nu X$, $ep \to jeX$, $ep \to jj\nu X$, $ep \to jjeX$ and W production include uncertainties in the parton distribution functions and those due to missing higher order corrections [15, 23, 27, 28]. The error attributed to $ep \to \mu\mu X$ and $ep \to eeX$ results mainly from the limited knowledge of the proton structure [21, 29]. The error on the QED Compton cross section is estimated to be 5% for elastic and 10% for inelastic production. An additional theoretical error of 20% is applied for each jet produced by parton shower processes (e.g. 20% for the j-j-j event class). An uncertainty of 50% is added to the prediction for NC DIS events with missing transverse momentum above 20 GeV and a high P_T electron. This uncertainty is estimated by a comparison of the missing transverse momentum distribution between NC DIS events with a low P_T electron ($P_T < 20$ GeV) and the SM prediction.

All systematic errors are added in quadrature and are assigned to the SM predictions. For example, the resulting total uncertainties for e-j events are 10% and 35% at low and high invariant mass M_{all}, respectively. In the j-j event class the errors are typically 20% and reach $40\% - 50\%$ for M_{all} and $\sum P_T$ values around 250 GeV.

4 Event yields

All possible event classes with at least two objects are investigated[5]. The event yields subdivided into event classes are presented for the data and SM expectation in figure 1. All event classes with a SM expectation greater than 0.01 events are shown. No other event class contains data events. The distributions of the scalar sum of transverse momenta $\sum P_T$ and of the invariant mass M_{all} of all objects are presented in figures 2 and 3 for classes with at least one event.

The dominant high P_T processes at HERA, i.e. photoproduction of jets, NC and CC DIS, dominate in the j-j, e-j and j-ν event classes, respectively. Events are observed with $\sum P_T$ and M_{all} values as large as 250 GeV. A good description of the data spectra by the prediction is observed. The prediction for the event classes j-j-γ and e-j-γ is dominated by photoproduction and NC DIS processes with the radiation of a photon, respectively. There is good agreement between the data and the prediction. No event is observed in the radiative CC classes ν-γ and j-ν-γ, consistent with the expectation of 2.1 ± 0.3 and 1.0 ± 0.1, respectively. The j-j-j, e-j-j, e-j-j-j, j-j-ν and j-j-j-ν event classes correspond to processes with additional jet production due to higher order QCD radiation. The yields of these event classes are also well described by the SM prediction.

The e-γ event class is dominated by QED Compton scattering processes and $\sum P_T$ and M_{all} values up to 160 GeV are measured. A good agreement with the SM is observed. The prompt photon j-γ event class extends up to $M_{all} \sim 150$ GeV and is well described by the prediction. The purity in this class is moderate ($40 - 50\%$) due to the high background from misidentified electrons in NC DIS. Backgrounds where hadrons are misidentified as photons are small. One

[5]The μ-ν event class is discarded from the present analysis. It is dominated by low transverse energy photoproduction events in which a poorly reconstructed muon gives rise to missing transverse momentum, which fakes the neutrino signature.

event is observed in the γ-γ event class for an expectation of 1.1 ± 0.5, which is dominated by the $ep \to e\gamma X$ process, where the electron is misidentified. Contributions of higher order QED processes, which could lead to two high transverse momentum photons, are negligible.

Lepton pair production from $\gamma\gamma$ processes dominates in event classes with several leptons. The e-e event class contains 8 events for an expectation of 11.2 ± 1.4. In this channel, a discrepancy with the SM expectation was previously reported for high masses by the H1 collaboration [29]. All multi-electron events mentioned in [29] and located in the phase space of this analysis are found. In the region $M_{all} > 100$ GeV, 3 events are observed and 1.16 ± 0.25 are expected. The higher SM prediction compared with the prediction of 0.3 in [29] is due to the extended polar angle range in the forward region. This leads to an additional ≈ 0.4 background events from fake electrons and ≈ 0.4 events from the $ep \to eeX$ processes. The e-e-e class contains no events. None of the tri-electron events of [29] are selected here due to the requirement of high transverse momentum. The predictions for the e-μ and μ-μ event classes are dominated by muon pair production from two-photon reactions. The e-μ event class is populated if the scattered electron and only one of the muons are selected. In the e-μ class, 4 events are observed compared with an expectation of 4.8 ± 0.6. A slight excess is observed in the μ-μ event class where 6 events are found and 2.7 ± 0.6 are expected. Muon pair production processes also contribute $\approx 85\%$ in the μ-j event class, where a good agreement is found. In the e-μ, μ-μ and μ-j event classes the $\sum P_T$ and M_{all} values of the data lie between 50 and 100 GeV.

The prediction for the event classes μ-j-ν and e-j-ν consists mainly of high P_T W production with a subsequent leptonic decay. A discrepancy between the data and the SM expectation is observed in the μ-j-ν event class, where 4 events are observed for an expectation of 0.8 ± 0.2. The $\sum P_T$ values reach 170 GeV and the M_{all} values 200 GeV. In this event class less than 0.002 background events are expected from the photoproduction of jets via QCD processes. Such a deviation was previously reported in [23] and will be further discussed in Section 5. In the e-j-ν event class 2 data events are observed for an expectation of 0.9 ± 0.2. Some of the e-j-ν events mentioned in [23] have an electron with a transverse momentum below 20 GeV and are therefore not selected as e-j-ν events in the present analysis. The event topology e-ν is also expected to contain events arising from W production together with background from NC DIS. In the e-ν event class, 9 data events are observed compared with an expectation of 12.9 ± 4.5.

A slight excess of the data compared with the prediction is observed in the j-j-j-j event class, with 10 data events observed and 5.2 ± 2.2 expected. One event is observed in the e-j-j-j-j event class, to be compared with an expectation of 0.026 ± 0.011. This event has a $\sum P_T$ of 207 GeV and an invariant mass M_{all} of 262 GeV. The NC DIS expectation for $M_{all} > 260$ GeV is $(9 \pm 6) \cdot 10^{-5}$ as derived using RAPGAP. The energy flow of the event in the $\eta - \phi$ view is presented in figure 4. The NC DIS and photoproduction SM predictions have been tested using a sample of j-j-j-j events with $P_T^{jet} > 15$ GeV and e-j-j-j-j events with $P_T^e > 10$ GeV and $P_T^{jet} > 5$ GeV. An adequate description of the $\sum P_T$ and M_{all} distributions of the data is obtained within the quoted SM uncertainties. Since the NC DIS prediction for $M_{all} > 260$ GeV is only of order 0.001 fb, rare SM processes not considered in this analysis such as W pair production may be dominant in this kinematic domain.

No events are found in any other event class, in agreement with the SM expectation (see figure 1).

5 Search for deviations from the Standard Model

5.1 Search algorithm and strategy

In order to quantify the level of agreement between the data and the SM expectation and to identify regions of possible deviations, a new search algorithm is developed. Detailed studies have shown that M_{all} and $\sum P_T$ have a large sensitivity to new physics (see appendix and [28]). The algorithm described in the following locates the region of largest deviation of the data from the SM in these distributions. The calculation of the significance of this deviation is inspired by [2].

Definition of regions A region in the $\sum P_T$ and M_{all} distributions is defined as a set of connected histogram bins[6] with a size of at least twice the resolution. All possible regions of any width and at any position in the histograms are considered. The number of data events (N_{obs}), the SM expectation (N_{SM}) and its total systematic uncertainty (δN_{SM}) are calculated for each region.

Determination of the most interesting region A statistical estimator p is defined to judge which region is of most interest. This estimator is derived from the convolution of the Poisson probability density function (pdf) to account for statistical errors with a Gaussian pdf, $G(b; N_{SM}, \delta N_{SM})$, with mean N_{SM} and width δN_{SM}, to include the effect of non negligible systematic uncertainties. The estimator is defined via

$$p = \begin{cases} A \int_0^\infty db\, G(b; N_{SM}, \delta N_{SM}) \sum_{i=N_{obs}}^{\infty} \frac{e^{-b} b^i}{i!} & \text{if } N_{obs} \geq N_{SM} \\ A \int_0^\infty db\, G(b; N_{SM}, \delta N_{SM}) \sum_{i=0}^{N_{obs}} \frac{e^{-b} b^i}{i!} & \text{if } N_{obs} < N_{SM} \end{cases}$$

$$\text{with} \quad A = 1/ \left[\int_0^\infty db\, G(b; N_{SM}, \delta N_{SM}) \sum_{i=0}^{\infty} \frac{e^{-b} b^i}{i!} \right].$$

The factor A ensures normalisation to unity. If G is replaced by a Dirac delta function $\delta(b - N_{SM})$ the estimator p becomes the usual Poisson probability. The value of p gives an estimate of the probability of a fluctuation of the SM expectation upwards (downwards) to at least (at most) the observed number of data events in the region considered. The region of greatest deviation is the region having the smallest p-value, p_{min}. Such a method is able to find narrow resonances and single outstanding events as well as signals spread over large regions of phase space in distributions of any shape [28].

[6] In order to minimise binning effects, a bin size smaller than or comparable with the resolution of the studied quantity is used. A 5 GeV bin size is used for all distributions. Further reduction of the bin size has a negligible effect on the results.

Significance per event class The probability that a fluctuation with a p-value at least as small as p_{min} occurs anywhere in the distribution is estimated using the following method. Many independent hypothetical data histograms are made by filling each bin with an event number diced according to the pdfs of the SM expectation (again a convolution of Poisson and Gaussian pdfs). For each of these hypothetical data histograms the algorithm is run to find the region of greatest deviation and the corresponding p^{SM}_{min} is calculated. The probability $\hat{P}$ is then defined as the fraction of hypothetical data histograms with a p^{SM}_{min} equal to or smaller than the p_{min} value obtained from the data. $\hat{P}$ is a measure of the statistical significance of the deviation observed in the data. If the event classes are exclusive, the $\hat{P}$ values can be used to compare the results of different event classes. Depending on the final state, a p_{min}-value of $5.7 \cdot 10^{-7}$ ("5σ") corresponds to a value of $-\log_{10} \hat{P}$ between 5 and 6.

Global significance The overall degree of agreement with the SM can be further quantified by taking into account the large number of event classes studied in this analysis. The probability of observing an event class with a given $\hat{P}$ value or smaller can be calculated with Monte Carlo (MC) experiments. A MC experiment is defined as a set of hypothetical data histograms (either in M_{all} or in $\sum P_T$) following the SM expectation with an integrated luminosity of 117 pb^{-1}, on which the complete search algorithm and statistical analysis are applied as for data. This procedure is repeated many times. The expectation for the $\hat{P}$ values observed in the data is then given by the distribution of $\hat{P}^{SM}$ values obtained from all MC experiments. The probability to find a $\hat{P}$ value smaller than the minimum observed in the data can thus be calculated and quantifies the global significance of the observed deviation.

5.2 Search results

The final $\hat{P}$ values obtained for event classes having at least one observed event are summarised in table 3. The regions selected by the algorithm are presented in figures 2 and 3.

The most significant deviation of the analysis is found in the μ-j-ν event class. This class has $\hat{P}$ values of 0.010 (M_{all}) and 0.001 ($\sum P_T$). The mass region ($155 < M_{all} < 200$ GeV) contains 3 data events for an expectation of 0.19 ± 0.05. In the chosen $\sum P_T$ region ($145 < \sum P_T < 170$ GeV) three data events are found while only 0.07 ± 0.03 are expected. This event topology was studied in [23] where this deviation at high P_T was already reported.

A $\hat{P}$ value of 0.019 is found in the e-e event class in a region at high transverse momenta, $100 < \sum P_T < 130$ GeV where 3 events are observed for an expectation of 0.18 ± 0.08. The deviation is less prominent in the region selected in the invariant mass distribution due to a higher background from NC DIS events. This corresponds to the excess of data events also identified in [29].

A deficit is observed in the e-j event class in the $\sum P_T$ distribution in the region $180 < \sum P_T < 210$ GeV. For a SM expectation of 31.2 ± 5.0 only 12 data events are observed. The derived $\hat{P}$ value is 0.021.

Due to the uncertainties in the SM prediction in the j-j-j-j and e-j-j-j-j event classes at the highest M_{all} and $\sum P_T$, where data events are observed (see section 4), no reliable $\hat{P}$ values

can be calculated for these classes. Consequently, these event classes are not taken into account to determine the overall degree of agreement between the data and the SM.

The $\hat{P}$ values for event classes with no data event observed and a small SM expectation are 1. This remains the case if an additional contribution is added from a possible further rare process not included here. Such classes can thus be considered in the calculation of the global significance.

The $\hat{P}$ values observed in the data in all event classes are compared in figure 5 with the distribution of $\hat{P}^{SM}$ obtained from the large set of MC experiments, normalised to one experiment. The comparison is presented for the scans of the M_{all} and $\sum P_T$ distributions. Most $\hat{P}$ values lie above 0.01, corresponding to event classes where no significant discrepancy between the data and the SM expectation is observed. The global probabilities to find at least one class with a $\hat{P}$ value smaller than the observation in the μ-j-ν channel are 3% and 28% for the $\sum P_T$ and M_{all} distributions, respectively (see appendix for details).

To test the dependence of the analysis on the *a priori* defined P_T cuts, the whole analysis is repeated with two other object P_T cuts. The P_T cut was raised to 40 GeV for all objects and lowered to 15 GeV. In the latter case it was still required that at least one object has a P_T larger than 20 GeV in order to maintain a high trigger efficiency. The analysis was also repeated separately on the e^+p and e^-p data samples. In these four test scenarios a similar overall agreement with the SM is observed. The μ-j-ν event class remains the one with the smallest $\hat{P}$ value in the scenario with a lowered P_T cut in the e^+p data sample and no new discrepancy is observed. When raising the P_T cut to 40 GeV, it is mainly the two particle event classes containing jets that are still populated and the largest deviation is observed in the e-e class with $\hat{P}$ = 0.01.

6 Conclusions

The data collected with the H1 experiment during the years 1994–2000 (HERA I) have been investigated in a search for deviations from the SM prediction at high transverse momentum. For the first time all event topologies involving isolated electrons, photons, muons, neutrinos and jets are investigated in a single analysis. A good agreement between the data and the SM expectation is found in most event classes. A better knowledge of rare processes may be required to search for deviations from the SM in final states with four jets at the highest invariant mass or transverse momentum. The distributions in the invariant mass and scalar sum of transverse momenta of the particles in each event class have been systematically searched for deviations using a statistical algorithm. The most significant deviation is found in the μ-j-ν event class, a topology where deviations have also been previously reported. About 3% (28%) of hypothetical Monte Carlo experiments would produce a deviation in at least one event class which is more significant than that observed in the corresponding sum of transverse momenta (invariant mass) distribution of the topology with a jet, a muon and a neutrino.

Acknowledgements

We are grateful to the HERA machine group whose outstanding efforts have made this experiment possible. We thank the engineers and technicians for their work in constructing and now maintaining the H1 detector, our funding agencies for financial support, the DESY technical staff for continual assistance and the DESY directorate for support and for the hospitality which they extend to the non DESY members of the collaboration. We wish to thank B. Knuteson for useful discussions.

Appendix

Signals for new physics may appear either as a single deviation or a small set of deviations. The following outlines how a significant deviation might be defined and presents tests of the sensitivity of this analysis to specific signals for new physics.

The probability P_X^n to observe in the data a $-\log_{10}\hat{P}$ greater than X in at least n event classes is given by the fraction of MC experiments having at least n event classes with a $-\log_{10}\hat{P}^{SM} > X$. The P_X^n values obtained for this analysis are presented in table 4. Up to 3 event classes are considered. Since very similar P_X^n values are found for the M_{all} and $\sum P_T$ distributions, averaged values are presented. For example, a P_X^n value smaller than 0.0005, which might be considered to represent a significant deviation, could be obtained from one event class with a $-\log_{10}\hat{P} > 5$, two event classes with a $-\log_{10}\hat{P} > 3.5$ or three event classes with a $-\log_{10}\hat{P} > 3$. It was found that one of these cases occurs either in M_{all} or $\sum P_T$ in around 0.1% of all MC experiments.

A set of pseudo data samples has been produced to test the sensitivity of the analysis procedure to some dedicated signals for new physics. The prediction of a specific model for new physics is added to the SM prediction and this new total prediction is used to generate pseudo data samples. Again a Monte Carlo technique is used to vary the distribution of signal events and generate many MC experiments. The complete algorithm is run on those MC experiments and the mean value of $-\log_{10}\hat{P}$ in all of them is derived as a measure of sensitivity of this analysis.

The exotic production of top quarks via a flavour-changing neutral current is first investigated. The decay $t \to bW$ with subsequent leptonic and hadronic W decays has been considered. The $\langle -\log_{10}\hat{P}\rangle$ values obtained are displayed in figure 6 (top) as a function of the cross section for producing a top when the proton beam energy is 920 GeV. Whereas $\langle -\log_{10}\hat{P}\rangle$ is around 0.43 if no signal is present, the value increases if a top is produced. In the j-j-j event class a $\langle -\log_{10}\hat{P}\rangle$ of 2 is obtained for a cross-section σ_{top} of ~ 0.5 pb. This value can be compared with the 95% confidence level exclusion limit on the top production cross section at $\sigma_{top} < 0.48$ pb already derived by the H1 experiment using the hadronic top decay channel only [30]. A deviation with three event classes with a $\langle -\log_{10}\hat{P}\rangle > 3$ would be found in this example for $\sigma_{top} \approx 1.5$ pb.

The second test concerns the production of leptoquarks (LQs) [31]. $S_{1/2,L}$ and $V_{0,L}$ type leptoquarks have been considered, which would mainly manifest themselves in the e-j and

j-ν channels. A λ coupling of 0.05 has been assumed and the sensitivity of the present analysis was tested for various LQ masses. The $\langle -\log_{10} \tilde{P} \rangle$ values obtained from searches in the M_{all} distributions are summarised in figure 6 (bottom), for both the $S_{1/2,L}$ and $V_{0,L}$ LQ appearing in the e-j and e-j-j as well as the j-ν and j-j-ν channels, respectively. This analysis is sensitive to both types of leptoquarks up to masses of $240 - 250$ GeV. These values can be compared with 95% confidence level limits of 265 GeV for $S_{1/2,L}$ LQs and 240 GeV for $V_{0,L}$ LQs, determined by dedicated analyses [32]. As for the case of single top production, the general search is thus found to have a sensitivity to leptoquark production which is comparable with that of dedicated searches.

References

[1] M. Kuze and Y. Sirois, Prog. Part. Nucl. Phys. **50** (2003) 1 [hep-ex/0211048].

[2] B. Abbott *et al.* [D0 Collaboration], Phys. Rev. D **62** (2000) 092004 [hep-ex/0006011]. B. Abbott *et al.* [D0 Collaboration], Phys. Rev. D **64** (2001) 012004 [hep-ex/0011067].

[3] R. Brun, F. Bruyant, M. Maire, A. C. McPherson and P. Zanarini, CERN-DD/EE/84-1.

[4] T. Sjöstrand *et al.*, Comput. Phys. Commun. **135** (2001) 238 [hep-ph/0010017]. (The PARP(67) parameter was set to 4 instead of its default value of 1).

[5] H. Jung, Comput. Phys. Commun. **86** (1995) 147.

[6] A. Kwiatkowski, H. Spiesberger and H. J. Möhring, Comput. Phys. Commun. **69** (1992) 155.

[7] G. A. Schuler and H. Spiesberger, "Django: The Interface for The Event Generators Heracles and Lepto".

[8] L. Lönnblad, Comput. Phys. Commun. **71** (1992) 15.

[9] C. Berger and P. Kandel, Prepared for Workshop on Monte Carlo Generators for HERA Physics Hamburg, Germany, 27-30 Apr 1998.

[10] T. Abe, Comput. Phys. Commun. **136** (2001) 126 [hep-ph/0012029].

[11] A. Mucke *et al.*, Comput. Phys. Commun. **124** (2000) 290 [astro-ph/9903478].

[12] U. Baur, J. A. Vermaseren and D. Zeppenfeld, Nucl. Phys. B **375** (1992) 3.

[13] K. P. Diener, C. Schwanenberger and M. Spira, Eur. Phys. J. C **25** (2002) 405 [hep-ph/0203269].

[14] K. P. Diener, C. Schwanenberger and M. Spira, [hep-ex/0302040].

[15] C. Adloff *et al.* [H1 Collaboration], Eur. Phys. J. C **25** (2002) 13 [hep-ex/0201006].

[16] I. Abt *et al.* [H1 Collaboration], Nucl. Instrum. Meth. A **386** (1997) 348; I. Abt *et al.* [H1 Collaboration], Nucl. Instrum. Meth. A **386** (1997) 310.

[17] B. Andrieu *et al.* [H1 Calorimeter Group Collaboration], Nucl. Instrum. Meth. A **336** (1993) 460.

[18] R. D. Appuhn *et al.* [H1 SPACAL Group Collaboration], Nucl. Instrum. Meth. A **386** (1997) 397.

[19] C. Adloff *et al.* [H1 Collaboration], Eur. Phys. J. C **30**, 1 (2003) [hep-ex/0304003].

[20] M. Peez, "Recherche de déviations au Model Standard dans les processus de grande énergie transverse sur le collisionneur électron - proton HERA", Ph.D. thesis, Université de Lyon (2003), DESY-THESIS-2003-023. (available at http://www-h1.desy.de/psfiles/theses/).

[21] A. Aktas *et al.* [H1 Collaboration], Phys. Lett. B **583** (2004) 28 [hep-ex/0311015].

[22] Z. Zhang, Habilitation Thesis, LAL preprint, LAL 00-57 (2000) [hep-ph/0012249].

[23] V. Andreev *et al.* [H1 Collaboration], Phys. Lett. B **561** (2003) 241 [hep-ex/0301030].

[24] S. D. Ellis and D. E. Soper, Phys. Rev. D **48** (1993) 3160 [hep-ph/9305266].

[25] S. Catani, Y. L. Dokshitzer, M. H. Seymour and B. R. Webber, Nucl. Phys. B **406** (1993) 187.

[26] W. T. Giele, E. W. N. Glover and D. A. Kosower, Phys. Rev. D **57** (1998) 1878 [hep-ph/9706210].

[27] G. Frising, "Rare Phenomena and W production in Electron-Proton Scattering at HERA", Ph.D. thesis, RWTH Aachen (2003) (available at http://www-h1.desy.de/psfiles/theses/).

[28] M. Wessels, "General Search for New Phenomena in ep Scattering at HERA", Ph.D. thesis, RWTH Aachen (2004) (available at http://www-h1.desy.de/psfiles/theses/).

[29] A. Aktas *et al.* [H1 Collaboration], Eur. Phys. J. C **31** (2003) 17 [hep-ex/0307015].

[30] A. Aktas *et al.* [H1 Collaboration], Eur. Phys. J. C **33**, 9 (2004) [hep-ex/0310032].

[31] C. Adloff *et al.* [H1 Collaboration], Eur. Phys. J. C **11** (1999) 447 [Erratum-ibid. C **14** (2000) 553] [hep-ex/9907002].

[32] S. Chekanov *et al.* [ZEUS Collaboration], Phys. Rev. D **68** (2003) 052004 [hep-ex/0304008].

Object	Energy Scale	θ (mrad)	Identification efficiency
Jet	2%	5–10	–
Electron	0.7–3%	1–3	2–7%
Photon	0.7–3%	1–3	2–7%
Muon	5%	3	5%

Table 1: Systematic uncertainties attributed to the measurement of energies and polar angles and to the identification efficiencies of particles.

Process	Uncertainty
$ep \to jjX$ and $ep \to j\gamma X$	15%
$ep \to j\nu X$ and $ep \to jeX$	10%
$ep \to jj\nu X$ and $ep \to jjeX$	15%
$ep \to \mu\mu X$ and $ep \to eeX$	3%
$ep \to WX$ and $ep \to WjX$	15%
$ep \to e\gamma X$ and $ep \to e\gamma j$	10%
$ep \to e\gamma p$	5%

Table 2: Theoretical uncertainties attributed to the simulation of different SM processes.

	M_{all}						$\sum P_T$					
event class	$\hat{P}$	N_{obs}	N_{SM}	$\pm$	δN_{SM}	p	$\hat{P}$	N_{obs}	N_{SM}	$\pm$	δN_{SM}	p
j-j	0.38	1	0.035	$\pm$	0.017	0.036	0.12	1	0.013	$\pm$	0.006	0.013
e-j	0.94	111	139	$\pm$	21	0.12	0.021	12	31.2	$\pm$	5.1	0.0028
μ-j	0.67	3	1.07	$\pm$	0.25	0.098	0.29	3	0.70	$\pm$	0.23	0.040
j-ν	0.34	83	116	$\pm$	14	0.028	0.22	20	36.7	$\pm$	6.2	0.023
e-ν	0.94	5	10.6	$\pm$	4.4	0.17	0.77	0	2.1	$\pm$	0.8	0.17
e-e	0.32	3	0.56	$\pm$	0.17	0.023	0.019	3	0.18	$\pm$	0.08	0.0013
e-μ	0.21	4	0.93	$\pm$	0.12	0.016	0.56	0	2.6	$\pm$	0.5	0.080
μ-μ	0.069	2	0.14	$\pm$	0.04	0.010	0.036	2	0.11	$\pm$	0.03	0.0060
j-γ	0.52	3	10.8	$\pm$	3.7	0.052	0.77	0	2.5	$\pm$	1.0	0.13
e-γ	0.38	9	19.2	$\pm$	2.0	0.014	0.64	8	15.7	$\pm$	1.9	0.040
γ-γ	0.47	1	0.16	$\pm$	0.09	0.15	0.31	1	0.11	$\pm$	0.09	0.12
j-j-j	0.41	12	5.9	$\pm$	2.0	0.050	0.58	14	7.8	$\pm$	2.5	0.077
e-j-j	0.69	39	59.6	$\pm$	10.7	0.058	0.085	9	23.9	$\pm$	4.4	0.0072
j-j-ν	0.62	5	1.79	$\pm$	0.41	0.043	0.51	5	1.74	$\pm$	0.45	0.040
e-j-ν	0.090	2	0.19	$\pm$	0.05	0.016	0.16	2	0.28	$\pm$	0.06	0.034
μ-j-ν	$9.7 \cdot 10^{-3}$	3	0.19	$\pm$	0.05	0.0011	$1.0 \cdot 10^{-3}$	3	0.068	$\pm$	0.029	$7.5 \cdot 10^{-5}$
j-j-γ	0.27	1	0.074	$\pm$	0.048	0.076	0.36	1	0.15	$\pm$	0.10	0.15
e-j-γ	0.47	1	5.7	$\pm$	1.6	0.050	0.39	1	5.6	$\pm$	1.4	0.045
e-j-j-j	0.98	0	1.6	$\pm$	0.5	0.23	0.87	1	0.18	$\pm$	0.06	0.17
j-j-j-ν	0.33	1	0.084	$\pm$	0.045	0.083	0.20	2	0.31	$\pm$	0.14	0.044

Table 3: The $\hat{P}$ values, the number of data events N_{obs} and the SM expectation N_{SM} for the region derived by the search algorithm using the M_{all} and $\sum P_T$ distributions for event classes containing at least one event and taken into account in the statistical procedure. The p value in the selected region is also presented.

n	P_1	$P_{1.5}$	P_2	$P_{2.5}$	P_3	$P_{3.5}$	P_4	$P_{4.5}$	P_5
1	95%	65%	28%	9%	3%	0.9%	0.2%	0.1%	<0.05%
2	79%	28%	4%	0.6%	0.1%	<0.05%	—	—	—
3	53%	8%	0.4%	0.05%	<0.05%	—	—	—	—

Table 4: The probability P_X^n to find at least n event classes with a $-\log \hat{P}$ value greater than X. The values are applicable to both the M_{all} and $\sum P_T$ analyses.

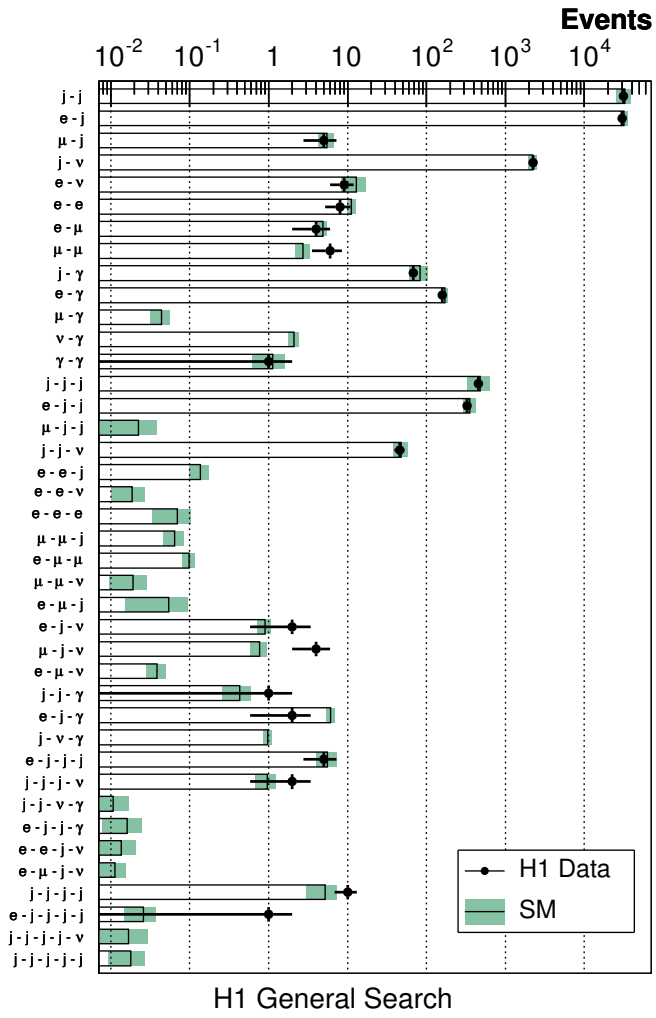

Figure 1: The data and the SM expectation for all event classes with a SM expectation greater than 0.01 events. The analysed data sample corresponds to an integrated luminosity of 117 pb^{-1}. The error bands on the predictions include model uncertainties and experimental systematic errors added in quadrature.

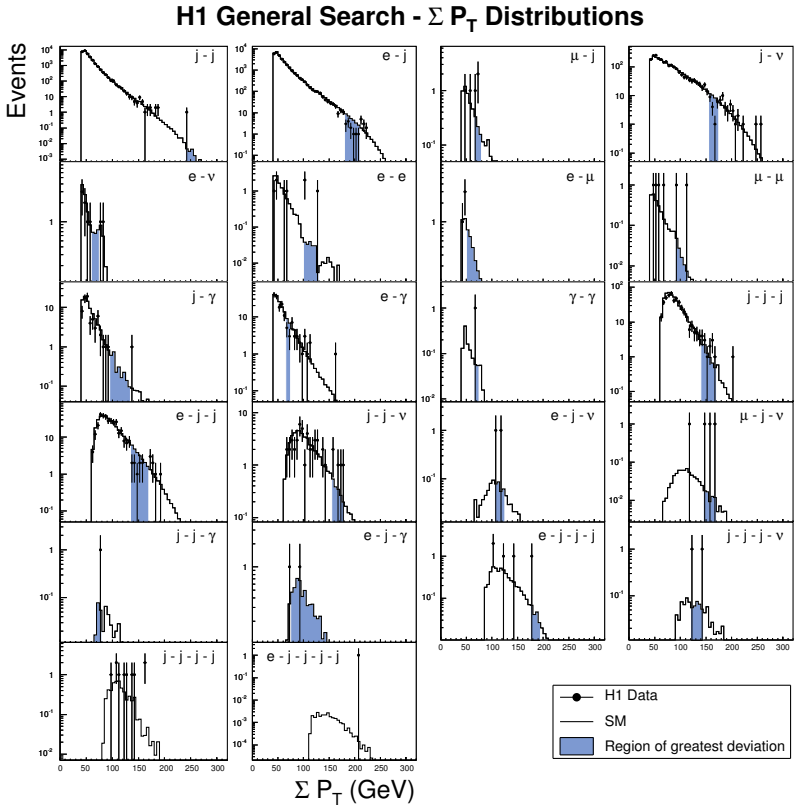

Figure 2: The number of data events and the SM expectation as a function of $\sum P_T$ for classes with at least one event. The shaded areas show the regions of greatest deviation chosen by the search algorithm. No search is performed for the j-j-j-j and e-j-j-j-j classes.

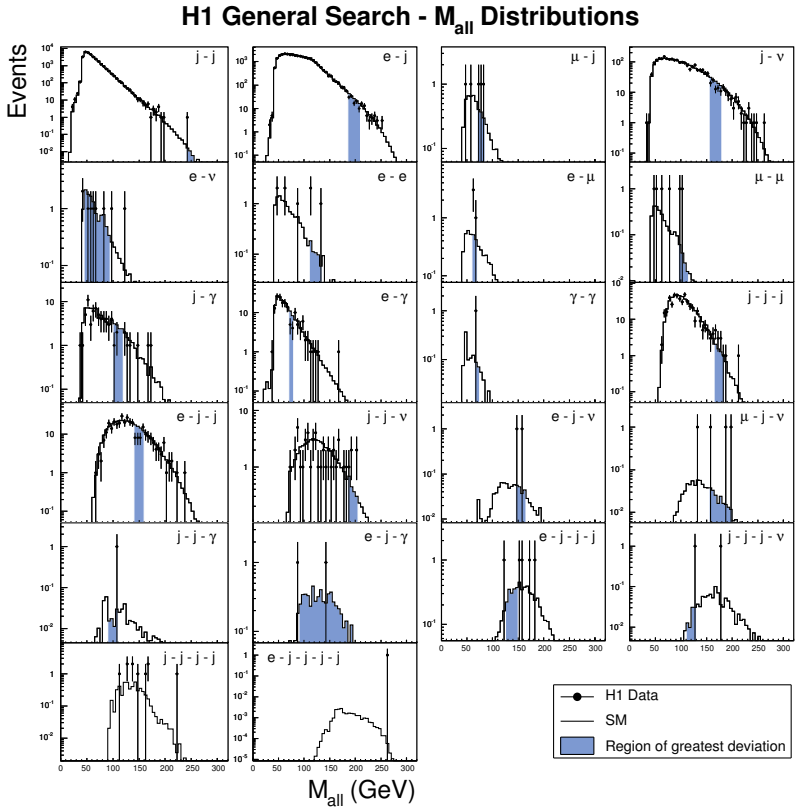

Figure 3: The number of data events and the SM expectation as a function of M_{all} for event classes with at least one event. The shaded areas show the regions of greatest deviation chosen by the search algorithm. No search is performed for the j-j-j-j and e-j-j-j-j classes.

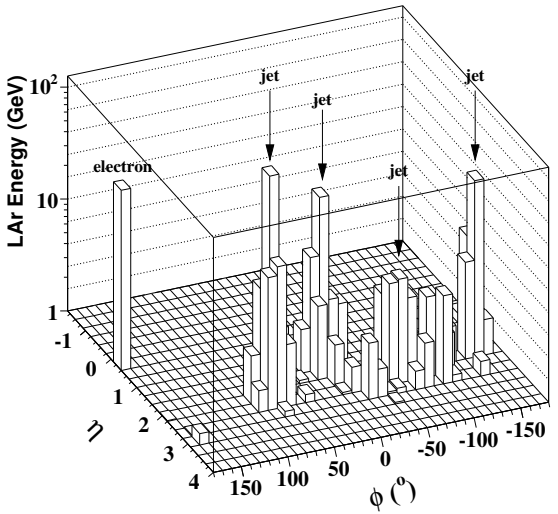

Figure 4: The calorimetric energy deposits of the e-j-j-j-j event as a function of η and ϕ.

Annexe M

A General Search for New Phenomena at HERA

F.D. Aaron *et al.* [H1 Collaboration],
Phys. Lett. B **674** (2009) 257,
arXiv:0901.0507

Abstract

A model–independent search for deviations from the Standard Model prediction is performed using the full $e^{\pm}p$ data sample collected by the H1 experiment at HERA. All event topologies involving isolated electrons, photons, muons, neutrinos and jets with transverse momenta above 20 GeV are investigated in a single analysis. Events are assigned to exclusive classes according to their final state. A dedicated algorithm is used to search for deviations from the Standard Model in the distributions of the scalar sum of transverse momenta or the invariant mass of final state particles and to quantify their significance. Variables related to angular distributions and energy sharing between final state particles are also introduced to study the final state topologies. No significant deviation from the Standard Model expectation is observed in the phase space covered by this analysis.

1 Introduction

At HERA electrons[1] and protons collide at a centre–of–mass energy of up to 319 GeV. The collected luminosity of high–energy electron-proton interactions gives access to rare processes with cross sections of the order of 0.1 pb, providing a testing ground for the Standard Model (SM) complementary to e^+e^- and $p\overline{p}$ scattering.

A large variety of possible extensions to the SM predicts new phenomena which may appear at high energies. Searches for new physics often compare the data to the predictions of specific models. A complementary approach is followed in signature based searches by looking for differences between data and SM expectation in various event topologies. As an advantage, such model independent analyses do not rely on any a priori definition of expected signatures for exotic phenomena. Therefore, they address the important question of whether unexpected phenomena may occur through a new pattern, not predicted by existing models. Following this approach, final states corresponding to rare SM processes such as single W boson or lepton pair production have already been investigated at HERA [1–5]. Model independent analyses are also performed at the Tevatron [6, 7].

The present paper reports on a general analysis of all high transverse momentum (P_T) final state configurations involving electrons (e), muons (μ), jets (j), photons (γ) or neutrinos (ν) in $e^{\pm}p$ collisions. This analysis searches for deviations from the SM prediction in phase space regions where the SM prediction is reliable. All final states containing at least two particles[2] (e, μ, j, γ, ν) with $P_T > 20$ GeV in the polar angle[3] range $10^\circ < \theta < 140^\circ$ are investigated. The present analysis follows the strategy of the previous H1 publication [8]. Selected events are classified into exclusive event classes according to the number and types of particles detected in the final state (e.g. e-j, μ-ν-j, j-j-j-j). In a first step the event yields are compared with the SM expectation. In a second step kinematical distributions are systematically investigated using a dedicated algorithm [8] which locates the region with the largest deviation of the data from the SM prediction.

The complete $e^{\pm}p$ data sample collected by the H1 experiment at HERA is used. The data are recorded at an electron beam energy of 27.6 GeV and proton beam energies of 820 GeV or 920 GeV, corresponding to centre–of–mass energies $\sqrt{s}$ of 301 GeV or 319 GeV, respectively. The total integrated luminosity of the data is 463 pb^{-1}, which represents a factor of four increase with respect to the previously published result [8]. The data comprise 178 pb^{-1} recorded in e^-p collisions and 285 pb^{-1} in e^+p collisions, of which 35 pb^{-1} were recorded at $\sqrt{s} = 301$ GeV. While the previous general search was dominated by e^+p collision data, a large data set recorded in e^-p scattering is now also analysed.

[1] In this paper the term "electron" is used generically to refer to both electrons and positrons, unless otherwise stated.

[2] In this context a high P_T jet is also called particle.

[3] The origin of the H1 coordinate system is the nominal ep interaction point, with the direction of the proton beam defining the positive z–axis (forward region). The transverse momenta are measured in the xy plane. The pseudorapidity η is related to the polar angle θ by $\eta = -\ln\tan(\theta/2)$.

2 Standard Model Processes and their Simulation

A precise estimate of all processes relevant at high transverse momentum in ep interactions is needed to ensure a reliable comparison to the SM. Several Monte Carlo (MC) generators are therefore combined to simulate events in all classes.

At high transverse momenta the dominant SM processes are photoproduction of two jets and neutral current (NC) deep–inelastic scattering (DIS). Direct and resolved photoproduction of jets and prompt photon production are simulated using the PYTHIA [9] event generator. The simulation is based on Born level hard scattering matrix elements with radiative QED corrections. The RAPGAP [10] event generator, which implements the Born, QCD Compton and boson gluon fusion matrix elements, is used to model NC DIS events. QED radiative effects arising from real photon emission from both the incoming and outgoing electrons are simulated using the HERACLES [11] program. In RAPGAP and PYTHIA, jet production from higher order QCD radiation is simulated using leading logarithmic parton showers. Hadronisation is modelled with Lund string fragmentation [9]. The leading order MC prediction of photoproduction and NC DIS processes with two or more high transverse momentum jets is scaled by a factor of 1.2 to account for the incomplete description of higher orders in the MC generators [8, 12]. Charged current (CC) DIS events are simulated using the DJANGO [13] event generator, which includes first order leptonic QED radiative corrections based on HERACLES. The production of two or more jets in DJANGO is accounted for using the colour–dipole–model [14]. Contributions from elastic and quasi–elastic QED Compton scattering are simulated with the WABGEN [15] generator. Contributions arising from the production of single W bosons and multi–lepton events are modelled using the EPVEC [16] and GRAPE [17] event generators, respectively.

All processes are generated with at least ten times the integrated luminosity of the data sample. Generated events are passed through the GEANT [18] based simulation of the H1 apparatus, which takes into account the running conditions of the different data taking periods, and are reconstructed and analysed using the same program chain as is used for the data.

3 Experimental Conditions

A detailed description of the H1 experiment can be found in [19]. Only the detector components relevant to the present analysis are briefly described here. The Liquid Argon (LAr) calorimeter [20] covers the polar angle range $4^\circ < \theta < 154^\circ$ with full azimuthal acceptance. Electromagnetic shower energies are measured with a precision of $\sigma(E)/E \simeq 11\%/\sqrt{E/\text{GeV}} \oplus 1\%$ and hadronic energies with $\sigma(E)/E \simeq 50\%/\sqrt{E/\text{GeV}} \oplus 2\%$, as measured in test beams [21,22]. In the backward region, energy measurements are provided by a lead/scintillating–fibre (SpaCal) calorimeter [23] covering the range $155^\circ < \theta < 178^\circ$. The central ($20^\circ < \theta < 160^\circ$) and forward ($7^\circ < \theta < 25^\circ$) inner tracking detectors are used to measure charged particle trajectories and to reconstruct the interaction vertex. The innermost central proportional chamber, CIP [24, 25] ($9^\circ < \theta < 171^\circ$) is used together with tracking detectors to veto charged particles for the identification of photons. The LAr calorimeter and inner tracking detectors are enclosed in a super–conducting magnetic coil with a field strength of 1.16 T. From the curvature

of charged particle trajectories in the magnetic field, the central tracking system provides transverse momentum measurements with a resolution of $\sigma_{P_T}/P_T = 0.005 P_T/\text{GeV} \oplus 0.015$ [26]. The return yoke of the magnetic coil is the outermost part of the detector and is equipped with streamer tubes forming the central muon detector ($4^\circ < \theta < 171^\circ$). In the forward region of the detector ($3^\circ < \theta < 17^\circ$) a set of drift chambers detects muons and measures their momenta using an iron toroidal magnet. The luminosity is determined from the rate of the Bethe–Heitler process $ep \to ep\gamma$, measured using a photon detector located close to the beam pipe at $z = -103$ m, in the backward direction.

The main trigger is provided by the LAr calorimeter [27]. Events with an electromagnetic deposit (electron or photon) in the LAr with an energy greater than 10 GeV are detected by the LAr trigger with an efficiency of almost 100% [28]. Events are also triggered by jets only, with a trigger efficiency above 95% for $P_T^{\text{jet}} > 20$ GeV and nearly 100% for $P_T^{\text{jet}} > 25$ GeV [29]. For events with missing transverse energy of 20 GeV, the trigger efficiency is about 90% and increases above 95% for missing transverse energy above 30 GeV [30]. The trigger for events with only muons is based on single muon signatures from the central muon detector, combined with signals from the central tracking detector. The trigger efficiency is about 95% for di–muon events with muon transverse momenta larger than 15 GeV [5].

4 Data Analysis

4.1 Event Reconstruction and Particle Identification

In order to remove background events induced by cosmic showers and other non–ep sources, the event vertex is required to be within 35 cm in z of the nominal interaction point. In addition, topological filters and timing vetoes are applied [31].

Calorimetric energy deposits and tracks are used to look for electron, photon and muon candidates. Electron and photon candidates are characterised by compact and isolated electromagnetic showers in the LAr calorimeter. The identification of muon candidates is based on a track measured in the inner tracking systems associated with signals in the muon detectors [1]. Calorimeter energy deposits and tracks not previously identified as electron, photon or muon candidates are used to form combined cluster–track objects, from which the hadronic final state is reconstructed [29, 32]. Jet candidates with a minimum transverse momentum of 2.5 GeV are reconstructed from these combined cluster–track objects using an inclusive k_T algorithm [33, 34] with a P_T weighted recombination scheme in which the jets are treated as massless. The missing transverse momentum P_T^{miss} of the event is derived from all detected particles and energy deposits in the event. In events with large P_T^{miss}, a neutrino candidate is reconstructed. The four–vector of this neutrino candidate is calculated assuming transverse momentum conservation and the relation $\sum_i (E^i - P_z^i) + (E^\nu - P_z^\nu) = 2E_e^0 = 55.2$ GeV, where the sum runs over all detected particles, P_z is the momentum along the proton beam axis and E_e^0 is the electron beam energy. The latter relation holds if no significant losses are present in the electron beam direction.

Additional requirements are applied to ensure an unambiguous identification of particles, while retaining good efficiencies. Strict isolation criteria are applied in order to achieve high purities in all event classes.

For electrons, the calorimetric energy measured within a distance in the pseudorapidity–azimuth (η, ϕ) plane $R = \sqrt{\Delta\eta^2 + \Delta\phi^2} < 0.75$ around the candidate is required to be below 2.5% of its energy. In the region of angular overlap between the LAr and the central tracking detectors ($20^\circ < \theta < 140^\circ$), hereafter referred to as the central region, the calorimetric electron identification is complemented by tracking information. In this region it is required that a well measured track geometrically matches the centre–of–gravity of the electromagnetic cluster within a distance of closest approach (DCA) of 12 cm. Furthermore, the distance from the first measured track point in the central drift chambers to the beam axis is required to be below 30 cm in order to reject photons that convert late in the central tracker material. In the central region, the transverse momentum of the associated electron track $P_T^{e_{tk}}$ is required to match the calorimetric measurement P_T^e such that $1/P_T^{e_{tk}} - 1/P_T^e < 0.02$ GeV^{-1} in order to reject hadronic showers. In the forward region ($10^\circ < \theta < 20^\circ$), a wider calorimetric isolation cone of $R < 1$ is required to reduce the contribution of fake electrons from hadrons. In this forward region, at least one track is required to be present with a DCA < 12 cm. The presence of at least one hit in the CIP, associated to the electron trajectory, is also required. Finally, the electron is required to be isolated from any other well measured track by a distance $R > 0.5$ ($R > 1$) to the electron direction in the central (forward) region. The resulting electron identification efficiency is $\sim 80\%$ in the central region and $\sim 40\%$ in the forward region, determined from NC DIS events.

The identification of photons relies on the same calorimetric isolation criteria as used in the electron identification. Vetoes on any track pointing to the electromagnetic cluster are applied. No track with a DCA to the cluster below 24 cm or within $R < 0.5$ should be present. An additional veto on any hits in the CIP associated to the electromagnetic cluster is applied. Furthermore, each photon must be isolated from jets by $R > 0.5$. The resulting photon identification efficiency as derived using elastic QED Compton events is $\sim 95\%$ in the central region and $\sim 50\%$ in the forward region.

A muon should have no more than 5 GeV deposited in a cylinder, centred on the muon track direction, of radius 25 cm and 50 cm in the electromagnetic and hadronic sections of the LAr calorimeter, respectively. Misidentified hadrons are strongly suppressed by requiring that the muon be separated from the closest jet and from any further track by $R > 1$. In di–muon events, the opening angle between the two muons is required to be smaller than 165°, in order to remove muons originating from cosmic rays. The efficiency to identify muons is $\sim 90\%$ [5].

The scattered electron may be misidentified as a hadron and reconstructed as a jet. To reject fake jet candidates, the first radial moment of the jet transverse energy [35, 36] is required to be greater than 0.02 and the quantity $M^{\text{jet}}/P_T^{\text{jet}}$ greater than 0.1 [12, 36], where the invariant mass M^{jet} is obtained using the four–vector sum of all particles belonging to the jet. If the fraction of the jet energy contained in the electromagnetic part of the LAr calorimeter is greater than 0.9, the above criteria are tightened to 0.04 and 0.15, respectively. These requirements are fulfilled by $\sim 97\%$ of the jets [36].

Missing transverse momentum, which is the main signature for neutrinos, may arise from mis–measurement of particles. By requiring $\sum_i (E^i - P_z^i) < 48$ GeV, fake neutrino candidates from NC DIS processes are rejected. If exactly one electron or muon candidate is found, a neutrino is only assigned to an event if $\Delta\phi_{(l-X_h)} < 160^\circ$, where $\Delta\phi_{(l-X_h)}$ is the difference in azimuthal angle between the lepton l and the direction of the hadronic final state X_h.

4.2 Event Selection and Classification

The common phase space for electrons, photons, muons and jets is defined by $10^\circ < \theta < 140^\circ$ and $P_T > 20$ GeV. The neutrino phase space is defined as missing transverse momentum above 20 GeV and $\sum_i (E^i - P_z^i) < 48$ GeV. All particles with $P_T > 20$ GeV, including the neutrino defined by its reconstructed four–vector, are required to be isolated with respect to each other by a minimum distance $R > 1$. The particles satisfying these requirements are referred to as bodies. The events are sorted depending on the number and types of bodies into exclusive event classes. All possible event classes with at least two bodies are investigated. Only the μ-ν event class is discarded from the analysis. This class is dominated by events in which a poorly reconstructed muon gives rise to missing transverse momentum, which fakes the neutrino signature.

Based on these identification criteria, purities have been derived for each event class. Purity is defined as the ratio of SM events reconstructed in the event class in which they are generated to the total number of reconstructed events in this class. Most purities are found to be above 60% and are close to 100% for the j-j, e-j, ν-j and μ-μ event classes.

4.3 Systematic Uncertainties

The following experimental systematic uncertainties are considered:

- The uncertainty on the electromagnetic energy scale varies depending on the polar angle from 0.7% in the central region to 2% in the forward region. The polar angle measurement uncertainty of electromagnetic clusters is 3 mrad. The identification efficiency of electrons (photons) is known with an absolute uncertainty of 3% (5%) to 5% (10%), depending on the polar angle.
- The scale uncertainty on the transverse momentum of high P_T muons is 2.5% [5]. The uncertainty on the reconstruction of the muon polar angle is 3 mrad. The identification efficiency of muons is known with an absolute uncertainty of 5%.
- The jet energy scale is known within 2% [30]. The uncertainty on the jet polar angle determination is 10 mrad.
- The absolute uncertainty on the trigger efficiency is estimated to be 6% if only muons are present in the final state and 3% in all other cases.
- The luminosity measurement has an uncertainty of 3%.

The effects of the above uncertainties on the SM expectation are determined by varying the experimental quantities by ± 1 standard deviation in the MC samples and propagating these variations through the whole analysis chain.

Additional model uncertainties are attributed to the SM Monte Carlo generators described in section 2. An error of 10% is attributed to NC and CC DIS processes with only one high

P_T jet. To account for the uncertainty on higher order QCD corrections, an error of 15% on the NC DIS and photoproduction processes with at least two high P_T jets is considered. The uncertainty of CC DIS processes with at least two high P_T jets is estimated to be 20% [30]. The errors include uncertainties from the proton parton distribution functions and from missing higher order QCD corrections. For each additional jet produced by parton shower processes, a further theoretical error of 20% is added [37], for example 20% for the j-j-j event class.

The error on the elastic and quasi–elastic QED Compton cross sections is conservatively estimated to be 5%. The error on the inelastic QED Compton cross section is 10%. The errors attributed to lepton–pair and W production are 3% and 15%, respectively. An uncertainty of 30% on the simulation of radiative CC DIS events is considered to account for the lack of QED radiation from the quark line in the DJANGO generator. This uncertainty is estimated for the specific phase space of the analysis by a comparison of the DJANGO result to the calculated cross section of the $e^- p \to \nu_e \gamma X$ process [38]. An uncertainty of 50% is added to the prediction for NC DIS events with measured missing transverse momentum above 20 GeV and a high P_T electron. This uncertainty is estimated by a comparison of the missing transverse momentum distribution of data events containing a low P_T electron ($P_T^e < 20$ GeV) with the SM prediction [37].

The total error on the SM prediction is determined by adding the effect of all model and experimental systematic uncertainties in quadrature.

5 Results

5.1 Event Yields

The event yields for all event classes are presented for the data and SM expectation in figures 1(a) and 1(b) for e^+p and e^-p collisions, respectively. All event classes with observed data events or with a SM expectation greater than 0.01 events are shown. The corresponding observed and predicted event yields for all $e^\pm p$ data are summarised in table 1. Events are observed in 27 classes and a good description of the number of observed data events by the SM prediction is seen in each class.

The j-j, j-j-j and j-j-j-j event classes are dominated by photoproduction processes. No event with five jets is observed. The SM prediction of the e-j, e-j-j, e-j-j-j and e-j-j-j-j event classes is dominated by NC DIS processes. One event, already discussed in a previous H1 publication [8], is observed in the e-j-j-j-j event class and compares to a SM prediction of 0.13 ± 0.06. The ν-j, ν-j-j, ν-j-j-j and ν-j-j-j-j event classes mainly contain events from CC DIS processes. One event is observed in the ν-j-j-j-j event class compared to a SM expectation of 0.05 ± 0.02.

Events from QED Compton processes populate the γ-e event class as well as the γ-e-j event class in the case of inelastic events. The γ-j event class corresponds to prompt photon events. The purity in this class is moderate ($\sim 50\%$) due to the high background from misidentified electrons in NC DIS. A slight deficit of data events is observed in the radiative CC DIS classes γ-ν and γ-ν-j.

Lepton pair production from $\gamma\gamma$ processes dominates in event classes with several leptons (e-e, μ-μ, e-μ and e-e-e). Compared to the results of a previous study of multi–lepton topologies [5], the phase space of the present analysis is restricted to higher P_T and extended to forward polar angles down to 10°. All multi–lepton events mentioned in [5] and located in the phase space of this analysis are found. The e-e event class contains 7 events with an invariant mass $M_{ee} > 100$ GeV compared to a SM expectation of 3.4 ± 0.5 of which 69% are from lepton pair processes. The e-e-e event class contains one event compared to a SM expectation of 0.22 ± 0.04.

The prediction for the event classes μ-ν-j and e-ν-j consists mainly of high P_T single W production with subsequent leptonic decay. In the μ-ν-j (e-ν-j) event class 5 (4) events are observed, with a SM expectation of 2.8 ± 0.5 (3.2 ± 0.5). Two events classified as μ-ν-j in the previous analysis [8] now migrate to μ-j and ν-j event classes, respectively, due to improvements in the energy and momentum reconstruction. Events arising from W production also enter in the e-ν event class. In this class 16 events are observed compared to an expectation of 21.5 ± 3.5, of which about 90% is due to W production processes.

5.2 Event Topology

The distributions of the scalar sum of transverse momenta $\sum P_T$ and of the invariant mass $M_{\rm all}$ of all bodies are presented in figures 2 and 3, respectively, for classes with at least one event. The data are in agreement with the SM prediction. In particular, multiple jets topologies, which are sensitive to QCD radiation, are well described by the simulation.

The final state topologies are also evaluated in terms of angular distributions and energy ratios, which are sensitive to spin and decay properties of hypothetical high mass particles. Variables used to study the decomposition of the final states, inspired by topological analyses of multi–jet events [39], are defined in the following. In each event a leading body is selected according to the following priority list between bodies of different types: γ, e, μ, ν, j. This order of preference allows a better separation of SM background from events originating from a new resonance decaying to a photon or a lepton. If two bodies of the same type are present, the one with the highest transverse momentum P_T^*, relative to the incident proton in the centre–of–mass frame defined by all bodies, is selected. For classes with exactly two bodies of the same type, the leading body is taken as the one with the highest P_T in the laboratory frame. The variable $\cos\theta^*_{\rm lead}$ is then defined as the cosine of the polar angle of the leading body relative to the incident proton in the centre–of–mass frame defined by all bodies. The variable $X_{\rm lead}$ is the energy fraction of the leading body and is defined for systems with three or more bodies as

$$X_{\rm lead} = \frac{2E^*_{\rm lead}}{\sum_i E^*_i}, \qquad (1)$$

where the sum runs over all bodies, and $E^*_{\rm lead}$ and E^*_i are calculated in the centre–of–mass frame of all bodies. For events with two bodies, the $\cos\theta^*_{\rm lead}$ distribution is related to the underlying $2 \to 2$ matrix element. Therefore, the angular distribution of a particle coming from the decay of a new resonance may be markedly different from that of particles produced in SM processes (see for example [40]). For final states with more than two bodies, $X_{\rm lead}$ is a Dalitz variable

and related to the dynamics of a possible multi–body decay of a new particle. The sensitivity of these two variables $\cos\theta^*_{\rm lead}$ and $X_{\rm lead}$ to new physics is tested using different MC samples of exotic processes, for example leptoquarks, excited fermions, or anomalous top production. It has been verified that SM and exotic events exhibit different spectra in these two variables, two examples of which are given in figure 4.

The distributions of $\cos\theta^*_{\rm lead}$ and $X_{\rm lead}$ are presented in figure 5 for event classes with only two bodies and for event classes with more than two bodies, respectively. A good overall agreement with the SM prediction is observed in all cases. This illustrates that the event topology and kinematics, as well as the global variables $\sum P_T$ and $M_{\rm all}$, are well described by the SM.

5.3 Search for Deviations from the Standard Model

In order to quantify the level of agreement between the data and the SM expectation and to identify regions of deviations in the $\sum P_T$, $M_{\rm all}$, $\cos\theta^*_{\rm lead}$ and $X_{\rm lead}$ distributions, the search algorithm developed in [8] is used. A region is defined as a set of connected histogram bins with at least twice the size of the resolution. A statistical estimator p is defined in order to judge which region is of largest interest. This estimator is derived from the convolution of the Poisson probability density function (pdf) to account for statistical errors and a Gaussian pdf to include the effect of systematic uncertainties [8]. The value of p gives an estimate of the probability of a fluctuation of the SM expectation upwards (downwards) to at least (at most) the observed number of data events in the region considered. The region of greatest deviation is the region having the smallest p–value, $p_{\rm min}$. The regions selected by the algorithm in $\sum P_T$ and $M_{\rm all}$ distributions of each class are presented for all $e^\pm p$ data in figures 2 and 3, respectively. The corresponding selected regions for $\cos\theta^*_{\rm lead}$ and $X_{\rm lead}$ distributions are shown in figure 5.

The fact that the deviation could have occurred at any point in the distribution is taken into account by calculating the probability $\hat{P}$ to observe a deviation with a p–value $p_{\rm min}$ at any position in the distribution. $\hat{P}$ is a measure of the statistical significance of the deviation observed in the data. The event class of most interest in the search for anomalies is the one with the smallest $\hat{P}$ value. Values of $\hat{P}$ larger than 0.01 indicate event classes where no significant discrepancy between data and the SM expectation is observed. The $\hat{P}$ values measured in each of the event classes are listed in table 1. Due to the uncertainties of the SM prediction in the j-j-j-j, e-j-j-j-j and ν-j-j-j-j event classes, no reliable $\hat{P}$ values can be calculated for them [8] and they are therefore not considered in the search for deviations from the SM.

The overall agreement with the SM can further be quantified by taking into account the large number of event classes in this analysis. Among all studied classes there is some chance that small $\hat{P}$ values occur. This probability can be calculated on a statistical basis with MC experiments. A MC experiment is defined as a set of hypothetical data histograms following the SM expectation with an integrated luminosity equal to the amount of data recorded. The complete search algorithm and statistical analysis are applied to MC experiments analogously as to the data. The expectation for the $\hat{P}$ values observed in the data is then given by the distribution of $\hat{P}$ values obtained from all MC experiments.

The $\hat{P}$ values observed in the data in all event classes are compared in figure 6 to the distribution of $\hat{P}$ obtained from a large set of MC experiments. The comparison is presented for

the scans of the $M_{\rm all}$ and $\sum P_T$ distributions for all $e^{\pm}p$ data and also separately for e^-p and e^+p data. The distribution of $\hat{P}$ values measured in the data is in agreement with the expectation from MC experiments. Using all $e^{\pm}p$ data, a lowest $\hat{P}$ value of 0.0044 is found in the e-j-j event class in a region at high transverse momenta, $175 < \sum P_T < 200$ GeV, where 27 events are observed for an expectation of 11.6 ± 1.2. In e^-p data, the lowest $\hat{P}$ value is 0.0071 and corresponds to the e-e-e event class where one data event is observed compared to a low SM expectation. The most significant deviation from SM predictions is measured in e^+p collisions in the e-e event class with $\hat{P} = 0.0035$. In the corresponding region ($110 < M_{\rm all} < 120$ GeV) five data events are found while 0.43 ± 0.04 are expected. The global probability to find in the e^+p data at least one class with a $\hat{P}$ value smaller than observed in the e-e event class is 12% as deduced from MC experiments.

In case of the $\cos\theta^*_{\rm lead}$ and $X_{\rm lead}$ distributions, no significant discrepancy between the data and the SM expectation is found. The lowest $\hat{P}$ value is 0.017, observed in the $X_{\rm lead}$ distribution of the ν-j-j-j event class. In event classes where the SM contribution is high (> 100 events), the correlation between $M_{\rm all}$ or $\sum P_T$ distributions and $\cos\theta^*_{\rm lead}$ and $X_{\rm lead}$ is further exploited. The variables $\cos\theta^*_{\rm lead}$ and $X_{\rm lead}$ are used to select events in a phase space region where the SM contribution is reduced and exotic event topologies may be favoured. Events where the leading body is emitted in the forward direction are selected by requiring $\cos\theta^*_{\rm lead} > 0$. The variable $X_{\rm lead}$ is used in three bodies event classes to select topologies corresponding to a sequential resonance decay by requiring $0.75 < X_{\rm lead} < 0.9$, as deduced from the study of different MC samples of exotic processes. After a cut on these variables, an overall good agreement between the data and the SM is still observed in $M_{\rm all}$ and $\sum P_T$ distributions. The complete search procedure and statistical analysis is applied to these distributions, the results of which are summarised in table 2. No significant deviation is observed in the reduced event samples.

The full analysis is also performed at lower and higher transverse momenta by changing the minimum P_T of particles to $P_T > 15$ GeV and $P_T > 40$ GeV, respectively. A good overall agreement with the SM is also observed with these cuts. With a cut $P_T > 15$ GeV, all spectra are well described by the MC, including the multi–jet event classes. The lowest $\hat{P}$ value is 0.01, observed in the e-j-j event class. When raising the P_T threshold to 40 GeV, mainly event classes containing jets remain populated and the largest deviation is observed in the e-j-j-j class with $\hat{P} = 0.01$.

6 Conclusion

The full $e^{\pm}p$ data sample collected by the H1 experiment at HERA is investigated in a general search for deviations from the SM prediction at high transverse momenta. This analysis encompasses all event topologies involving isolated electrons, photons, muons, neutrinos and jets with transverse momenta above 20 GeV. Data events are found in 27 different final states and events with up to five high P_T particles are observed. In each event class deviations from the SM are searched for in the invariant mass and sum of transverse momenta distributions using a dedicated algorithm. In addition, the final state topologies are also evaluated in terms of angular distributions and energy sharing between final state particles. A good agreement with the SM expectation is observed in the phase space covered by this analysis. The largest deviation

is found in the e-e event class, in e^+p collisions, at high invariant masses and corresponds to a probability of 0.0035. The probability to observe a SM fluctuation with that significance or higher for at least one event class is 12%. This comprehensive analysis demonstrates the very good understanding of high P_T SM phenomena achieved at the HERA collider.

Acknowledgements

We are grateful to the HERA machine group whose outstanding efforts have made this experiment possible. We thank the engineers and technicians for their work in constructing and maintaining the H1 detector, our funding agencies for financial support, the DESY technical staff for continual assistance and the DESY directorate for the hospitality which they extend to the non–DESY members of the collaboration.

References

[1] V. Andreev *et al.* [H1 Collaboration], Phys. Lett. B **561** (2003) 241 [hep-ex/0301030].

[2] F. D. Aaron *et al.* [H1 Collaboration], "Events with Isolated Leptons and Missing Transverse Momentum and Measurement of W Production at HERA", DESY 08-170.

[3] A. Aktas *et al.* [H1 Collaboration], Eur. Phys. J. C **31** (2003) 17 [hep-ex/0307015].

[4] A. Aktas *et al.* [H1 Collaboration], Phys. Lett. B **583** (2004) 28 [hep-ex/0311015].

[5] F. D. Aaron *et al.* [H1 Collaboration], Phys. Lett. B **668** (2008) 268 [arXiv:0806.3987 [hep-ex]].

[6] B. Abbott *et al.* [D0 Collaboration], Phys. Rev. D **62** (2000) 092004 [hep-ex/0006011]; B. Abbott *et al.* [D0 Collaboration], Phys. Rev. D **64** (2001) 012004 [hep-ex/0011067].

[7] T. Aaltonen *et al.* [CDF Collaboration], Phys. Rev. D **78** (2008) 012002 [arXiv:0712.1311 [hep-ex]].

[8] A. Aktas *et al.* [H1 Collaboration], Phys. Lett. B **602** (2004) 14 [hep-ex/0408044].

[9] T. Sjöstrand *et al.*, PYTHIA version 6.1, Comput. Phys. Commun. **135** (2001) 238 [hep-ph/0010017].

[10] H. Jung, RAPGAP version 3.1, Comput. Phys. Commun. **86** (1995) 147.

[11] A. Kwiatkowski, H. Spiesberger and H. J. Möhring, Comput. Phys. Commun. **69** (1992) 155.

[12] C. Adloff *et al.* [H1 Collaboration], Eur. Phys. J. C **25** (2002) 13 [hep-ex/0201006].

[13] G. A. Schuler and H. Spiesberger, DJANGOH version 1.4, "Django: The Interface for The Event Generators Heracles and Lepto", Proceedings of the Workshop "Physics at HERA", eds. W. Buchmüller and G. Ingelman, DESY (1991), vol. 3, p. 1419.

[14] L. Lönnblad, Comput. Phys. Commun. **71** (1992) 15.

[15] C. Berger and P. Kandel, "A New Generator For Wide Angle Bremsstrahlung", Proceedings of the Workshop "Monte Carlo Generators for HERA Physics", eds. A. T. Doyle *et al.*, DESY (1998).

[16] U. Baur, J. A. Vermaseren and D. Zeppenfeld, Nucl. Phys. B **375** (1992) 3.

[17] T. Abe, GRAPE-Dilepton version 1.1, Comput. Phys. Commun. **136** (2001) 126 [hep-ph/0012029].

[18] R. Brun *et al.*, "GEANT3", CERN-DD/EE/84-1.

[19] I. Abt *et al.* [H1 Collaboration], Nucl. Instrum. Meth. A **386** (1997) 310;
I. Abt *et al.* [H1 Collaboration], Nucl. Instrum. Meth. A **386** (1997) 348.

[20] B. Andrieu *et al.* [H1 Calorimeter Group Collaboration], Nucl. Instrum. Meth. A **336** (1993) 460.

[21] B. Andrieu *et al.* [H1 Calorimeter Group Collaboration], Nucl. Instrum. Meth. A **336** (1993) 499.

[22] B. Andrieu *et al.* [H1 Calorimeter Group Collaboration], Nucl. Instrum. Meth. A **350** (1994) 57.

[23] R. D. Appuhn *et al.* [H1 SPACAL Group Collaboration], Nucl. Instrum. Meth. A **386** (1997) 397.

[24] K. Muller *et al.*, Nucl. Instrum. Meth. A **312** (1992) 457.

[25] J. Becker *et al.*, Nucl. Instrum. Meth. A **586** (2008) 190 [physics/0701002].

[26] C. Kleinwort [H1 Collaboration], "H1 Alignment Experience", Proceedings of the "First LHC Detector Alignment Workshop", eds. S. Blusk *et al.*, CERN (2006), CERN-2007-04.

[27] C. Adloff *et al.* [H1 Collaboration], Eur. Phys. J. C **30** (2003) 1 [hep-ex/0304003].

[28] A. Nikiforov, "Measurements of the Neutral Current $e^{\pm}p$ Cross Sections Using Longitudinally Polarised Lepton Beams at HERA II", Ph.D. thesis, Ludwig–Maximilians University (2007), available at http://www-h1.desy.de/publications/theses_list.html.

[29] M. Peez, "Recherche de déviations au Modèle Standard dans les processus de grande énergie transverse sur le collisionneur électron – proton HERA", Ph.D. thesis, Université de Lyon (2003), DESY-THESIS-2003-023, available at http://www-h1.desy.de/publications/theses_list.html.

[30] T. N. Trinh, "Recherche de leptons excités sur le collisionneur HERA avec le détecteur H1", Ph.D. thesis, Université de la Méditerranée Aix–Marseille II (2008), available at http://www-h1.desy.de/publications/theses_list.html.

[31] I. Negri, "Recherche de fermions excités dans l'expérience H1 auprès du collisionneur positron-proton HERA", Ph.D. thesis, Université de la Méditerranée Aix–Marseille II (1998), CPPM-T-1998-02, DESY-THESIS-1998-022, available at http://www-h1.desy.de/publications/theses_list.html.

[32] B. Portheault, "Première mesure des sections efficaces de courant chargé et neutre avec le faisceau de positrons polarisé à HERA II et analyses QCD-électrofaibles", Ph.D. thesis, Université Paris XI (2005), LAL-05-05, available at http://www-h1.desy.de/publications/theses_list.html.

[33] S. D. Ellis and D. E. Soper, Phys. Rev. D **48** (1993) 3160 [hep-ph/9305266].

[34] S. Catani *et al.*, Nucl. Phys. B **406** (1993) 187.

[35] W. T. Giele, E. W. N. Glover and D. A. Kosower, Phys. Rev. D **57** (1998) 1878 [hep-ph/9706210].

[36] G. Frising, "Rare Phenomena and W production in Electron-Proton Scattering at HERA", Ph.D. thesis, RWTH Aachen (2003), available at http://www-h1.desy.de/publications/theses_list.html.

[37] M. Wessels, "General search for new phenomena in ep scattering at HERA", Ph.D. thesis, RWTH Aachen (2004), available at http://www-h1.desy.de/publications/theses_list.html.

[38] T. Helbig and H. Spiesberger, Nucl. Phys. B **373** (1992) 73.

[39] S. Geer and T. Asakawa, Phys. Rev. D **53** (1996) 4793 [hep-ph/9510351].

[40] A. Aktas *et al.* [H1 Collaboration], Phys. Lett. B **629** (2005) 9 [hep-ex/0506044].

[41] F. D. Aaron *et al.* [H1 Collaboration], Phys. Lett. B **666** (2008) 131 [arXiv:0805.4530 [hep-ex]].

[42] F. D. Aaron *et al.* [H1 Collaboration], Phys. Lett. B **663** (2008) 382 [arXiv:0802.1858 [hep-ex]].

H1 General Search at HERA ($e^{\pm}p$, 463 pb^{-1})

Event class	Data	SM	$\hat{P}_{\sum P_T}$	$\hat{P}_{M_{\rm all}}$	$\hat{P}_{\cos\theta^*_{\rm lead}}$	$\hat{P}_{X_{\rm lead}}$
j-j	156724	153278 ± 27400	0.57	0.33	0.98	
e-j	125900	127917 ± 15490	0.090	0.99	0.40	
μ-j	21	19.5 ± 3.0	0.30	0.46	0.024	
ν-j	11081	11182 ± 1165	0.33	0.31	0.25	
e-ν	16	21.5 ± 3.5	0.13	0.084	0.62	
e-e	36	40.0 ± 3.7	0.35	0.041	0.52	
e-μ	19	21.0 ± 2.1	0.46	0.83	0.81	
μ-μ	18	17.5 ± 3.0	0.31	0.50	0.88	
γ-j	563	538 ± 86	0.31	0.21	0.77	
γ-e	619	648 ± 62	0.93	0.99	0.10	
γ-μ	0	0.22 ± 0.04	1	1	1	
γ-ν	4	9.6 ± 2.8	0.076	0.33	0.22	
γ-γ	1	1.1 ± 0.6	0.66	0.35	0.11	
j-j-j	2581	2520 ± 725	0.54	0.65		0.18
e-j-j	1394	1387 ± 270	0.0044	0.70		0.28
μ-j-j	1	0.46 ± 0.18	0.12	0.072		0.99
ν-j-j	355	338 ± 62	0.80	0.48		0.62
e-e-j	0	0.31 ± 0.04	1	1		1
e-e-ν	0	0.06 ± 0.01	1	1		1
e-e-e	1	0.22 ± 0.04	0.15	0.031		0.14
μ-μ-j	0	0.16 ± 0.03	1	1		1
e-μ-μ	0	0.37 ± 0.07	1	1		1
μ-μ-ν	0	0.010 ± 0.005	1	1		1
e-μ-j	0	0.16 ± 0.04	1	1		1
e-ν-j	4	3.2 ± 0.5	0.24	0.57		0.095
μ-ν-j	5	2.8 ± 0.5	0.27	0.30		0.35
e-μ-ν	0	0.05 ± 0.01	1	1		1
γ-j-j	5	6.7 ± 1.3	0.41	0.25		0.91
γ-e-j	12	19.4 ± 4.0	0.31	0.28		0.53
γ-ν-j	1	4.5 ± 1.5	0.35	0.62		0.47
e-j-j-j	19	22 ± 6.5	0.84	0.80		0.14
ν-j-j-j	7	5.2 ± 1.4	0.47	0.39		0.017
γ-ν-j-j	0	0.16 ± 0.07	1	1		1
e-ν-j-j	0	0.15 ± 0.09	1	1		1
γ-e-j-j	0	0.22 ± 0.07	1	1		1
e-e-ν-j	0	0.10 ± 0.06	1	1		1
e-μ-ν-j	0	0.08 ± 0.05	1	1		1
j-j-j-j	40	33 ± 13				
e-j-j-j-j	1	0.13 ± 0.06				
ν-j-j-j-j	1	0.05 ± 0.02				
j-j-j-j-j	0	0.14 ± 0.09				

Table 1: Observed and predicted event yields for all event classes with observed data events or a SM expectation greater than 0.01 for all $e^{\pm}p$ data. Each event class is labeled with the leading body listed first. The errors on the predictions include model uncertainties and experimental systematic errors added in quadrature. The $\hat{P}$ values obtained in the scan of $\sum P_T$, $M_{\rm all}$, $\cos\theta^*_{\rm lead}$ and $X_{\rm lead}$ distributions are also given.

H1 General Search at HERA ($e^{\pm}p$, 463 pb^{-1})

Event class	Selection	Data	SM	$\hat{P}_{\sum P_T}$	$\hat{P}_{M_{\rm all}}$
j-j	$\cos\theta^*_{\rm lead} > 0$	83155	82800 ± 15610	0.46	0.44
e-j	$\cos\theta^*_{\rm lead} > 0$	6532	6603 ± 783	0.23	0.033
ν-j	$\cos\theta^*_{\rm lead} > 0$	2177	2076 ± 240	0.61	0.75
γ-j	$\cos\theta^*_{\rm lead} > 0$	123	118 ± 20	0.15	0.016
γ-e	$\cos\theta^*_{\rm lead} > 0$	227	260 ± 25	0.12	0.19
j-j-j	$\cos\theta^*_{\rm lead} > 0$	1359	1218 ± 340	0.36	0.63
e-j-j	$\cos\theta^*_{\rm lead} > 0$	65	74 ± 13	0.75	0.37
ν-j-j	$\cos\theta^*_{\rm lead} > 0$	58	53 ± 12	0.62	0.26
j-j-j	$0.75 < X_{\rm lead} < 0.9$	1672	1658 ± 482	0.096	0.40
e-j-j	$0.75 < X_{\rm lead} < 0.9$	419	419 ± 81	0.018	0.07
ν-j-j	$0.75 < X_{\rm lead} < 0.9$	133	109 ± 22	0.26	0.19

Table 2: Observed and predicted event yields for considered event classes after a cut on the topological variables. Each event class is labeled with the leading body listed first. The errors on the predictions include model uncertainties and experimental systematic errors added in quadrature. The $\hat{P}$ values obtained in the scan of $\sum P_T$ and $M_{\rm all}$ distributions are indicated in the last two columns.

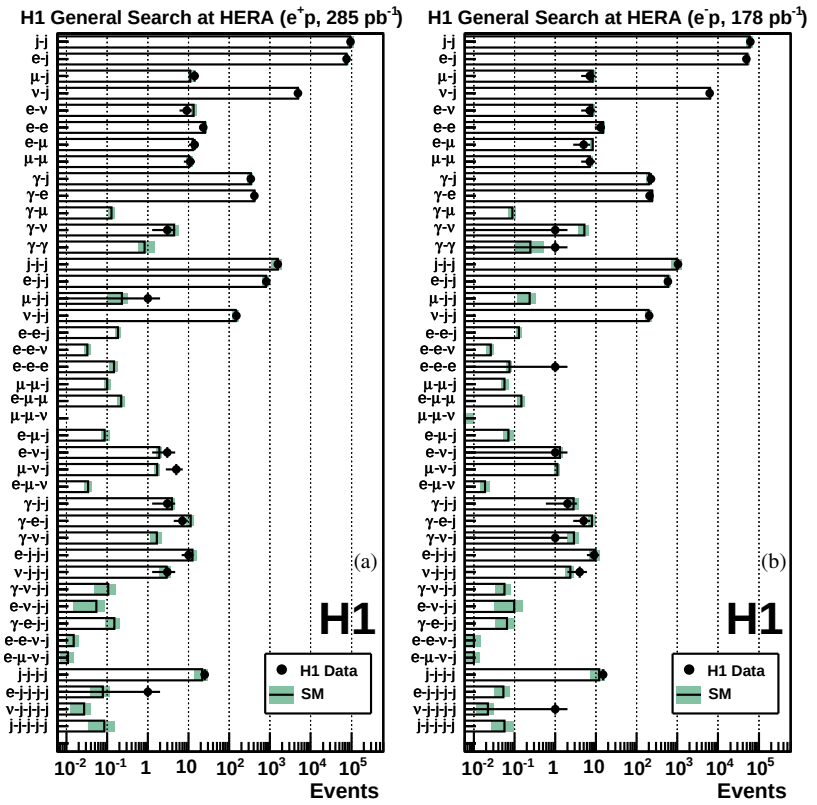

Figure 1: The data and the SM expectation for all event classes with observed data events or a SM expectation greater than 0.01 events for e^+p collisions (a) and e^-p collisions (b). The error bands on the predictions include model uncertainties and experimental systematic errors added in quadrature.

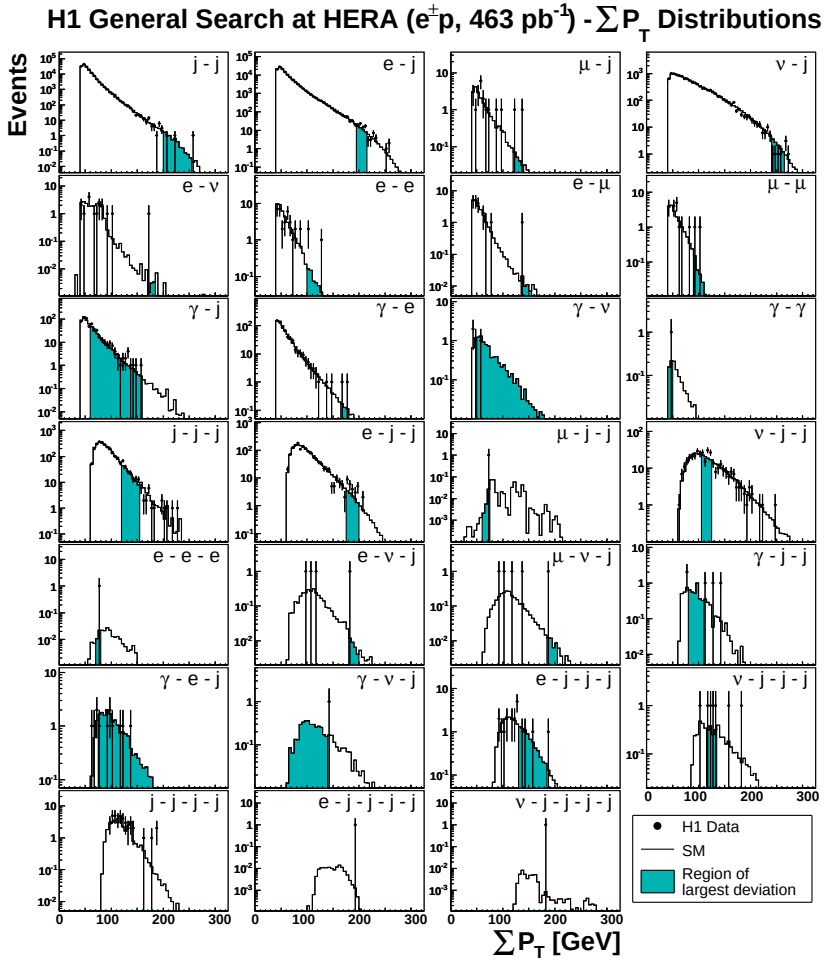

Figure 2: The number of data events and the SM expectation as a function of $\sum P_T$ for classes with at least one event. The shaded areas show the regions of largest deviation identified by the search algorithm. No such search is performed for the j-j-j-j, e-j-j-j-j and ν-j-j-j-j classes.

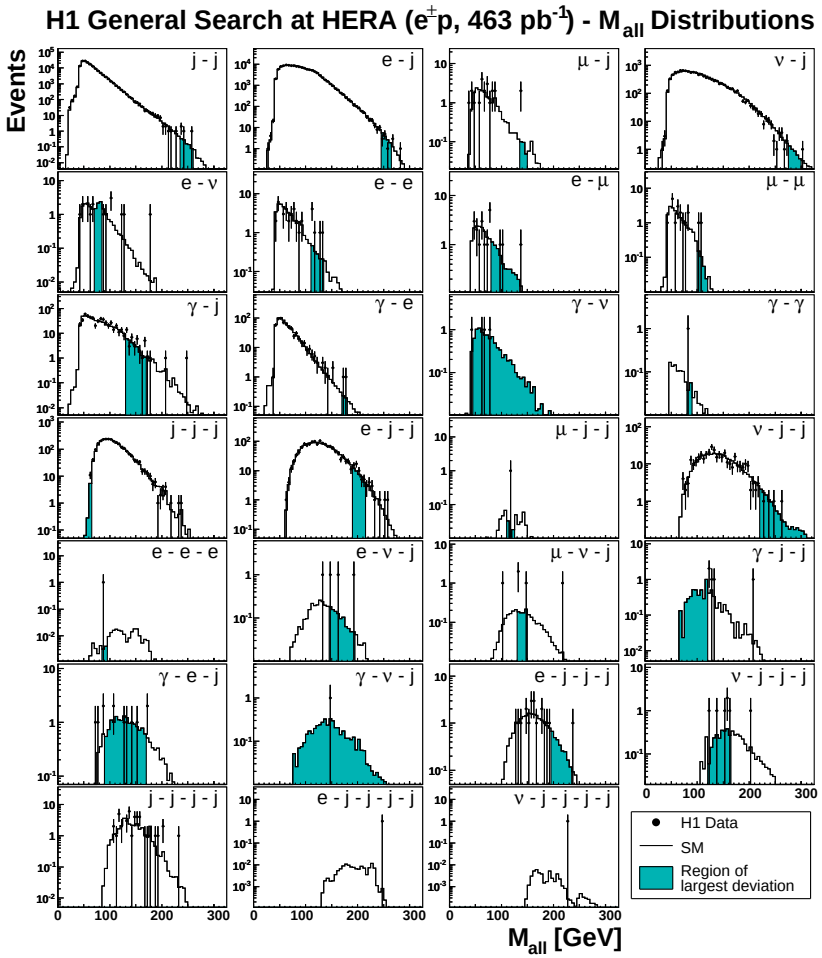

Figure 3: The number of data events and the SM expectation as a function of $M_{\rm all}$ for classes with at least one event. The shaded areas show the regions of largest deviation identified by the search algorithm. No such search is performed for the j-j-j-j, e-j-j-j and ν-j-j-j classes.

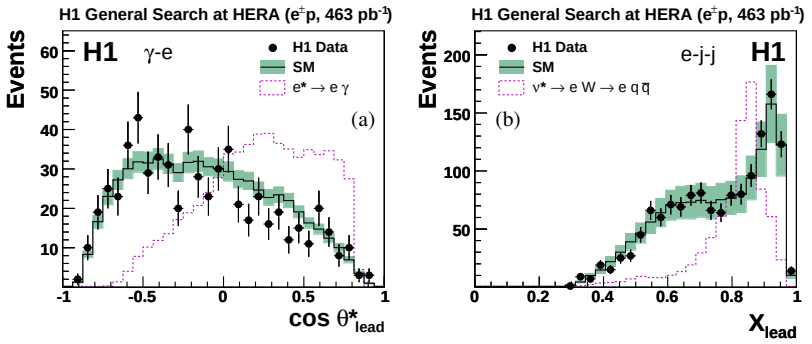

Figure 4: The $\cos\theta^*_{\rm lead}$ distribution in the γ-e event class (a) and the $X_{\rm lead}$ distribution in the e-j-j event class (b). The points correspond to the observed data events and the histograms to the SM expectation. The error bands on the SM prediction include model uncertainties and experimental systematic errors added in quadrature. The dashed line represents, with an arbitrary normalisation, the distribution corresponding to an exotic resonance with a mass of 200 GeV (e^* [41] in (a) and ν^* [42] in (b)).

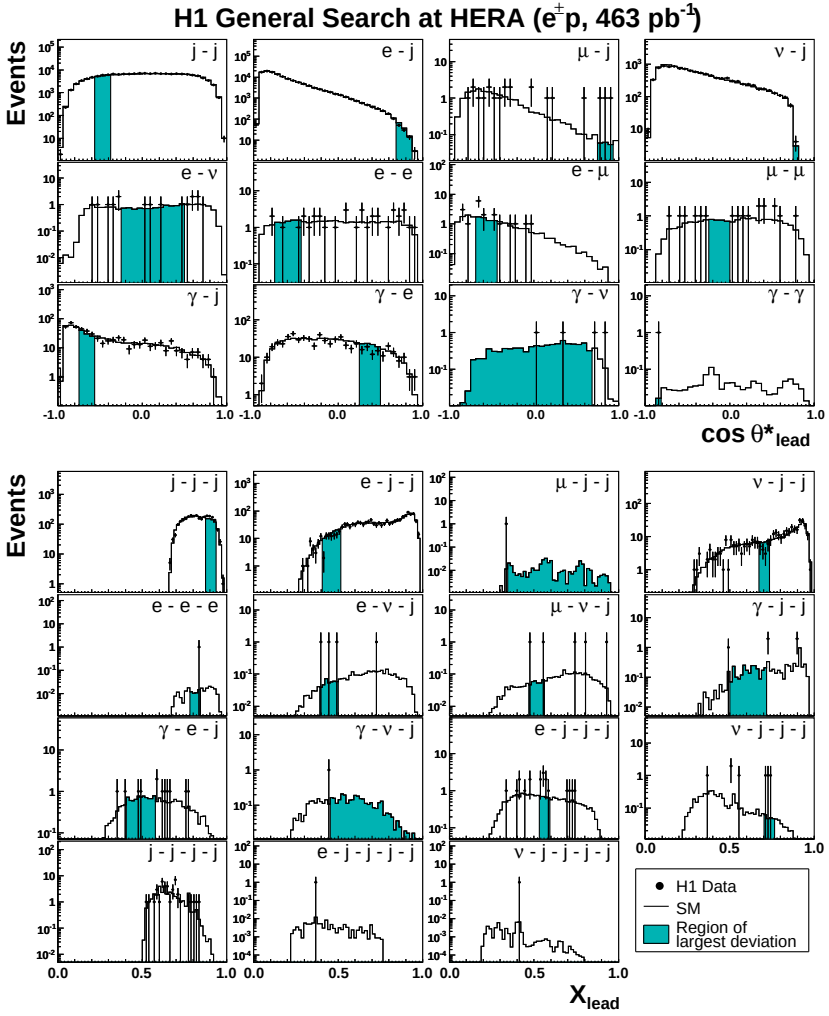

Figure 5: The distribution of $\cos\theta^*_{\rm lead}$ for event classes with two bodies (top) and of $X_{\rm lead}$ for event classes with more than two bodies (bottom). The points correspond to the observed data events and the open histograms to the SM expectation. Only event classes with at least one data event are presented. The shaded areas show the regions of largest deviation identified by the search algorithm. No such search is performed for the j-j-j-j, e-j-j-j-j and ν-j-j-j-j classes.

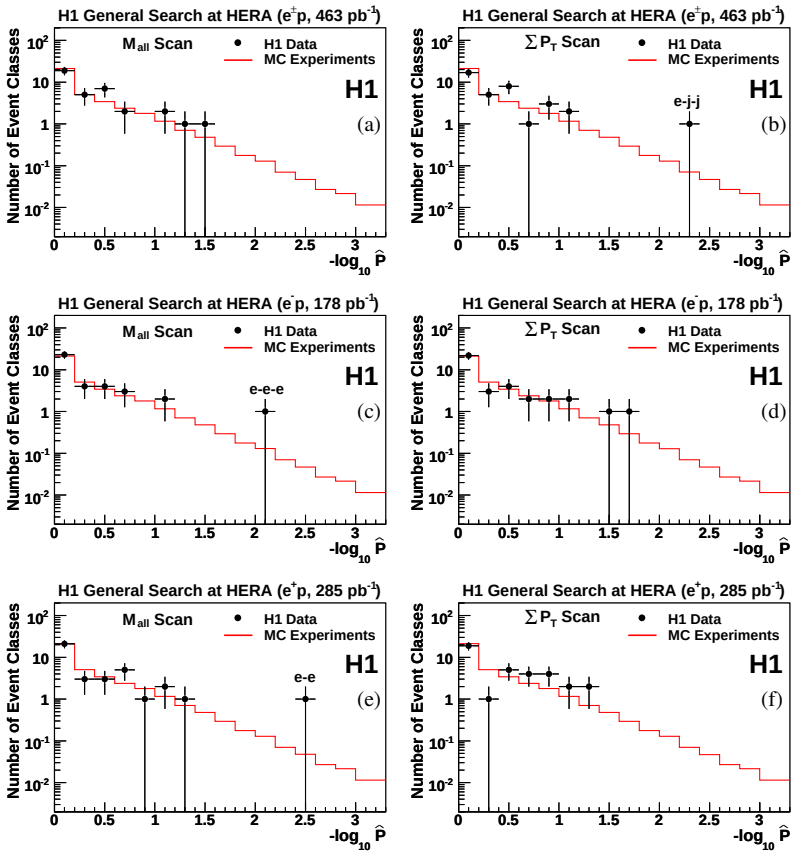

Figure 6: The $-\log_{10}\hat{P}$ values for the data event classes and the expected distribution from MC experiments as derived with the search algorithm by investigating the $M_{\rm all}$ distributions (left column) and $\sum P_T$ distributions (right column). The results of the scan are presented for all data (a and b), and separately for e^-p (c and d) and e^+p (e and f) data.